OBSERVATION AND ANALYSIS OF THE SPIN PERIOD VARIATIONS OF INACTIVE BOX-WING TELECOMMUNICATIONS SATELLITES IN GEOSYNCHRONOUS ORBIT

OBSERVATION ET ANALYSE DES VARIATIONS DES PÉRIODES DE ROTATION DES SATELLITES DE TÉLÉCOMMUNICATIONS NON-OPÉRATIONELS EN ORBITE GÉOSYNCHRONE

A Thesis Submitted to the Division of Graduate Studies of the

Royal Military College of Canada

by

Michael Anthony Earl, BSc

In Partial Fulfillment of the Requirements for the Degree of

Master of Science in Physics

May 2013

ROYAL MILITARY COLLEGE OF CANADA
COLLÈGE MILITAIRE ROYAL DU CANADA

DIVISION OF GRADUATE STUDIES AND RESEARCH
DIVISION DES ÉTUDES SUPÉRIEURES ET DE LA RECHERCHE

This is to certify that the thesis prepared by / Ceci certifie que la thèse rédigée par

MICHAEL ANTHONY EARL

entitled / intitulée

OBSERVATION AND ANALYSIS OF THE SPIN PERIOD VARIATIONS OF INACTIVE BOX-WING TELECOMMUNICATIONS SATELLITES IN GEOSYNCHRONOUS ORBIT / OBSERVATION ET ANALYSE DES VARIATIONS DES PÉRIODES DE ROTATION DES SATELLITES DE TÉLÉCOMMUNICATIONS NON-OPÉRATIONELS EN ORBITE GÉOSYNCHRONE

complies with the Royal Military College of Canada regulations and that it meets the accepted standards of the Graduate School with respect to quality, and, in the case of a doctoral thesis, originality, / satisfait aux règlements du Collège militaire royal du Canada et qu'elle respecte les norms acceptées par la Faculté des études supérieures quant à la qualité et, dans le cas d'une thèse de doctorat, l'originalité,

for the degree of / pour le diplôme de

MASTER OF SCIENCE – PHYSICS /
MAÎTRISE EN SCIENCES - PHYSIQUE

Signed by the final examining committee: /
Signé par les membres du comité examinateur de la soutenance de thèse

____________________, Chair / Président

___________________, External Examiner / Examinateur externe

_________________, Main Supervisor / Directeur de thèse principal

____

Approved by the Head of Department : /
Approuvé par le Directeur du Département :____________ Date:__________

To the Librarian: This thesis is not to be regarded as classified. /
Au Bibliothécaire: Cette thèse n'est pas considérée comme à publication restreinte.

____
Main Supervisor / Directeur de thèse principal

This thesis is dedicated to the following individuals who have greatly motivated and supported me throughout my many journeys in life:

Ms. Mary Theresa Earl
Mr. Anthony Lloyd Earl
Mrs. Viola Arsenault
Mr. Lowell O. Christiansen
Dr. David Paterson
Lt. Col. Philip W. Somers
Mr. Paul Gregory Comision
Mr. Alan Stones
Dr. Thomas J. Racey
Ms. Jane Elizabeth Yaeger

My deepest thanks to all of you.

ACKNOWLEDGEMENTS

I wish to thank Dr. Gregg Wade for his invaluable advice and assistance throughout the past two academic years.

I wish to thank Lt. Col. Philip Somers for his assistance and his always wise and professional leadership.

I wish to thank Robert (Lauchie) Scott at Defence Research and Development Canada (DRDC) for his valuable assistance.

I especially wish to thank Jane E. Yaeger for her extraordinary patience and her second-to-none editing skills.

AUTHOR’S STATEMENT

“This thesis represents the continuation of an exciting journey of discovery that began with observations of the Moon and planets through small backyard telescopes. This journey has exposed me to professional and scientific experiences that I had never imaged were possible. May the journey continue to motivate and inspire.”

Michael A. Earl

April 8, 2013

ABSTRACT

Earl, Michael Anthony

Master of Science (MSc) - Physics

Royal Military College of Canada

May 2013

Observation and Analysis of the Spin Period Variations of Inactive Box-wing Telecommunications Satellites in Geosynchronous Orbit

Supervisor: Dr. Gregg Wade

For a number of years, research has been conducted to determine the feasibility of rescue / salvage missions to geosynchronous (GEO) satellites. The success of any such mission would rely upon knowing the satellite's spin dynamics. In order to determine the true spin dynamics of a satellite, the external forces acting upon the satellite and the difference between the synodic spin rate and sidereal spin rate must be known.

The geosynchronous satellite population offers a large selection of research candidates that can be used to study the effects of external forces on their spin dynamics and to determine their true spin rates.

From a list of over 1,200 geosynchronous satellites, several inactive "box-wing" satellites were selected for study. The best candidates were unclassified inactive box-wing GEO telecommunications satellites that were detectable with small-aperture telescopes and charge-coupled device (CCD) cameras. These satellites were required to be accessible from the observation site in Sandhurst, Ontario for the majority of the time from March 2012 to March 2013. The satellites chosen for study were Solidaridad 1

(NORAD #22911), Telstar 401 (NORAD #22927), Echostar 2 (NORAD #24313) and Hughes-1 (HGS-1) (NORAD #25126).

A comprehensive observation strategy was developed to obtain images of the selected satellites from the chosen observation site. The time between observation sessions was normally several days to two weeks, weather permitting. Image data extraction software was developed in “Matrix Laboratory” (MATLAB) to extract the time tag and satellite flux data from all of the images in a timely manner.

The extracted time and flux data was used to produce light curves for each selected satellite. Similar and recurring light curve characteristics were used to identify the selected satellites’ apparent spin periods. The average apparent spin periods ranged from 160 seconds (for Telstar 401) to 1,550 seconds (for HGS-1).

The apparent spin periods for all four selected satellites were, for the first time, observed to vary with time. Telstar 401’s and Echostar 2’s apparent spin period variations appeared to vary in a periodic fashion. The spin period variation period of Telstar 401 was estimated to be 290 days. Echostar 2 appeared to have a 364-day spin period variation period. Solidaridad 1’s and HGS-1’s spin period variations were too slow to estimate their periods from the observations made over one year.

Outside of this research, little work has been done to determine the cause of these newly observed spin period variations. Satellite operators routinely correct for attitude drift due to solar radiation pressure (SRP) forces acting upon the satellite’s large solar panels. However, once the satellite is no longer active, the spacecraft’s attitude dynamics are no longer being monitored or controlled and therefore are less understood. This thesis explores the external disturbing forces that act to vary an inactive satellite’s apparent spin period.

This research has found that the combination of solar radiation pressure and the large cross-sectional area of the box-wing's solar panels were able to account for much of the observed spin period variation's amplitude. A simple theoretical model was developed which considered a small offset (< 1°) in the solar panels' relative orientations. However, when this theoretical model was compared with the observed spin period variation, discrepancies appeared. It was found that this model did not fully explain the period of the observed spin period variations, nor did it completely account for the observed spin period variations with time. To understand these discrepancies, a preliminary investigation of the potential synodic effects that could have contributed to the apparent observed spin period was performed.

Synodic spin period to sidereal spin period transformation equations were derived using three specific scenarios. These scenarios took into account the specific orientations of the satellite's spin axis relative to a reflecting surface. It was found that the second and third scenarios could account for the amplitude of the remaining variation.

RÉSUMÉ

Earl, Michael Anthony

Maîtrise en Sciences - Physique

Collège militaire royal du Canada

Mai 2013

Observation et Analyse des Variations des Périodes de Rotation des Satellites de Télécommunications Non-opérationels en Orbite Géosynchrone

Directeur de thèse: Dr. Gregg Wade

Pendant de nombreuses années, des études ont étés menées pour déterminer la possibilité de récupération des satellites de missions géosynchrones (GEO). Le succès de telles missions de récupération nécessite la connaissance de la rotation du satellite. Afin d'évaluer la rotation réelle du satellite, les forces externes agissant sur le satellite et la différence entre le taux de rotation synodique et le taux de rotation sidéral doit être connue.

Le nombre de satellites géosynchrones offre une large sélection de candidats qui peuvent être utilisés pour l'étude des effets des forces externes sur la rotation des satellites et pour déterminer leur mouvement réel.

Plusieurs satellites "box-wing" sont sélectionnés à partir d'une liste de plus de 1200 satellites géosynchrones. Les meilleurs candidats sont des satellites de télécommunications GEO box-wing inactifs que peuvent être détectés avec des télescopes à petite ouverture et des appareils photographiques équipés de "charge-coupled device" (CCD). Ces satellites doivent aussi être visible du site d'observation à Sandhurst en

Ontario durant la période de mars 2012 à mars 2013. Les satellites choisis pour cette étude sont les satellites Solidaridad 1 (NORAD #22911), Telstar 401 (NORAD #22927), Echostar 2 (NORAD #24313) et Hughes-1 (HGS-1) (NORAD #25126).

Une stratégie d'observation exhaustive fût développée pour obtenir les images des satellites choisis à partir du site d'observation. Le temps entre les sessions d'observation varie en général de quelques jours à deux semaines, dépendent des effets météorologiques. Le logiciel de traitement des données est développé avec "Matrix Laboratory" (MATLAB) pour extraire le temps et le flux de données des satellites des images.

Les données extraites sont utilisées pour produire des courbes de lumière pour chaque satellite. Des courbes de lumière similaires et périodiques permettent d'identifier la rotation apparente de chaque satellite. Les moyennes des périodes de rotation apparentes vont de 160 secondes (pour Telstar 401) à 1550 secondes (pour HGS-1).

La variation temporelle des périodes de rotation apparentes des satellites choisis est observée pour la première fois. Les périodes de rotation de Telstar 401 et Echostar 2 semble varier de façon périodique avec une période de 290 jours et 364 jours respectivement. Les variations temporelles de la période de rotation de Solidaridad 1 et HGS-1 sont trop lente pour pouvoir évaluer leurs périodicités durant une seule année d'observation.

En dehors de l'étude présentée ici, il y a peu de recherche visant à déterminer la cause de ces nouvelles observations des variations temporelles des périodes de rotation. Les opérateurs de satellites corrigent systématiquement pour les changements d'attitudes dues aux forces liées à la pression de la radiation solaire (PRS) agissant sur les larges panneaux solaires des satellites. Cependant, une fois que le satellite n'est plus en

opération, la dynamique de l’attitude du vaisseau n’est plus suivie ou contrôlée et donc elle est moins bien comprise. Le travail présenté dans cette thèse examine les forces externes perturbatrices qui agissent sur un satellite inactif et font varier sa période de rotation apparente.

Cette étude a déterminé que la combinaison entre la pression de la radiation solaire et l’aire effective des panneaux solaire d’un satellite "box-wing" est la cause principale de la variation de l’amplitude de la période de rotation. Un modèle simplifié fût développé considérant un petit décalage (< 1°) de l’orientation relative des panneaux solaires. Cependant, la comparaison de ce modèle avec les valeurs observées de la période de rotations est divergente. Le modèle n’explique pas complètement les variations des périodes de rotation observées et ne prend pas en compte les variations temporelles. De façon à comprendre ces différences, une étude préliminaire des effets du potentiel synodique qui peut avoir contribué aux variations de la période de rotation fût effectuée.

Les équations de transformation de la période de rotation synodique à la période de rotation sidérale furent dérivées à l’aide de trois scénarios. Ces trois scénarios prennent en compte les orientations spécifiques de l’axe de rotation du satellite relativement à une surface réfléchissante. Le second scénario et le troisième scénario peuvent expliquer le restant des variations de l’amplitude.

TABLE OF CONTENTS

LIST OF TABLES

LIST OF FIGURES

LIST OF SYMBOLS

°	Degrees of Arc
‘	Minutes of Arc (Arc-minutes)
“	Seconds of Arc (Arc-seconds)
$\mathbf{a}$	Distance from Center of Satellite “Box” to Closest Edge of Solar Panel
$\mathbf{a}$	Semi-Major Axis
$\mathbf{A}$	Area
α	Angular Acceleration
α	Right Ascension
$\mathbf{b}$	Semi-Minor Axis
β	Phase Angle Bisector
$\mathbf{c}$	Speed of Light in Vacuum
°C	Degrees Celsius of Temperature
$\mathbf{C}_{\mathbf{drag}}$	Atmospheric Drag Coefficient
$\mathbf{D}$	Dipole Moment
δ	Declination
$\mathbf{e}$	Orbit Eccentricity
$\mathbf{e}^{-}$	Electrons
$\mathbf{F}$	Force
γ	Angular Separation
γ	Apparent Spin Angle
η	Angle between Spin Axis Unit Vector and Surface Normal Unit Vector
$\mathbf{H}$	Angular Momentum
$\mathbf{i}$	Orbit Inclination
$\mathbf{I}$	Moment of Inertia (Rotational Inertia)
$\mathbf{I}$	Infrared Magnitude
l	length
λ	Geodetic Latitude on the Earth
$\mathbf{M}$	Magnetic Moment of the Earth
$\mathbf{M}$	Mass
μ	Angle Difference of Right Ascension (ΔRA)
μ	Gravitational Parameter of the Earth
$\hat{\mathbf{n}}$	Surface Normal Unit Vector
ν	Orbit True Anomaly
$\mathbf{P}$	Pressure
$\rho_{\mathbf{atm}}$	Atmospheric Density
ρ	Phase Angle
ψ	Azimuthal Angle of Sidereal Spin
$\mathbf{q}$	Reflectivity Coefficient
θ	Sunlight Incidence Angle
ϕ	Orientation Angle between Solar Panels
Φ	Solar Radiation Flux
$\mathbf{r}_{\mathbf{CM}}$	Distance between Center of Mass of “Box” and Center of Mass of Solar Panel
$\mathbf{R}$	Orbit Radius (Distance of Satellite from Earth’s Center)
$\mathbf{R}$	Reflectivity

$\mathbf{t}$	Time
$\mathbf{T}$	Period
$\mathbf{T_{side}}$	Sidereal Spin Period
$\mathbf{T_{syn}}$	Synodic Spin Period
$\mathbf{T}$	Period (of Wavelength Cycle)
$\mathbf{T}$	Telsa
$\boldsymbol{\tau}$	Torque
$\mathbf{v}$	Velocity
$\mathbf{V}$	Visual Magnitude
$\boldsymbol{w}$	width
$\boldsymbol{\omega}$	Angular Velocity
$\boldsymbol{\omega}_{\mathbf{side}}$	Sidereal Angular Velocity
$\boldsymbol{\omega}_{\mathbf{syn}}$	Synodic Angular Velocity
$\boldsymbol{\Omega}$	Ascending Node
$\boldsymbol{\chi}$	Synodic Offset Angle

LIST OF ABBREVIATIONS

3-J	Triple Junction (Solar Cell)
AAS	American Astronautical Society
ABC	American Broadcasting Company
ACTS	Advanced Communications Technology Satellite
ADCS	Attitude Determination and Control System
ADU	Analogue-Digital Units
AEOS	Advanced Electro Optical System
AGI	Analytical Graphics Incorporated
AMOS	Air Force Maui Optical and Supercomputing observatory
BOL	Beginning of Life (of Satellite)
BSS	Boeing Satellite Services
BWGS	Belgian Working Group Satellites
CASTOR	Canadian Satellite Tracking and Optical Research
CBS	Columbia Broadcasting Service
CCD	Charge-Coupled Device
CM	Center of Mass
CME	Coronal Mass Ejection
COSPAR	Committee on Space Research
CSC	CASTOR Satellite Catalogue
dA	Infinitesimal Area
dd	Days
Dec.	Declination
dF	Infinitesimal Force
DRDC	Defence Research and Development Canada
dτ	Infinitesimal Torque
ECF	Earth-Centered Fixed
ECI	Earth-Centered Inertial
EM	Electro-magnetic
EOL	End of Life (of Satellite)
FITS	Flexible Image Transport System
FOV	Field of View
GaAs	Gallium-Arsenide (Solar Cell)
GEO	Geosynchronous Earth Orbit or “Geosynchronous”
GOES	Geostationary Operational Environmental Satellite
GPS	Global Positioning System
GTO	Geosynchronous Transfer Orbit
HEO	High Earth Orbit
HGS	Hughes Global Services
HP	High Power
hr	Hours
Hz	Hertz (Frequency)
ID	Identification
IMAGE	Imager for Magnetopause-to-Aurora Global Exploration
ISAPE	International Symposium on Antennas, Propagation and EM Theory

ISS	International Space Station
LAGEOS	Laser Geodynamics Satellite
LEO	Low Earth Orbit
MATLAB	Matrix Laboratory
MEO	Medium Earth Orbit
MOI	Moment of Inertia
N/A	Not Applicable
NaN	Not a Number (MATLAB)
NASA	National Aeronautics and Space Administration
NCP	North Celestial Pole
NORAD	North American Aerospace Defense Command
NTP	Network Time Protocol
OS	Operating System
PA	Phase Angle
PAB	Phase Angle Bisector
PAS	PanAmSat
PBS	Public Broadcasting Service
PPAS	Photometric Periods of Artificial Satellites
RA	Right Ascension
RASC	Royal Astronomical Society of Canada
RMC	Royal Military College of Canada
RR	Railroad
RSO	Resident Space Object
SBIG	Santa Barbara Instrument Group
SBS	Satellite Business Systems
SCP	South Celestial Pole
SLR	Satellite Laser-Ranging
S/N	Signal to Noise Ratio
SRP	Solar Radiation Pressure
SSN	Space Surveillance Network
SSO	Sayan Solar Observatory
SSRAL	Space Surveillance Research and Analysis Laboratory
STK	Satellite Tool Kit
TLE	Two Line Element
TRM	Tracking Rate Mode
U.S.	United States
USA	United States of America
USB	Universal Serial Bus
UTC	Universal Time Coordinate
UT	Universal Time

CHAPTER 1: INTRODUCTION

Every satellite that has ever been launched into Earth orbit has been perturbed by forces from solar emissions, the Earth's magnetic field, atmospheric drag and/or gravity from the Earth, Moon and Sun. More specifically, a satellite's orientation in space (its attitude) will be perturbed by these forces unless compensating forces are present. Many satellites are equipped with attitude determination and control systems (ADCS), not only to point sensors and antennas towards intended targets, but also to compensate for external torques that will otherwise change the spacecraft's attitude.

For example, several Canadian geostationary satellites that were procured and operated by Telesat Canada, deliver satellite television, high-speed internet, telephone and other vital data services to their customers 24 hours a day, 7 days a week[1]. The orbits and attitudes of these satellites have to be rigidly controlled by their on-board ADCS systems or the aforementioned forces will, in a short time, move the satellites out of contact with their customers.

A "geostationary satellite" orbits in the same plane as the Earth's equator at an altitude of 35,786 km [2], as shown in Figure 1.1. At this altitude, the satellite's orbit period is the same as the Earth's rotation period; 23 hours, 56 minutes and 4 seconds (one sidereal day)[3]. As a result, the satellite will appear to an Earth-bound observer to be stationary in his/her local sky. This is why it is not necessary for satellite television subscribers to move their satellite dishes. If an observer were to take a several-second exposure image of a geostationary satellite, the stars would appear to streak by, but the

---

[1] Telesat Canada: http://www.telesat.com/about-us/why-satellite

[2] Vallado, D.; Fundamentals of Astrodynamics and Applications – 3rd. ed.; p. 31

[3] Chapman, D.M.F. ed.; Observer's Handbook 2013 – The Royal Astronomical Society of Canada; p.29

satellite would appear to be a stationary dot. The satellite would actually be moving, however it is moving at a relative angular velocity of 0 with respect to the Earth's surface.

Figure 1.2 shows a 10-second exposure image of Anik F1 and Anik F1-R; two co-located geostationary satellites owned by Telesat. The streaks are background stars. The telescope used to capture this image had its tracking turned off so it was not moving with respect to the Earth's surface; however it was still moving at the same rate as the Earth's rotation.

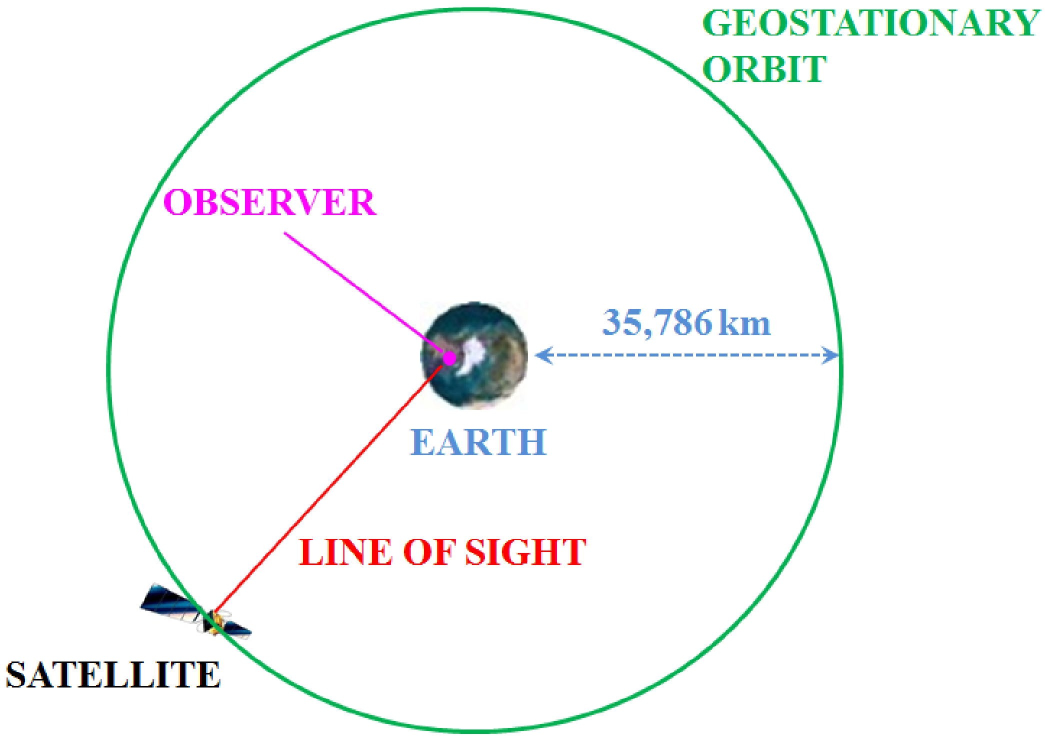

Figure 1.1: The Geostationary Satellite Orbit

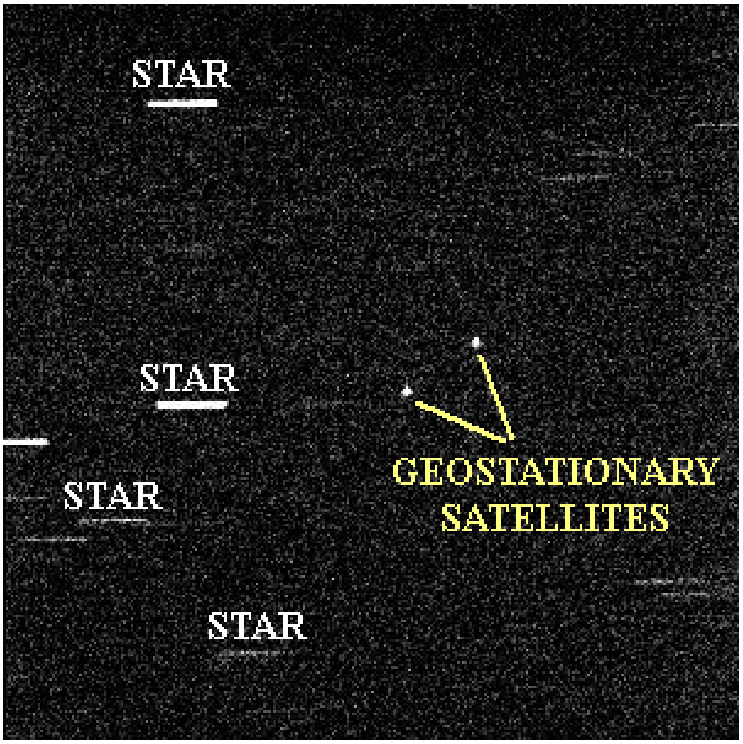

Figure 1.2: 10-Second Exposure of Anik F1 and Anik F1-R Geostationary Satellites[4]

When a geostationary satellite can no longer reliably perform its duties for its customers, the owner maneuvers the satellite into a "graveyard orbit" where it will orbit with other derelict GEO satellites for an indefinite period of time. When the satellite is shut down, its ADCS is also shut down. This means that the newly derelict satellite's orbit and attitude will be at the mercy of the solar, magnetic, atmospheric and gravitational forces.

Once shut down, all derelict satellites will begin to spin around their centers of mass. These satellites can be considered rigid (solid) bodies and therefore will be subject to rigid body dynamics. They will all have an angular velocity about some spin axis and an angular acceleration due to the torques caused by the external forces acting upon them.

---

[4] Earl, Michael A.; A Sea of Satellite Dishes; Royal Astronomical Society of Canada; http://ottawa-rasc.ca/articles/earl_mike/Satellite_Tracking/Dishes/Satellite_Dishes.html

The external forces will also slowly change the orbit of the satellite. The satellite's orbit plane will gradually incline with respect to the Earth's equatorial plane and the orbit's shape will no longer be nearly circular. A "geosynchronous" satellite orbits with (nearly) the same period as the Earth's rotation but in a plane that can be inclined to the Earth's equatorial plane, as shown in Figure 1.3. The abbreviation "GEO" can be used for either geostationary or geosynchronous orbits. A geostationary orbit can be considered a special type of geosynchronous orbit.

When an observer on Earth observes a geosynchronous satellite over time, the satellite might not be seen to be sitting in one spot in the sky. Over one GEO orbit period, a very thin "Figure 8" will be seen to be traced out in the local sky because of the satellite's inclined and slightly eccentric orbit. Most of this apparent motion is perpendicular to the Earth's equatorial plane. If an observer sees a portion of a GEO's "Figure 8" pattern over several hours, it is normally indicative of a derelict satellite with an inclined orbit.

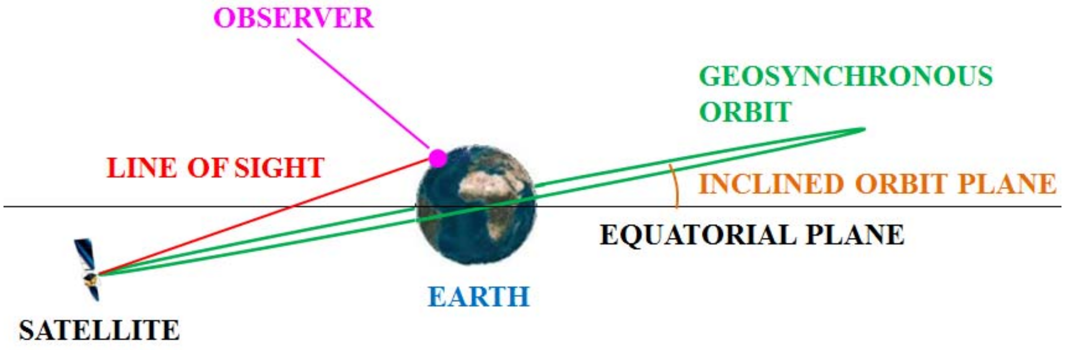

Figure 1.3: The Geosynchronous Satellite Orbit

When observing a derelict (inactive) geosynchronous satellite over time using a telescope and a digital camera, a varying brightness over time, or "light curve" will be detected. This light curve will be the result of the satellite's spinning motion as different parts of the satellite are being illuminated by the Sun and sunlight is reflected off of these parts to the observer. Most geostationary satellites are designed for practicality and not aesthetics, so the reflectivity of each part of the satellite will be different. As a result, the light curve might appear choppy because each surface will have its own unique reflectivity and its own unique location on the satellite. The light curve that the observer sees at any one time will depend on the satellite's spin rate, the satellite's geometry, the satellite surface's reflectivity and the orientation of the satellite's spin axis relative to the observer and to the light source (the Sun).

A light curve of the inactive Olympus 1 geosynchronous satellite is shown in Figure 1.4. The light curve has a periodic signature because the satellite is spinning about some axis, showing the same parts of the satellite to the Sun with each complete spin. However, the satellite's orbit motion will change the perspective from which the observer sees the reflected sunlight. Therefore, the observer would see a slow change in the light curve over time.

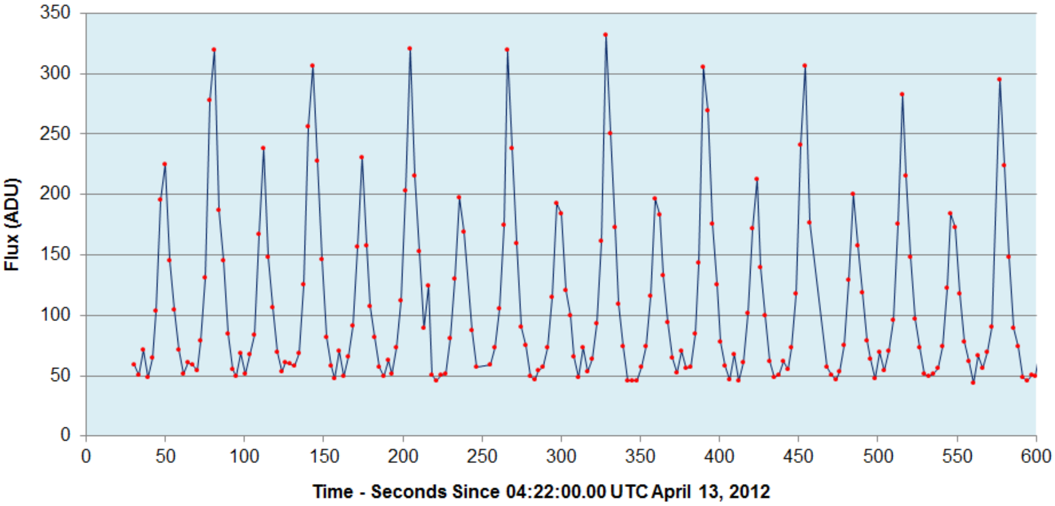

Figure 1.4: Light Curve of Inactive Geosynchronous Satellite Olympus 1[5]

---

[5] Earl, Michael A.; Observation of the Olympus 1 Inactive GEO Box-wing Satellite: April 13, 2012 (UTC)

An inactive satellite's apparent spin period can be determined by measuring the time elapsed between recurring similar characteristics of the light curve; for example, two adjacent peaks (maxima) of distributions that possess similar shapes and widths. In this way, a satellite's apparent spin period can be monitored for an extended period of time to observe any variations of this spin period.

In several studies (see Chapter 2), the apparent spin periods of several geosynchronous satellites have been reported to vary, at different rates, over time spans of several years. However, in most of these studies, the frequency of the observations (temporal resolution) was low; normally several weeks to several years between observations. Although these studies clearly indicated that the satellites' apparent spin periods were varying in the long term, they did not show how much they were varying in the short term. One aim of this thesis was to observe several inactive geosynchronous satellites over a one year time span to observe their apparent spin periods in greater resolution; approximately one observation every two weeks or less, weather permitting.

One type of geosynchronous satellite of particular interest is the "box-wing" type, illustrated in Figure 1.5. This satellite design has been used from 1975 to the present day[6]. The "box-wing" has a cubical central bus structure (the "box") with two large solar panels (the "wings") attached to opposite sides of the "box". The solar panels generate the power required to operate the satellite.

The dynamics of the inactive "box-wing" geosynchronous satellites are not presently well understood. A primary aim of this thesis is to better understand how external forces influence the dynamics of this type of inactive satellite.

---

[6] Lockheed Martin Press Release; Lockheed Martin Commercial GEO Satellites Surpass 1,000 Years in Orbit

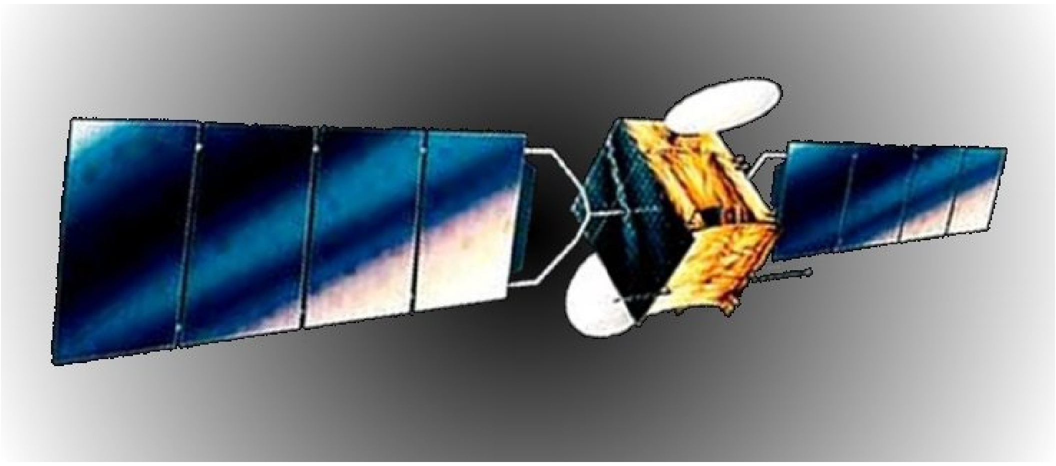

Figure 1.5: Artist's Conception of the American "Echostar 2" Box-wing Satellite [7]

The retrograde motion of a solar system planet observed from the Earth is caused by the relative motion of the planet and the Earth as they both orbit the Sun. The apparent orbit period of the planet as seen from the Earth is called the planet's "synodic orbit period". The synodic orbit period of a solar system planet can be very different from its true (sidereal) orbit period. For example, the planet Mars has a sidereal orbit period of 687 days and a synodic orbit period of 780 days[8].

A spinning inactive geosynchronous satellite will have a relative motion with respect to the incoming sunlight and to the observer as it orbits the Earth. As a result the observer will see the satellite's "synodic spin period" and not its true (sidereal) spin period. The determination of the sidereal spin period using observations of the synodic spin period has been accomplished for geosynchronous satellites with cylindrical designs, such as the HS-376 types (see Chapter 2), but not for the "box-wing" designs. This thesis offers a preliminary investigation into the primary factors that cause a spinning "box-wing" geosynchronous satellite to appear to spin with a specific synodic spin period.

---

[7] Dirk Krebs, Gunter; "Gunter's Space Page": http://space.skyrocket.de/doc_sdat/echostar-1.htm

[8] Chapman, D.M.F. ed.; Observer's Handbook 2013 – The Royal Astronomical Society of Canada; p.23

From March 5, 2012 to March 31, 2013, light curves of several selected inactive "box-wing" geosynchronous telecommunications satellites were obtained using ground-based optical observations. The satellites' synodic spin periods were determined by measuring the time elapsed between similar recurring characteristics of the light curve. The apparent variation of each satellite's spin period was plotted to monitor how it varied over time.

Variations of the synodic spin periods were analyzed to determine the most likely external forces that were acting on each of the satellites. Models based on the most likely external forces were fitted to the observed spin period variations. This was done to estimate the deviations from the ideal curves. Finally, the maximum deviation between the ideal curves and the observed plots were used to estimate the differences between the synodic and sidereal spin periods.

The primary goals of this thesis were:

i. to select several accessible inactive box-wing GEO satellites that would be suitable for study from March 2012 to March 2013 (Chapter 3 and Chapter 8);
ii. to develop an observation and data collection strategy that would be used to obtain light curves of the selected box-wing GEO satellites (Chapter 4);
iii. to develop reliable light curve generation software that would automatically extract time and brightness data from all images obtained of the inactive GEO satellites (Chapter 5 and Chapter 6);
iv. to monitor the apparent spin periods of the selected inactive GEO satellites from March 2012 to March 2013 (Chapter 7 and Chapter 9);

v. to determine the most likely cause of apparent spin period variation of the selected inactive box-wing GEO satellites using the satellites' estimated moments of inertia (Chapter 10 to Chapter 13);

vi. to develop a preliminary theoretical model of how solar radiation pressure affects the attitude of an inactive box-wing satellite (Chapter 14);

vii. to subtract the theoretical solar radiation pressure effects from the observed spin period variations in order to determine the remaining effects on a satellite's attitude (Chapter 14); and

viii. to develop a theoretical analytical relationship between a satellite's synodic (observed) spin periods and their sidereal (true) spin periods (Chapter 15).

CHAPTER 2: LITERATURE REVIEW

The first geosynchronous satellite, Syncom 1, had an attitude control system on board for antenna-pointing[9]. Therefore, the effects of external torques on a spacecraft's attitude have been known since the early days of satellite communications. Solar emissions, the gravity gradients of the Earth and the Moon, the magnetic field of the Earth and, in some cases, atmospheric drag, continuously attempt to affect the attitudes of our man-made satellite population. All of the presently active box-wing GEO satellites contain an attitude determination and control system (ADCS) that continuously analyzes, and corrects for, the drift from optimal operational attitude that is due to any of the aforementioned external torques.

Inactive satellites no longer have a functioning ADCS and therefore they are all subject to attitude disturbance torques, most of which are dependent on the satellite's altitude above the Earth's surface. The largest disturbances that can affect a satellite's attitude are atmospheric drag, Earth's magnetic field, gravity gradient and solar radiation pressure. Only the disturbances caused by solar radiation pressure influence the spacecraft independently of its altitude[10].

In-depth investigations of inactive satellites' apparent spin period variations are not often discussed in the literature[11]. However, several sources describe long-period apparent spin period observations of several satellites, some of which are of box-wing design. The Belgian Working Group of Satellites' (BWGS) "Photometric Periods of

---

[9] Glover, D.; NASA Experimental Communications Satellites; Beyond the Ionosphere: Fifty Years of Satellite Communication; The NASA History Series; p.55

[10] Wertz, J.; Orbit Constellation Design and Management; p.171

[11] Papushev, P. et al.; Investigations of the evolution of optical characteristics and dynamics of proper rotation of uncontrolled geostationary artificial satellites; Advances in Space Research 43 (2009); p.1416

Artificial Satellites” (PPAS) is an electronic catalogue of the apparent flash periods of satellites. The catalogue is based mainly on optical observations of satellite specular sunlight reflections by amateur astronomers obtained with hand-held binoculars and optical telescopes compiled from 1962 to the present day[12]. The catalogue currently contains flash period data for nearly 2,500 individual satellites that have been launched over this time period. A “flash period” is normally defined as the period of time between (observable) specular reflections.

The flash period data in the PPAS catalogue include the COSPAR identifier of the satellite, the date and time of observation, the observer identification (observer’s initials), the calculated flash period, the calculated accuracy (uncertainty) of the flash period, the number of complete flash periods observed and the perceived brightness (visual magnitude) of the flashes. A sample of the PPAS flash period data for the Iranian satellite “Navid” (COSPAR #12-005A) and its corresponding Safir 2 rocket body (COSPAR #12-005B) is shown in Figure 2.1. No headers were included in the original file, but explanations of the text format are described at the PPAS website (see Chapter 17: References).

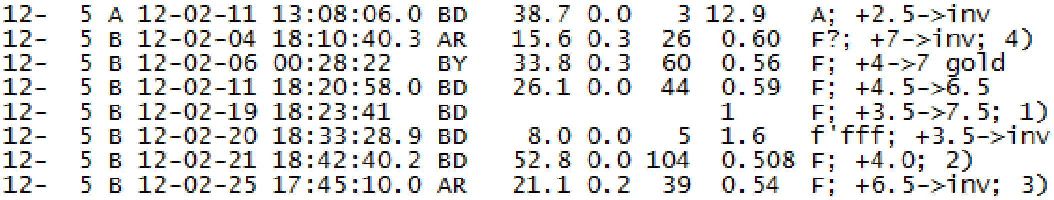

```
12-   5 A 12-02-11 13:08:06.0 BD   38.7 0.0   3 12.9   A; +2.5->inv
12-   5 B 12-02-04 18:10:40.3 AR   15.6 0.3  26  0.60  F?; +7->inv; 4)
12-   5 B 12-02-06 00:28:22   BY   33.8 0.3  60  0.56  F; +4->7 gold
12-   5 B 12-02-11 18:20:58.0 BD   26.1 0.0  44  0.59  F; +4.5->6.5
12-   5 B 12-02-19 18:23:41   BD                1      F; +3.5->7.5; 1)
12-   5 B 12-02-20 18:33:28.9 BD    8.0 0.0   5  1.6   f'fff; +3.5->inv
12-   5 B 12-02-21 18:42:40.2 BD   52.8 0.0 104  0.508 F; +4.0; 2)
12-   5 B 12-02-25 17:45:10.0 AR   21.1 0.2  39  0.54  F; +6.5->inv; 3)
```

Figure 2.1: PPAS Flash Period Observations of the “Navid” Satellite and its Rocket[13]

Papushev et al. investigated the optical characteristics of the inactive GEO satellites that were observed by the Sayan Solar Observatory (SSO) from 1995 to 2003[14].

---

[12] Papushev, P. et al.; Investigations of the evolution of optical characteristics and dynamics of proper rotation of uncontrolled geostationary artificial satellites; Advances in Space Research 43 (2009); p.1420

[13] McCants, M.; PPAS Database; http://www.prismnet.com/~mmccants/bwgs/

An example light curve of the inactive Raduga 14 GEO satellite from SSO observations is shown in Figure 2.2. The light curve shows a complex periodic behaviour with repeating maxima of nearly constant amplitude in the 250-second sampling time. Most of the satellites surveyed were the Russian Raduga (rainbow), Gorizont (horizon) and Ekran (eye) type[15], all of which strongly resemble the box-wing design shown in Figure 1.1. Papushev et al. concluded that the apparent spin periods of most of these satellites were varying at different rates[16]. The authors attributed this variation to internal and/or external forces acting on the satellite. The internal forces included the momentary reactivation of reaction wheels (gyroscopes) and, to a lesser extent, the sloshing of unspent maneuvering fuel. The external forces included solar radiation pressure, the Lorentz force (which is caused by the charged satellite moving within the Earth's magnetic field), and micro-jets caused by small holes in the satellites' pressurized cabins[17]. However, the authors did not elaborate further on the overall cause of the observed spin period variations.

---

[14] Papushev, P. et al.; Investigations of the evolution of optical characteristics and dynamics of proper rotation of uncontrolled geostationary artificial satellites; Advances in Space Research 43 (2009); p.1417

[15] Papushev, P. et al.; Investigations of the evolution of optical characteristics and dynamics of proper rotation of uncontrolled geostationary artificial satellites; Advances in Space Research 43 (2009); p.1418

[16] Papushev, P. et al.; Investigations of the evolution of optical characteristics and dynamics of proper rotation of uncontrolled geostationary artificial satellites; Advances in Space Research 43 (2009); p.1420

[17] Papushev, P. et al.; Investigations of the evolution of optical characteristics and dynamics of proper rotation of uncontrolled geostationary artificial satellites; Advances in Space Research 43 (2009); p.1420

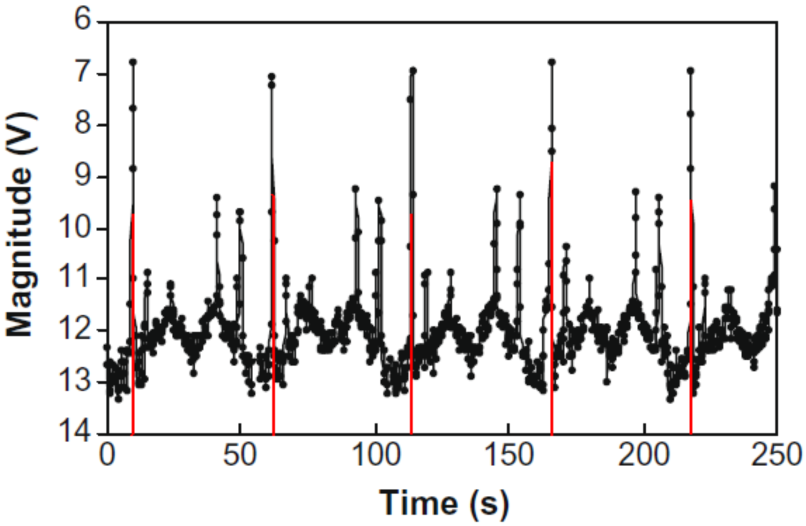

Figure 2.2: Light Curve of GEO Satellite Raduga 14[18]
Red Lines Added to Show Apparent Spin Period
"V" Stands for Visual Magnitude

Papushev et al. indicated that the sharp spikes (long and thin distributions) seen in the light curve in Figure 2.2 resulted from specular reflections from Raduga 14's solar panels[19]. In contrast, the light curve of Ekran 2, shown in Figure 2.3, did not exhibit any of these sharp spikes. Papushev, et al. concluded that they had confirmed the break-up of Ekran 2 (originally reported by the Soviet government in the late 1980's[20]) due to the lack of these sharp spikes in its light curve[21].

Karavaev et al. (2005) also used the SSO to obtain light curves of the Ekran 2 and Ekran 4 satellites from January 21, 2004 to April 24, 2004. They found that Ekran 2's

---

[18] Papushev, P. et al.; Investigations of the evolution of optical characteristics and dynamics of proper rotation of uncontrolled geostationary artificial satellites; Advances in Space Research 43 (2009); p.1418

[19] Papushev, P. et al.; Investigations of the evolution of optical characteristics and dynamics of proper rotation of uncontrolled geostationary artificial satellites; Advances in Space Research 43 (2009); p.1419

[20] Whitlock, D.; History of On-orbit Satellite Fragmentations – 13th ed.; May 2004; Orbital Debris Program Office; NASA; p. 3

[21] Papushev, P. et al.; Investigations of the evolution of optical characteristics and dynamics of proper rotation of uncontrolled geostationary artificial satellites; Advances in Space Research 43 (2009); p.1422

apparent spin period was nearly constant at about 69 seconds[22] but Ekran 4's apparent spin period varied between 5.18 seconds and 232.26 seconds[23]. The NORAD satellite catalogue currently indicates that the Ekran 2 satellite has four detectable pieces of debris while the Raduga 14 and Ekran 4 satellites have none[24]. This implies that Ekran 2 could have lost its solar panels due to the break-up.

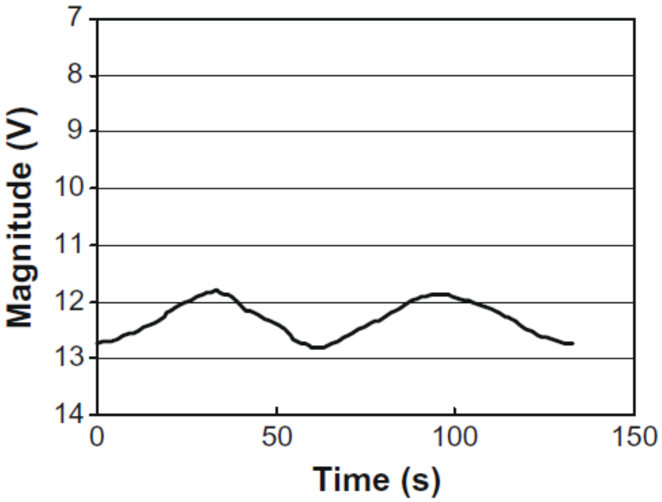

Figure 2.3: Light Curve of GEO Satellite Ekran 2[25]

Papushev et al. compared some of their long-term apparent spin period measurements with those obtained from the PPAS database. The comparisons for Gorizont 16, Gorizont 14 and ETS-6 are shown in Figure 2.4. The hollow squares in the figure indicate the data that Papushev et al. obtained for the same satellites using SSO data.

---

[22] Karavaev, Yu. et al.; Astrophotometrical Observation of Artificial Satellites and Study of the Technical Status of Parental Bodies of Space Debris at Geostationary Ring; Proceedings of the Fourth Conference on Space Debris, 18-20 April 2005; p.160

[23] Karavaev, Yu. et al.; Astrophotometrical Observation of Artificial Satellites and Study of the Technical Status of Parental Bodies of Space Debris at Geostationary Ring; Proceedings of the Fourth Conference on Space Debris, 18-20 April 2005; p.160

[24] Space-Track: The Source for Space Surveillance Data: https://www.space-track.org

[25] Papushev, P. et al.; Investigations of the evolution of optical characteristics and dynamics of proper rotation of uncontrolled geostationary artificial satellites; Advances in Space Research 43 (2009); p.1421

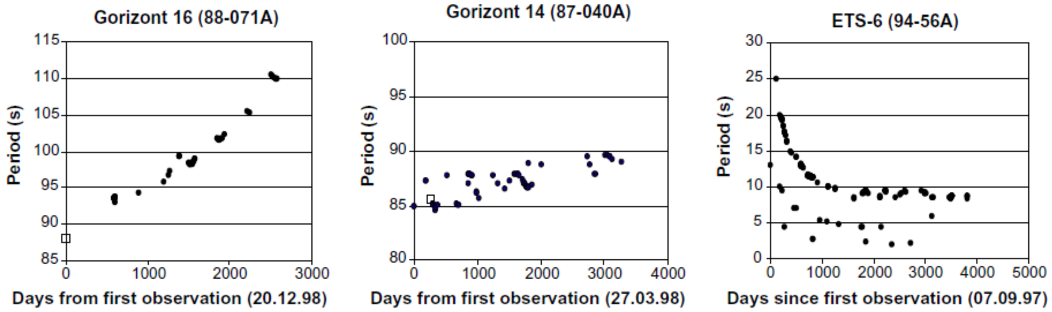

Figure 2.4: PPAS "Flash Period" Plots for Gorizont 16, Gorizont 14 and ETS-6[26]

The time scale that Figure 2.4 depicts is in the order of 3000 days (for Gorizont 16) to 5000 days (for ETS-6). This represents a time scale of 8.2 to 13.7 years. At face value, each of the three plots appears to be showing a definite spin period variation. However, the number of data points that were plotted within these time scales is few such that the resolution might be inadequate to show the finer details of these variations. As a result, several questions arise from looking at Figure 2.4.

The PPAS records the apparent flash period of observed satellites[27]. Does the PPAS consider the "flash period" to be the same as the "spin period"? Figure 2.2 shows that there were approximately 5 "flashes" (local maxima due to specular reflections) per apparent spin period of Raduga 14. Do the PPAS compilers discern between observations of flash period and apparent spin period?

The apparent spin period plots for Gorizont 14 and ETS-6 (Figure 2.4) appear to show (at least) two different trend lines each. Are the satellites' apparent spin frequencies higher than the sampling frequency, i.e. are only a small portion of the oscillations being represented, or are the plots showing an apparent spin period that contains at least two

---

[26] Papushev, P. et al.; Investigations of the evolution of optical characteristics and dynamics of proper rotation of uncontrolled geostationary artificial satellites; Advances in Space Research 43 (2009); p.1421

[27] McCants, M.; Description of the PPAS Format; http://www.prismnet.com/~mmccants/bwgs/ppasfmt.html

specular reflections per apparent spin period? If the latter is true, it may well be that some of the observers misinterpreted the period between flashes as the true spin period.

The spin period of the Laser Geodynamics Satellite 2 (LAGEOS 2) (Figure 2.5) laser-ranging satellite was regularly observed over a 16-year period; from October 23, 1992 to August 15, 2007 (Kucharski et al.)[28]. LAGEOS 2 is a spherical satellite that carries 426 retro-reflectors for the purpose of satellite laser ranging (SLR)[29]. The spin period observed via satellite laser ranging (SLR) is plotted in Figure 2.6. Both LAGEOS 2 and its predecessor, LAGEOS 1, orbit at nearly 6,000 km in altitude[30]. Using the precise knowledge of the distribution of the retro-reflectors on the satellite, it was possible to determine which "latitude" of the satellite was being optically observed[31]. Figure 2.7 shows the sidereal spin period of LAGEOS 2 colour-coded by the number of optically detected reflectors per row.

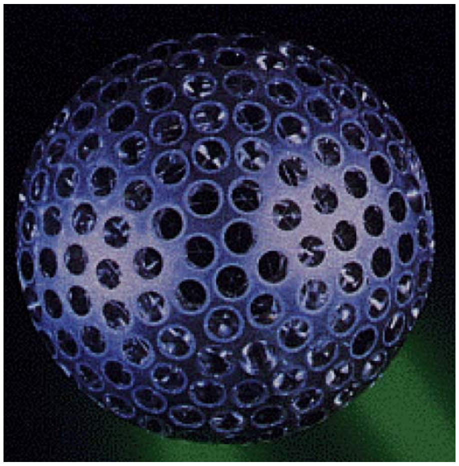

Figure 2.5: The LAGEOS 2 Satellite[32]

---

[28] Kucharski, D. et al.; 16 years of LAGEOS-2 Spin Data from launch to present; 16th International Workshop on Laser Ranging; Presentation Slides; Slide 5

[29] Wood, R. et al.; Lageos 2 spin rate and orientation; p.1

[30] Space-Track: The Source for Space Surveillance Data: https://www.space-track.org

[31] Wood, R. et al.; Lageos 2 spin rate and orientation; pp.1-2

[32] Wood, R. et al.; Lageos 2 spin rate and orientation; p.2

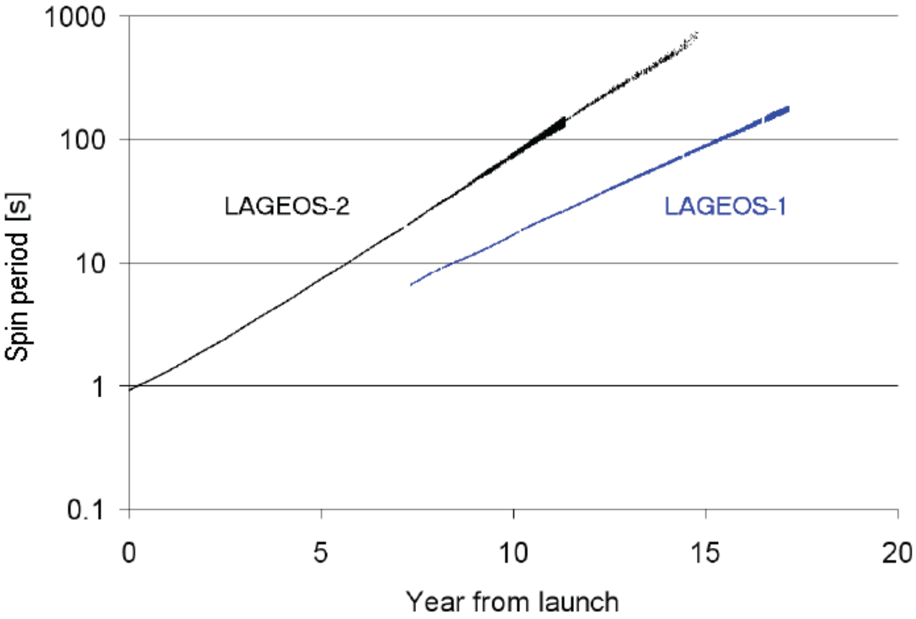

Figure 2.6: SLR-Observed Sidereal Spin Period of LAGEOS 2: 1992 to 2007[33]
Image Modified from Original

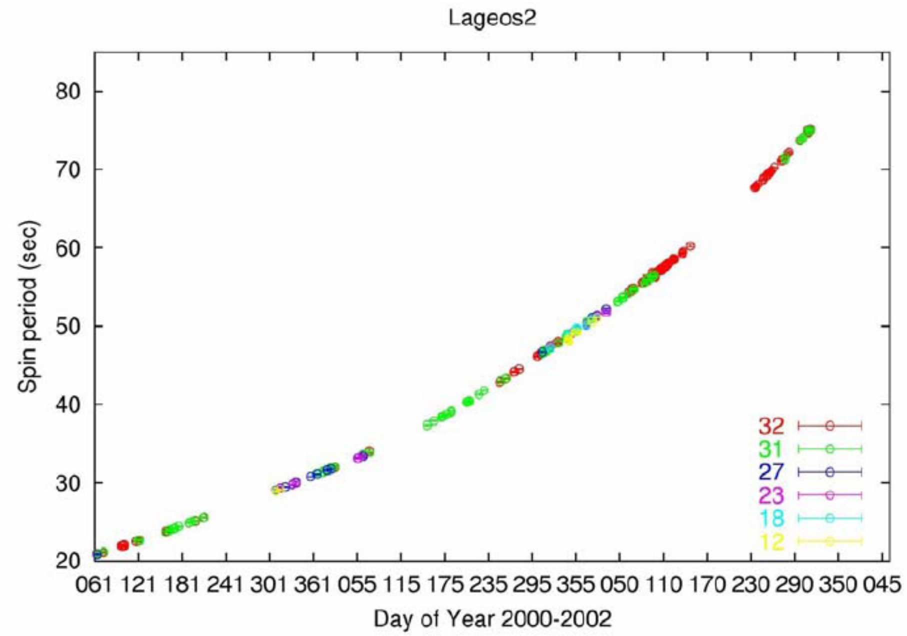

Figure 2.7: Optically Observed Sidereal Spin Period of LAGEOS 2: 2000 to 2002[34]

---

[33] Kucharski, D. et al.; 16 years of LAGEOS-2 Spin Data from launch to present; 16th International Workshop on Laser Ranging; Presentation Slides; Slide 5

[34] Wood, R. et al.; Lageos 2 spin rate and orientation; p.7

LAGEOS 2 did not have any attitude control systems on board. Figures 2.6 and 2.7 imply that some external force is slowing the rotation rate of LAGEOS 2. The Earth's gravitational field was causing the spin axis orientation of LAGEOS 2 to change[35]. This affected the rate of change of the spin period variation. The evolution of LAGEOS 2's spin period could also contain information about those forces which could perturb the satellite's orbit. An accurate and high resolution determination of spin periods over many years could be used to update models of these perturbing forces[36].

Although the duration of the observations in all of the examples mentioned were from several months to several years, the resolution of the spin period data for all but LAGEOS 2 was very low; on average in the order of several weeks to several months between observations. The PPAS had large gaps of several years between observations for some spacecraft, which is not suitable if a detailed long-term study of satellite spin behaviour is to be conducted. This suggests that further study is required which utilizes data collected with a greater frequency (at least one observation per week), for durations of several years or more. This could be the only way to truly understand the external (and possibly internal) forces acting on each satellite on a regular basis.

All owners of active box-wing GEO satellites must compensate for perturbing forces on their orbit elements (eccentricity, semi-major axis and inclination)[37] and their attitudes in order to reliably service their Earth-based customers. For example, the current generation of the Geostationary Operational Environmental Satellites (GOES) weather satellites must fire thrusters in order to remain within a 1° longitude-latitude box in their allocated geostationary orbit slots and in order to correct for any angular accelerations

---

[35] Kucharski, D. et al.; 16 years of LAGEOS-2 Spin Data from launch to present; 16th International Workshop on Laser Ranging; Presentation Slides; Slide 16

[36] Kucharski, D. et al.; 16 years of LAGEOS-2 Spin Data from launch to present; 16th International Workshop on Laser Ranging; Presentation Slides; Slide 16

[37] Chu, D. et al.; GOES-R Stationkeeping and Momentum Management; 29th Annual AAS Guidance and Control Conference – Feb. 4-8, 2006; pp.4-6

that change the satellites' attitudes[38]. The effect of solar radiation pressure (SRP) is especially troublesome because the GOES-R series of satellites are axially-symmetric with a single solar array, as shown in Figure 2.8[39]. Light from the sun is incident almost orthogonally to the solar panels at all times during the satellites' lifetimes. As a result, the torque from SRP is also attempting to change the attitude of the spacecraft during their lifetimes. The reaction wheels have to compensate for this very small, but constant torque by constantly increasing their angular momentum. The total increase of GOES-R's angular momentum (including the reaction wheels), which is a consequence of compensating for SRP over an 80-hour period, is shown in Figure 2.9. The reaction wheels can't continue speeding up forever, so a "momentum dump" is required. This is accomplished by briefly activating thrusters on the satellite to remove the excess reaction wheels' angular momenta in order to maintain the wheels' speeds within their designed operating ranges[40]. Momentum dumps, using delta-vs of about 1 cm·s^{-1}, are scheduled daily for each GOES-R spacecraft[41].

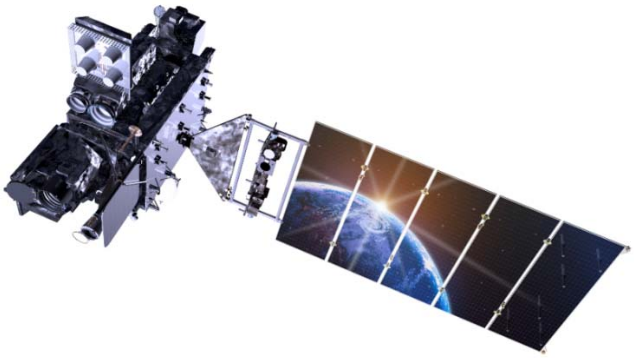

Figure 2.8: The GOES-R Satellite[42]

---

[38] Chu, D. et al.; GOES-R Stationkeeping and Momentum Management; 29th Annual AAS Guidance and Control Conference – Feb. 4-8, 2006; p.1

[39] Chu, D. et al.; GOES-R Stationkeeping and Momentum Management; 29th Annual AAS Guidance and Control Conference – Feb. 4-8, 2006; p.6

[40] Wertz, J.; Orbit Constellation Design and Management; p.127

[41] Chu, D. et al.; GOES-R Stationkeeping and Momentum Management; 29th Annual AAS Guidance and Control Conference – Feb. 4-8, 2006; p.2

[42] GOES-R Mission Website: http://www.goes-r.gov/multimedia/sc_images.html

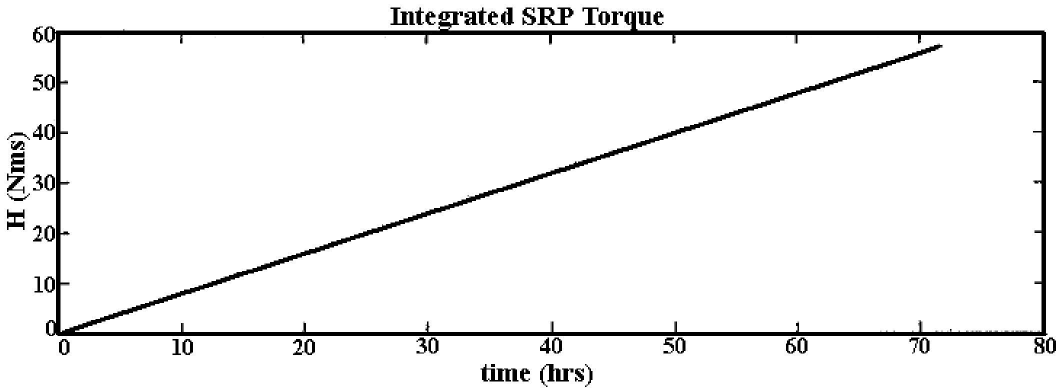

Figure 2.9: Increase in Reaction Wheel Angular Momentum, H, due to SRP[43]
Original Image Modified to Improve Clarity

Any ground-based or space-based observer will not directly observe the true spin period of any GEO satellite because of the relative motion of the satellite's geometry with respect to the sunlight vector and the observer. This motion will cause the satellite's spin period to appear larger or smaller than the real (sidereal) spin period. This apparent spin period is called the synodic spin period.

The synodic effect has been understood for hundreds of years. The synodic orbit period of the Moon (the time between observations of identical phases) is approximately 29.5 days. However, the Moon's true (sidereal) orbit period is 27.3 days[44]. This discrepancy occurs because the Earth's orbit motion changes the Moon's location with respect to the Sun and therefore its lighting perspective with respect to the Earth. In one sidereal lunar orbit period, the Earth moves approximately 27° in its own orbit. The Moon's apparent spin rate is also caused by the synodic effect. From an observer on the Earth, the Moon does not appear to spin at all because its spin period is exactly the same as its orbit period; also known as "synchronous rotation" or "tidal locking".

---

[43] Chu, D. et al.; GOES-R Stationkeeping and Momentum Management; 29th Annual AAS Guidance and Control Conference – Feb. 4-8, 2006; p.7

[44] Chapman, D.M.F. ed.; Observer's Handbook 2013 – The Royal Astronomical Society of Canada; p.22

The Earth has a synodic spin period of exactly 24 hours. This is also called the Solar Day. The sidereal spin period of the Earth is 23 hours, 56 minutes and 4 seconds long. This can be confirmed by using a distant star instead of the nearby Sun as a reference.

The orbit motion of the GEO satellites will change their perspectives with respect to the incoming sunlight. For example, a hypothetical non-rotating GEO satellite will have a synodic spin period of 24 hours when seen by an observer on the Earth.

The observed synodic effect is not uniform over time. Lambert et al. observed the inactive HS-376-design cylindrical SBS-B geosynchronous satellite on June 15, 2003 using the Advanced Electro-Optical Sensor (AEOS) located at the summit of Mount Haleakala (Maui, Hawaii)[45]. The satellite's observed (synodic) spin period was observed to increase over a single night's observation, as shown in Figure 2.10. Over the time span indicated in Figure 2.10, the spin period increased from less than 50 seconds to nearly 200 seconds, as shown in Figure 2.11.

---

[45] Lambert, J. et al.; Observations of Retired Boeing 376 Spacecraft; pp. 2, 7

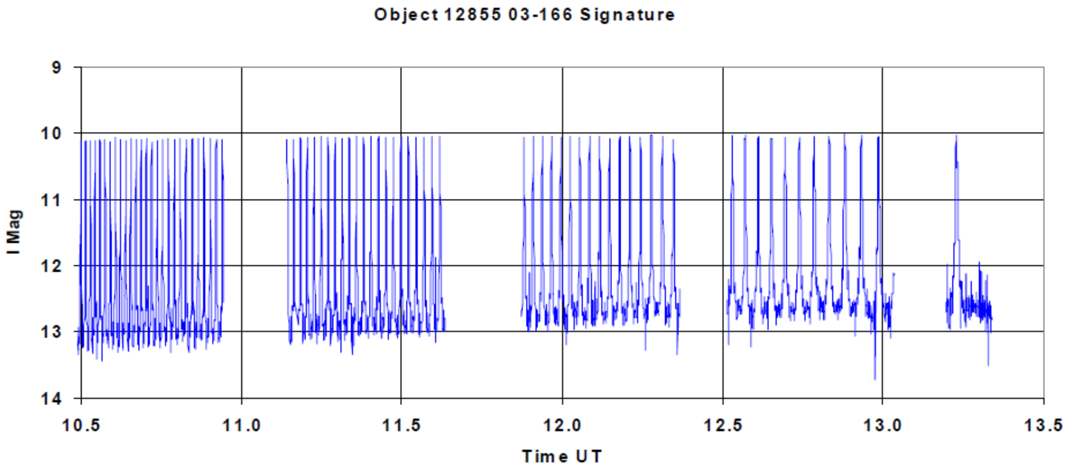

Figure 2.10: Light Curve of SBS-B (NORAD #12855) – June 15, 2003[46]
Brightness Measured in the Infrared (I) Wavelengths

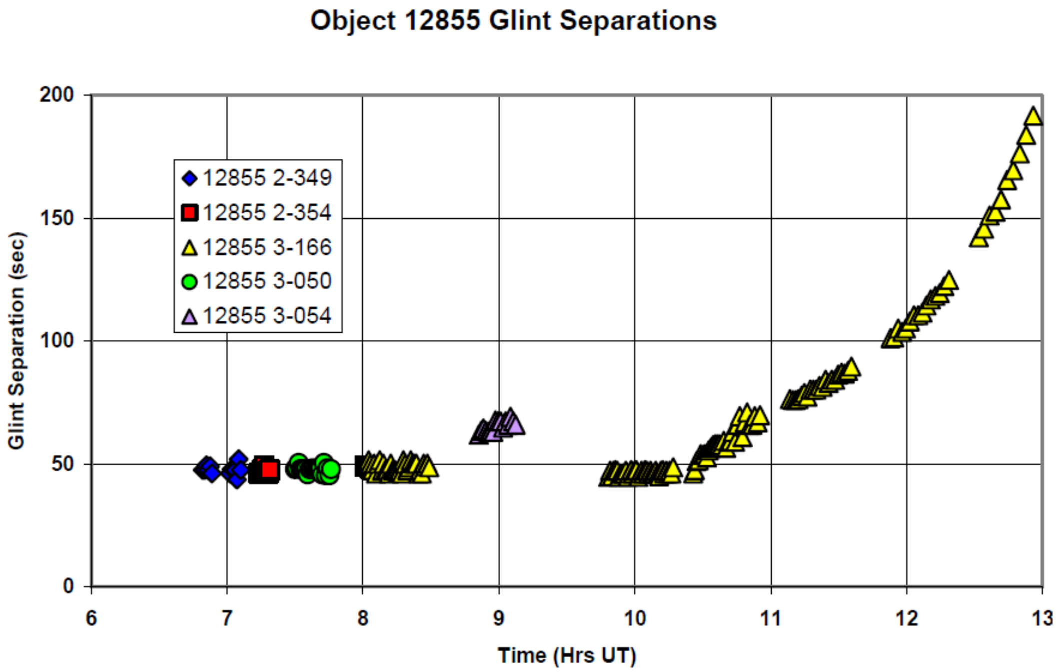

Figure 2.11: SBS-B (NORAD #12855) Glint Separations on June 15, 2003 and Earlier[47]
Legend Shows the NORAD ID (#12855), the Year (2002 or 2003) and the Day of Year

---

[46] Lambert, J. et al.; Observations of Retired Boeing 376 Spacecraft; p. 6

[47] Lambert, J. et al.; Observations of Retired Boeing 376 Spacecraft; p. 7

Lambert et al. hypothesized that the reason for the large increase in the apparent spin period was two-fold:

i) the reflecting surface normal was located within 10° of the satellite's spin axis orientation; and

ii) the spin axis' precession motion was in the same direction as the motion of the reflecting surface normal[48].

If a spinning inactive box-wing GEO satellite is to be captured and/or rescued by some future robotic service module, the mission planners would be required to precisely know the satellite's sidereal (true) spin period and spin axis orientation[49]. Otherwise, the service module would risk being "swatted" by a massive solar panel with a very large momentum and/or the module could possibly further damage the very satellite it is trying to rescue.

Fortunately, several methods have already been developed to determine the sidereal spin periods and spin axis orientations of solar system asteroids. The most reliable of these is the Epoch Method, also known as Photometric Astrometry. This method uses the asteroid's observed synodic spin period to determine its most likely sidereal spin period and spin axis orientation[50]. Four similar approaches can be used to achieve this; two involve the synodic reference frame and the other two involve the sidereal reference frame. Many use the synodic reference frame approach because the

---

[48] Lambert, J. et al.; Observations of Retired Boeing 376 Spacecraft; p. 11

[49] Wallace, B. et al.; Determination of spin axis orientation of Geosynchronous objects using space-based sensors: an initial feasibility investigation; p.1

[50] Magnusson P. et. al; Determination of Pole Orientations and Shapes of Asteroids; Asteroids II; pp. 78-80

synodic spin period can be easily measured from identical features of the light curve (maxima, minima, or a phase of a Fourier component)[51].

The Epoch Method has been used to successfully determine the sidereal spin periods and spin axis orientations for a number of inactive spinning satellites, such as NASA's IMAGE satellite[52] and cylindrical satellites such as Russian SL-6 rocket bodies and HS-376 geosynchronous satellites[53]. However, it has not been demonstrated if this method can also be used for inactive box-wing GEO satellites.

The concept of the Epoch Method is very similar to that of the determination of an outer or an inner planet's sidereal orbit period using its observed synodic orbit period, except that a satellite's spin axis is originally unknown. This method begins with the comparison of the synodic angular velocity, the sidereal angular velocity and the angular velocity of the phase angle bisector's azimuthal angle as a function of the satellite's spin axis orientation in right ascension and declination, as shown in Eq. 2.1[54].

Eq. 2.1[55]

$$\vec{\boldsymbol{\omega}}_{\mathbf{syn}} = \vec{\boldsymbol{\omega}}_{\mathbf{side}} - \frac{\boldsymbol{\partial}\vec{\boldsymbol{\Psi}}(\mathbf{t}, \boldsymbol{\alpha}_{\mathbf{axis}}, \boldsymbol{\delta}_{\mathbf{axis}})}{\mathbf{dt}}$$

The symbols for synodic angular velocity (ω_{syn}), sidereal spin angular velocity (ω_{side}), right ascension (α) and declination (δ) have been changed from the original symbols, ω', Ω, ϕ and θ, respectively, used in the reference (Hall, et al.)[56]. This was done to preserve the consistency of the symbols used throughout this thesis. The variable Ψ refers to the

---

[51] Magnusson P. et. al; Determination of Pole Orientations and Shapes of Asteroids; Asteroids II; p. 79

[52] Hall, D. et al.; AMOS Observations of NASA's IMAGE Satellite; p.1

[53] Somers, P.; Cylindrical RSO Signatures, Spin Axis Orientation and Rotation Period Determination; p.7

[54] Hall, D. et al.; AMOS Observations of NASA's IMAGE Satellite; p.6

[55] Hall, D. et al.; AMOS Observations of NASA's IMAGE Satellite; p.6

[56] Hall, D. et al.; AMOS Observations of NASA's IMAGE Satellite; p.6

azimuthal angle of the reflecting surface's normal that is swept out as it rotates around the spin axis (see Chapter 15). If the spin period is desired, the reciprocals of the moduli of the components in Eq. 2.1 would be required. An example is shown in Eq. 2.2.

Eq. 2.2

$$\mathbf{T_{syn}} = \frac{\mathbf{2\pi}}{\left|\overrightarrow{\boldsymbol{\omega}}_{\mathbf{syn}}\right|}$$

The partial differential term in Eq. 2.1 depends on the reflecting surface's orientation with respect to the spin axis as well as the spin axis' orientation with respect to the Earth's equatorial plane or the North Celestial Pole (NCP), as Lambert et al. observed with the SBS-B satellite in 2003[57]. However, the relationship between the satellite's orbit plane, its spin axis orientation and its reflecting surface normal's orientation with respect to the spin axis has not been fully explained in the cited literature. Hall et al. come close when describing the Epoch Method used for the IMAGE satellite spin axis determination by explaining the preliminary Eulerian transformations used for the spin axis determination[58].

The primary goal of this thesis was to select several accessible inactive box-wing design GEO satellites in order to study their apparent spin period variations from March 2012 to March 2013. The most likely cause of these spin period variations was investigated. The synodic effect on the apparent spin period of the selected satellites was also explored.

A description of the satellite selection process (first conducted in early 2012) is first discussed, followed by the data collection process, including the criteria for

---

[57] Lambert, J. et al.; Observations of Retired Boeing 376 Spacecraft; p. 7

[58] Hall, D. et al.; AMOS Observations of NASA's IMAGE Satellite; pp.5-6

observing the satellites, the equipment (hardware and software) used and the observation procedures. The image data extraction (time tag and satellite flux) was then discussed, describing a manual and software-automated data extraction. The extracted data would be used to generate light curves of the selected satellites. The methods of determining the satellites’ apparent spin period from their periodic light curves were then explained. The final satellite selection, based on the first light curves for each candidate satellite is discussed. The apparent spin period variation for each selected satellite measured from March 2012 to March 2013 was shown and the interesting relationships noticed for each are discussed. The unique characteristics of each of the selected satellites were listed to provide the physical characteristics required to determine each satellite’s moment of inertia (MOI).

CHAPTER 3: PRELIMINARY SATELLITE SELECTION

The preliminary satellite selection process depended on specific criteria, which involved careful sifting through the GEO satellite population, as shown in Table 3.1. The GEO orbit region contains over 1,100 individual satellites[59], including active and inactive payloads (which include all GEO satellites of box-wing design), spent rockets and debris.

THE CASTOR SATELLITE CATALOGUE

From January 1, 2007 to December 31, 2011, the author conducted an extensive optical survey of the satellite population in order to determine the portion of the NORAD satellite catalogue that could be detected using small aperture telescopes and unfiltered optical wavelength CCD cameras. The results of this survey were organized into a satellite catalogue named the CASTOR Satellite Catalogue (CSC). The CSC lists nearly 4,100 unique detected satellites from all major orbit regions, including LEO, MEO, GEO and HEO[60]. The CSC contains images of 763 GEOs, which is nearly 75% of all known GEO satellites[61]. The majority of those GEO satellites that are not in the CSC reside on the opposite side of the Earth from the southern Ontario survey sites and therefore could not be accessed.

The CSC has been particularly useful for this thesis because it lists those GEO satellites that could be detected using equipment similar to that which conducted the CSC survey. The list of GEO satellites in the CSC was used as the preliminary GEO candidate list for this thesis.

---

[59] Space-Track: The Source for Space Surveillance Data: https://www.space-track.org
[60] Earl, Michael A.: CASTOR Satellite Catalogue: http://www.castor2.ca/13_Catalogue/05_Stats
[61] Earl, Michael A.: CASTOR Satellite Catalogue: http://www.castor2.ca/13_Catalogue/05_Stats

INITIAL SATELLITE SELECTION CRITERIA

The criteria listed in the order shown in Table 3.1 were used to filter the number of viable GEO satellites to a number that could be realistically studied for this thesis. The GEO candidates remaining after each criterion was applied are shown in the “GEOs Remaining” column of Table 3.1. These criteria were used to select those inactive GEO satellites that were of box-wing design and had been verified to be the brightest detected for the CSC.

Table 3.1: Criteria Used for the Inactive Box-wing Satellite Selection Process

CRITERIA		DESCRIPTION	GEOS REMAINING
1	**In the CSC**	GEOs that can be detected with small aperture telescopes and unfiltered CCD cameras in Ontario Canada	763
2	**Payload**	GEOs that are categorized as payloads according to the NORAD definition	528
3	**Unclassified**	GEO payloads that appear within the unclassified NORAD satellite catalogue	480
4	**Inactive**	Unclassified GEO payloads that are no longer functioning. Most of the inactive GEO satellites were identified by their non-zero orbit inclinations [62] or their variable brightness in CSC images	347
5	**Box-wing Design**	Those inactive unclassified GEO payloads that are similar in structure to the box-wing design shown in Figure 1.1	141
6	**High Signal**	Those box-wing GEOs that had exhibited signal to noise ratios (S/N) greater than 2 in CSC survey images	42
7	**Accessible**	High signal box-wing GEOs predicted to be greater than 15° in elevation for all nights from March 1, 2012 to March 31, 2013	7

---

[62] Active GEO satellites (in the geostationary belt) normally have an orbit inclination of less than 1 degree. Some active GEO satellites have greater than 1 degree orbit inclinations, but they are normally months away from being retired.

Those satellites that were initially selected for study for this thesis are listed in Table 3.2. The common names are the same as those shown on the Space-Track website. The “NORAD #” is the 5-digit number assigned to a satellite when it is first detected by the Space Surveillance Network (SSN). This number remains with the satellite even after its orbit has decayed. For example, the International Space Station (ISS) is NORAD #25544. The “COSPAR #” (also called the International #) indicates the four-digit year of launch, the three-digit launch number in the indicated year and a designator letter which identifies the primary payload, secondary payload, etc. “A” usually signifies the primary payload, “B” the secondary payload, etc. The last letters in the list normally signify the rocket stages which placed the payloads into their orbits.

Table 3.2: Inactive GEO Box-wing Satellites Initially Selected for Thesis Research

NORAD #	COSPAR #	COMMON	OWNER	DESIGN [63]
19483	1988-081-A	G-Star 3	USA	AS-3000
22796	1993-058-B	ACTS	USA	AS-4000
22911	1993-073-A	Solidaridad 1	Mexico	HS-601
22927	1993-077-A	Telstar 401	USA	AS-7000
23670	1995-049-A	Telstar 402R	USA	AS-7000
24313	1996-055-A	Echostar 2	USA	AS-7000
25126	1997-086-A	HGS-1	USA	HS-601HP

Subsequent observations of each satellite were obtained to determine which satellites listed in Table 3.2 would be most suitable for further study. The satellites chosen from Table 3.2 for further study were Solidaridad 1, Telstar 401, Echostar 2 and HGS-1, using the criteria discussed in Chapter 8.

---

[63] Dirk Krebs, Gunter; “Gunter’s Space Page”: http://space.skyrocket.de

CHAPTER 4: DATA COLLECTION

The raw data for this thesis consisted of time-tagged unfiltered optical CCD images. The satellite observation criteria, data collection site, apparatus used, equipment setup procedure and data collection procedure are explained in this chapter.

MANDATORY CRITERIA FOR DATA COLLECTION

The mandatory criteria for data collection are described in Table 4.1.

Table 4.1: The Mandatory Conditions for Data Collection

CONDITION	CRITERIA
Sky Transparency	Visible clouds must not be present in the site’s southern skies. This includes a “Moon halo” due to cirrus activity Visible ground fog must not be present at the site Relative humidity at the site must be less than 75%
Light Pollution	The Sun’s elevation must be equal to or less than -12° When appearing above the site’s local horizon, the Moon’s phase must not exceed 50% All outdoor lights at site must be switched off during data collection Aurorae must not appear in the site’s southern skies
Wind Speed	Wind speed must be less than 15 $\mathrm{km \cdot h^{-1}}$, including gusts
Satellite Accessibility	Satellite elevation must be greater than 15° Satellite must not be in eclipse Satellite phase angle (PA) must be between 0° and 90° The satellite should not be observed when it appears within the summer Milky Way

DATA COLLECTION SITE

The characteristics of the primary site are shown in Table 4.2.

Table 4.2: Characteristics of the Primary Data Collection Site

CHARACTERISTIC	VALUE	COMMENTS
Physical Location	214 Old Orchard Road, RR1 Sandhurst, Ontario Canada	Private Residence Located 35 km west of Kingston and 20 km south of Napanee
Geodetic Coordinates [64]	Longitude: -76° 53’ 25”.8 Latitude: +44° 07’ 23”.8	From Google Earth
Limiting Unfiltered Naked-eye Stellar Magnitude	5.5	Summer and winter Milky Way can be easily viewed with the dark-adapted naked eye The Moon is not above the local horizon Relative humidity is less than 75%
GEO Belt Accessibility	Excellent	GEO satellites accessible greater than 10° above the eastern horizon and greater than 20° above the western horizon

DATA COLLECTION APPARATUS

The hardware and software that were used to obtain all of the optical data for this thesis are described in Table 4.3 and Table 4.4, respectively. The telescope and optical CCD camera used throughout this thesis are shown at the observation site in Figure 4.1. The combined performance of the optical telescope and the unfiltered optical camera

---

[64] Google Earth

hardware is summarized in Table 4.5. Orbit elements of the selected GEO satellites for the epoch nearest to the date of the first images acquired (March 5, 2012) are shown in Figure 4.2. The predicted positions of the selected satellites in the observing location's sky at 01:00 UTC March 6, 2012 are shown in Figure 4.3.

Table 4.3: Hardware Used for Optical Data Collection

HARDWARE	BRAND AND MODEL	SPECIFICATIONS
Optical Telescope	Celestron NexStar 11 GPS	Aperture Size: 0.28m (11 inches) Mount Type: Fork equatorial Heritage: 10 years of extensive use
Charge-coupled Device (CCD) [65]	Santa Barbara Instrument Group (SBIG) ST-9XE	Detector: Kodak KAF-0261E Array: 512 x 512 pixels Pixel Size: 20 μm (square) Quantum Efficiency: 67% at λ=600nm Bias Noise: 100 ADU Read Noise: 15 e^- Gain: 2.2 e^- Shutter Type: Rotating wheel Chip Cooling: 40°C below ambient Filtering: None Heritage: 10 years of use
Controlling Computer	Toshiba Portege M780 Notebook	OS: Windows 7 Enterprise Service Pack 1 Heritage: Over 1.5 years of extensive use

---

[65] SBIG ST-9XE CCD User Manual: http://www.sbig.com/site/assets/files/18223/usbmanrev14.pdf

Table 4.4: Software Used for Optical Data Collection and Manual Image Analysis

SOFTWARE	BRAND / MAKE / VERSION	SPECIFICATIONS
Planetarium and Telescope Control	Software Bisque / TheSky / Level IV Version 5.00.108	Used mainly as a planetarium tool for displaying stars and solar system objects on the celestial sphere Propagates satellite TLEs and displays the predicted positions and apparent real-time motion of satellites against the background stars Used to control computer-controlled goto telescopes Heritage: 15 years of extensive use
CCD Camera Control	Software Bisque / CCDSoft / Version 5.00.210	Used to control CCD cameras Used for image post-processing and analysis Heritage: 10 years of extensive use
Manual FITS Image Analysis	SBIG / CCDOps / Version 5.53	Used to manually extract satellite brightness data from CCD images Used for image post-processing and analysis Heritage: 10 years of extensive use
Extraction of GEO Orbit Elements	Michael Earl / TLESort / Version 2	Originally developed at RMC’s SSRAL by Michael Earl Extracts satellite orbit element files from U.S. Space-Track master text files and sorts them by critical orbit type, including LEO, MEO, GEO and HEO Heritage: used extensively for 10 years by Michael Earl

Figure 4.1: The Author, the NexStar 11 GPS Telescope, and the ST-9XE CCD Camera

Table 4.5: Combined Performance of Optical Telescope and CCD Camera

SPECIFICATION	VALUE	CONDITIONS
Pixel Angular Resolution	1.56 arc-seconds	CCD at telescope’s prime focus Astrometric analysis of star fields containing more than 20 stars
Field of View (FOV)	13.3 arc-minutes	CCD at telescope’s prime focus Astrometric analysis of star fields containing more than 20 stars
Limiting Stellar Magnitude (Unfiltered)	20	Single 30 second exposure Sidereal tracking mode No image stacking Elevation of over 30° Low light pollution Low humidity 1x1 binning
Limiting GEO Satellite Magnitude (Unfiltered)	18	Single 1 second exposure All telescope tracking switched off Elevation of over 30° Low light pollution Low humidity 1x1 binning

EQUIPMENT SETUP PROCEDURE

The equipment setup procedure shown in Table 4.6 was conducted, in the order shown and without deviation. Setup commenced between Civil Twilight and Nautical Twilight and took about 30 minutes notwithstanding technical problems and other delays.

The telescope tracking mode for all of the GEO detections was “OFF” (no tracking). During the image acquisition, the user would manually slew the telescope to reacquire the target in the telescope’s FOV, as described in Table 4.7. This manual tracking rate mode (TRM) was used to minimize any periodic or secular tracking errors that could have increased the satellite signal distribution over a larger amount of pixels.

Table 4.6: Equipment Setup Procedure

STEP		DESCRIPTION	TIME (min)
1	**Download and Input Orbit Elements**	The Two-Line Orbit Elements (TLEs) of the selected satellites are downloaded from the Space-Track web site (Figure 4.2) and loaded into TheSky. TheSky propagates the orbit elements and displays the predicted satellites' locations amongst the virtual sky (Figure 4.3)	1
2	**Polar Alignment**	The telescope's RA axis of rotation is aligned to the North Celestial Pole (NCP)	5
3	**Telescope Cable Connections**	The telescope's RS-232 computer interface cable and power cable are connected	1
4	**Telescope Initiation**	The telescope is powered and allowed to determine its time and location using its built-in GPS	5
5	**Telescope Alignment**	Using an eyepiece, the telescope is aligned with the equatorial coordinate system using two naked eye stars that are greater than 20° apart in both RA and Dec.	5
6	**Link Telescope to Computer**	RS-232 (serial) communications is established between the telescope and the controlling computer using TheSky	0.5
7	**Attach CCD to Telescope**	The eyepiece is removed and the CCD is attached to the telescope's prime focus. The CCD is oriented such that increasing Dec. is bottom to top and increasing RA is right to left in the images	5
8	**CCD Cable Connections**	The CCD's USB computer interface cable and power cable are connected	1
9	**Power CCD and Link to Computer**	The CCD is powered up and USB communication is established between the CCD and the controlling computer using CCDSoft	1
10	**Cool CCD Chip**	The CCD chip is cooled to between -30°C and -15°C (depending on the site's ambient temperature) using the CCDSoft interface	10
11	**Slew to First Satellite**	The telescope is slewed to the first satellite's predicted location using TheSky	1
12	**Focus Telescope**	The telescope is manually focused using CCD images as guides. The stars should appear as small as possible in the images	5
13	**Disable Sidereal Tracking**	All automatic tracking for the telescope is switched off using TheSky	0.5

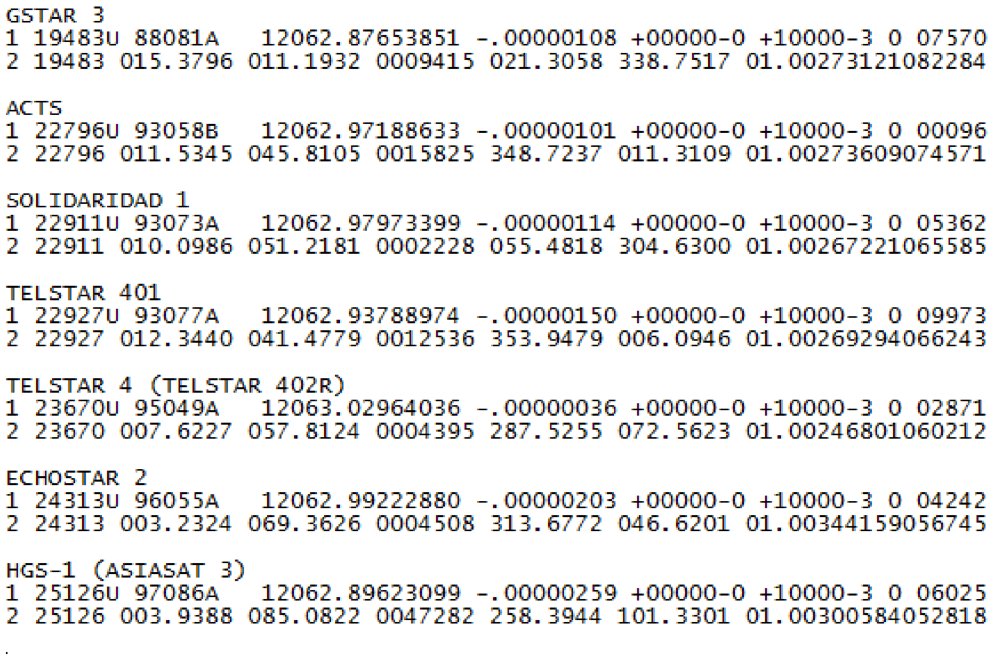

```
GSTAR 3
1 19483U 88081A   12062.87653851 -.00000108 +00000-0 +10000-3 0 07570
2 19483 015.3796 011.1932 0009415 021.3058 338.7517 01.00273121082284

ACTS
1 22796U 93058B   12062.97188633 -.00000101 +00000-0 +10000-3 0 00096
2 22796 011.5345 045.8105 0015825 348.7237 011.3109 01.00273609074571

SOLIDARIDAD 1
1 22911U 93073A   12062.97973399 -.00000114 +00000-0 +10000-3 0 05362
2 22911 010.0986 051.2181 0002228 055.4818 304.6300 01.00267221065585

TELSTAR 401
1 22927U 93077A   12062.93788974 -.00000150 +00000-0 +10000-3 0 09973
2 22927 012.3440 041.4779 0012536 353.9479 006.0946 01.00269294066243

TELSTAR 4 (TELSTAR 402R)
1 23670U 95049A   12063.02964036 -.00000036 +00000-0 +10000-3 0 02871
2 23670 007.6227 057.8124 0004395 287.5255 072.5623 01.00246801060212

ECHOSTAR 2
1 24313U 96055A   12062.99222880 -.00000203 +00000-0 +10000-3 0 04242
2 24313 003.2324 069.3626 0004508 313.6772 046.6201 01.00344159056745

HGS-1 (ASIASAT 3)
1 25126U 97086A   12062.89623099 -.00000259 +00000-0 +10000-3 0 06025
2 25126 003.9388 085.0822 0047282 258.3944 101.3301 01.00300584052818
```

Figure 4.2: TLEs of the Initial Selected Satellites – March 2, 2012[66]

Figure 4.3: Predicted Positions of the Selected Satellites at 01:00 UTC March 6, 2012

---

[66] Space-Track: The Source for Space Surveillance Data: https://www.space-track.org

DATA COLLECTION PROCEDURE

The data collection procedure followed for all satellites observed is shown in Table 4.7. In order to ensure that the maximum signal was being detected from each selected satellite and that the maximum sampling cadence would be realized, no filtering was used for any of the images obtained for this thesis.

Table 4.7: Data Collection Procedure

STEP		DESCRIPTION
1	**Determine Satellite Direction**	The satellite's apparent direction of travel is determined using TheSky. Since no automated telescope tracking is used, the satellite appears to travel south-to-north (increasing Dec.) or north-to-south (decreasing Dec.)
2	**Position Satellite in CCD FOV**	The telescope is positioned using TheSky so that the satellite appears near the bottom center of the CCD FOV (for south-to-north motion) or near the top center of the CCD FOV (for north-to-south motion)
2	**Set CCD Exposure Time**	The default exposure time for the CCD camera is 1 second. Lower or higher exposure times are sometimes used, depending on the apparent brightness of the satellite. By default, the time between exposures (delay time) is set to 0 seconds to maximize the sampling cadence.
3	**Auto Save**	Using CCDSoft, the prefix for all auto-saved files is entered as the local date of the first image in the format of two-digit year, two digit month and two digit day (yymmdd). The image format for all auto-saved data is uncompressed Flexible Image Transport System (FITS). NTP time stamps are automatically recorded in the image FITS headers in Universal Time Coordinates (UTC). CCDSoft's "AutoSave On" and "Save focus images" radio buttons are activated
4	**CCD Binning**	The default CCD chip binning is 1x1. 2x2 binning can be used if increased sampling cadence is required
5	**Begin Imaging Satellite**	Continuous imaging of the satellite is started using CCDSoft. Each image will contain the prefix and the sequential image number within the specific observing session. Dark frames are automatically subtracted from every image obtained. No bias or flat fields were required because the background signal pixels differed by under 20 ADU over the entire CCD array.

Table 4.7 Continued

6	**Reposition Satellite in CCD FOV**	When the satellite has nearly exited the CCD's FOV, the telescope is manually moved with TheSky so that the satellite is repositioned in the FOV similar to that specified in Step 2. This step is performed only if imaging of the same satellite is continuing. CCD imaging is not suspended. This step is repeated as many times as necessary to obtain the desired number of images of the satellite for the session
7	**End Imaging Satellite**	When the final image of the satellite has been obtained, the imaging is stopped using CCDSoft

FIRST IMAGES OF SELECTED SATELLITES

The particulars of all CCD images obtained for this thesis are shown in Appendix A. The first CCD image of Telstar 401 obtained for this thesis is shown in Figure 4.4.

By default, the exposure time of each image was 1 second. If the satellite could not be visually detected in the image by eye, the exposure time was increased in 0.5 second increments until the satellite became visible on the computer screen. If, for a second exposure, the satellite was visible and had a signal greater than 200 ADU over the background signal, the exposure was first decreased to 0.5 seconds. If the satellite's signal was still greater than 200 ADU over the background signal, the exposure was decreased in increments of 0.1 seconds until the suitable signal was reached or the CCD camera's minimum exposure time (0.1 seconds) was reached. Typical exposure times were 0.5 seconds and 1 second.

Due to intrinsic brightness variations, the satellite signal could drop to less than the background signal during an imaging session. When this occurred, the amount of time the satellite's signal was lower than the background signal was monitored. If the time the satellite signal was lower than the background signal exceeded the time the satellite was visible in the image, the exposure time was increased by 0.5 seconds or more if required.

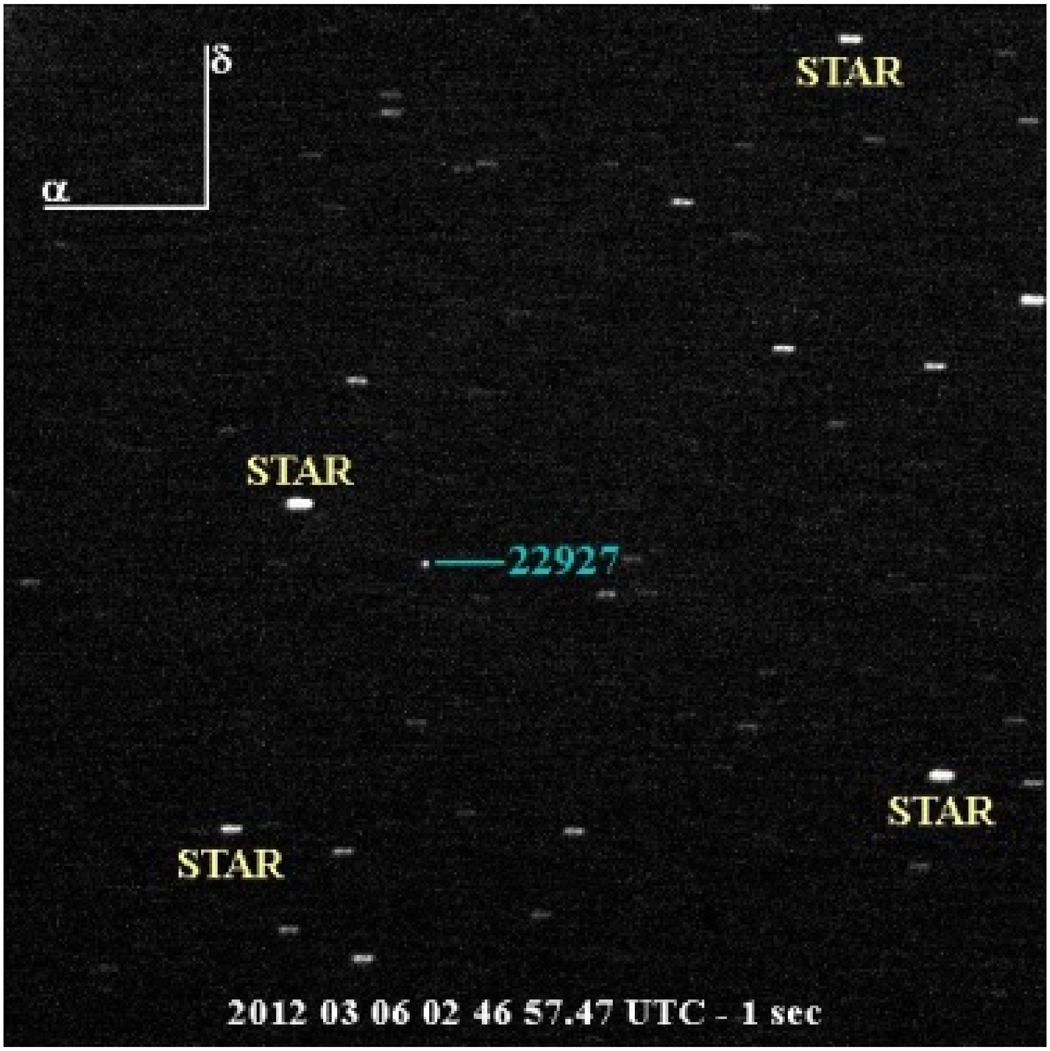

Figure 4.4: First CCD Image of Telstar 401 (NORAD #22927)

CHAPTER 5: MANUAL IMAGE DATA EXTRACTION

The data extracted from each raw FITS CCD image consisted of the following:

- The time tag from the FITS file header; and
- The apparent satellite brightness.

The satellite identifier was not required because the images corresponding to the target satellite were automatically stored in a folder (corresponding to the satellite observed) that was indicated by the user during the image acquisition process.

The time tag and brightness data were first manually extracted from the images for the purpose of comparison with automated data extraction (see Chapter 6) from the same images. The process by which the manually extracted data were created assisted in the development of automated data extraction software, described in Chapter 6.

Within a CCD image, the satellite would appear to cover a number of pixels (not just one). In order to determine the total brightness (flux) of the satellite within an image, the sum of all of the pixels that include the satellite signal was required. This required the use of a sample box that would encompass the entire satellite distribution.

The selection of an initial sample box size for manual data extraction was performed by determining the area that would encompass the entire satellite signal distribution. In all cases, an 11x11 pixel sample area encompassed the entire satellite signal that was greater than the background signal.

The steps taken to manually extract the time and brightness data from the images are described in Table 5.1.

Table 5.1: Manual Image Data Extraction Process

STEP		DESCRIPTION
1	**Open Image in CCDOps**	The image to be analyzed is opened using the CCDOps software
2	**Inspect Image Quality**	The sharpness of the stars within the image is checked. The stars should appear as horizontal streaks in the image because of the sidereal spin rate of the Earth, as shown in Figure 5.1. If the stars do not appear horizontal, for example due to a sudden gust of wind, as shown in Figure 5.2, the image is not used in the analysis. In this case, the corresponding image is closed and the next image is opened and inspected
3	**Detect Satellite in Image**	The satellite is found within the image. The satellite appears as a small dot amongst the star streaks. A subsequent image is used to verify that the satellite “dot” is seen in both images. The image is not used if the satellite cannot be positively identified in the image
4	**Check Satellite Position in FOV**	The image is not used if the center of the satellite’s apparent signal distribution is less than 6 pixels from any edge of the FOV
5	**Check Satellite Vicinity to Star or CCD Artefact**	The vicinity of the satellite to a background star is checked. The image is not used if the edge of the satellite signal distribution appears less than 10 pixels from the visible edge of a star distribution or a bright CCD artefact
6	**Determine Brightest Pixel of Satellite**	Using the CCDOps “Crosshair” window, which contains a magnified portion of the image (Figure 5.3), the brightest pixel of the satellite distribution is found; normally near its center
7	**Check Sample Box Size**	An 11x11 pixel sample area was used for the manual analysis. The sample area (box) is indicated at the bottom of the CCDOps “X Hair” window, as shown in Figure 5.3
8	**Determine Average ADU Count of 11x11 Sample Box**	With the cursor still on the satellite distribution’s brightest pixel, the average ADU count of the 11x11 box is read from the CCDOps “AvgVal” portion of the “X hair” window (Figure 5.3)
9	**Open Same Image in CCDSoft to Read Time Tag**	The same image is opened in CCDSoft to read the image’s time tag from the FITS header (Figure 5.4)
10	**Record Time and Average ADU Brightness**	The time tag and the average ADU count are recorded in a Microsoft Excel spreadsheet (Figure 5.5). The time tag is recorded as seconds elapsed from the first image time tag rounded down to the nearest minute

Figure 5.1: Image of 1-second Exposure Showing Acceptable Horizontal Star Distributions

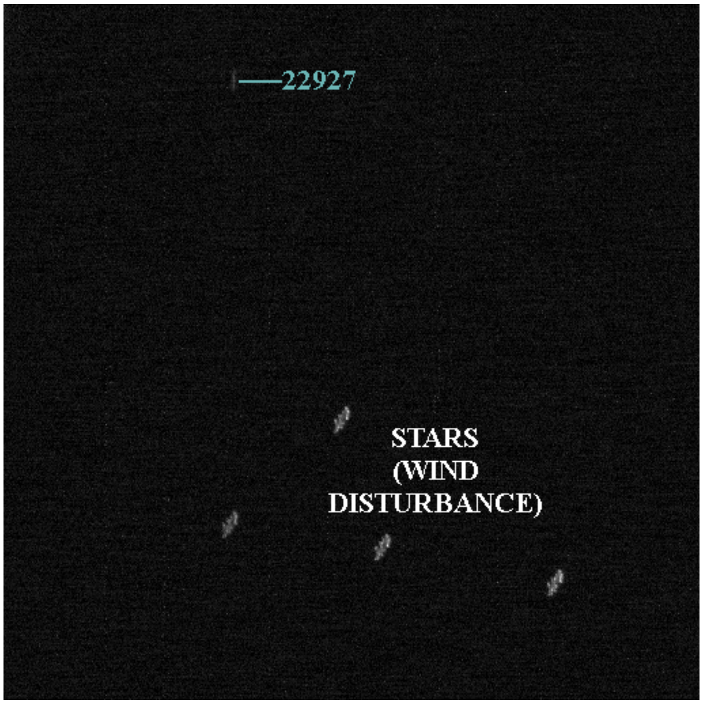

Figure 5.2: Image of 1-second Exposure Showing Unacceptable Star Distributions

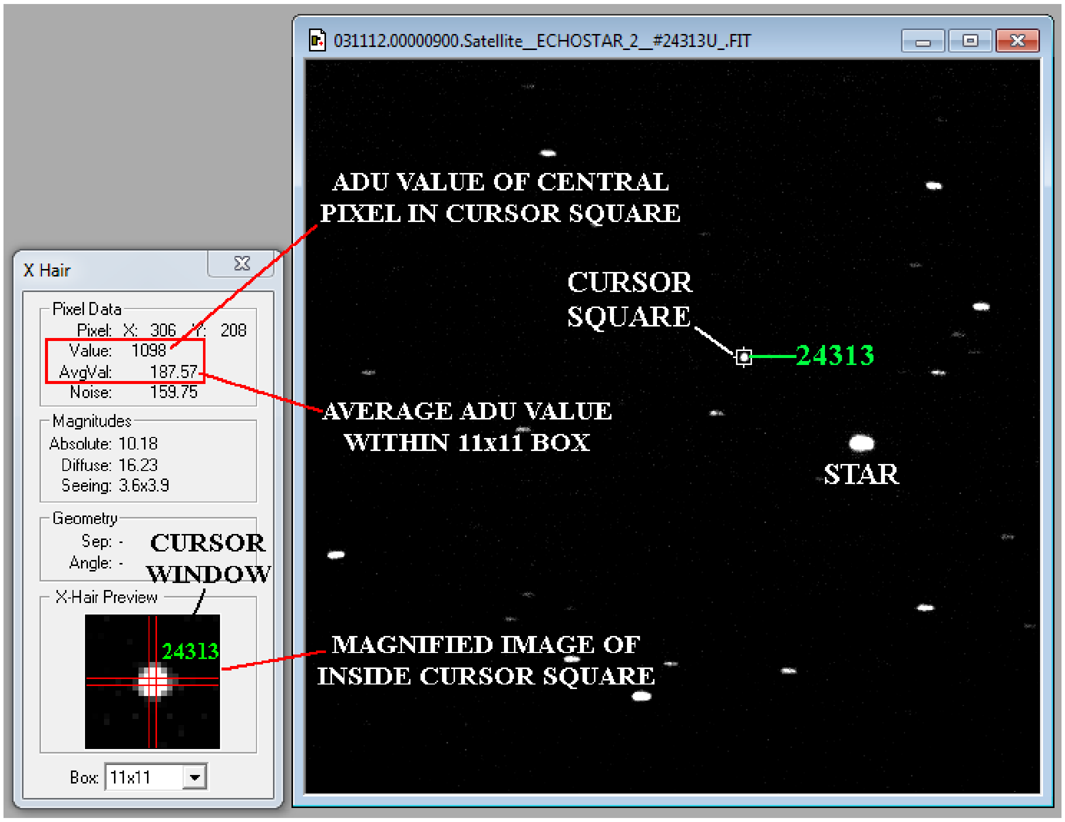

X Hair

Pixel Data
Pixel: X: 306 Y: 208
Value: 1098
AvgVal: 187.57
Noise: 159.75

Magnitudes
Absolute: 10.18
Diffuse: 16.23
Seeing: 3.6x3.9

Geometry
Sep: -
Angle: -

X-Hair Preview

Box: 11x11

Figure 5.3: Determining the Satellite's Average Brightness with CCDOps

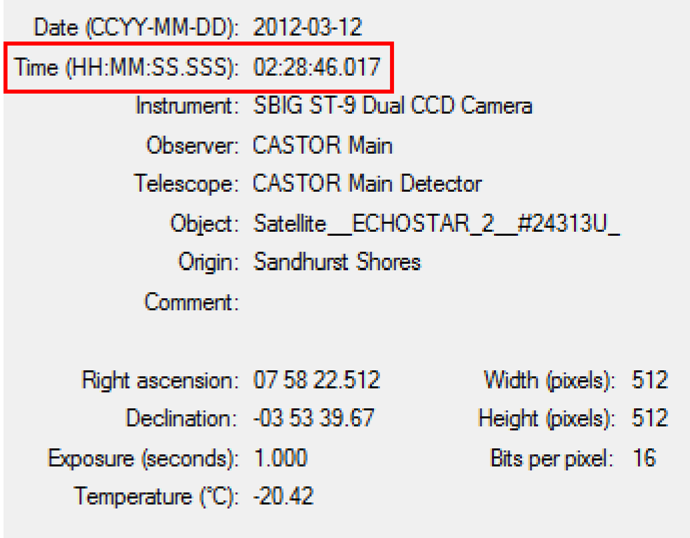

Date (CCYY-MM-DD): 2012-03-12
Time (HH:MM:SS.SSS): 02:28:46.017
Instrument: SBIG ST-9 Dual CCD Camera
Observer: CASTOR Main
Telescope: CASTOR Main Detector
Object: Satellite__ECHOSTAR_2__#24313U_
Origin: Sandhurst Shores
Comment:

Right ascension: 07 58 22.512
Declination: -03 53 39.67
Exposure (seconds): 1.000
Temperature (°C): -20.42

Width (pixels): 512
Height (pixels): 512
Bits per pixel: 16

Figure 5.4: The Time Tag from the FITS Header Read by CCDSoft

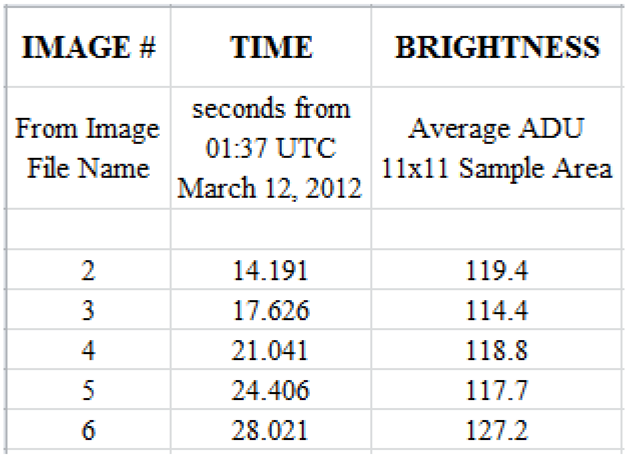

IMAGE #	TIME	BRIGHTNESS
From Image File Name	seconds from 01:37 UTC March 12, 2012	Average ADU 11x11 Sample Area
2	14.191	119.4
3	17.626	114.4
4	21.041	118.8
5	24.406	117.7
6	28.021	127.2

Figure 5.5: Recording Elapsed Time and ADU Brightness in a Microsoft Excel Spreadsheet

After the manual data extraction had been completed for a satellite, its light curve was plotted using an X-Y scatter plot in Microsoft Excel. Figures 5.6 to 5.10 show the first light curves of the ACTS, Solidaridad 1, Telstar 401, Echostar 2 and HGS-1 satellites, respectively. Figures 5.6 to 5.10 correspond to the dates and times of the first images of each corresponding satellite in Chapter 4. Throughout this thesis, plots of a particular satellite are colour-coded so that the reader can more easily associate a plot with a particular satellite.

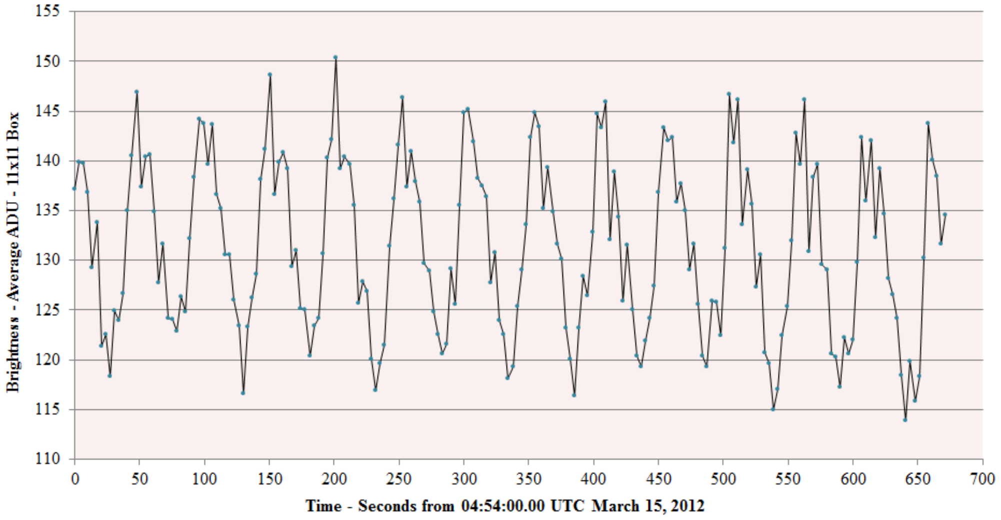

Figure 5.6: The Preliminary Light Curve of ACTS
“Average ADU” Refers to the Total ADU within a 11x11 Sample Box Divided by 121 Pixels

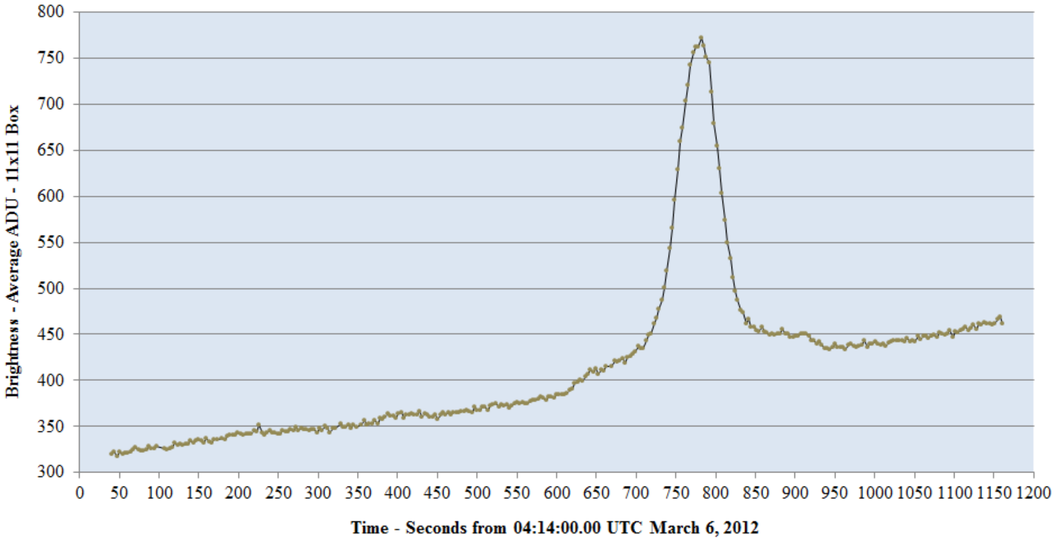

Figure 5.7: The Preliminary Light Curve of Solidaridad 1

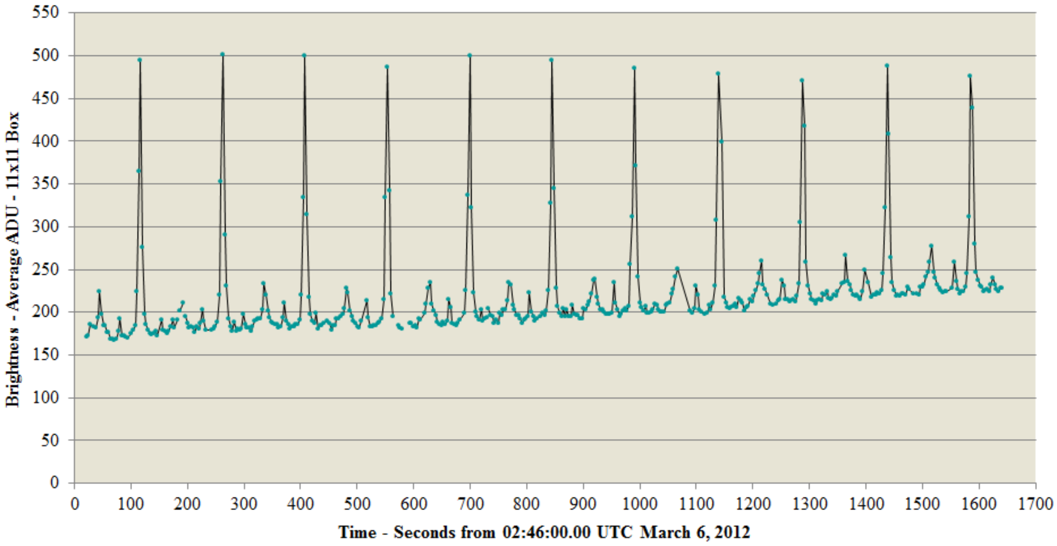

Figure 5.8: The Preliminary Light Curve of Telstar 401

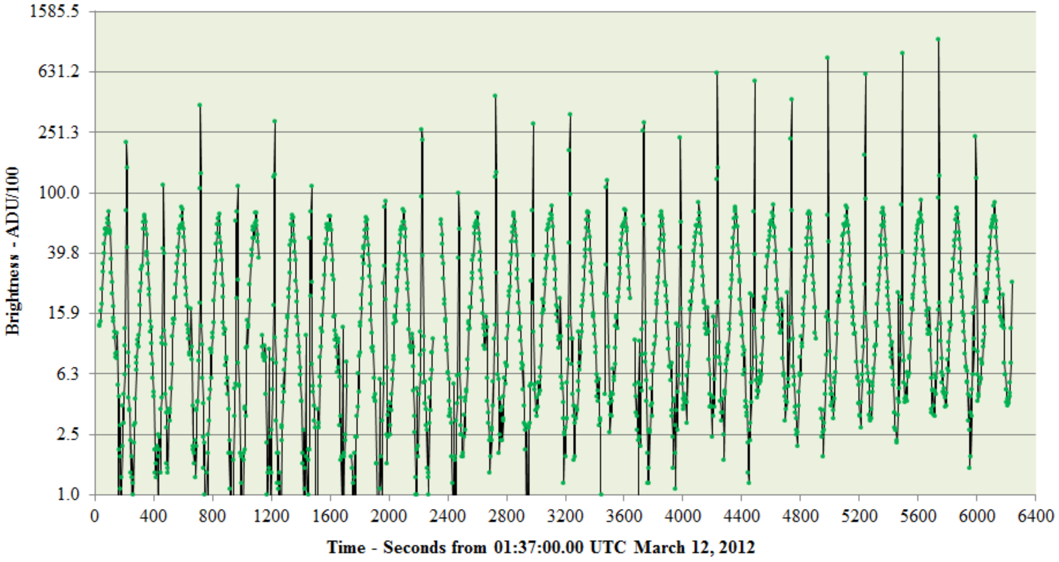

Figure 5.9: The Preliminary Light Curve of Echostar 2

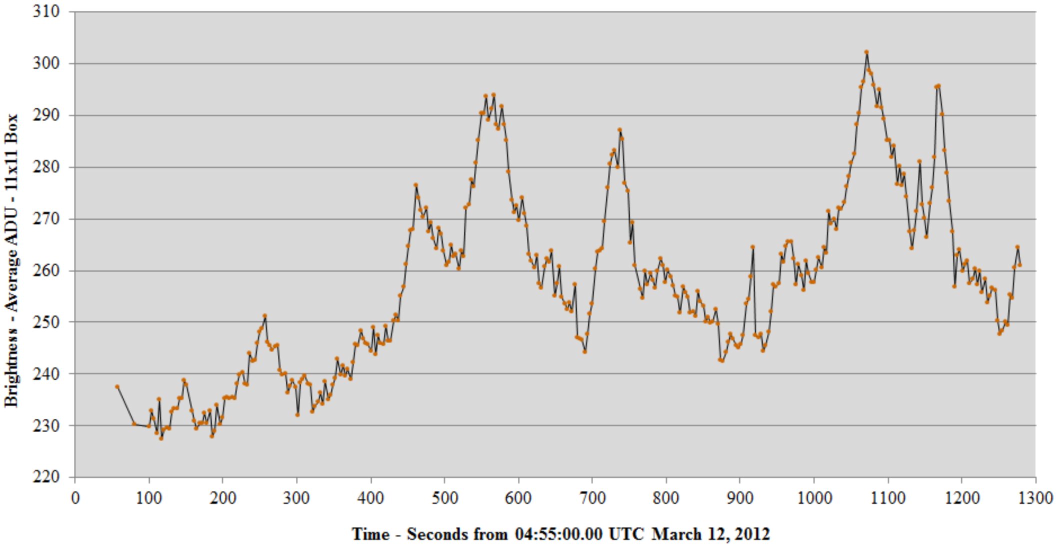

Figure 5.10: The Preliminary Light Curve of HGS-1

BACKGROUND SIGNAL SUBTRACTION

On the night the preliminary images of Solidaridad 1, Telstar 401 and HGS-1 were obtained, the 93% Moon was above the local horizon. As the images were being obtained, the angular separation between the satellites and the Moon was decreasing. This resulted in light curves that had increasing background signal floors with time. These results prompted the inclusion of an additional step of subtracting the background signal found in each image during the manual data extraction process.

The background signal of each of the images used to produce the light curves shown in Figures 5.6 to Figure 5.10 was determined using the steps shown in Table 5.2. Each average background signal was subtracted from the original light curve brightness value that it corresponded to. Figure 5.12 shows the background-subtracted light curve of Telstar 401 superimposed onto the preliminary light curve shown in Figure 5.8. Subtracting the background signal effectively normalized the light curve such that the signal floor appeared constantly low.

Figure 5.13 shows the background signal vs. time of all of the images used to produce the light curve of Figure 5.8. Figure 5.13 shows the residual background signal that includes the moonlight as the angular separation between the Moon and the satellite decreased from 31° to 24° during the observations of Telstar 401.

Table 5.2: Steps to Manually Subtract the Background Signal from Each Image

STEP		DESCRIPTION
1	**Open Image in CCDOps**	The image to be used for background subtraction is opened using the CCDOps software
2	**Detect Satellite in Image**	The satellite is found within the image
3	**Check for Space Free of Stars and Artefacts**	The immediate area around the satellite is checked for areas devoid of stars and CCD artefacts. An area about 20 to 50 pixels to the left of the satellite is arbitrarily chosen for background analysis (Figure 5.11). If the satellite appears near the left-hand edge of the image, the area 20 to 50 pixels to the right of the satellite is used instead.
4	**Check Sample Box Size is the same as the Original**	The CCDOps software is checked to verify that the background signal sample box size is the same as the satellite signal sample box size originally used to determine the brightness of the satellite
5	**Determine Average ADU of Background**	The average ADU count of the background signal sample box is determined using the “AvgVal” number in the “X Hair” window (Figure 5.11)
6	**Record Average Background Signal ADU**	The average ADU value of the background signal is recorded in the Excel spreadsheet in a column adjacent to the satellite signal column

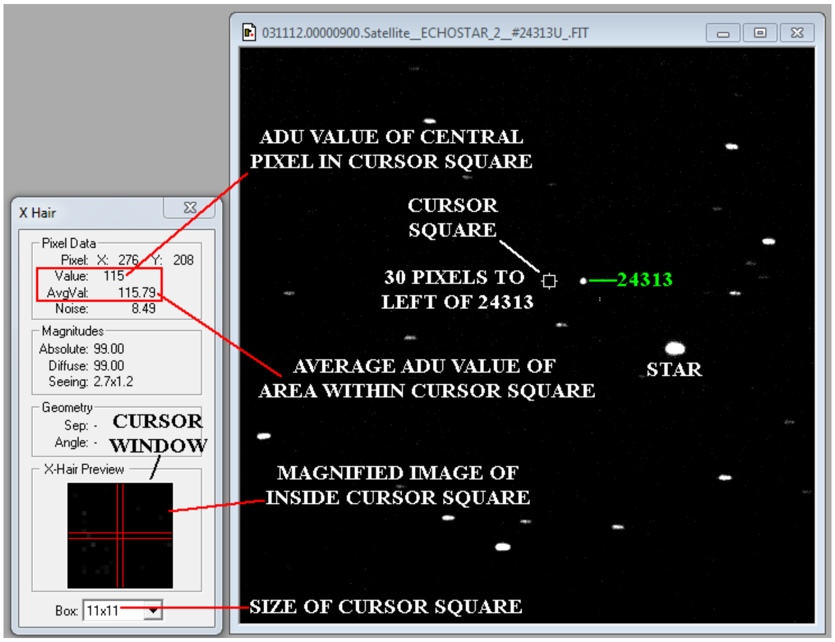

031112.00000900.Satellite__ECHOSTAR_2__#24313U_.FIT

X Hair

Pixel Data
Pixel: X: 276 Y: 208
Value: 115
AvgVal: 115.79
Noise: 8.49

Magnitudes
Absolute: 99.00
Diffuse: 99.00
Seeing: 2.7x1.2

Geometry
Sep: -
Angle: -

Box: 11x11

Figure 5.11: Determining Average Background Noise Subtraction in CCDOps

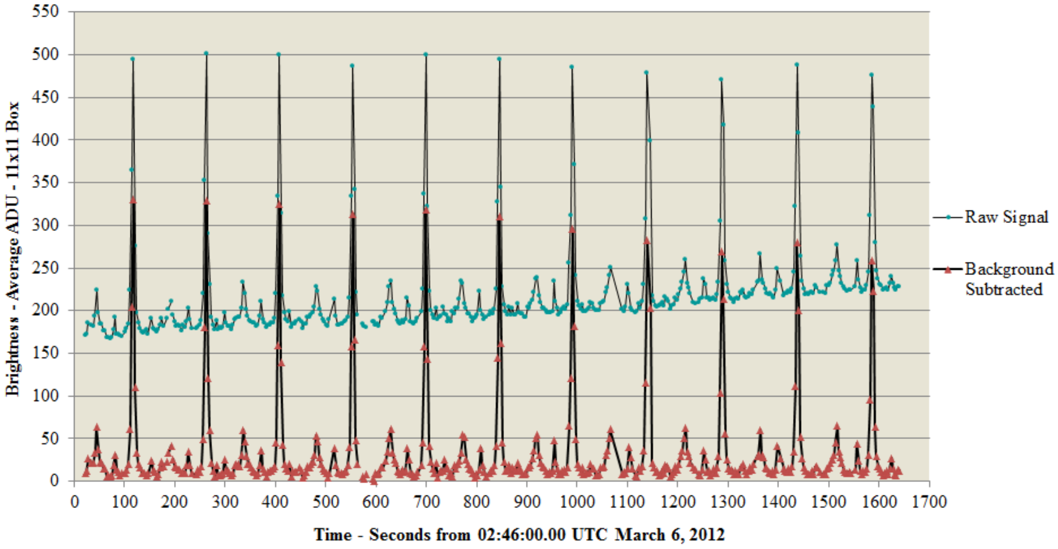

Figure 5.12: Background Subtracted Light Curve of Telstar 401 Compared to Figure 5.8

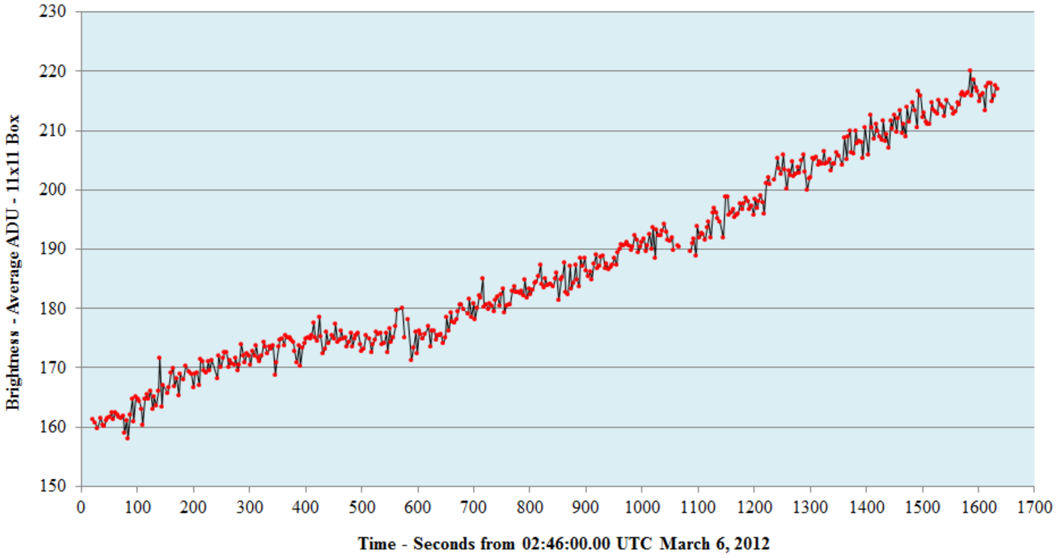

Figure 5.13: Residual Background Signal from Figure 5.8
Raw Signal minus the Background Signal shown in Figure 5.12
“Average ADU” Refers to the Total ADU within a 11x11 Sample Box Divided by 121 Pixels

CHAPTER 6: IMAGE DATA EXTRACTION SOFTWARE

The manual data extraction process was very time consuming, with every image requiring an average of 5 minutes to analyze. In one case, a single Echostar 2 light curve required two weeks to produce. In order to speed up this process, MATLAB software was created to automatically extract the time tags and satellite brightness from each image. The output of the prototyped MATLAB software was compared with the manually extracted time tags and satellite brightness for the same images of the same satellites mentioned in Chapter 5.

The MATLAB image data extraction software was designed to extract the required data from each image and to place them into text files. The contents of these text files were copied and pasted into their respective Excel spreadsheets to generate the light curves. The MATLAB image data extraction software created for this thesis was not designed to be turnkey or user-friendly. However, this software could be used to develop more robust data extraction software in the future.

TIME TAG EXTRACTION SOFTWARE

The time tag for each image is stored in each CCD image’s FITS header as text characters. The FITS headers can be easily accessed with MATLAB and therefore can be extracted and placed into text files. The process to automatically extract the time tags was very similar to the manual process, except that the software had to open and close files in sequence. The complete time tag extraction process using the MATLAB software is shown in Step 1 to Step 6 of Table 6.1.

The time tag extraction file contains the time elapsed since the very first image's time tag truncated to the minute. For example, if the first image of the imaging session had a time tag of 01:56:27.159 UTC, the first entry in the time tag extraction file will be 27.159 seconds. If the second image has a time tag of 01:56:30.660 UTC, then its entry in the time tag extraction file will be 30.660 seconds. If another image in the set has a time tag of 03:01:54.998 UTC, its entry in the time tag extraction file will be 3954.998 seconds, etc.

SATELLITE BRIGHTNESS EXTRACTION SOFTWARE – DESIGN CRITERIA

The MATLAB satellite brightness extraction process was more complicated than the time tag extraction process. The satellite brightness extraction software was developed separately from the time tag extraction software in order to test them out separately from one another. In the future, both modules can be combined to create more robust image data extraction software for satellite light curve generation.

In most cases, the variables used in this process were identical to those used in the time tag extraction software. Assuming the same images were used in each process, the "date" and "suf" variables (described in Step 2 of Table 6.1) would have the same values that were used in the time tag extraction process.

The software was not designed to automatically locate the satellite in the first image. That would still be accomplished manually through image inspection by eye, as described in Chapter 5. The position of the satellite in subsequent images would be predicted using a linear extrapolation of the apparent motion of the satellite determined from the two most recently analyzed images. Using only the first two images to determine the overall satellite motion would result in the compounding of errors as subsequent positions are predicted.

A problem to overcome during the software’s initial design was that the satellite would eventually reach the FOV’s edge and would appear to jump to the opposite side of the image (during satellite reacquisition; described in Chapter 4). Another problem was that during the reacquisition process, the CCD would still continuously acquire images, thus resulting in some images containing large vertical streaks (stars) due to the telescope’s sudden declination motion. The software would not know how to process any such anomalous images and thus could crash or produce nonsensical data from that point onward, having lost the satellite’s position.

The short-term solution to both of these problems was to define the four edges of the FOV within the software and to manually reacquire the satellite for the software. Any anomalous images obtained during satellite reacquisition would be manually deleted during analysis as they would contain no useful satellite brightness data.

A “block” of images was defined as that subset of contiguous images showing a satellite pass from one side of the FOV to the other. The light curve would be created with the first block of images and amended with each subsequent block of images. By inspecting the light curve during its creation, the majority of anomalies could be quickly identified and deleted. For example, the software was not designed to tell the difference between a satellite and a star (or a bright CCD artefact). If a star was mistaken for a satellite, the light curve would show a sudden departure from the brightness behaviour for that one observation. The corresponding image could be manually inspected and the observation deleted from the Excel spreadsheet if a star (or CCD anomaly) was detected near (or at) the satellite’s position.

The number of images that represent the full pass of the satellite through the FOV could have been estimated, but this would have taken too much time to do manually. Instead, the software was designed to show the user when the satellite had reached the edge of the FOV and that some anomalous images had been encountered. The output text file showed the useful data up to the point when the satellite reached the edge of the FOV. Beyond that point, the software would show “NaN” (not a number) or very low brightness values, showing the user that the subsequent analysis would be invalid. The user would then manually open the images that came after the last valid data extraction and would delete all anomalous images. Finally, the user would identify the two new starting images which would begin the extraction process for the next block of images.

The “block” variable used for the time tag extraction would also be used for the satellite brightness extraction process, but only for smaller blocks of images (unless the satellite remained in the FOV for the entire session). However, when the session’s first images were being analyzed, the “block” variable was assigned the very first and very last image numbers. The user did not need to determine which image corresponded to a full pass of the satellite though the FOV. Once the first iteration was complete, the user would then have had an estimate of how many images would constitute a full pass of the satellite through the FOV.

When beginning the satellite brightness extraction process, the user would manually determine the first two satellite positions corresponding to the first two images of the block. These first two satellite positions are the x and y pixel positions that roughly correspond to the center of each satellite signal distribution. The x and y image coordinates correspond to the column and row, respectively. These pixel positions were defined by the “guess” variable in the MATLAB software. This “guess” variable consists of four integers. The first two integers denote the y-x (column, row) pixel location of the satellite in the first image of the block and the last two integers denote the pixel location of the satellite in the second image.

Once the “date”, “suf”, “block” and “guess” variables have been defined, the software can be run to perform automated satellite brightness extraction for the specific block of images. The complete process to follow is described in Step 8 to Step 17 of Table 6.1.

The generated output text file is named “photo.txt”. This file contains the background subtracted brightness values in units of ADU. In order to reduce the size of the numbers involved, the software divides the total ADU by 100 for each image.

Since they are generated separately, the output of the time tag extraction and the output of the satellite brightness extraction are initially uncorrelated. The user must correlate each brightness value with its corresponding time tag by checking if the image file number and the decimal seconds of the FITS header time tag are the same as those entered in the Excel file. This correlation does not have to be done for every single image analyzed; however checking the correlation at the beginning of every new image block would minimize the possibility of human error. This correlation check was performed with every image block for all satellites in the analysis.

Future developments of this software will include automated satellite detection (for the beginning of each block), automated block size determination, automated star detection and automated light curve generation using MATLAB graphs. The time tag and satellite brightness data will also be automatically correlated.

SATELLITE LOCATION DETERMINATION

The satellite brightness extraction software first uses the user-supplied estimated satellite centroid positions in the first two images in the image block to extrapolate the position of the satellite centroid position in the third image of the block (Figure 6.1). This is done by subtracting the centroid position of the satellite in the first image from the centroid position of the satellite in the second image. The difference of the two centroid positions is then added to the centroid position of the satellite in the second image which results in a predicted x, y centroid position of the satellite in the third image. This method ensures that no matter what the apparent speed or direction of the satellite, the software can automatically predict the satellite’s position in subsequent images. This strategy also minimizes the search area so that the probability of accidental star (or anomaly) detection is minimized. In order for this strategy to work, the time between each image in the block would have to be similar to the others.

After the software predicts a subsequent satellite location, a search area is established. As images are acquired, air masses will move and the air density will change. As a result, the air’s index of refraction will be constantly changing. This effect is known as “scintillation”. Even if perfectly tracked, the satellite’s position and centroid will seem to randomly shift by several pixels from image to image. The software was designed to search within a 9x9 pixel box centered at the predicted centroid position. The software then uses all possible 3x3 pixel boxes within the search area to find the maximum average brightness. The center of the 3x3 pixel box corresponding to the maximum average brightness is considered to be the real centroid of the satellite distribution (Figure 6.1).

Once the software finds the real satellite centroid location, it is stored as the new second satellite location. Similarly, the previous image’s satellite location is stored as the new first satellite location. These two satellite locations will be used to predict the next satellite location, etc. throughout the block of images.

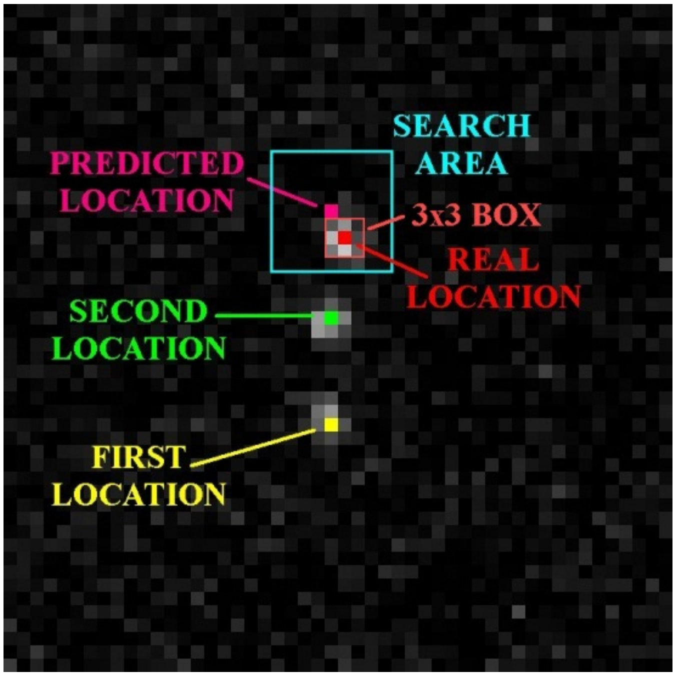

Figure 6.1: Predicting the Subsequent Satellite Location from Apparent Motion

BACKGROUND SIGNAL DETERMINATION

The software next determines the background signal in the immediate vicinity of the predicted location of the satellite in a specific image. A single sample box could not be used because a star could easily be located within that box. More than one area of the image had to be tested to determine the area of minimum brightness. The software uses four 11x11 pixel test boxes; one above, one below, one to the left and one to the right of the predicted satellite location, as shown in Figure 6.2. The center of each test box is 15 pixels from the satellite's predicted centroid. Figure 6.1 illustrates that the predicted satellite location does not have to be exactly the same as the actual satellite location. The pixels within each test box are summed to produce the total signal of each test box. The four total signal values are then compared. The test box with the smallest total signal is deemed to be the background signal of the image. This step differs from the manual background subtraction method because the software has to test out different sample boxes to determine which one can be considered the true background signal. This background signal is used as the signal floor when the software is determining the size of the satellite signal distribution.

If the satellite is near the edge of the FOV, the software automatically avoids placing any portion of a test box outside of the image matrix values. If a test box is allowed to be placed outside of the image boundaries, the software will crash and an error message will appear saying that the value exceeds the matrix limits.

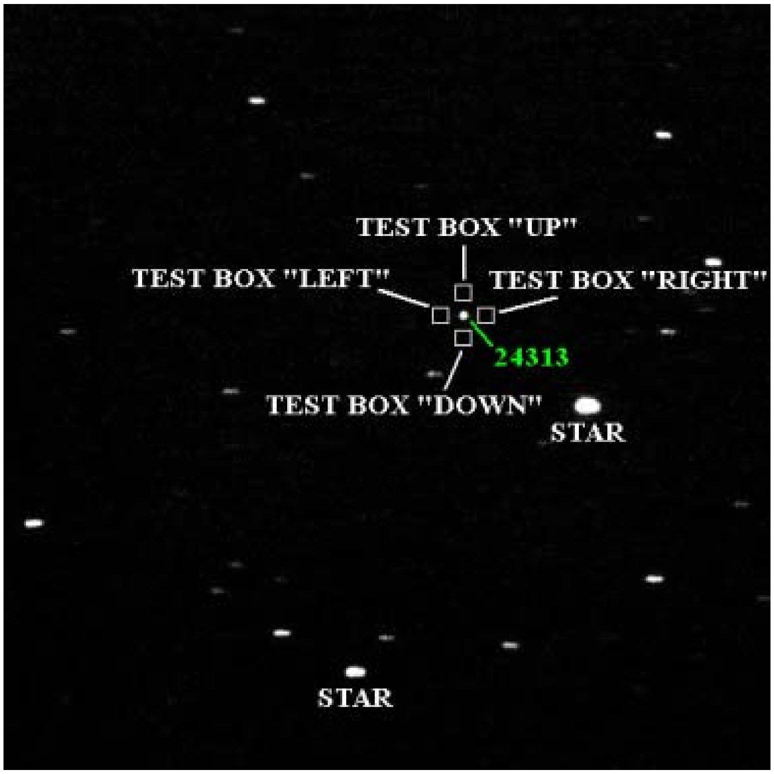

Figure 6.2: Satellite Distribution Surrounded by Four Background Test Boxes

SATELLITE DISTRIBUTION SIZE DETERMINATION

A problem that was encountered with the initial method of brightness data extraction was that a constant sample box size (such as 11x11 pixels, etc.) could be either too small or too large for the actual satellite distribution. If the sample box size was too large, background signal could be included with the satellite signal, despite background signal subtraction. If the sample box size was too small, a significant portion of the satellite brightness distribution would be omitted from the data point, thus introducing systematic errors in the final light curve.

The software automatically determines the size of the satellite distribution for each image. The software determines the edges of each satellite distribution so that the sample box would be tailored to the size of that distribution. The determined satellite brightness would therefore be more accurate than that determined using the constant sample box size. As a result, a “sample box” would become a “sample rectangle” since its dimensions would not necessarily define a square.

Starting from the determined centroid location, the software determines the size of the satellite signal distribution by comparing each pixel horizontally and vertically away from the centroid to the determined background signal plus 20 ADU. This value was arbitrarily chosen to make sure that when the software tried to find the edge of the satellite distribution, it would not include much of the signal background as well. This process is illustrated in Figure 6.3. It is not necessary for the software to determine the distribution’s edges to the point at which they blended in with the background signal. The full sample size of the distribution used in determining the total satellite signal in each image is thus determined.

Once the total area of the satellite signal is determined, the software sums the ADU pixel values within it and counts the number of pixels. If a pixel is found to have a brightness of less than the average background signal plus 20 ADU, the pixel is not used. The satellite brightness is determined by subtracting the total background signal for the distribution (average background signal multiplied by the number of signal pixels) from the total sample area brightness. Finally, the software divides the determined value by 100.

Despite using this sample area size determination method, stars and CCD artefacts can still be detected, thus producing erroneous values. The probability of producing erroneous values depends greatly on the density of stars within the FOV. For this reason, a satellite should not be viewed when it appears within the summer Milky Way (as originally stated in Table 4.1).

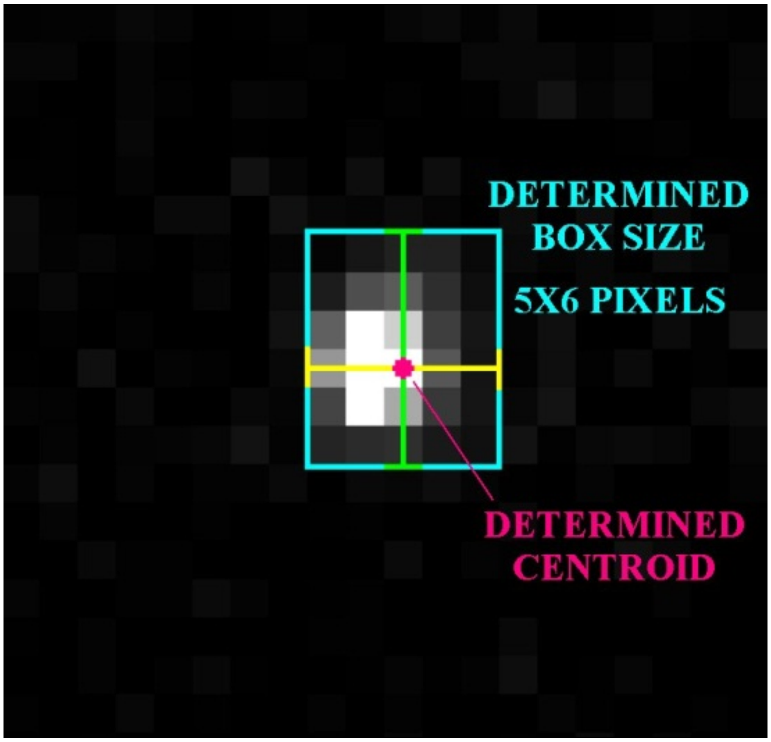

Figure 6.3: Determining the Satellite Distribution Sample Box Size

Table 6.1: Use of the MATLAB Image Data Extraction Software

STEP		DESCRIPTION
1	**Copy Image Files into MATLAB Directory**	The user manually copies all of the FITS image files that are to be analyzed into the directory that MATLAB can access
2	**Specify Filename Prefixes**	The filename prefix corresponding to the date (mmddyy) is specified in MATLAB using the “date” variable. For example, the “date” value for March 11, 2012 would be ‘031112’. The default value of the “suf” variable is ‘’ (no value) unless additional information is included in the file name other than the date and the sequential image number Syntax: date = ‘mmddyy’; suf = ‘remainder of image filename’; (not including the file extension)
3	**Specify First and Last Image Numbers to be Analyzed**	The sequential image number of the first and last image to be analyzed is specified. The “block” variable contains two integers, denoting the first image and the last image in the sequence. Syntax: block = [first image number, final image number];
4	**Run the “timetag.m” Script in MATLAB**	The “timetag.m” MATLAB script is run using the “date”, “suf” and “block” variables. The software will automatically create and fill a file called “ttag.txt” containing the time tags of all of the specified images. The format of these time tags will be the number of decimal seconds since the first image’s truncated time tag Syntax: time = timetag (date,suf,block);
5	**Open the “ttag.txt” file**	The “ttag.txt” file is opened using a text editor. All of the time tags in the correct format are listed in a single column
6	**Copy the Time Tags of the “ttag.txt” File**	All of the time tags in the “ttag.txt” file are highlighted and copied for pasting into an Excel spreadsheet column. The time tags are normally copied into the “B” column in Excel
7	**Add the Image Identification Numbers into the Excel Spreadsheet**	The first image ID number is entered into the first available row of Column A in the Excel spreadsheet. Subsequent rows will have the value of the subsequent image numbers as required

Table 6.1: Continued

8	**Open First Two FITS Images of the Block**	The first two FITS images in the block are opened using CCDSoft
9	**Determine Location of the Satellite in the Two Images**	The location of the satellite in both open images are determined and the approximate centers of their distributions (in x-y pixel coordinates) are located
10	**Enter the Satellite's x-y Pixel Coordinates**	The x-y pixel coordinates of the satellite distribution's approximate center in both images are the values used in the "guess" variable. Syntax: guess = [y1,x1,y2,x2];
11	**Run the MATLAB Satellite Brightness Extraction Program**	The MATLAB satellite brightness extraction software is run using the defined "date", "suf", "block" and "guess" variables Syntax: bright = photometry3 (date,suf,block,guess);
12	**Open the "photo.txt" Data File**	The "photo.txt" file is opened to show the extracted satellite brightness from each image
13	**Find the End of the Valid Data**	The satellite brightness values are numbers with values larger than 2 ADU. The valid data ends when the numbers begin to have values less than 2 ADU or "NaN"
14	**Copy the Satellite Brightness Values of the "photo.txt" File**	The satellite brightness values (in ADU) stored in the "photo.txt" file are highlighted to the end of the valid data and copied for pasting into an Excel spreadsheet column. The satellite brightness values are normally copied into the "C" column in Excel. The brightness values have to correlate with their respective time tags. The first and last image number of the block serve as guides for this correlation
15	**Delete Anomalous Image Files**	The end of the valid data in the "photo.txt" file normally corresponds to the point when the software finds the anomalous image files corresponding to the reacquisition of the satellite in the FOV. The user would have to open several image files after the last valid image and delete any image that contains large star streaks and/or no satellite detection

Table 6.1: Continued

16	**Determine Next Block of Images to Analyze**	The first image that contains a valid satellite detection (corresponding to the satellite's reacquisition) will be the first image to be used in the next block. The image after that will become the second image. These two images are used to determine the apparent satellite motion for the "guess" variable
17	**Repeat Step 8 to Step 17 As Required**	The satellite brightness extraction of the next block of images is performed by repeating Step 8 to Step 17 until all of the images for that satellite have been analyzed

COMPARISON WITH MANUALLY EXTRACTED DATA

When the prototype brightness extraction software's output was tested against the manually-extracted data, there were several discrepancies of less than 1ADU, which were confirmed to have been caused by typos made during the manual data entry into Excel. This comparison quickly proved that the automated process was more trustworthy than the manual process as long as careful correlation between the time tags and the satellite brightness was performed in Excel. One example of the difference between the manual brightness extraction and the automated brightness extraction for the ACTS satellite is shown in Figure 6.4.

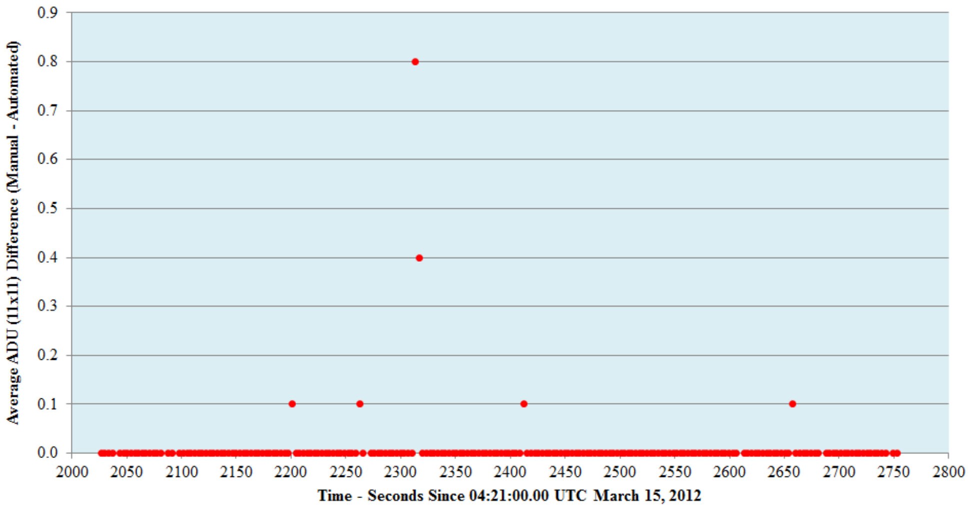

Figure 6.4: Manual vs. Automated Brightness Extraction for the ACTS Satellite

Figure 4.6 shows the difference between the manually extracted satellite brightness and the software-extracted satellite brightness for each image of ACTS obtained on March 15, 2012. With a few exceptions, most of these differences are 0. The values that are not 0 turned out to be typos made during the manual data entry.

As subsequent modifications were made to the software, comparisons of the output brightness with the original manual extractions became less and less useful. Automated satellite distribution size determination no longer correlated with the constant 11x11 sample box. However, the order of magnitude of the satellite brightness values was still very similar (within 50 ADU)

CHAPTER 7: SPIN PERIOD DETERMINATION

When an object is rotating about a spin axis, an observer will see differing perspectives of the object during its spin period, assuming that the object is non-symmetric reflectively. Assuming a static spin axis, the same observer will, over subsequent spin periods, see the same sides of the object pass within the FOV. If the observer measures the sunlight that is reflected off of the rotating object, a light curve consisting of recurring and periodic distributions will be observed. By locating and measuring the time elapsed between these recurring distributions, the object's apparent spin period can be determined.

The light curves shown in Figure 5.4, Figure 5.6 and Figure 5.7 show a periodic behaviour that suggest that the corresponding satellites are spinning. Subsequent observations of the inactive Solidaridad 1 and HGS-1 satellites have also suggested spinning behaviour.

IDENTIFYING RECURRING LIGHT CURVE CHARACTERISTICS

A "recurring light curve characteristic" is a light curve feature that appears to repeat in a periodic fashion. This characteristic could be a brightness maximum, brightness minimum or any other unique feature of the light curve. A "family" of recurring characteristics contains every occurrence of a specific recurring light curve characteristic. Figure 7.1 shows a sub-section of the Echostar 2 light curve originally shown in Figure 5.7. Figure 7.1 uses a logarithmic scale (base 2.5) to accentuate the light curve's recurring characteristics. Figure 7.1 identifies 2 unique families (named "1" and "2") contained within the light curve, each with its own recurring characteristic. Note that each family contains a recurring characteristic that appears to repeat approximately every

500 seconds. This behaviour suggests that the satellite's apparent spin period is approximately 500 seconds.

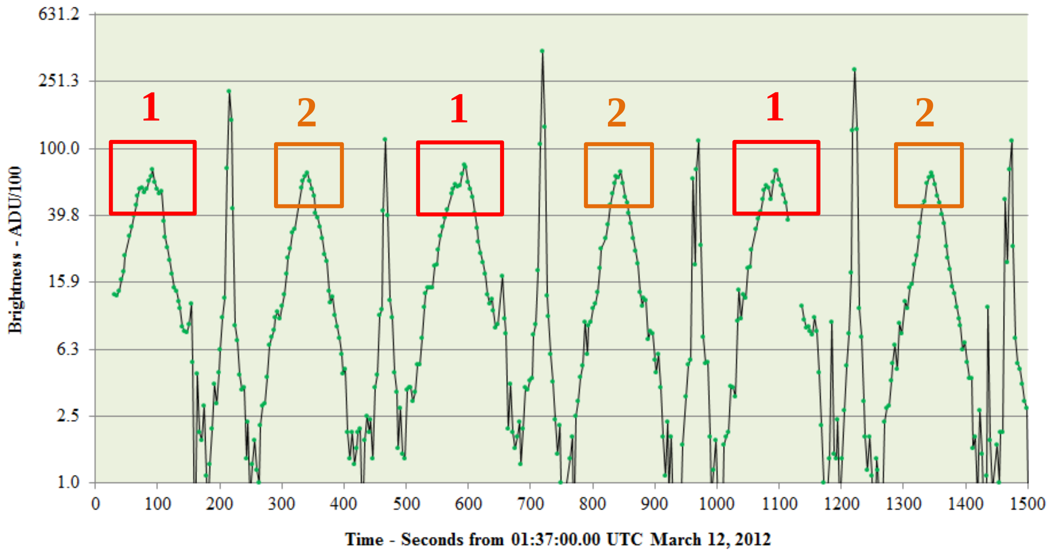

Figure 7.1: Identifying the Recurring Light Curve Characteristics for Echostar 2

The characteristics of the very tall, thin distributions in the light curve in Figure 7.1 could not be identified because these distributions were not well sampled (low resolution). If the satellite's spin had been slower and/or the sampling frequency had been higher, these particular distributions might have been better sampled in order to reveal their unique characteristics. However, once the acceptable recurring characteristics had been identified, the tall, thin distributions could be used to assist in determining the apparent spin period of the satellite, as shown later in this chapter. Since the tall, thin distributions were sharper than the wider distributions, they could be used to determine spin periods with narrower tolerances.

Note that Family 1's three components, shown in Figure 7.1, do not look absolutely identical to one another. However, Family 2's three components look much more similar to one another. The subtle changes to the recurring characteristic of Family 1 might be due to the satellite's slowly changing perspective with respect to the observer and the Sun. Another factor that can change the observed light curve is the precession of the spin axis. The reliable identification of the periodic behaviour within any spinning satellite's light curve relies on these two effects being small and/or having a much longer period than the satellite's spin period.

Once the recurring characteristics have been identified in the light curve, the satellite's apparent spin period can be determined using at least one of three methods. Each method is dependent on accurate timing, as described in the next section.

TIMING

Finding an apparent spin period requires determining the time elapsed between at least two observations that correspond to a family of recurring characteristics. The only absolute time indicator was the CCD time stamp in each image's FITS header. Each time tag indicated the time when the initial command to open the CCD shutter was given. The time tag indicates the beginning of a CCD duty cycle, as illustrated in Figure 7.2. The CCD shutter actually opened 0.7 seconds after the command to open the shutter, as shown in Figure 7.2. Light from the satellite was collected during the exposure time and downloaded to the computer during the download time, as shown in Figure 7.2. The elapsed time of the duty cycle changed as the exposure time and the pixel binning changed.

The average elapsed time for a duty cycle (for the CCD model listed in Table 4.3), containing a 1-second exposure and using a 1x1 pixel binning was determined to be (3.32±0.05) seconds. 7,500 CCD images of Echostar 2 obtained on May 11, 2012 were used for this determination. A histogram containing all of these elapsed times is shown in Figure 7.3.

Each light curve data point corresponded to the total satellite brightness collected over its exposure time. The exact time of a recurring light curve characteristic (such as maximum or minimum brightness, etc.) occurred at any time within the exposure time or between exposures. Therefore, the uncertainty of each light curve data point corresponding to a recurring characteristic was deemed to be the CCD duty cycle's elapsed time.

The total uncertainty of the difference between two FITS header time stamps was determined by using the quadrature (square root of the sum of the squares) of the time stamp uncertainties.

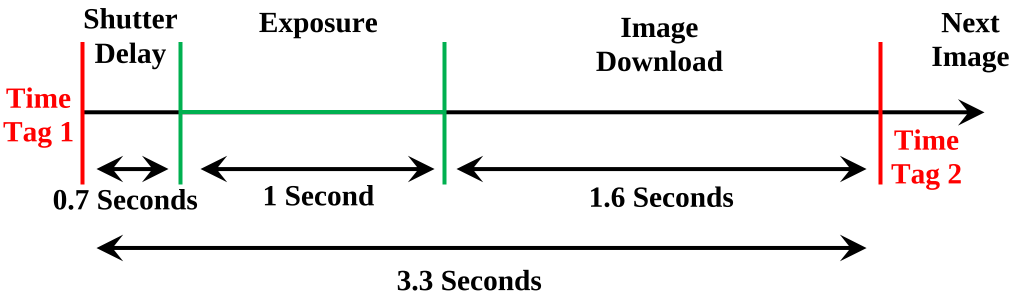

Figure 7.2: Duty Cycle for a ST-9XE CCD 1-Second Exposure with 1x1 Pixel Binning

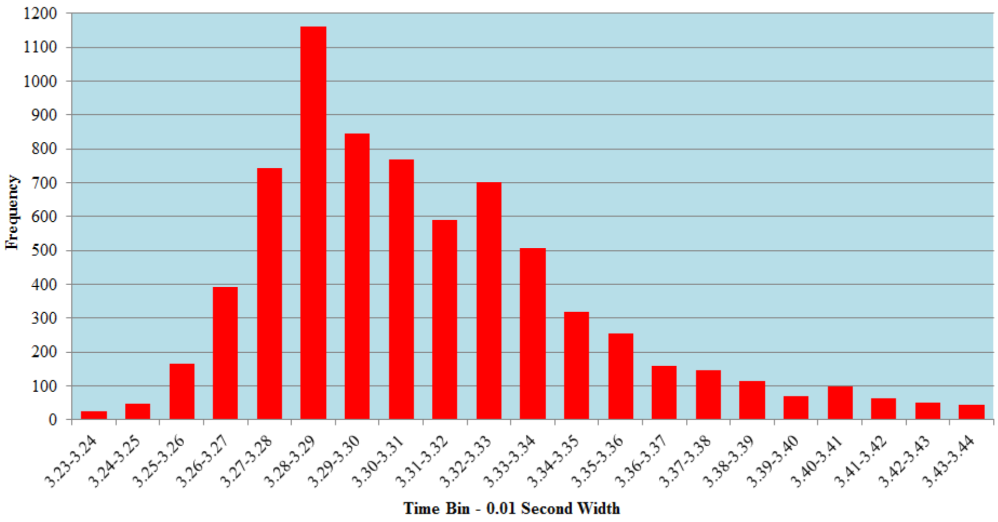

Figure 7.3: Histogram of ST-9XE Duty Cycle: 1-Second Exposure and 1x1 Binning

METHOD 1: ADJACENT SIMILAR LOCAL MAXIMA

Each of the recurring characteristics shown in Figure 7.1 has a maximum brightness value associated with it. A preliminary estimation of the satellite’s apparent spin period can be made using the elapsed time between the maxima of two adjacent recurring characteristics; also known as “adjacent maxima” or “maxima pair”. Maxima are used because they represent the areas of highest signal within each distribution.

Measuring the time elapsed between a single “maxima pair” will result in a determined apparent spin period with the highest uncertainty. However, using many maxima pairs will reduce the statistical uncertainty of the resultant apparent spin period. Figure 7.4 shows all of the local maxima for the Echostar 2 example light curve shown in Figure 7.1. Each maximum in Figure 7.4 contains two numbers. The first number identifies the family. The second number identifies the order of occurrence in time (temporal occurrence) of that recurrent characteristic within that family. Note that the tall, thin distributions are included in Figure 7.4 because the spacing between adjacent recurrent characteristics had been previously identified.

Table 7.1 lists the times of all local maxima contained within the Echostar 2 light curve of Figure 5.7. The apparent spin periods were determined from the adjacent maxima pair in each family by calculating the difference of the time tags in the FITS headers of the corresponding images. The uncertainties of the apparent spin periods in Table 7.1 were determined using the quadrature of the uncertainties (±3.32 seconds) of the elapsed time between the FITS header time tags corresponding to the maxima.

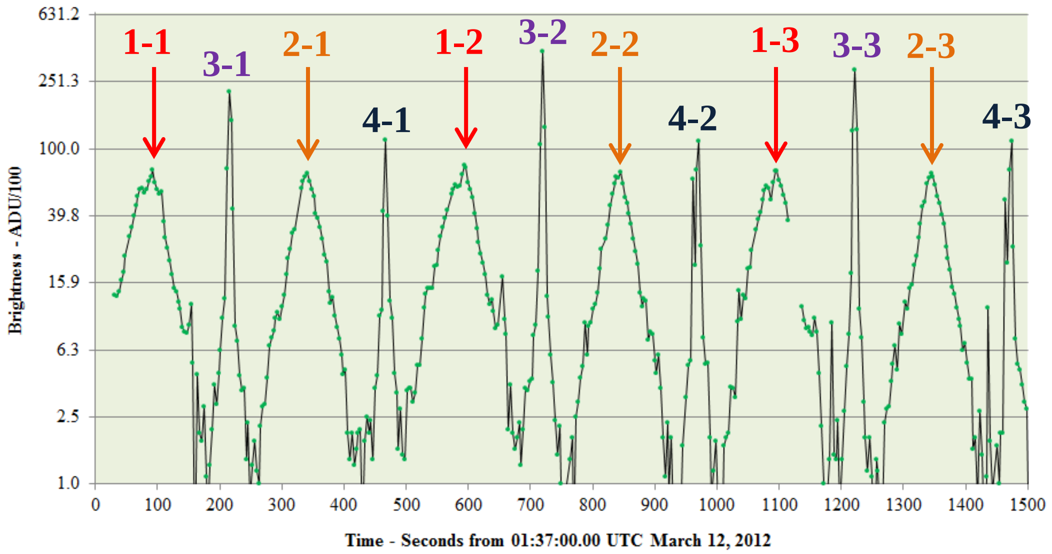

Figure 7.4: Local Maxima for Apparent Spin Period Determination

Table 7.1: Determined Apparent Spin Periods Using Adjacent Maxima Method

FAMILY	TEMPORAL OCCURRENCE	TIME OF MAXIMUM (s)	APPARENT SPIN PERIOD (s)
1	1	92.8±3.3	-------------
1	2	593.3±3.3	500.5±4.7
1	3	1097.0±3.3	503.7±4.7
1	4	1599.7±3.3	502.7±4.7
1	5	2099.2±3.3	499.5±4.7
1	6	2602.3±3.3	503.1±4.7
1	7	3106.0±3.3	503.7±4.7
1	8	3606.3±3.3	500.3±4.7
1	9	4109.7±3.3	503.4±4.7
1	10	4613.4±3.3	503.7±4.7
1	11	5114.5±3.3	501.1±4.7
1	12	5617.9±3.3	503.4±4.7
1	13	6121.4±3.3	503.5±4.7
2	1	341.2±3.3	-------------
2	2	845.2±3.3	504.0±4.7
2	3	1344.5±3.3	499.3±4.7
2	4	1843.8±3.3	499.3±4.7
2	5	N/A	-------------
2	6	2850.9±3.3	-------------
2	7	3351.2±3.3	500.3±4.7
2	8	3857.7±3.3	506.6±4.7
2	9	4361.6±3.3	503.9±4.7
2	10	N/A	-------------

Table 7.1 Continued

2	11	5363.4±3.3	-------------
2	12	5864.4±3.3	501.0±4.7
3	1	215.3±3.3	-------------
3	2	719.2±3.3	503.8±4.7
3	3	1221.9±3.3	502.8±4.7
3	4	N/A	-------------
3	5	2225.2±3.3	-------------
3	6	2728.4±3.3	503.2±4.7
3	7	3232.0±3.3	503.7±4.7
3	8	3735.1±3.3	503.1±4.7
3	9	4235.6±3.3	500.5±4.7
3	10	4739.4±3.3	503.8±4.7
3	11	5241.3±3.3	501.9±4.7
3	12	5742.9±3.3	501.6±4.7
4	1	467.3±3.3	-------------
4	2	971.2±3.3	503.9±4.7
4	3	1473.7±3.3	502.5±4.7
4	4	1976.6±3.3	502.9±4.7
4	5	2476.3±3.3	499.7±4.7
4	6	2980.2±3.3	503.9±4.7
4	7	3483.8±3.3	503.5±4.7
4	8	3983.7±3.3	499.9±4.7
4	9	4487.4±3.3	503.7±4.7
4	10	4989.2±3.3	501.8±4.7
4	11	5492.3±3.3	503.1±4.7
4	12	5992.9±3.3	500.6±4.7

Figure 7.5 shows the apparent spin periods grouped with respect to their respective families. The figure shows that there is no discernible trend over the observing session time of nearly 6,300 seconds (1.75 hours). Table 7.2 shows the average and standard deviation for all of the spin periods and the spin periods from each unique family of similar maxima shown in Table 7.1.

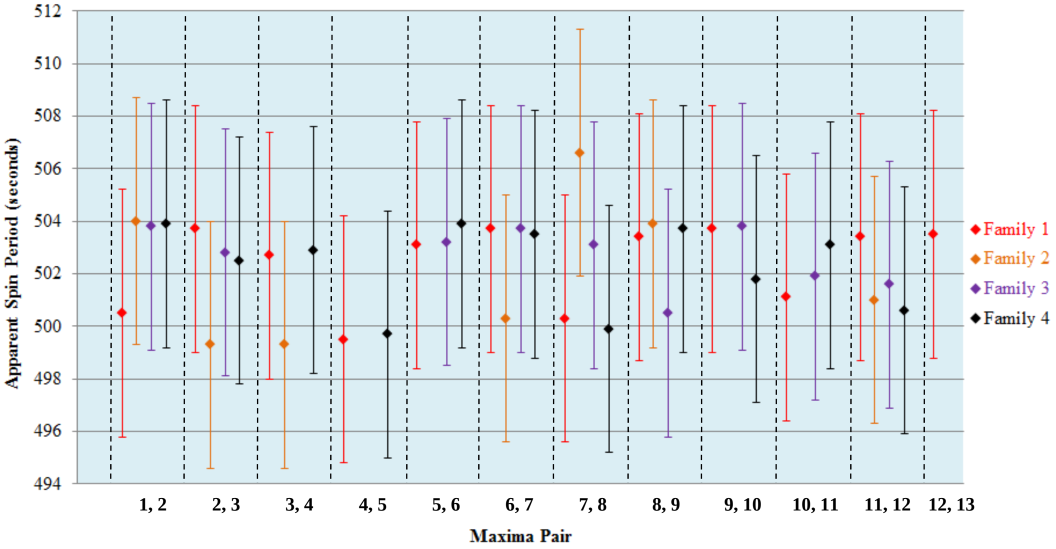

Figure 7.5: Apparent Spin Periods – Adjacent Maxima Method

Table 7.2: Average Spin Periods for Each Family of Similar Adjacent Maxima

FAMILY	POPULATION	APPARENT SPIN PERIOD (s)
1	12	502.4±1.6
2	6	501.3±2.4
3	9	502.7±1.2
4	11	502.3±1.6
ALL	**38**	**502.3±1.6**

METHOD 2: MAXIMA CLUSTERS

This method is very similar to Method 1, except that the maxima pairs used are not adjacent. The two components of the maxima pair are still within the same family, but they are separated by an integer number of periods. In this case the spin period is found by dividing the determined elapsed time by the integer number of spin periods between them. As an example, Figure 7.6 shows a maxima pair determination using separations of three integer spin periods, although any integer number can be used. The determined apparent spin period will have an uncertainty that is an integer fraction of a single period's uncertainty. Table 7.3 shows the results of using maxima clusters containing three integer spin periods. The apparent spin period was determined in the same way as in Table 7.1, but the uncertainty was divided by the integer number of period between the maxima pairs. Table 7.4 lists the results of the apparent spin period if the individual spin periods in every family were combined.

If the satellite's spin period exhibits no detectable spin period variability when using Method 1, then this method can be used to reduce the statistical uncertainty of the determined spin period. If a sudden change in spin period is detected anywhere in the light curve, either the light curve could contain an error or the apparent spin period is genuinely varying.

If required, different combinations and/or different sizes of maxima clusters can be used to verify the initial findings of the apparent spin period. One such combination, described in Method 3, involves using only the first and final maximum of a specific family.

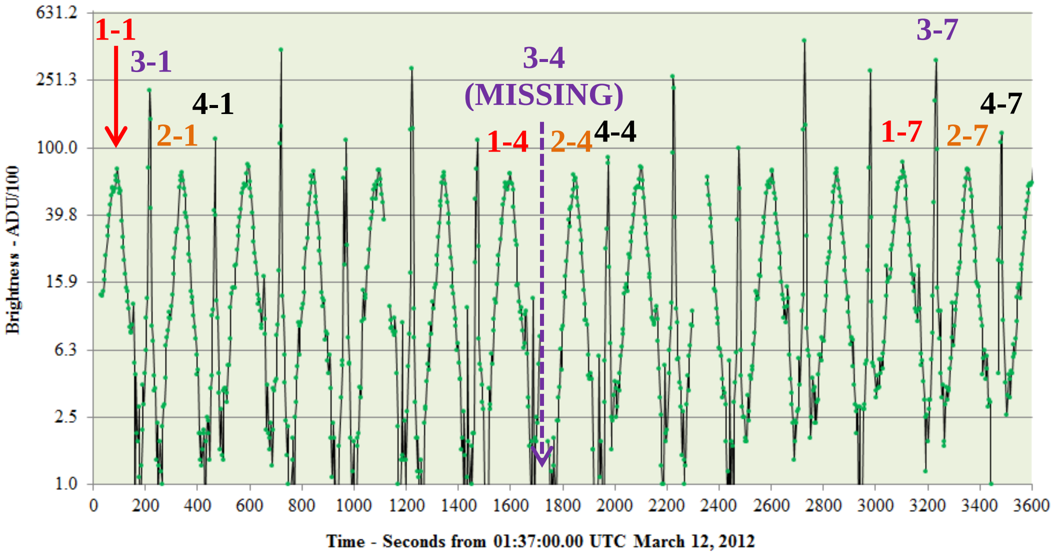

Figure 7.6: Locating Similar Maxima Three Integer Periods Apart

Table 7.3: Determined Apparent Spin Periods Using Maxima Cluster Method

FAMILY	TEMPORAL OCCURRENCE	TIME OF MAXIMUM (s)	ELAPSED TIME (s)	APPARENT SPIN PERIOD (s)
1	1	92.8±3.3	-------------	-------------
1	4	1599.7±3.3	1506.9±4.7	502.3±1.6
1	7	3106.0±3.3	1506.3±4.7	502.1±1.6
1	10	4613.4±3.3	1507.4±4.7	502.5±1.6
1	13	6121.4±3.3	1508.0±4.7	502.7±1.6
2	3	1344.5±3.3	-------------	-------------
2	6	2850.9±3.3	1506.4±4.7	502.1±1.6
2	9	4361.6±3.3	1510.7±4.7	503.6±1.6
2	12	5864.4±3.3	1502.8±4.7	500.9±1.6
3	3	1221.9±3.3	-------------	-------------
3	6	2728.4±3.3	1506.4±4.7	502.1±1.6
3	9	4235.6±3.3	1507.3±4.7	502.4±1.6
3	12	5742.9±3.3	1507.3±4.7	502.4±1.6
4	1	467.3±3.3	-------------	-------------
4	4	1976.6±3.3	1509.3±4.7	503.1±1.6
4	7	3483.8±3.3	1507.2±4.7	502.4±1.6
4	10	4989.2±3.3	1505.4±4.7	501.8±1.6

Table 7.4: Average Spin Periods for Each Family of Maxima Clusters

FAMILY	POPULATION	APPARENT SPIN PERIOD (s)
1	4	502.4±0.3
2	3	502.2±1.4
3	3	502.3±0.2
4	3	502.4±0.7
ALL	**13**	**502.3±0.6**

METHOD 3: EXTREME MAXIMA

Once the consistency of Echostar 2’s apparent spin periods had been confirmed, this method was used to determine its apparent spin period. In this method, the time difference between the extreme (first and last) maxima for each light curve’s family was determined, as shown in Figure 7.7. The apparent spin period was found by dividing the determined elapsed time by the maximum integer number of spin periods allowed for the specific family in the light curve.

In Method 3, care was taken to ensure that the compared maxima were from the same family, especially when analyzing light curves with many integral spin periods between the extreme maxima. The results of determining the apparent spin period of Echostar using Method 3 is shown in Table 7.5.

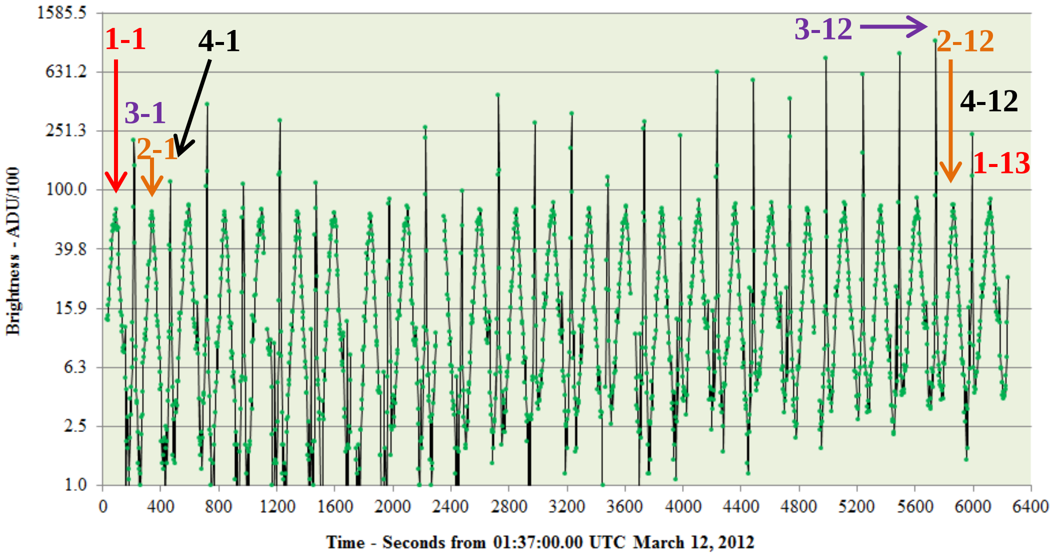

Figure 7.7: Locating Extreme Maxima

Table 7.5: Determined Apparent Spin Periods Using Extreme Maxima Method

FAMILY	TEMPORAL OCCURRENCE	TIME OF MAXIMUM (s)	ELAPSED TIME (s)	APPARENT SPIN PERIOD (s)
1	1	92.8±3.3	-------------	-------------
1	13	6121.4±3.3	6028.6±4.7	502.4±0.4
2	1	341.2±3.3	-------------	-------------
2	12	5864.4±3.3	5523.2±4.7	502.1±0.4
3	1	215.3±3.3	-------------	-------------
3	12	5742.9±3.3	5527.6±4.7	502.5±0.4
4	1	467.3±3.3	-------------	-------------
4	12	5992.9±3.3	5525.7±4.7	502.3±0.4
ALL	--------	------------------	---------------	**502.3±0.2**

SPIN PERIOD DETERMINATION METHOD COMPARISONS

The spin period determination methods described in this chapter differ only by the number of integer periods between the maxima pairs being analyzed. Table 7.6 lists specific advantages, disadvantages and guidelines for each of the three methods.

Table 7.6: Spin Period Determination Methods - Advantages, Disadvantages and Guidelines

METHOD	ADVANTAGES	DISADVANTAGES	GUIDELINES
1 ADJACENT MAXIMA	- spin period behaviour can be monitored from maximum to maximum - a few missing maxima will not compromise the results - maximum amount of data for average and standard deviation - most accurate method for variable apparent spin periods	- can be very time-consuming to apply for longer duration light curves - spin period error from each maxima pair can be large	- verify that all adjacent maxima are from the same family of similar light curve distributions - missing maxima can be omitted or replaced by the next available maximum in the same family
2 MAXIMA CLUSTERS	- a good compromise between Method 1 and Method 3 - can be used to check the behaviour of the spin period during light curve generation without using the more time-consuming adjacent maxima method	- determining the best integral number of spin periods can be time-consuming - missing maxima can complicate logistics - missing maxima could compromise average spin period accuracy	- use the same integral number of spin periods throughout to find any trends - the value of the integer number of spin periods should be between 1 and the light curve's maximum value
3 EXTREME MAXIMA	- quickest determination - easiest to use - very statistically accurate - averaging seldom required	- spin period behaviour is not resolved within the light curve - accuracy of determined spin period will depend on only two data points per family - might be the least accurate for variable apparent spin periods	- each extreme maxima pair must correspond to the same family - verify the number of spin periods between maxima - use the maximum number of integer periods between maxima

CHAPTER 8: FINAL SATELLITE SELECTION

The seven selected GEO box-wing satellites shown in Table 5.2 were found to be detectable using the equipment listed in Table 4.3. However, it was not yet known whether the detector's sampling frequency was adequate to enable the accurate determination of the satellites' apparent spin periods. The preliminary observations of ACTS, Telstar 401 and Echostar 2 were reanalyzed with the MATLAB data extraction software described in Chapter 6. Their new light curves are shown in Figure 8.1, Figure 8.2 and Figure 8.3 respectively. The spin periods of ACTS, Telstar 401 and Echostar 2 were determined using the Adjacent Maxima Method and the Extreme Maxima Method. The results are listed in Table 8.1 and Table 8.2 respectively (for ACTS), Table 8.3 and Table 8.4 respectively (for Telstar 401) and Table 8.5 and Table 8.6 respectively (for Echostar 2).

Subsequent observations of Solidaridad 1 and HGS-1 were obtained in June 2012 to determine if their light curves (Figure 8.4 and Figure 8.5, respectively), also suggested spinning behaviour. The spin periods of Solidaridad 1 and HGS-1 were determined using the Adjacent Maxima Method and the Extreme Maxima Method. The results are listed in Table 8.7 and Table 8.8 respectively (for Solidaridad 1) and Table 8.9 and Table 8.10 respectively (for HGS-1).

Preliminary observations of GStar 3 and Telstar 402R were analyzed with the MATLAB data extraction software and their resultant light curves are shown in Figure 8.6 and Figure 8.7, respectively. The GStar 3 satellite's light curve suggested that the system's sampling frequency of (0.356±0.008) Hz was too low to adequately sample the satellite's brightness variability. The Telstar 402R light curve did not appear to contain any recurring light curve characteristics which suggested that the satellite's apparent spin period was greater than 2400 seconds. This spin period was considered too long for subsequent spin period determination because the maximum imaging session duration was set at 2 hours. These two satellites were not considered as candidates for further study and thus subsequent light curves were not obtained.

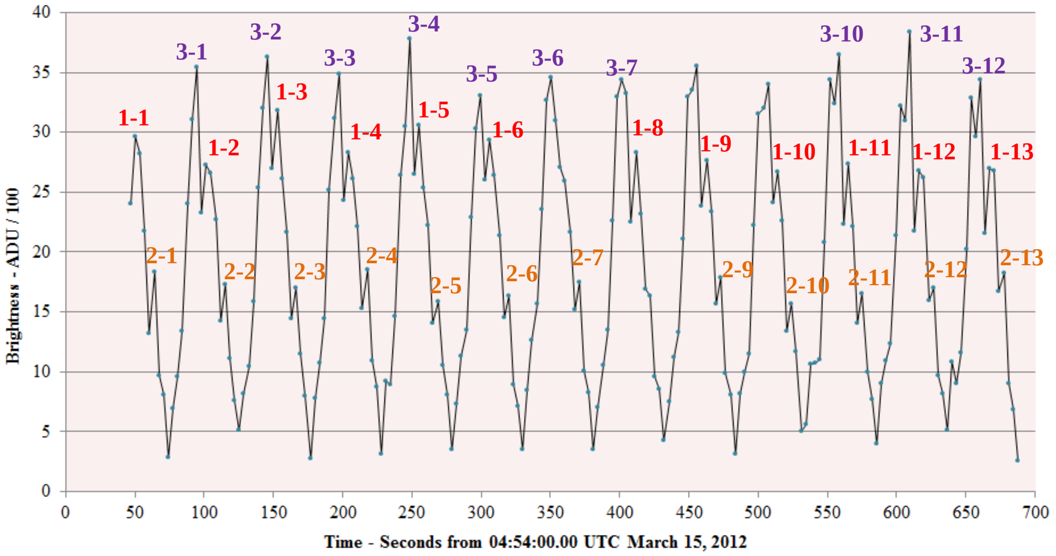

Figure 8.1: ACTS Light Curve – Data Extraction Software

Table 8.1: Apparent Spin Periods of ACTS - Adjacent Maxima Method

FAMILY	TEMPORAL OCCURRENCES	APPARENT SPIN PERIOD (s)
1	1, 2	51.1±4.8
1	2, 3	51.5±4.8
1	3, 4	51.2±4.8
1	4, 5	51.1±4.8
1	5, 6	51.1±4.8
1	8, 9	51.1±4.8
1	9, 10	51.2±4.8
1	10, 11	51.1±4.8
1	11, 12	51.0±4.8
1	12, 13	51.1±4.8
2	1, 2	51.2±4.8
2	2, 3	51.3±4.8
2	3, 4	51.3±4.8
2	4, 5	51.1±4.8

Table 8.1 Continued

2	5, 6	51.1±4.8
2	6, 7	51.1±4.8
2	9, 10	51.2±4.8
2	10, 11	51.1±4.8
2	11, 12	51.1±4.8
2	12, 13	50.9±4.8
3	1, 2	51.5±4.8
3	2, 3	51.2±4.8
3	3, 4	51.0±4.8
3	4, 5	51.1±4.8
3	5, 6	51.1±4.8
3	6, 7	51.1±4.8
3	10, 11	51.1±4.8
3	11, 12	51.1±4.8
ALL	--------	**51.15±0.13**

Table 8.2: Apparent Spin Periods of ACTS - Extreme Maxima Method

FAMILY	TEMPORAL OCCURRENCES	APPARENT SPIN PERIOD (s)
1	1, 13	**51.4±0.4**
2	1, 13	**51.1±0.4**
3	1, 12	**51.5±0.4**

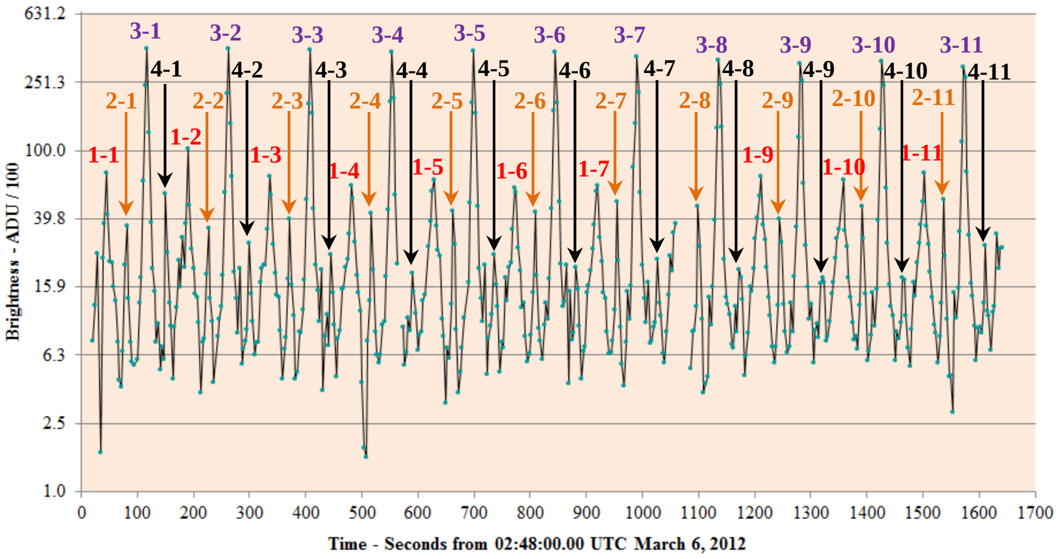

Figure 8.2: Telstar 401 Light Curve – Data Extraction Software

Table 8.3: Apparent Spin Periods of Telstar 401 – Adjacent Maxima Method

FAMILY	TEMPORAL OCCURRENCES	APPARENT SPIN PERIOD (s)
1	1, 2	145.4±4.7
1	2, 3	145.4±4.7
1	3, 4	145.6±4.7
1	4, 5	148.2±4.7
1	5, 6	143.0±4.7
1	6, 7	148.8±4.7
1	9, 10	146.0±4.7
1	10, 11	145.4±4.7
2	1, 2	145.4±4.7
2	2, 3	145.4±4.7
2	3, 4	145.4±4.7
2	4, 5	145.1±4.7
2	5, 6	146.4±4.7
2	6, 7	145.4±4.7
2	7, 8	145.5±4.7
2	8, 9	145.4±4.7
2	9, 10	145.9±4.7
2	10, 11	145.8±4.7
3	1, 2	145.4±4.7
3	2, 3	145.4±4.7
3	3, 4	145.5±4.7
3	4, 5	146.0±4.7
3	5, 6	145.4±4.7
3	6, 7	145.4±4.7
3	7, 8	145.5±4.7
3	8, 9	145.4±4.7
3	9, 10	146.0±4.7
3	10, 11	145.3±4.7
4	1, 2	148.7±4.7
4	2, 3	145.4±4.7
4	3, 4	145.0±4.7
4	4, 5	146.4±4.7
4	5, 6	145.4±4.7
4	6, 7	145.4±4.7
4	7, 8	145.5±4.7
4	8, 9	148.7±4.7
4	9, 10	142.7±4.7
4	10, 11	147.7±4.7
ALL	**-------**	**145.5±0.3**

Table 8.4: Apparent Spin Periods of Telstar 401 - Extreme Maxima Method

FAMILY	TEMPORAL OCCURRENCES	APPARENT SPIN PERIOD (s)
1	1, 11	**145.9±0.5**
2	1, 11	**145.6±0.5**
3	1, 11	**145.5±0.5**
4	1, 11	**146.1±0.5**

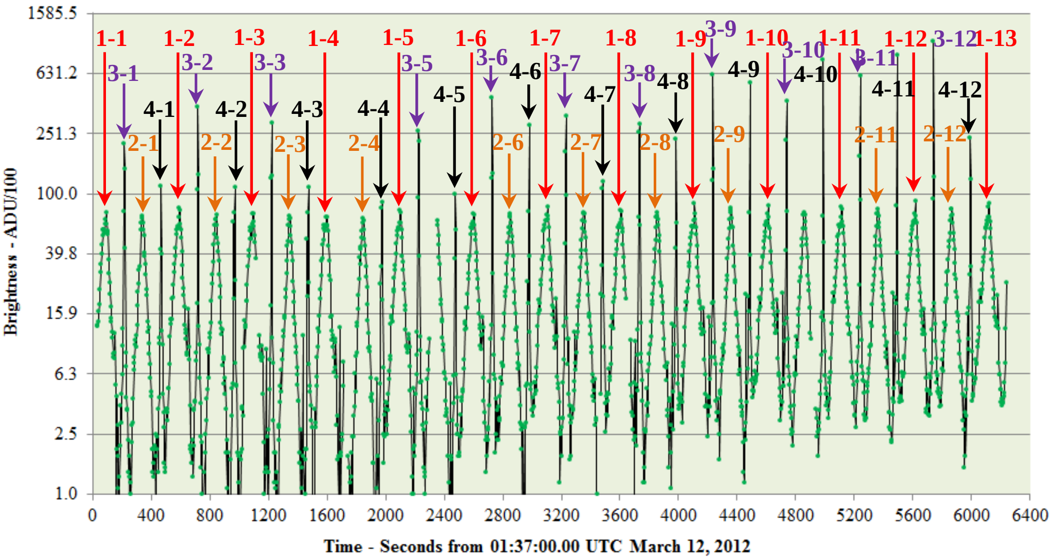

Figure 8.3: Echostar 2 Light Curve – Data Extraction Software

Table 8.5: Apparent Spin Periods of Echostar 2 – Adjacent Maxima Method

FAMILY	TEMPORAL OCCURRENCES	APPARENT SPIN PERIOD (s)
1	1, 2	500.5±4.8
1	2, 3	503.7±4.8
1	3, 4	502.7±4.8
1	4, 5	499.5±4.8
1	5, 6	503.1±4.8
1	6, 7	503.7±4.8
1	7, 8	500.3±4.8
1	8, 9	503.4±4.8
1	9, 10	503.7±4.8
1	10, 11	501.1±4.8
1	11, 12	503.4±4.8
1	12, 13	503.5±4.8
2	1, 2	504.0±4.8
2	2, 3	499.3±4.8

Table 8.5 Continued

2	3, 4	499.3±4.8
2	6, 7	500.3±4.8
2	7, 8	506.6±4.8
2	8, 9	503.9±4.8
2	11, 12	501.0±4.8
3	1, 2	503.8±4.8
3	2, 3	502.8±4.8
3	5, 6	503.2±4.8
3	6, 7	503.7±4.8
3	7, 8	503.1±4.8
3	8, 9	500.5±4.8
3	9, 10	503.8±4.8
3	10, 11	501.9±4.8
3	11, 12	501.6±4.8
4	1, 2	503.9±4.8
4	2, 3	502.5±4.8
4	3, 4	502.9±4.8
4	4, 5	499.7±4.8
4	5, 6	503.9±4.8
4	6, 7	503.5±4.8
4	7, 8	499.9±4.8
4	8, 9	503.7±4.8
4	9, 10	501.8±4.8
4	10, 11	503.1±4.8
4	11, 12	500.6±4.8
ALL	**--------**	**503.1±0.9**

Table 8.6: Apparent Spin Periods of Echostar 2 – Extreme Maxima Method

FAMILY	**TEMPORAL OCCURRENCES**	**APPARENT SPIN PERIOD (s)**
1	1, 13	**502.4±0.4**
2	2, 12	**502.1±0.4**
3	3, 12	**502.5±0.4**
4	4, 12	**502.3±0.4**

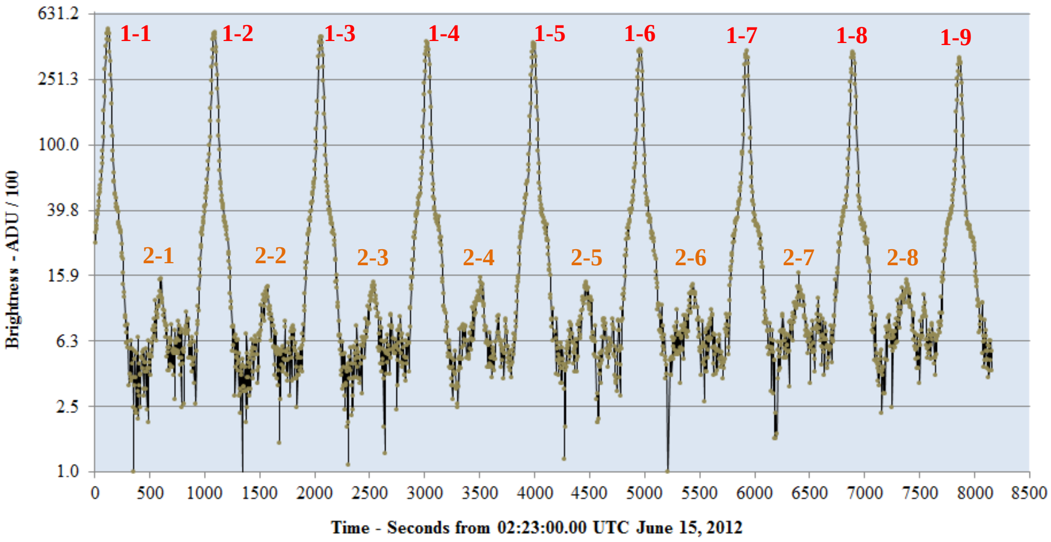

Figure 8.4: Solidaridad 1 Light Curve – June 15, 2012 (UTC)

Table 8.7: Apparent Spin Periods of Solidaridad 1 – Adjacent Maxima Method

FAMILY	TEMPORAL OCCURRENCES	APPARENT SPIN PERIOD (s)
1	1, 2	968.0±5.1
1	2, 3	964.5±5.1
1	3, 4	965.4±5.1
1	4, 5	970.5±5.1
1	5, 6	966.3±5.1
1	6, 7	970.1±5.1
1	7, 8	965.7±5.1
1	8, 9	964.8±5.1
2	1, 2	966.1±5.1
2	2, 3	964.2±5.1
2	3, 4	967.9±5.1
2	4, 5	970.0±5.1
2	5, 6	970.5±5.1
2	6, 7	971.1±5.1
2	7, 8	970.3±5.1
ALL	--------	**968±3**

Table 8.8: Apparent Spin Periods of Solidaridad 1 – Extreme Maxima Method

FAMILY	TEMPORAL OCCURRENCES	APPARENT SPIN PERIOD (s)
1	1, 9	**966.9±0.6**
2	1, 8	**968.6±0.7**

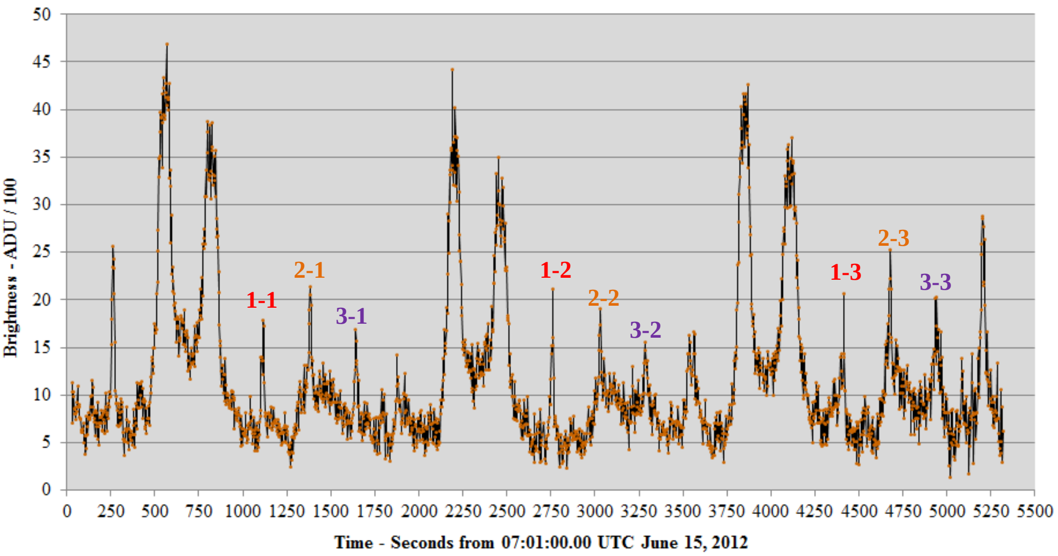

Figure 8.5: HGS-1 Light Curve – June 15, 2012 (UTC)

Table 8.9: Apparent Spin Periods of HGS-1 – Adjacent Maxima Method

FAMILY	TEMPORAL OCCURRENCES	APPARENT SPIN PERIOD (s)
1	1, 2	1643.2±3.7
1	2, 3	1653.2±3.7
2	1, 2	1648.6±3.7
2	2, 3	1647.0±3.7
3	1, 2	1643.0±3.7
3	2, 3	1657.9±3.7
ALL	**--------**	**1649±6**

Table 8.10: Apparent Spin Periods of HGS-1 – Extreme Maxima Method

FAMILY	TEMPORAL OCCURRENCES	APPARENT SPIN PERIOD (s)
1	1, 3	**1648±2**
2	1, 3	**1648±2**
3	1, 3	**1650±2**

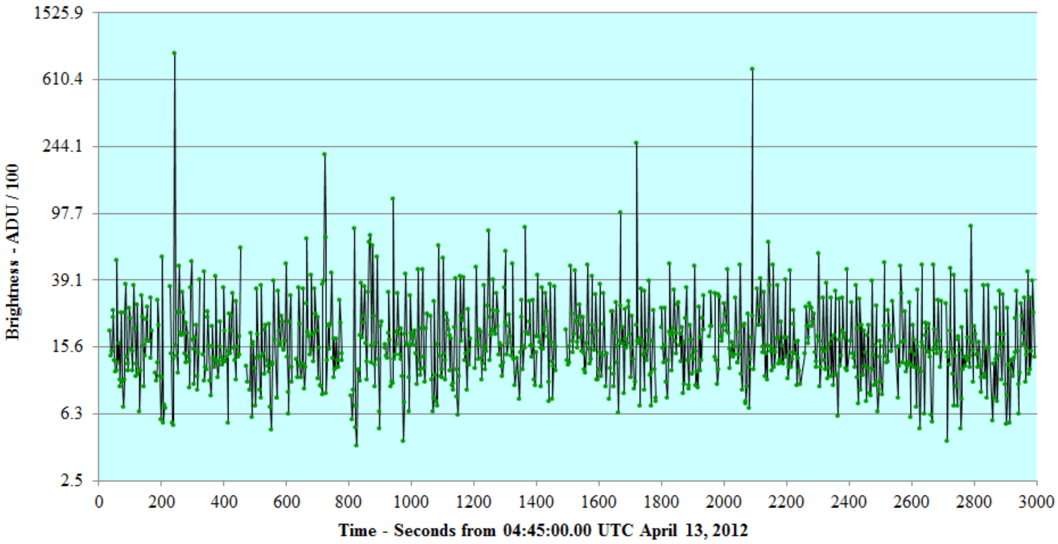

Figure 8.6: GStar 3 Preliminary Light Curve – Data Extraction Software

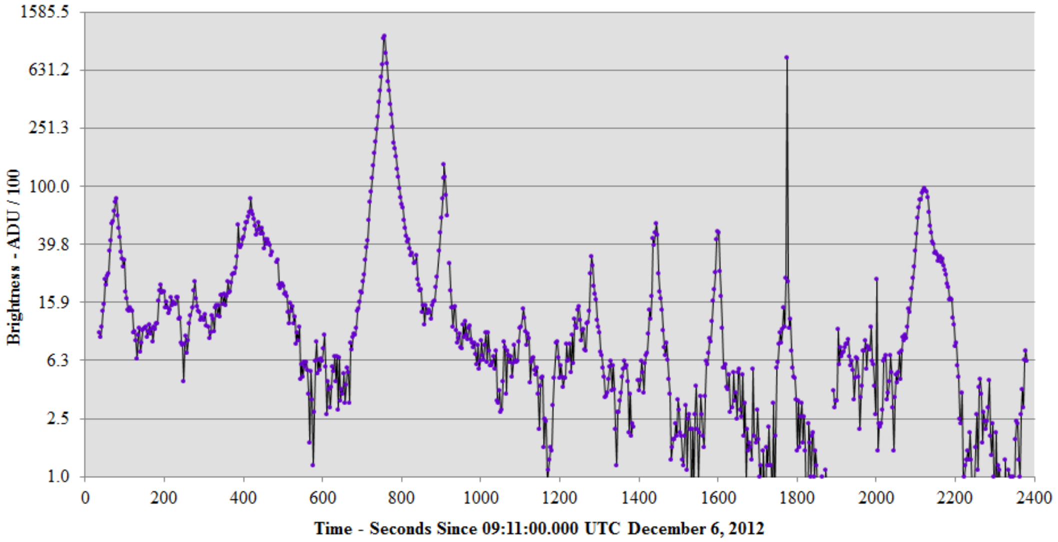

Figure 8.7: Telstar 402R Preliminary Light Curve – Data Extraction Software

The apparent spin period of the ACTS satellite could be determined reliably. However, it was not known at the time if the spin period of this satellite would vary. If the spin period decreased enough such that the CCD camera's sampling frequency was no longer adequate to allow reliable determination of the satellite's spin period, then time would have been lost researching this satellite. Therefore, the ACTS satellite was removed from the list of candidates for this thesis.

The data in Tables 8.1 to 8.10 suggest that there is some correlation between the apparent spin period and its corresponding uncertainty. The statistical uncertainty is inversely proportional to the amount of sampling data. For a given sampling time, the satellites with longer spin periods will have less sampling data and therefore higher statistical errors than those satellites with shorter spin periods.

The satellites that were considered to be the best candidates for further study are listed in Table 8.11.

Table 8.11: Inactive GEO Box-wing Satellites Selected for Thesis Research

NORAD #	COSPAR #	COMMON	OWNER	DESIGN [67]
22911	1993-073-A	Solidaridad 1	Mexico	HS-601
22927	1993-077-A	Telstar 401	USA	AS-7000
24313	1996-055-A	Echostar 2	USA	AS-7000
25126	1997-086-A	HGS-1	USA	HS-601HP

---

[67] Dirk Krebs, Gunter: “Gunter’s Space Page”: http://space.skyrocket.de

CHAPTER 9: APPARENT SPIN PERIOD VARIABILITY

Echostar 2’s apparent spin period was measured for the second time on May 12, 2012 using observations obtained from 01:53 to 09:03 UTC (see Appendix A) and was found to be 447.2 ± 0.1 seconds. This apparent spin period was approximately 55.1 seconds less than the one measured for Echostar 2 two months earlier on March 12, 2012; (502.3 ± 0.4) seconds. This suggested that Echostar 2’s angular velocity had increased over that time. Similar phenomena occurred for Telstar 401, Solidaridad 1 and HGS-1. All four satellites exhibited some spin period variation (positive and negative) but the trends all looked different from one another.

Over the year (March 2012 to March 2013), Telstar 401’s and HGS-1’s apparent spin periods reached a maximum and then dropped to a minimum but not at the same time, nor at the same value. Echostar 2’s apparent spin period reached a minimum in early September 2012 and then turned around, slowly climbed over a period of approximately 6 months; reaching a maximum in early March 2013. Solidaridad 1’s apparent spin period dropped at a nearly constant rate from June 2012 until mid-October 2012. For nearly 3 months, its apparent spin period did not appear to change appreciably and then it resumed its decrease in January 2013.

All of the apparent spin variations of Solidaridad 1, Telstar 401, Echostar 2 and HGS-1 obtained for the purposes of this thesis are shown in Figures 9.1 to 9.4 respectively. These figures confirmed what Papushev et al. had observed in 2006 with respect to the variation of spin periods over time. The apparent spin periods of inactive geosynchronous satellites are observed to vary with different rates and amplitudes.

However, Figures 9.1 to 9.4 show variations within a smaller time scale than Papushev et al. had indicated.

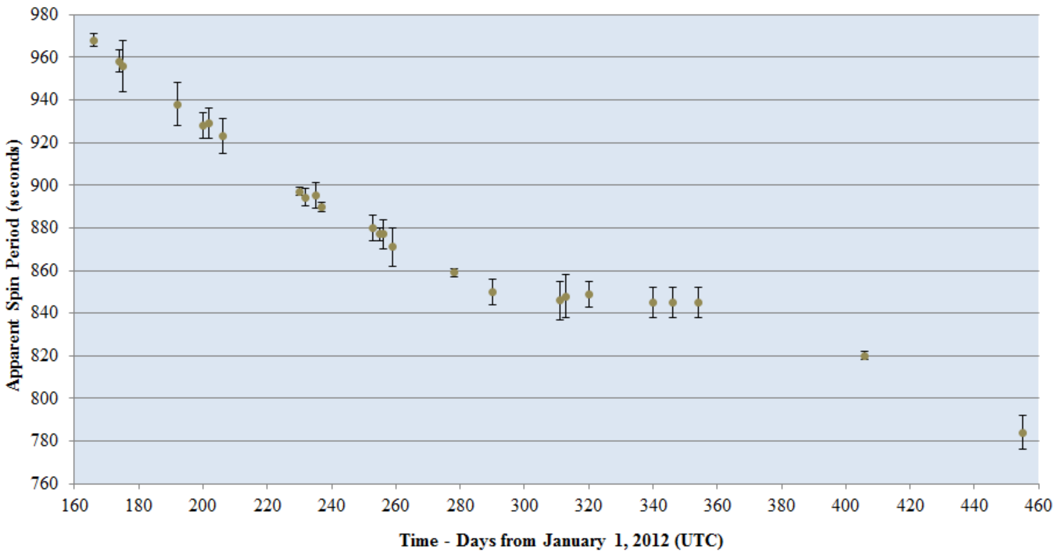

Figure 9.1: Solidaridad 1 - Apparent Spin Period Variation

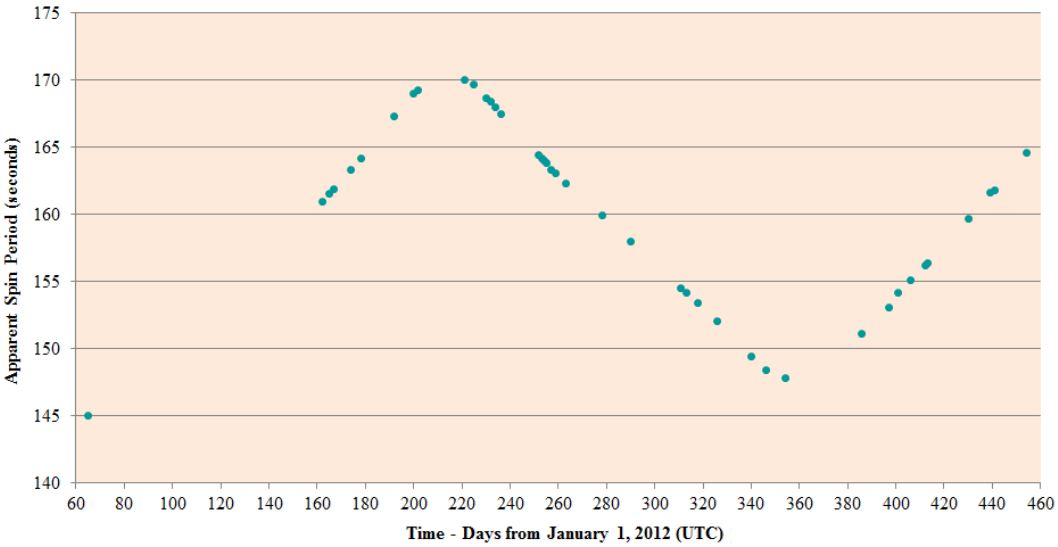

Figure 9.2: Telstar 401 - Apparent Spin Period Variation

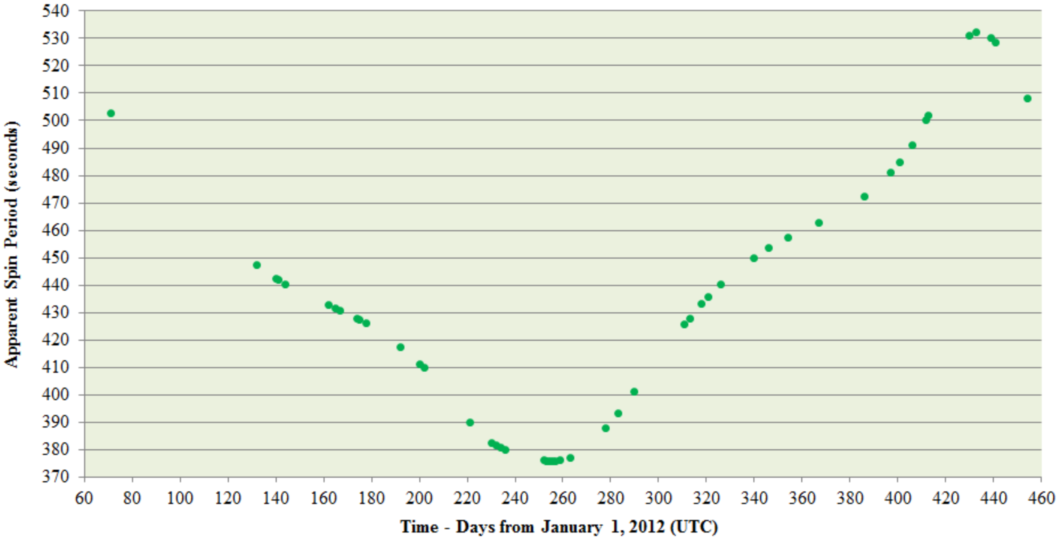

Figure 9.3: Echostar 2 - Apparent Spin Period Variation

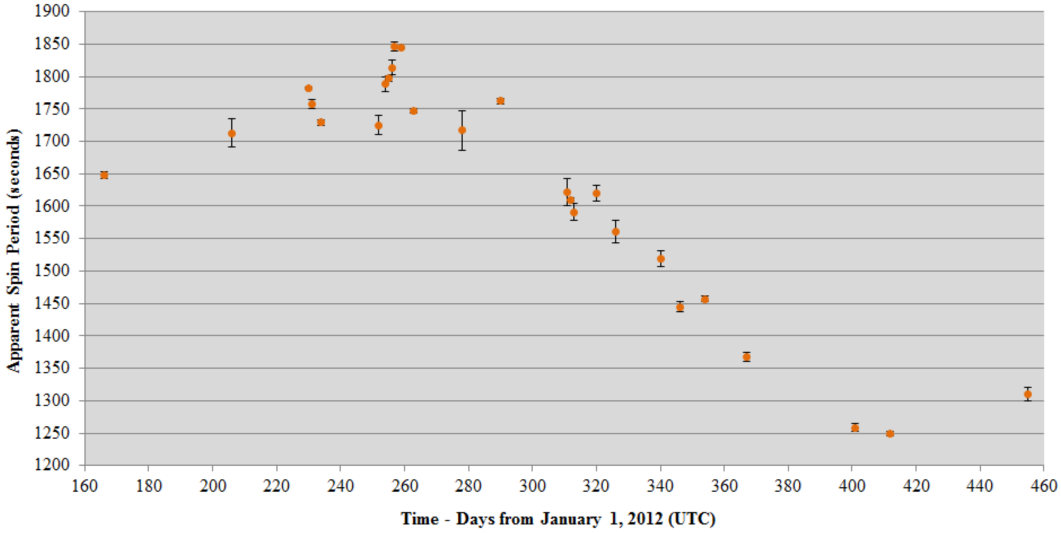

Figure 9.4: HGS-1 - Apparent Spin Period Variation

The error bars shown for the Solidaridad 1 and HGS-1 apparent spin periods (Figures 9.1 and 9.4, respectively), were determined by calculating the average of the highest and lowest apparent spin periods observed for the corresponding observing session. The amount of time for each observing session is shown in Appendix A. The apparent spin period uncertainties for the two satellites were in the order of 0.1 to 0.8 seconds, depending on the amount of apparent spin periods observed for each epoch. Therefore, the error bars for the Telstar 401 and Echostar 2 apparent spin period variations (Figures 9.2 and 9.3, respectively), were too small for the scale of the graph and therefore were not shown. All uncertainties for all of the satellites' apparent spin period measurements are listed in Appendix A.

Each apparent spin period variation appears to have a periodic behaviour; however secular behaviour could become apparent with additional observations. At present, the precise period of these spin period variations are not known with certainty. Each satellite's maximum (and minimum) spin period do not occur at the same time, which suggests that systematic errors are not a concern. However, each satellite's apparent spin period variation period can be estimated by assuming that this period is double the time elapsed between a maximum and a minimum apparent spin period. Using this method, the period of Telstar 401's apparent spin period variation is estimated to be 290 days (0.79 years). The period of Echostar 2 is estimated to be 364 days (approximately 1 year). HGS-1's period is estimated to be 330 days (0.9 years). Solidaridad 1's period cannot be estimated at this time because no maximum or minimum apparent spin periods have been detected for this satellite. However, based on the slow progression of its spin period variation curve, Solidaridad 1's period could be longer than 2 years; the longest of the four satellites.

The amplitude of each of the satellites' cycles is also very different from one another. The amplitude of Telstar 401's spin period variations appears to be about 11.5 seconds (using half of the difference between maximum and minimum apparent spin periods); approximately 7% above (or below) its average observed spin period. The amplitude of Echostar 2's spin period variations appears to be about 78 seconds;

approximately 17% above (or below) its average observed spin period. The amplitude of HGS-1’s spin period variations appears to be about 297 seconds; approximately 19% above (or below) its average observed spin period. The amplitude of Solidaridad 1’s spin period variations is currently unknown because of its apparently much longer cycle period. However, it might be equal to or greater than 123 seconds. These amplitudes present an interesting correlation. Telstar 401 has the lowest average spin period and it also appears to have the lowest spin period variation amplitude of the four satellites. On the other extreme, HGS-1’s has the highest average spin period and it appears to have the highest spin period variation amplitude of the four satellites. Echostar 2’s spin period variation is in between the spin period variations of Telstar 401 and HGS-1.

Echostar 2’s spin period variation does not appear to be the same shape as Telstar 401’s spin period variation. The Echostar 2 curve appears to deviate from the “sine wave” trend nearly half way between its minimum and maximum apparent spin period. A closer inspection of the Telstar 401 curve reveals that it also has a deviation between its maximum and minimum, but its deviation is much smaller. At the other extreme, Solidaridad 1’s curve deviation appears to be more pronounced than the Echostar 2 curve deviation. This suggests that as the spin period increases the deviation away from the “sine wave” trend between maximum and minimum also increases. This deviation could possibly be some indication of a synodic effect.

The curve of HGS-1 appears to reach a maximum then turn around to reach what appears to be a minimum near the end of the observations. However, this might not be a minimum, but another deviation located midway between the observed maximum and a yet unseen minimum. If this is true, then the spin period deviation of HGS-1 is even larger than that observed for Solidaridad 1.

Telstar 401's and Echostar 2's curves shown in Figures 9.2 and 9.3 respectively appear to be very smooth relative to Solidaridad 1's and HGS-1's curves (Figures 9.1 and 9.4, respectively). HGS-1's curve appears especially "noisy"; having larger error bars and short-term fluctuations about the overall trend. These fluctuations do not appear to be the result of underestimated error bars because in well sampled locations of the curve (for example, around day 260 of Figure 9.4) the data points are indicating the sudden jump in the apparent spin period. Since HGS-1 has the largest average spin period of the four, perhaps this fluctuation is directly related to the higher apparent spin period.

The slope of Telstar 401's curve near minimum and maximum appears to have the same absolute value; about 0.2 seconds·day^{-1}. However, the slope near the minimum of Echostar 2's curve has a smaller absolute value than the slope near the maximum value; 0.3 seconds·day^{-1} near minimum vs. 1.5 seconds·day^{-1} near maximum. The contrast between the spin period variability trends of these two satellites is very interesting, especially with the knowledge that they are both AS-7000 series satellites (see Chapter 10).

In summary, the observed spin period variation curves of the four selected satellites are very different from each other with respect to their overall shape, their amplitude, their estimated variation period and their amplitude's percentage of average spin period. Each of the curves appear to vary with a sinusoidal behaviour, however in the cases of Solidaridad 1, Telstar 401 and Echostar 2, deviations from this sinusoidal trend is evident around midway between the maximum and minimum apparent spin periods.

In order to begin investigating the possible reason(s) for the apparent spin period behaviour discussed in this chapter, the specific satellite characteristics are required. These are discussed in the next chapter.

CHAPTER 10: SATELLITE CHARACTERISTICS

Before any in-depth investigation into the external forces acting on any of the four selected satellites could be undertaken, the characteristics of each had to be researched. Information about the satellites' masses, the dimensions of all major components, launch, the beginning of life (BOL) specifics, the end of life (EOL) specifics and any other notable characteristic was researched. This information was used to determine the satellites' moments of inertia (MOI) (detailed in the next chapter). The MOI of each satellite was required to determine the torques needed to provide the spin angular accelerations.

The dimensions of the critical components of all four satellites were determined from the artist's conceptions (Figures 10.2, 10.4 and 10.7) by using the published total satellite length ("wing" span) as the reference length. It should be noted that the artist's conceptions might not have been the true representations of the satellite designs and might not have represented the true aspects of the satellites before launch or after launch.

#22911 – SOLIDARIDAD 1

Solidaridad 1 (English: Solidarity 1) was a Mexican government telecommunications satellite. It was constructed by Hughes Space and Communications; now called Boeing Satellite Systems (BSS). The satellite was launched aboard a French Ariane 44LP rocket on November 20, 1993. The satellite was equipped with 16 Ku-band transponders and 18 C-band transponders to provide television, radio and telecommunications services to Mexico, the southwestern United States and the Caribbean islands[68].

The satellite’s designed lifetime was 14 years, but it served for only half of that time. In 1999 its main satellite control processor (SCP) failed due to a short circuit of a tin-plated electromagnetic relay to its ground casing likely caused by a tin (solder) whisker growth[69]. The satellite had a backup SCP, but it failed (possibly for the same reason), on August 27, 2000, thus ending the lifetime of the satellite [70]. The satellite’s operators could not communicate with the satellite, so they could not instruct it to maneuver into a GEO graveyard orbit. An artist’s conception of Solidaridad 1 is shown in Figure 10.1. The dimensions of the satellite are shown in Figure 10.2. The physical characteristics of Solidaridad 1 are listed in Table 10.1.

Figure 10.1: Artist’s Conception of Solidaridad 1[71]

---

[68] Krebs, Gunter: “Gunter’s Space Page”: http://space.skyrocket.de/doc_sdat/solidaridad-1.htm
[69] NASA: Whisker Failures: http://nepp.nasa.gov/whisker/failures/index.htm
[70] Krebs, Gunter: “Gunter’s Space Page”: http://space.skyrocket.de/doc_sdat/solidaridad-1.htm
[71] Boeing Defense Space and Security: Solidaridad 1: http://www.boeing.com/boeing/defense-space/space/bss/factsheets/601/solidaridad/solidaridad.page

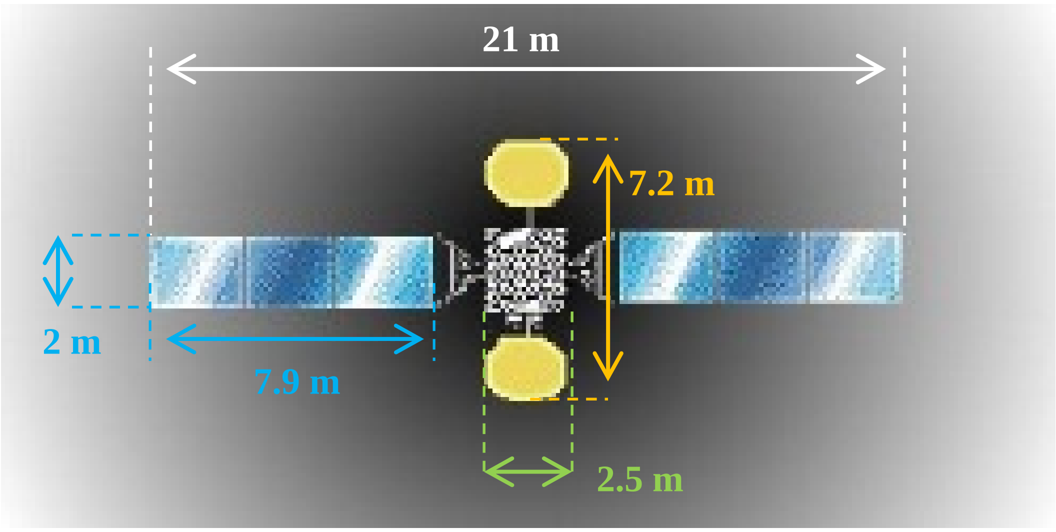

Figure 10.2: Dimensions of Solidaridad 1 [72]

---

[72] Boeing BSS: http://web.archive.org/web/20091230143546/http://boeing.com/defense-space/space/bss/factsheets/601/solidaridad/solidaridad.html

Table 10.1: Physical Characteristics of Solidaridad 1

CHARACTERISTIC	VALUE	NOTES AND ASSUMPTIONS
Original Design	HS-601	Now known as BSS-601
Launch Date	November 20, 1993	Ariane 44LP rocket
Designed Lifetime	14 years [73]	
End of Life (EOL) Date	August 27, 2000 [74]	Main and redundant SCP failures
Time from BOL to EOL	6.75 years	Approximately half of fuel left
Solar Panel Material	"Black" Silicon	Area density: 2.25 kg·m^{-2} [75]
Total Satellite Length	(21.0±0.5) m [76]	"Wing Span"
Total Satellite Width	(7.2±0.2) m [77]	Includes dishes (Figure 10.1)
Solar Panel Length	(7.9±0.2) m	One solar panel Using total length and Figure 10.2
Solar Panel Width	(2.0±0.1) m	One solar panel Using total length and Figure 10.2
Solar Panel Area	(16±1) m^2	One solar panel
"Box" Length	(2.5±0.2) m	Using total length and Figure 10.2
"Box" Width	(2.5±0.2) m	Using total length and Figure 10.2 Without large dishes
On-Orbit (BOL) Mass	(2780±50) kg [78]	Assumes orbit insertion fuel already used
Fuel Mass at BOL	(1660±50) kg [79]	Assumes orbit insertion fuel already used
Estimated Dry Mass	(1120±70) kg	Difference of on-orbit mass and fuel mass at BOL
Estimated Current Total Mass	(1980±70) kg	Constant fuel consumption from BOL to EOL
"Wing" Mass	(36±2) kg	Each "Wing"
"Box" Mass	(1910±70) kg	Difference of solar panel mass and estimated current total mass Includes all dishes

---

[73] Krebs, Gunter: "Gunter's Space Page": http://space.skyrocket.de/doc_sdat/solidaridad-1.htm

[74] NASA: Whisker Failures: http://nepp.nasa.gov/whisker/failures/index.htm

[75] Reddy, M. Raja: "Space solar cells – tradeoff analysis": Solar Energy Materials & Solar Cells 77 (2003) p.204

[76] Boeing BSS: http://web.archive.org/web/20091230143546/http://boeing.com/defense-space/space/bss/factsheets/601/solidaridad/solidaridad.html

[77] Boeing BSS: http://web.archive.org/web/20091230143546/http://boeing.com/defense-space/space/bss/factsheets/601/solidaridad/solidaridad.html

[78] Encyclopedia Astronautica: http://www.astronautix.com/craft/hs601.htm

[79] Encyclopedia Astronautica: http://www.astronautix.com/craft/hs601.htm

#22927 – TELSTAR 401

Telstar 401 was an American telecommunications satellite constructed by Lockheed Martin for AT&T. The satellite was launched aboard an American Atlas-2AS rocket on December 16, 1993[80]. The satellite was equipped with 16 Ku-band transponders and 24 C-band transponders to provide television, radio and telecommunications services to all 50 U.S. States, Puerto Rico and the Virgin Islands[81]. Telstar 401 was the main satellite hub for major U.S. television networks, including CBS, PBS, ABC and FOX[82].

Telstar 401 is one of the most famous examples of a geostationary satellite that failed early in its life. The satellite's designed lifetime was 15 years, but served for just over 3 years. On January 11, 1997, the spacecraft was highly charged with ions from a recent solar coronal mass ejection (CME). The satellite suffered a catastrophic power failure which cut off communications with the ground station and ended the satellite's life[83]. Without any power for station-keeping, the satellite began to drift in the geostationary belt, threatening nearby active GEO satellites. An artist's conception of Telstar 401 is shown in Figure 10.3. The dimensions of the satellite are shown in Figure 10.5. Figure 10.5 is also used to show the dimensions of the Echostar 2 satellite because it is also a Lockheed Martin AS-7000 design. The physical characteristics of Telstar 401 are listed in Table 10.2.

---

[80] Space-Track – The Source for Space Surveillance Data: www.space-track.org

[81] NASA National Space Science Data Center: http://nssdc.gsfc.nasa.gov/nmc/spacecraftDisplay.do?id=1993-077A

[82] NASA Goddard Space Flight Center: http://www-istp.gsfc.nasa.gov/istp/cloud_jan97/att.html

[83] Krebs, Gunter: "Gunter's Space Page": http://space.skyrocket.de/doc_sdat/telstar-4.htm

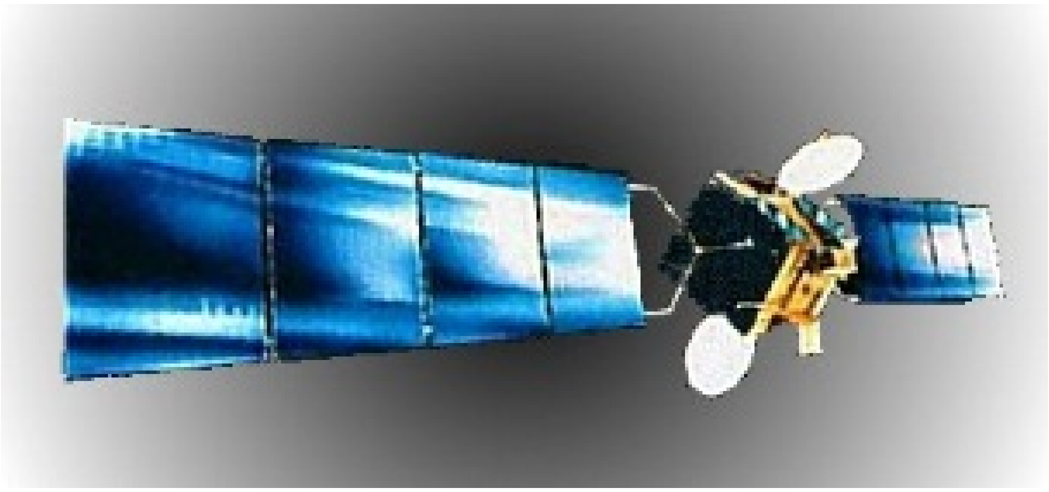

Figure 10.3: Artist's Conception of Telstar 401[84]

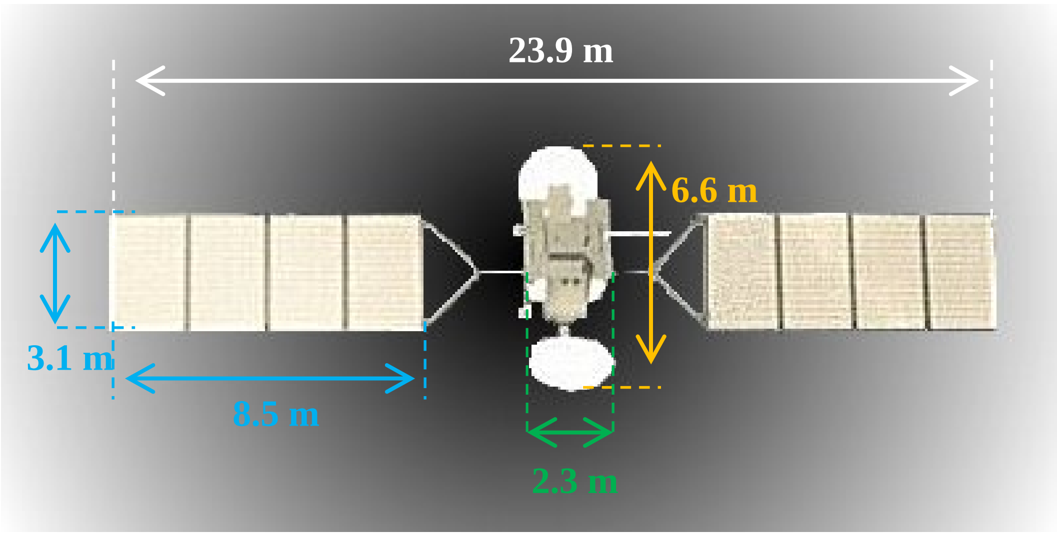

Figure 10.4: Dimensions of Telstar 401 and Echostar 2[85]

---

[84] Krebs, Gunter: "Gunter's Space Page": http://space.skyrocket.de/doc_sdat/telstar-4.htm

[85] Cattabiani, Mario F; "One small step along the information highway"; The Morning Call, September 29, 1993

Table 10.2: Physical Characteristics of Telstar 401

CHARACTERISTIC	VALUE	NOTES AND ASSUMPTIONS
Original Design	AS-7000	Also known as LM-7000
Launch Date	December 16, 1993[86]	Atlas II-AS rocket
Designed Lifetime	15 years	Assumed from average GEO lifetime
End of Life (EOL) Date	January 11, 1997	Catastrophic power failure due to particles from solar CME storm
Time from BOL to EOL	3.1 years	Approximately four fifths of the maneuvering fuel was left
Solar Panel Material	“Black” Silicon	Area density: 2.25 kg·m^{-2} [87]
Total Satellite Length	(23.9±0.5) m[88]	Assumed the same as Echostar 2
Total Satellite Width	(6.6±0.2) m	Including both dishes Using total length and Figure 10.4
Solar Panel Length	(8.5±0.2) m	One solar panel Using total length and Figure 10.4
Solar Panel Width	(3.1±0.1) m	One solar panel Using total length and Figure 10.4
Solar Panel Area	(26±1) m^2	One solar panel
“Box” Length	(2.3±0.2) m	Using total length and Figure 10.4
“Box” Width	(2.3±0.2) m	Using total length and Figure 10.4 Without large dishes
On-Orbit (BOL) Mass	(2885±50) kg[89]	Assumed the same as Echostar 2 Assumes orbit insertion fuel already used
Fuel Mass at BOL	(885±70) kg	Assumes orbit insertion fuel already used Difference of on-orbit mass and dry mass
Dry Mass	(2000±50) kg[90]	
Estimated Current Total Mass	(2710±80) kg	Assuming constant station-keeping fuel consumption from BOL to EOL
“Wing” Mass	(60±2) kg	Each “Wing”
“Box” Mass	(2590±80) kg	Difference of solar panel mass and estimated current total mass Includes all dishes

---

[86] Space-Track – The Source for Space Surveillance Data: www.space-track.org

[87] Reddy, M. Raja: “Space solar cells – tradeoff analysis”: Solar Energy Materials & Solar Cells 77 (2003) p.204

[88] Ricardo’s GEO-Orbit Quick-Look: http://www.geo-orbit.org/westhemipgs/fecho2specp.html

[89] Krebs, Gunter; “Gunter’s Space Page”: http://space.skyrocket.de/doc_sdat/echostar-1.htm

[90] Ricardo’s GEO-Orbit Quick-Look: http://www.geo-orbit.org/westhemipgs/fecho2specp.html

#24313 – ECHOSTAR 2

Echostar 2 was an American telecommunications satellite constructed by Lockheed Martin for the Echostar Corporation and its subsidiary the Dish Network. The satellite was launched aboard a French Ariane 42P rocket on September 10, 1996[91]. The satellite was equipped with 16 Ku-band transponders to provide television, radio and telecommunications services to the continental United States. Later in its life, it served Alaska and several other small markets[92].

Echostar 2's designed lifetime was 12 years and it served for nearly that long. On July 14, 2008, the spacecraft "experienced a substantial failure that appears to have rendered the satellite a total loss."[93] It is unclear if the failure was power-related like Telstar 401. It is likely that the critical failure cut communications between the spacecraft and the ground station, thus preventing its proper parking into the GEO graveyard orbit.

An artist's conception of Echostar 2 is shown in Figure 10.5. The dimensions of the satellite are shown in Figure 10.4 (with Telstar 401). The physical characteristics of Echostar 2 are listed in Table 10.3.

---

[91] Space-Track – The Source for Space Surveillance Data: www.space-track.org

[92] Bergin, Chris; "Sea Launch lofts Echostar 11 – Echostar 2 dies on orbit"; NASA Spacefilight.com: www.nasaspaceflight.com/2008/07/sea-launch-lofts-echostar-11-echostar-2-dies-on-orbit

[93] Kinney, Linda; Michalopolous, Pantelis; "Before the Federal Communications Commission – In the Matter of Echostar Corporation - Amendment to Application for New Earth Station Under Call Sign E080120 to Add EchoStar 8 Operating as a Mexican Licensed Satellite at 77° W.L. as a Point of Communication"; File No. SES-LIC-20080516-00652; July 24, 2008; p. 3

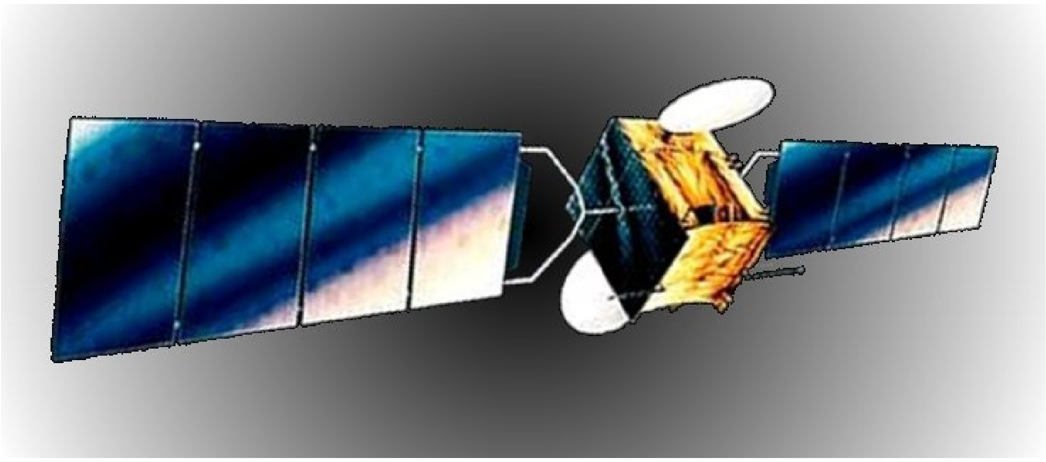

Figure 10.5: Artist's Conception of Echostar 2 [94]

---

[94] Krebs, Gunter; "Gunter's Space Page": http://space.skyrocket.de/doc_sdat/echostar-1.htm

Table 10.3: Physical Characteristics of Echostar 2

CHARACTERISTIC	VALUE	NOTES AND ASSUMPTIONS
Original Design	AS-7000	Also known as LM-7000
Launch Date	September 10, 1996 [95]	Ariane 42P rocket
Designed Lifetime	12 years[96]	
End of Life (EOL) Date	July 14, 2008[97]	Due to "Substantial failure"
Time from BOL to EOL	11.8 years	Little of the maneuvering fuel was left
Solar Panel Material	"Black" Silicon	Area density: 2.25 $kg \cdot m^{-2}$ [98]
Total Satellite Length (Wing Span)	(23.9±0.5) m[99]	Including both solar panels (Figure 10.4)
Total Satellite Width	(6.6±0.2) m	Including both dishes Using total length and Figure 10.4
Solar Panel Length	(8.5±0.2) m	One solar panel Using total length and Figure 10.4
Solar Panel Width	(3.1±0.1) m	One solar panel Using total length and Figure 10.4
Solar Panel Area	(26±1) m^2	One solar panel
"Box" Length	(2.3±0.2) m	Using total length and Figure 10.4
"Box" Width	(2.3±0.2) m	Using total length and Figure 10.4 Without large dishes
On-Orbit (BOL) Mass	(2885±50) kg [100]	Assumes orbit insertion fuel already used
Fuel Mass at BOL	(885±70) kg	Assumes orbit insertion fuel already used Difference of on-orbit mass and dry mass
Dry Mass	(2000±50) kg [101]	
Estimated Current Total Mass	(2020±80) kg	Assuming constant station-keeping fuel consumption from BOL to EOL
"Wing" Mass	(60±2) kg	Each "Wing"
"Box" Mass	(1900±80) kg	Difference of solar panel mass and estimated current total mass Includes all dishes

---

[95] Space-Track – The Source for Space Surveillance Data: www.space-track.org

[96] Satbeams SPRL: www.satbeams.com/satellites?norad=24313

[97] Bergin, Chris; "Sea Launch lofts Echostar 11 – Echostar 2 dies on orbit"; NASA Spacefilight.com: www.nasaspaceflight.com/2008/07/sea-launch-lofts-echostar-11-echostar-2-dies-on-orbit

[98] Reddy, M. Raja: "Space solar cells – tradeoff analysis": Solar Energy Materials & Solar Cells 77 (2003) p.204

[99] Ricardo's GEO-Orbit Quick-Look: http://www.geo-orbit.org/westhemipgs/fecho2specp.html

[100] Krebs, Gunter; "Gunter's Space Page": http://space.skyrocket.de/doc_sdat/echostar-1.htm

[101] Ricardo's GEO-Orbit Quick-Look: http://www.geo-orbit.org/westhemipgs/fecho2specp.html

#25126 - HUGHES-1 (HGS-1) (ASIASAT 3) (PAS-22)

HGS-1 is a satellite with a very interesting life. The satellite's original name was Asiasat 3. It was constructed by Hughes Aerospace for the China-based Asia Satellite Telecommunications Company (Asiasat)[102]. The satellite's original purpose was to deliver television distribution and telecommunications services throughout Asia, the Middle East and the Australasian regions[103].

Asiasat 3 was launched on December 24, 1997 aboard a four-stage Russian Proton-K rocket[104]. The LEO orbit insertion and geostationary transfer orbit (GTO) insertion were successful. The rocket's 4th stage (DM-3) was to complete the Hohmann transfer into GEO orbit but it malfunctioned. The satellite was stranded in a highly inclined and highly elliptical GTO. The satellite did not possess enough fuel on board to maneuver the satellite into a GEO orbit from a highly inclined GTO. At the time, Asiasat 3 was declared a total loss by the insurers[105].

Most failed GEO satellites that are trapped in GTO are of no use to customers. They experience a slow death as the satellite's apogee slowly decreases due to high atmospheric drag at the orbit's low perigee. However, in Asiasat 3's case, a rescue scenario was proposed. The Moon's gravity could be used to circularize the orbit and reduce the orbit inclination to maneuver the satellite into a useable geosynchronous orbit. Over a period of several months, two lunar fly-bys would be executed to change the orbit of the spacecraft[106]. Hughes Global Services (HGS) obtained the title of the satellite from

---

[102] Boeing BSS: www-prd-09.boeing.com/boeing/defense-space/space/bss/factsheets/601/asiasat_3/asiasat_3.page

[103] Boeing BSS: www-prd-09.boeing.com/boeing/defense-space/space/bss/factsheets/601/asiasat_3/asiasat_3.page

[104] Space-Track – The Source for Space Surveillance Data: www.space-track.org

[105] Krebs, Gunter: "Gunter's Space Page": http://space.skyrocket.de/doc_sdat/asiasat-3.htm

[106] Ocampo, Cesar: "Trajectory analysis for the lunar flyby rescue of AsiaSat-3/HGS-1"; Annals of the New York Academy of Sciences – 2005 Dec; 1065; p.232

the insurers in order to make the attempt. The satellite was subsequently renamed Hughes-1 (HGS-1)[107].

On June 17, 1998, the HGS-1 satellite arrived at a nearly circular geosynchronous orbit with an inclination of approximately 11°. The satellite was parked in a slot over the mid Pacific Ocean. When Hughes attempted to release the solar panels (they had been stowed throughout the maneuvering), controllers found that one of them would not move. Hughes engineers determined that a tether was malfunctioning due to the extreme temperature cycles during the two lunar fly-bys. However, the satellite was still semi-operational[108].

The lunar maneuvers had depleted about half of the on-board fuel which had been originally allocated for station-keeping over a 15-year designed life span. Nevertheless, PanAmSat (PAS) (now defunct) acquired HGS-1 from Hughes in early 1999 and renamed it PAS-22. PAS-22 remained active for another 3 years before it was decommissioned in July 2002 and was parked into the graveyard GEO orbit[109].

Asiasat 3 was the first commercial satellite to fly by the Moon and the last lunar spacecraft of the 20th century, albeit unintentionally[110]. HGS-1 is the only one of the four GEO satellites selected for this study that was parked in the GEO graveyard orbit and intentionally switched off from the ground.

An artist's conception of the original Asiasat 3 satellite design is shown in Figure 10.6. A modified version of the artist's conception to show the un-deployed solar panel is

---

[107] Krebs, Gunter: "Gunter's Space Page": http://space.skyrocket.de/doc_sdat/asiasat-3.htm

[108] Krebs, Gunter: "Gunter's Space Page": http://space.skyrocket.de/doc_sdat/asiasat-3.htm

[109] Krebs, Gunter: "Gunter's Space Page": http://space.skyrocket.de/doc_sdat/asiasat-3.htm

[110] Ocampo, Cesar: "Trajectory analysis for the lunar flyby rescue of AsiaSat-3/HGS-1"; Annals of the New York Academy of Sciences – 2005 Dec; 1065; p.232

shown in Figure 10.7. The dimensions of the HGS-1 satellite are shown in Figure 10.8. The physical characteristics of HGS-1 are listed in Table 10.4.

Figure 10.6: Artist's Conception of Asiasat 3[111]

Figure 10.7: Possible True Appearance of HGS-1 (PAS-22)
Image from Figure 10.6 Modified

---

[111] Krebs, Gunter: "Gunter's Space Page": http://space.skyrocket.de/doc_sdat/asiasat-3.htm

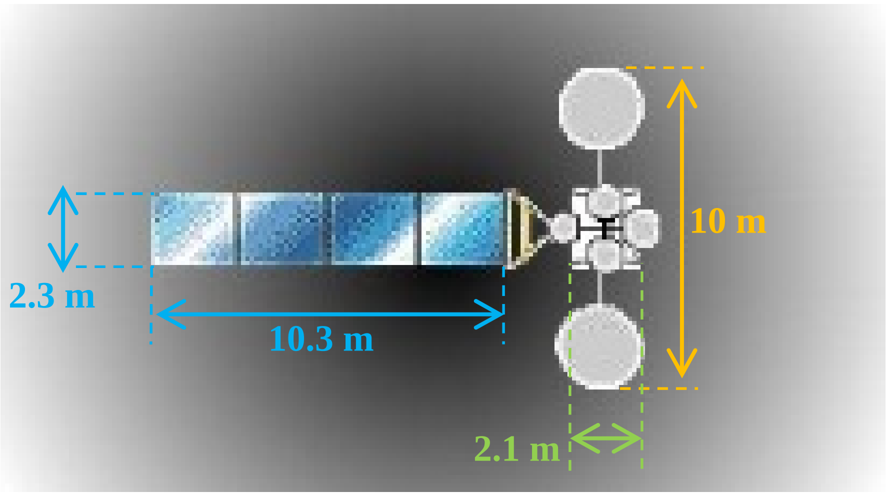

Figure 10.8: Dimensions of HGS-1 (PAS-22)[112]

---

[112] Boeing BSS: www-prd-09.boeing.com/boeing/defense-space/space/bss/factsheets/601/asiasat_3/asiasat_3.page

Table 10.4: Physical Characteristics of HGS-1 (Asiasat 3) (PAS-22)

CHARACTERISTIC	VALUE	NOTES AND ASSUMPTIONS
Original Design	HS-601HP	Also known as BSS-601HP High power version of HS-601 design
Launch Date	December 24, 1997[113]	Proton-K rocket
Designed Lifetime	15 years[114]	
End of Life (EOL) Date	July 2002[115]	Station-keeping fuel depleted
Time from BOL to EOL	4.5 years	No maneuvering fuel remained
Solar Panel Material	GaAs Triple Junction (3-J)	Area density: 2.75 kg·m^{-2} [116]
Total Intended Satellite Length (Wing Span)	(26.2±0.5) m [117]	Assuming both solar panels deployed (Figure 10.6)
Total Satellite Width	(10.0±0.2) m [118]	Including large dishes (Figure 10.6)
Solar Panel Length	(10.3±0.2) m	One deployed solar panel Using total length and Figure 10.8
Solar Panel Width	(2.3±0.1) m	One deployed solar panel Using total length and Figure 10.8
Solar Panel Area	(23±1) m^2	One deployed solar panel
"Box" Length	(2.1±0.2) m	Using total length and Figure 10.8
"Box" Width	(2.6±0.2) m	Using total length and Figure 10.8 Without large dishes
On-Orbit (BOL) Mass	(2534±50) kg [119]	Assumes orbit insertion fuel already used
Fuel Mass at BOL	(860±70) kg	Difference of on-orbit mass and dry mass
Dry Mass	(1670±50) kg[120]	
Estimated Current Total Mass	(1670±80) kg	Assuming no fuel remains at EOL
"Wing" Mass	(64±2) kg	Each "Wing"
"Box" Mass	(1540±80) kg	Difference of solar panel mass and estimated current total mass Includes all dishes

---

[113] Space-Track – The Source for Space Surveillance Data: www.space-track.org

[114] Krebs, Gunter: "Gunter's Space Page": http://space.skyrocket.de/doc_sdat/asiasat-3.htm

[115] Krebs, Gunter: "Gunter's Space Page": http://space.skyrocket.de/doc_sdat/asiasat-3.htm

[116] Reddy, M. Raja: "Space solar cells – tradeoff analysis": Solar Energy Materials & Solar Cells 77 (2003) p.204

[117] Boeing BSS: www-prd-09.boeing.com/boeing/defense-space/space/bss/factsheets/601/asiasat_3/asiasat_3.page

[118] Boeing BSS: www-prd-09.boeing.com/boeing/defense-space/space/bss/factsheets/601/asiasat_3/asiasat_3.page

[119] Boeing BSS: www-prd-09.boeing.com/boeing/defense-space/space/bss/factsheets/601/asiasat_3/asiasat_3.page

[120] The Satellite Encyclopedia: www.tbs-satellite.com/tse/online/sat_asiasat_3.html

CHAPTER 11: MOMENTS OF INERTIA

If any portion of the observed spin period variations shown in Figures 9.1 to 9.4 is caused by one or more external torques, then an angular acceleration would be occurring. The magnitude of this angular acceleration would be dependent on the satellite's (mass) moment of inertia (MOI), also known as the rotational inertia.

For simplicity's sake, it was assumed that each of the four selected box-wing GEO satellites was a rigid body, despite any unused fuel that could potentially slosh around when the spacecraft was accelerated.

An estimate of the MOIs of Solidaridad 1, Telstar 401 and Echostar 2 was obtained by treating each satellite as a uniform density solid cube with sides of length "a" with two large flat (2-dimensional) rectangular plates of length "*l*" and width "*w*" attached to two opposite sides of the cube, as shown in Figure 11.1. The two larger communications dishes were not considered because little information could be found concerning their physical characteristics. However, their masses would not likely significantly contribute to the MOI as a whole. The spacecraft was considered to be symmetrical, therefore the system's center of mass was considered to be at the center of the box (spacecraft bus).

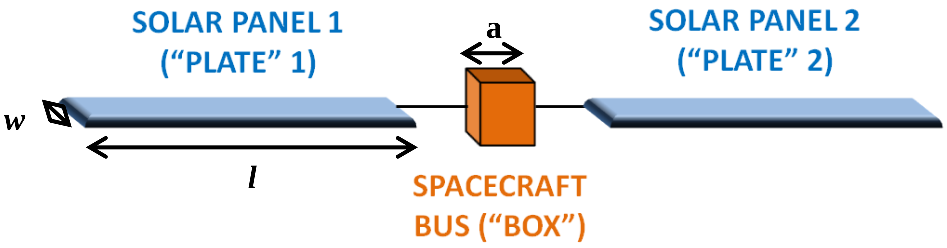

Figure 11.1: Basic Box-Wing Satellite Components Used for MOI Determination

The total MOI of the system was considered to be comprised of the MOIs of the solid cube and each solar panel with respect to the center of mass of the system. The center of mass of the system was considered to be at the geometric center of the cube. The solar panels were assumed to be symmetrical and of uniform density. The center of mass of each of the solar panels was assumed to be at its geometric center.

For simplicity's sake, three specific MOI scenarios for the system were considered. The three scenarios are illustrated in Figures 11.2, 11.3 and 11.4. The total "wing span" of the satellite (l_{tot}) and the distance r_{CM} between the center of mass of the plate and the center of mass of the cube is shown in Figure 11.5.

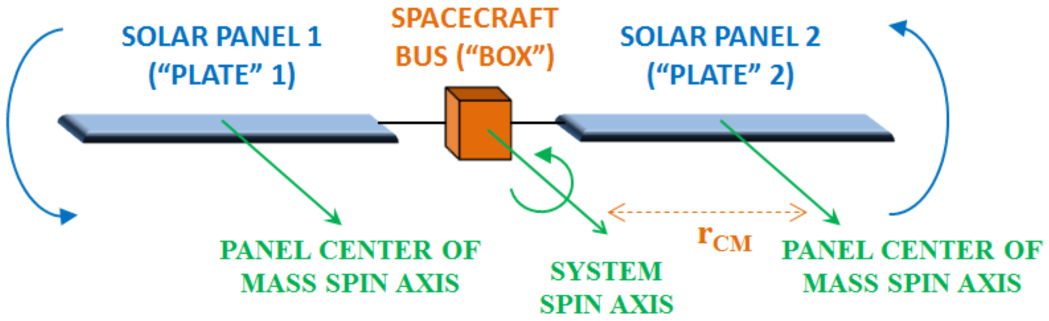

Figure 11.2: Scenario 1 MOI: Panel Spin Axis along Plane and Parallel to System Spin Axis

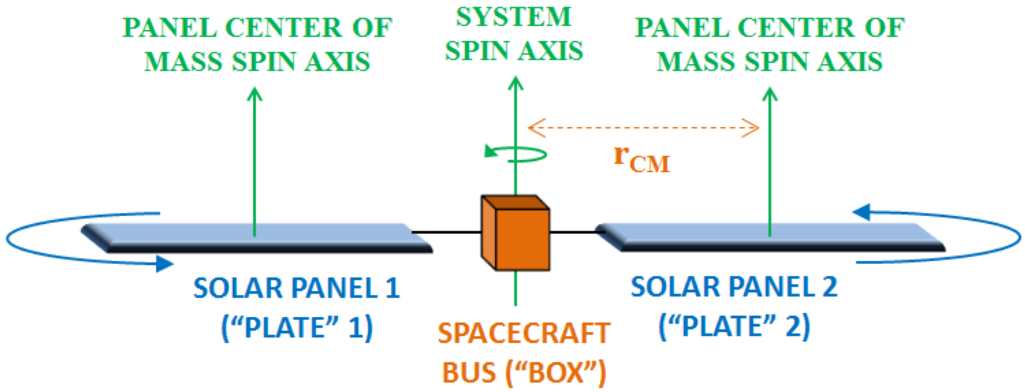

Figure 11.3: Scenario 2 MOI: Panel Spin Axis Orthogonal to Plane and Parallel to Cube Spin Axis

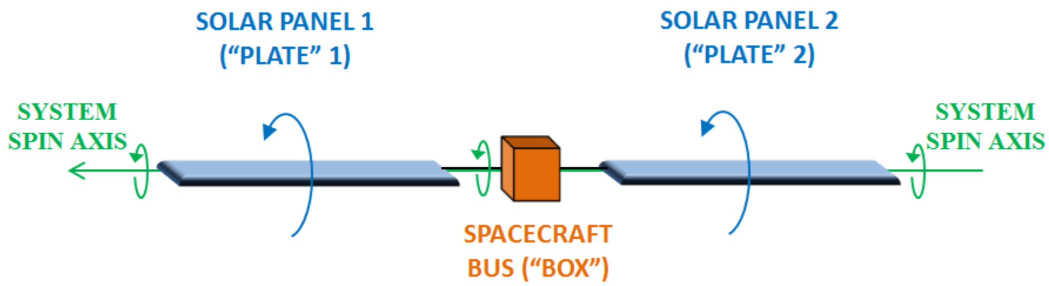

Figure 11.4: Scenario 3 MOI: Panel Spin Axis Coincident with Cube Spin Axis

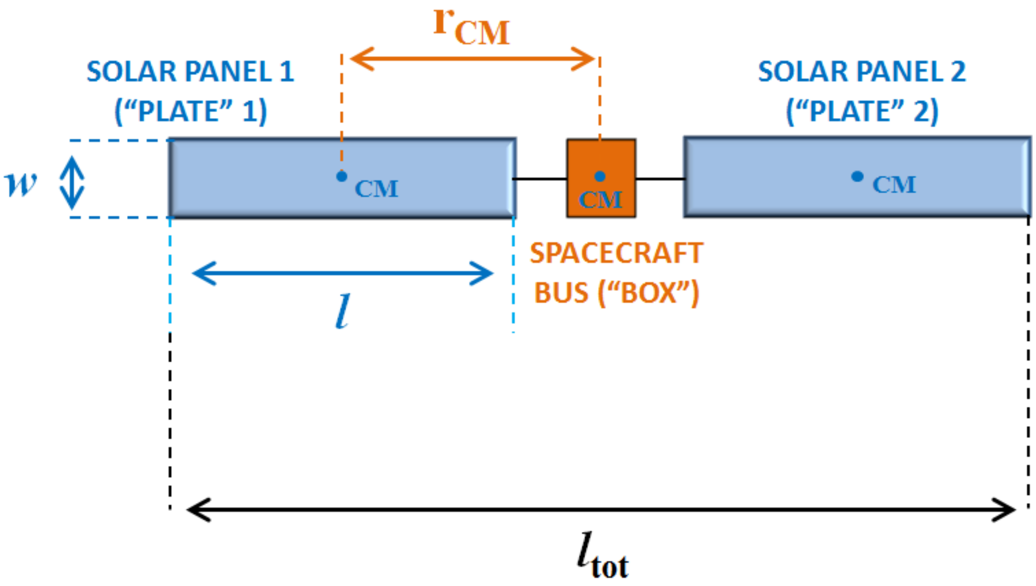

Figure 11.5: Distance between Plate Center of Mass and Cube Center of Mass

The MOI of a solid uniform density cube with a mass of "M_{cube}", a side length of "a" and a spin axis (of any orientation) passing through its center of mass is shown in Eq. 11.1.

Eq. 11.1[121]

$$\mathbf{I_{cube} = \frac{1}{6} M_{cube} a^2}$$

---

[121] Serway, Raymond A.; Physics for Scientists and Engineers; 3rd ed.; p. 254

The distance between the center of mass of the cube (box) and the center of mass of a solar panel (flat rectangular plate) (r_{CM}) is calculated using the total “wing span” of the satellite (l_{tot}) and the solar panel length (l) with Eq. 11.2.

Eq. 11.2

$$\mathbf{r_{CM}} = \frac{1}{2}(l_{tot} - l)$$

The MOI of a single solar panel of the system shown in Figure 11.2 is calculated using the mass of the solar panel (M_{plate}), the solar panel length (l) and the distance between the centers of mass (r_{CM}) with Eq. 11.3. Eq. 11.3 relies upon the parallel axis theorem, which relates the MOI of the single solar panel with the center of mass of the system.

Eq. 11.3[122]

$$\mathbf{I_1} = \mathbf{M_{plate}}\left[\frac{1}{12}l^2 + \mathbf{r_{CM}}^2\right]$$

The MOI of a single solar panel of the system shown in Figure 11.3 is calculated using the length and width of the solar panel (l and w respectively) with Eq. 11.4. Eq. 11.4 also relies upon the parallel axis theorem.

---

[122] Serway, Raymond A.; Physics for Scientists and Engineers; 3rd ed.; p. 254

Eq. 11.4[123]

$$\mathbf{I_2 = M_{plate}\left[\frac{1}{12}(\boldsymbol{l}^2 + \boldsymbol{w}^2) + r_{CM}{}^2\right]}$$

The MOI of a solar panel of the system shown in Figure 11.4 is shown in Eq. 11.5.

Eq. 11.5[124]

$$\mathbf{I_3 = \frac{1}{12} M_{plate}\boldsymbol{w}^2}$$

The MOI of the entire system is found by adding the MOIs of the central cube portion and both of the solar panels, as shown in Eq. 11.6. The variable "i" (having values of 1, 2 or 3) refers to the total MOI of the systems shown in Figure 11.2, Figure 11.3 and Figure 11.4, respectively.

Eq. 11.6

$$\mathbf{I_{tot\,i} = I_{cube} + 2I_i\,, \qquad i = 1, 2, 3}$$

All of the values used in the calculation of all three MOIs for Solidaridad 1, Telstar 401 and Echostar 2 are shown in Table 11.2.

The MOIs calculated using Eq. 11.2 through to Eq. 11.6 is only valid for satellites with two fully deployed solar panels (shown in Figure 11.1). HGS-1 had only one solar panel successfully deploy, as discussed in Chapter 10. When stored before launch, the solar panels of HGS-1 were folded like an accordion against the sides of the central cube. The MOI of HGS-1's un-deployed (stored) solar panel was different from

---

[123] Serway, Raymond A.; Physics for Scientists and Engineers; 3rd ed.; p. 254

[124] Serway, Raymond A.; Physics for Scientists and Engineers; 3rd ed.; p. 254

its deployed solar panel. The mass of the un-deployed solar panel was considered to be the same as the successfully deployed solar panel. The un-deployed solar panel was considered to be a flat rectangular plate with dimensions of one quarter the length of the deployed panel and having the same width as the deployed panel, as shown in Figure 11.6. The un-deployed panel was considered to be stored against that side of the cube that was opposite the deployed panel. This un-deployed panel was considered to be a 2-dimensional plate.

The deployed solar panel was called “Plate 1” and the un-deployed solar panel was called “Plate 2”, as shown in Figure 11.6.

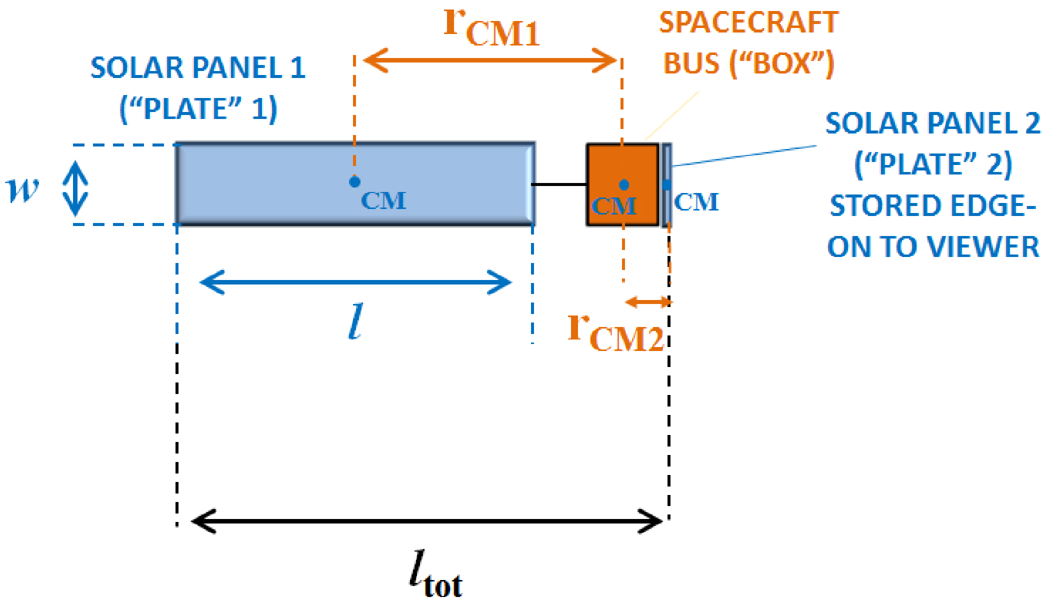

Figure 11.6: Configuration of HGS-1 for MOI Determination

The MOI of the central cube structure was calculated the same way as shown in Eq. 11.1. The distance between Plate 1’s center of mass and the cube’s center of mass was calculated the same way as shown in Eq. 11.2. The MOI of the deployed solar panel

(Plate 1) was calculated the same way as shown in Eq. 11.3, Eq. 11.4 and Eq. 11.5, depending on the spin axis of the system.

The un-deployed solar panel's center of mass was considered to be located at the geometric center of the side of the cube it is attached to. The distance between Plate 2's center of mass and the cube's center of mass (r_{CM2}) was considered to be one half the length of the cube's side (a), as shown in Eq. 11.7.

Eq. 11.7

$$\mathbf{r_{CM2}} = \frac{1}{2}\mathbf{a}$$

The MOI of the un-deployed solar panel, corresponding to the same spin axis as shown in Figure 11.2, is calculated with Eq. 11.8.

Eq. 11.8[125]

$$\mathbf{I_{1\,panel2}} = \mathbf{M_{plate}}\left[\frac{1}{12}\left(\frac{1}{4}l\right)^{2} + (\mathbf{r_{CM2}})^{2}\right]$$

The MOI of the un-deployed solar panel, corresponding to the same spin axis as shown in Figure 11.3, is calculated with Eq. 11.9.

Eq. 11.9[126]

$$\mathbf{I_{2\,panel2}} = \mathbf{M_{plate}}\left[\frac{1}{12}w^{2} + (\mathbf{r_{CM2}})^{2}\right]$$

The MOI of the un-deployed solar panel, corresponding to the same spin axis as shown in Figure 11.4, is calculated with Eq. 11.10.

---

[125] Serway, Raymond A.; Physics for Scientists and Engineers; 3rd ed.; p. 254

[126] Serway, Raymond A.; Physics for Scientists and Engineers; 3rd ed.; p. 254

Eq. 11.10[127]

$$\mathbf{I_{3\ panel\ 2}} = \frac{\mathbf{1}}{\mathbf{12}}\mathbf{M_{plate}}\left[\left(\frac{\mathbf{1}}{\mathbf{4}}\boldsymbol{l}\right)^{\mathbf{2}} + \boldsymbol{w}^{\mathbf{2}}\right]$$

The total MOIs of HGS-1, corresponding to all three system spin axes, were estimated by summing the MOIs of the central cube, the deployed solar panel and the un-deployed solar panel, as shown in Eq. 11.11.

Eq. 11.11

$$\mathbf{I_{HGS-1\ i}} = \mathbf{I_{cube}} + \mathbf{I_{i\ panel\ 1}} + \mathbf{I_{i\ panel\ 2}} \quad \mathbf{i = 1, 2, 3}$$

All of the values used in the calculation of all three HGS-1 MOIs are shown in Table 11.2.

---

[127] Serway, Raymond A.; Physics for Scientists and Engineers; 3rd ed.; p. 254

Table 11.1: Estimated MOI for Solidaridad 1, Telstar 401 and Echostar 2

QUANTITY	**SATELLITE**		
	Solidaridad 1	**Telstar 401**	**Echostar 2**
Cube Mass (M_{cube}) (kg)	1910 ± 70	2590 ± 80	1900 ± 80
Cube Side Length (a) (m)	2.5 ± 0.2	2.3 ± 0.2	2.3 ± 0.2
Panel Mass (M_{plate}) (kg)	36 ± 2	60 ± 2	60 ± 2
“Wing” Span (l_{tot}) (m)	21.0 ± 0.5	23.9 ± 0.5	23.9 ± 0.5
Panel Length (l) (m)	7.9 ± 0.2	8.5 ± 0.2	8.5 ± 0.2
Panel Width (w) (m)	2.0 ± 0.1	3.1 ± 0.1	3.1 ± 0.1
Distance between Centers of Mass (r_{CM}) (m)	6.6 ± 0.3	7.7 ± 0.3	7.7 ± 0.3
Cube MOI (I_{cube}) (kg·m^2)	1990 ± 390	2280 ± 470	1680 ± 360
Panel MOI 1 (I_1) (kg·m^2)	1730 ± 230	3920 ± 400	3920 ± 400
Panel MOI 2 (I_2) (kg·m^2)	1740 ± 230	3970 ± 400	3970 ± 400
Panel MOI 3 (I_3) (kg·m^2)	12 ± 2	48 ± 5	48 ± 5
Total MOI 1 ($I_{tot\ 1}$) (kg·m^2)	**5450 ± 610**	**10120 ± 920**	**9510 ± 870**
Total MOI 2 ($I_{tot\ 2}$) (kg·m^2)	**5480 ± 610**	**10220 ± 930**	**9610 ± 880**
Total MOI 3 ($I_{tot\ 3}$) (kg·m^2)	**2010 ± 390**	**2380 ± 470**	**1770 ± 360**

Table 11.2: Estimated MOI for HGS-1

QUANTITY	VALUE
Cube Mass (M_{cube}) (kg)	1540 ± 80
Cube Side Length (a) (m)	2.6 ± 0.2
Panel Mass (M_{plate}) (kg)	64 ± 2
Total Length (l_{tot}) (m)	14.4 ± 0.3
Panel 1 Length (l_1) (m)	10.3 ± 0.2
Panel 1 Width (w_1) (m)	2.3 ± 0.1
Panel 2 Length (l_2) (m)	2.6 ± 0.1
Panel 2 Width (w_2) (m)	2.3 ± 0.1
Distance between Centers of Mass for Panel 1 (r_{CM1}) (m)	8.5 ± 0.2
Distance between Centers of Mass for Panel 2 (r_{CM2}) (m)	1.3 ± 0.1
Cube MOI (I_{cube}) (kg·m^2)	1740 ± 360
Panel 1 MOI 1 ($I_{panel\ 1\ 1}$) (kg·m^2)	5190 ± 380
Panel 2 MOI 1 ($I_{panel\ 1\ 1)}$ (kg·m^2)	140 ± 20
Panel 1 MOI 2 ($I_{panel\ 1\ 2}$) (kg·m^2)	5220 ± 380
Panel 2 MOI 2 ($I_{panel\ 2\ 2}$) (kg·m^2)	140 ± 20
Panel 1 MOI 3 ($I_{panel\ 1\ 3}$) (kg·m^2)	28 ± 3
Panel 2 MOI 3 ($I_{panel\ 2\ 3}$) (kg·m^2)	64 ± 7
Total MOI 1 ($I_{tot\ 1}$) (kg·m^2)	**7070 ± 520**
Total MOI 2 ($I_{tot\ 2}$) (kg·m^2)	**7089 ± 520**
Total MOI 3 ($I_{tot\ 3}$) (kg·m^2)	**1830 ± 360**

CHAPTER 12: DETERMINATION OF MAXIMUM TORQUE

The spin period variations shown in Figures 9.1 to 9.4 suggest that one or more external forces are acting on the four selected satellites to change their apparent spin periods. These external forces provide a torque which consequently changes each of the satellites' angular acceleration.

In order to determine the external torque(s) that could have caused the observed apparent spin period variations, the maximum angular acceleration for each satellite was determined. The total torque that would have caused each maximum apparent angular acceleration was determined by using Eq. 12.1.

Eq. 12.1[128]

$$\vec{\boldsymbol{\tau}} = \mathbf{I}\,\vec{\boldsymbol{\alpha}}$$

The magnitude of the apparent angular acceleration of each satellite was determined by estimating the magnitude of the rate of change of its apparent angular velocity, as shown in Eq. 12.2.

Eq. 12.2

$$\boldsymbol{\alpha} = \frac{\mathbf{d\omega}}{\mathbf{dt}} \approx \frac{\boldsymbol{\Delta\omega}}{\boldsymbol{\Delta}\mathbf{t}}$$

The change in the apparent angular velocity is related to the apparent spin period by Eq. 12.3. The variables T_1 and T_2 are two apparent spin periods that are used to determine the change in the angular velocity between the two corresponding epochs.

---

[128] Serway, Raymond A.; Physics for Scientists and Engineers; 3rd ed.; p. 258

Eq. 12.3

$$\mathbf{\Delta\omega = 2\pi\left[\frac{1}{T_2} - \frac{1}{T_1}\right]}$$

Eq. 12.4 determines the spin angular acceleration as a function of the estimated rate of change of the apparent spin period. The variable Δt is the difference between the two epochs that correspond to the two apparent spin periods ($\Delta t = t_2 - t_1$).

Eq. 12.4

$$\mathbf{\alpha \approx \frac{2\pi}{\Delta t}\left[\frac{1}{T_2} - \frac{1}{T_1}\right]}$$

The spin angular acceleration vs. time was computed for all four satellites, as shown in Figures 12.1 to 12.4. In order to avoid large uncertainties, elapsed times equal to or greater than 3 days were used. Elapsed times of greater than 10 days were used only if no other data was available for the specific time of year. All combinations of elapsed times between 3 and 10 days (and sometimes greater than 10 days) were used to determine the apparent spin angular acceleration for each of the plots.

For all Figures 12.1 to 12.4, the epoch time (horizontal axis value) is the midpoint between the epochs of two corresponding apparent spin period measurements.

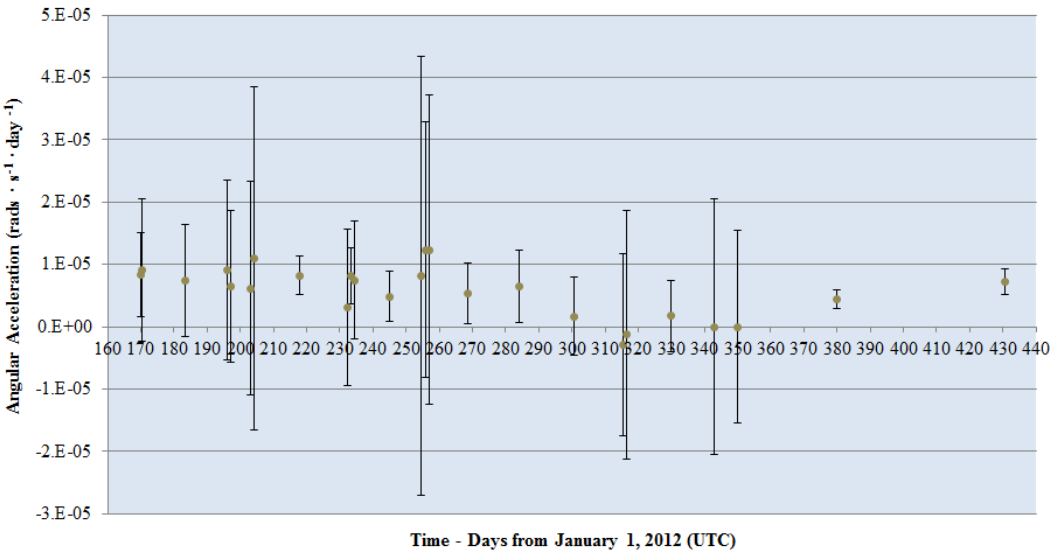

Figure 12.1: The Apparent Spin Angular Acceleration of Solidaridad 1

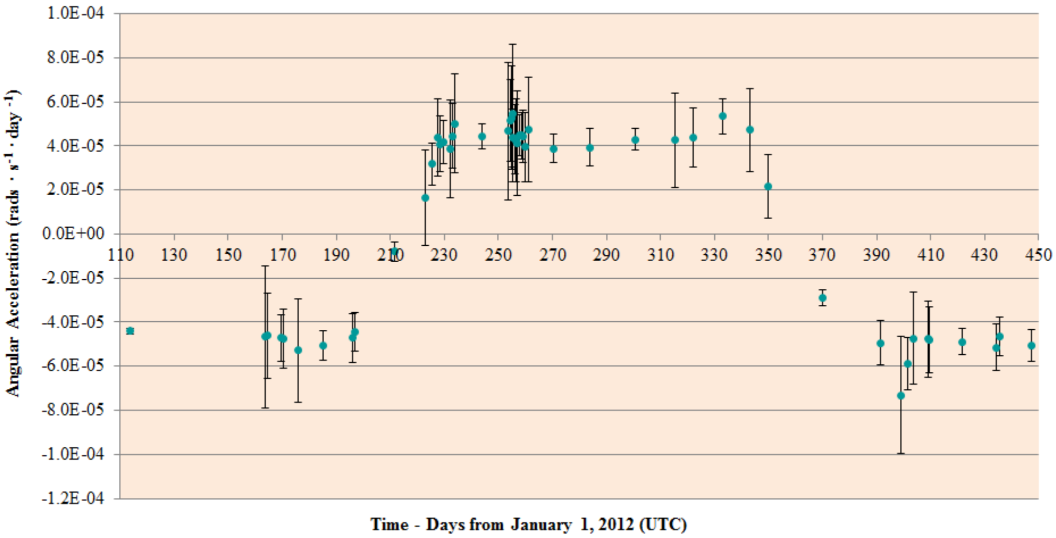

Figure 12.2: The Apparent Spin Angular Acceleration of Telstar 401

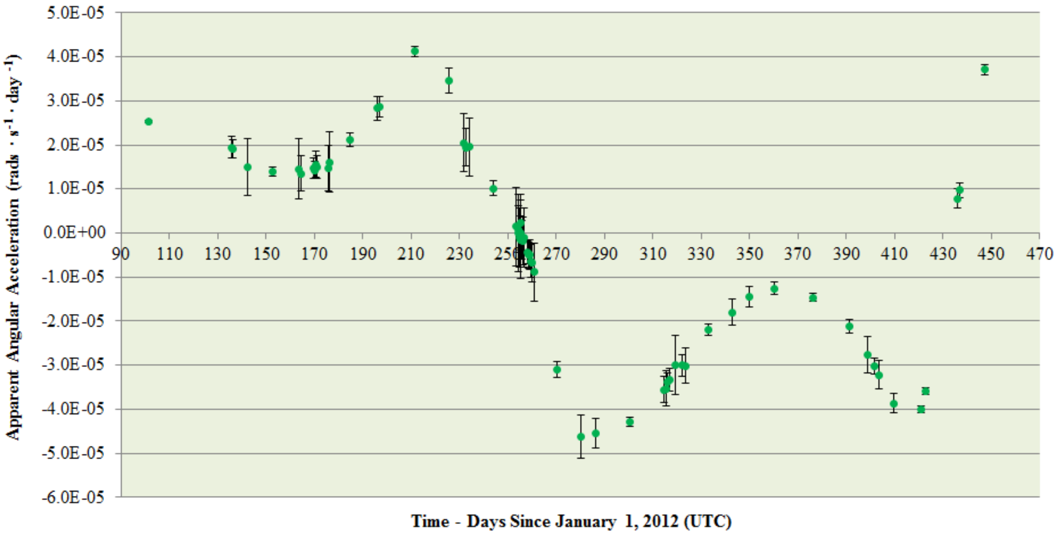

Figure 12.3: The Apparent Spin Angular Acceleration of Echostar 2

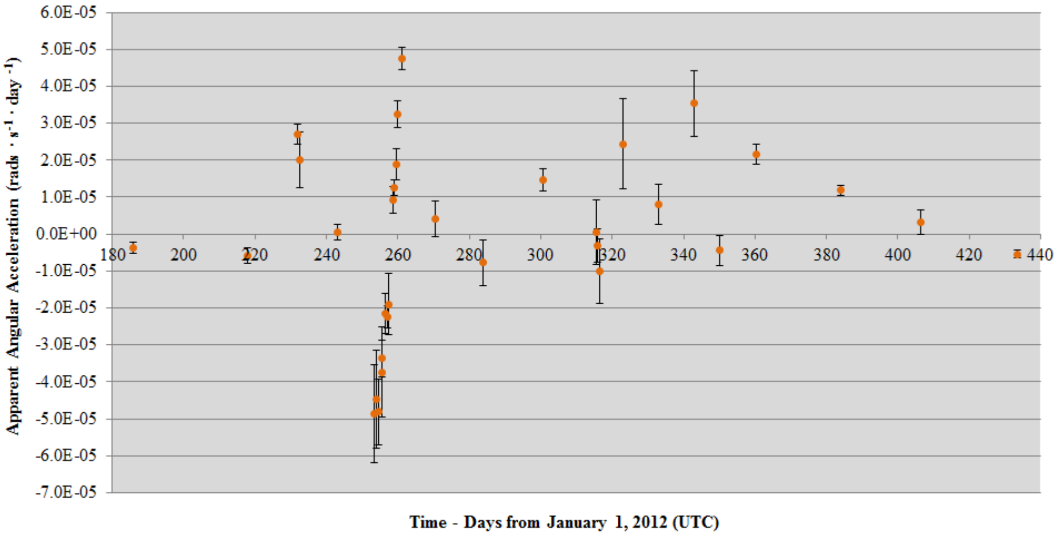

Figure 12.4: The Apparent Spin Angular Acceleration of HGS-1

The maximum absolute apparent angular acceleration from each plot was identified and tabulated with the corresponding required external torque, as shown in Table 12.1. Each satellite had three estimated torques corresponding to the three total MOIs shown in Tables 11.1 and 11.2.

Table 12.1: Maximum Apparent Angular Acceleration and Estimated Torque Required

QUANTITY	**SATELLITE**			
	Solidaridad 1	**Telstar 401**	**Echostar 2**	**HGS-1**
Maximum Absolute Angular Acceleration (α_{max}) (μrad·s^{-1}·day^{-1})	12 ± 21	55 ± 31	46 ± 5	49 ± 13
Torque for MOI 1 (τ_1) (μN·m)	**0.8 ± 1.4**	**6.4 ± 4.2**	**5.1 ± 1.0**	**4.0 ± 1.4**
Torque for MOI 2 (τ_2) (μN·m)	**0.8 ± 1.4**	**6.5 ± 4.3**	**5.1 ± 1.0**	**4.0 ± 1.4**
Torque for MOI 3 (τ_3) (μN·m)	**0.28 ± 0.54**	**1.5 ± 1.2**	**0.94 ± 0.29**	**1.04 ± 0.47**

Telstar 401's and Echostar 2's angular acceleration graphs are particularly interesting because they contain specific regions that are similar to one another. For instance, around the corresponding epochs for the maximum and minimum spin periods, there appears a "linear region" in which the slope appears constant. Further from the maximum or minimum spin periods, there exists a nearly symmetrical "non-linear" region. These non-linear regions correspond to the deviations from the apparent spin period "sinusoid" that was observed in Chapter 9.

Solidaridad 1's apparent spin angular acceleration appears to be nearly constant from epoch 160 to 290 and then decreases quickly to nearly zero. The angular acceleration remains near zero for at least 60 days before increasing again. The rate at which these trends vary for Solidaridad 1 is much slower than the other three, as was the case with Solidaridad 1's spin period variation rate in Figure 9.1.

HGS-1's apparent spin angular acceleration graph appears very different from the other three graphs. Only one clear trend is seen during the high time resolution observations around epoch 260. The apparent spin angular acceleration at this epoch is clearly increasing very quickly, which is different from the smooth behaviours of the other three graphs.

In order for any external torque to change the angular acceleration by the maximum determined value, the net torque would have to be in the order of several μN·m or greater, according to Table 12.1. The next chapter compares the largest external disturbances that could have acted on the spacecraft.

The minimum torque required to accelerate Solidaridad 1's spin rate to the maximum observed value is noticeably smaller than those for the other three satellites for all of the spin axes specified. Solidaridad 1 also has the smallest individual solar panel area of the four selected satellites (see Table 10.1).

Despite having the same design (AS-7000), Telstar 401 and Echostar 2 have different MOIs. This is probably due to the estimation of the remaining maneuvering fuel on board the satellites. Telstar 401 was active for nearly 3 years before it suffered its power failure. Echostar 2 survived for 12 years before it suffered its serious malfunction.

CHAPTER 13: TORQUE SOURCE ANALYSIS

While a spacecraft is orbiting, it will encounter external forces that will affect its attitude (orientation). Figures 12.1 to 12.4 suggest one or more external torques is/are acting on each spacecraft to change its apparent angular acceleration and consequently its apparent spin period.

The four largest external disturbance torques that can affect a spacecraft's attitude are listed in Table 13.1[129]. Aerodynamic torques are caused by atmospheric drag on the satellite's surfaces, such as large solar panels. This effect is normally most relevant in the case of LEO satellites. Gravity-gradient torques are the result of small tidal forces due to slightly different gravitational attractions acting on the extended spacecraft. A gravity-gradient torque normally stabilizes a satellite's attitude such that the satellite's long axis is oriented toward the center of the Earth if the satellite is in a nearly circular orbit. If the satellite's orbit is elliptical, the satellite's attitude will liberate about an orientation, much like the Moon liberates to reveal a total of 59% of its total surface area to the Earth[130]. A typical geosynchronous satellite has an orbit eccentricity of less than 0.005 [131]. The gravity-gradient is also known as "gravity-gradient stabilization". Magnetic torque is due to the Earth's magnetic field attempting to align magnetic dipoles within the spacecraft to itself. SRP torque is due to the force of the Sun's photons striking exposed surfaces of the spacecraft. Note that only the torque due to SRP is independent of the satellite's distance from the Earth's center.

---

[129] Wertz, James R.; "Orbit and Constellation Design and Management"; p. 171
[130] Wertz, James R.; "Orbit and Constellation Design and Management"; pp. 133-134
[131] Space-Track: The Source for Space Surveillance Data: https://www.space-track.org

The torque associated with each of these sources was calculated for each satellite and the results are shown Table 12.1. This was done in order to evaluate how each torque source can vary the satellites' apparent spin periods. For the aerodynamic and the SRP evaluations, it was assumed that a single solar panel was causing the torque. If two identical solar panels with equal orientations on opposite sides of the box had been assumed for the ideal aerodynamic and SRP cases, the net torque would have been zero.

Uncertainties were not considered in this chapter because in order to select the most likely external torque(s) that was(were) acting on the satellites, only the order of magnitude of each torque was required.

Table 13.1: Largest External Disturbance Torques on a Spacecraft's Attitude[132]

TORQUE	EFFECT ON ATTITUDE	DEPENDENCIES
Aerodynamic	- Nearly constant for Earth-oriented attitude control - Variable for inertial attitude control	- Spacecraft's cross-sectional area - Spacecraft's geometry - Location of spacecraft's center of mass - Spacecraft's radius of orbit
Gravity Gradient	- Nearly constant for Earth-oriented attitude control - Cyclical (over orbit period) for inertial attitude control	- Spacecraft's moments of inertia - Spacecraft's radius of orbit
Magnetic Field	- Cyclical (over orbit period)	- Spacecraft's residual magnetic dipole - Spacecraft's orbit inclination - Spacecraft's radius of orbit
Solar Radiation Pressure	- Nearly constant for Earth-oriented attitude control - Cyclical (over orbit period) for inertial attitude control	- Spacecraft's cross-sectional area - Spacecraft's geometry - Location of spacecraft's center of mass - Spacecraft's reflectivity

---

[132] Wertz, James R.; "Orbit and Constellation Design and Management"; p. 171

AERODYNAMIC TORQUE

The aerodynamic torque for the spacecraft was determined using Eq. 13.1. The maximum possible cross-sectional area (A) of a single solar panel was assumed. For this case, the atmospheric drag acting orthogonally on the solar panel would cause the satellite to spin around its center of mass (near the center of the box) with the maximum angular velocity. The drag coefficient (C_{drag}) was assumed to be its maximum value (2.5)[133]. The atmospheric volume density (ρ_{atm}) at a distance of 42,000 km from the center of the Earth (GEO orbit radius) is less than 10^{-17} $kg \cdot m^{-3}$ [134]. The average orbit (tangential) velocity of a typical GEO satellite ($3070\ m \cdot s^{-1}$) was used for the velocity (v) in Eq. 13.1.

Eq. 13.1[135]

$$\boldsymbol{\tau_{aero} = \frac{1}{2}\rho_{atm}C_{drag}Av^2r_{CM}}$$

Table 13.2 lists the maximum aerodynamic torque and the percentage of the observed minimum and maximum apparent torque for each satellite. The first row shows the calculated maximum aerodynamic torque calculated for all four satellites. The second row shows the percentage of the torque required to cause the angular acceleration listed in Table 12.1 corresponding to the smallest MOI. The third row shows the percentage of the torque required to cause the angular acceleration listed in Table 12.1 corresponding to the largest MOI.

Based on these results, the aerodynamic torque is not adequate to produce the torque required to cause the apparent spin period variations of any of the satellites.

---

[133] Wertz, James R.; “Orbit and Constellation Design and Management”; p. 171
[134] Wertz, James R.; “Orbit and Constellation Design and Management”; p. 943
[135] Wertz, James R.; “Orbit and Constellation Design and Management”; p. 171

Table 13.2: Maximum Aerodynamic Torque for each Satellite

QUANTITY	**SATELLITE**			
	Solidaridad 1	**Telstar 401**	**Echostar 2**	**HGS-1**
Maximum Aerodynamic Torque (μN·m)	0.012	0.024	0.024	0.024
Percentage of Minimum Required Torque (Table 12.1)	4.3	1.6	2.6	2.3
Percentage of Maximum Required Torque (Table 12.1)	1.5	0.4	0.5	0.6

GRAVITY-GRADIENT TORQUE

Each spacecraft's gravity-gradient torque was determined using Eq. 13.2, where "μ" is the gravity parameter of the Earth and "R" is the distance of the satellite from the Earth's center. The maximum gravity-gradient torque was determined by assuming that the deviation angle of the satellite's Z-axis from the local vertical (θ) was π/4.

Eq. 13.2[136]

$$\boldsymbol{\tau}_{\mathbf{grav}} = \frac{\mathbf{3\mu}}{\mathbf{2R^3}}\left|\mathbf{I}_{\mathbf{largest}} - \mathbf{I}_{\mathbf{smallest}}\right|\mathbf{sin}(\mathbf{2\theta})$$

Table 13.3 lists the maximum gravity-gradient torque and the percentage of the observed maximum apparent torque for each satellite. Table 13.3 uses the same format as described for Table 13.2. At face value, Table 13.3 suggests that the maximum gravity-gradient torque is enough in all four cases to cause the maximum apparent angular acceleration. However, gravity-gradient is an attitude-stabilizing torque which attempts to align the longest axis of a satellite with the radial vector from the center of the Earth. The orbit eccentricity of each of the four selected satellites is very small so the libration about

---

[136] Wertz, James R.; "Orbit and Constellation Design and Management"; p. 171

the stable attitude would likely be small. If the long axis of the satellite were nearly aligned along the radial vector from the Earth's center at all times, could each of the satellites exhibit the light curves that have been observed? If the satellites could be observed throughout their 24-hour synodic orbit period, would a diurnal period be detected and how would this differ from the change in perspective of the satellite with respect to the incident sunlight as the satellites orbit the Earth?

Table 13.3: Maximum Gravity-Gradient Torque for each Satellite

QUANTITY	SATELLITE			
	Solidaridad 1	**Telstar 401**	**Echostar 2**	**HGS-1**
Maximum Gravity Gradient Torque (μN·m)	28	63	63	42
Percentage of Minimum Required Torque (Table 12.1)	10,000	4,200	6,700	4,000
Percentage of Maximum Required Torque (Table 12.1)	3,500	970	1,200	1,000

MAGNETIC FIELD TORQUE

Each spacecraft's magnetic field torque was determined using Eq. 13.3, assuming an equatorial orbit. The magnetic moment of the Earth (M) was assumed to be $7.96\text{x}10^{15}$ T·m^3 [137]. The total residual magnetic dipole moment (D) of each satellite was assumed to be a maximum of 1 N·m·T^{-1}. This value is likely much lower since there are very few ferromagnetic components on board the satellites. Since all of the satellites have inactive power systems, there would be very little possibility of internally induced magnetic fields.

---

[137] Wertz, James R.; "Orbit and Constellation Design and Management"; p. 171

Eq. 13.3[138]

$$\tau_{mag} = \frac{DM}{R^3}$$

Table 13.4 lists the maximum magnetic field torque and the percentage of the maximum torque required to cause the maximum apparent angular acceleration for each satellite. Table 13.4 uses the same format as described for Table 13.2. Based on these results, the magnetic field torque is not solely responsible for the apparent spin period variations of any of the satellites.

Table 13.4: Maximum Magnetic Field Torque for each Satellite

QUANTITY	SATELLITE			
	Solidaridad 1	**Telstar 401**	**Echostar 2**	**HGS-1**
Maximum Magnetic Field Torque (μN·m)	0.11	0.11	0.11	0.11
Percentage of Minimum Required Torque (Table 12.1)	39	7.3	12	11
Percentage of Maximum Required Torque (Table 12.1)	14	1.7	2.2	2.8

SOLAR RADIATION PRESSURE TORQUE

Satellites in geosynchronous orbit are exposed to strong sunlight (photons) for the majority of the year, except when they are in eclipse around the equinoxes (March 21 and September 21). When a large solar panel is exposed to these photons, it may act as a solar sail and be accelerated in the direction of the photons' velocity. If the solar panel is attached to a "box" with a larger mass, as shown in Figure 13.1, a torque will be produced

---

[138] Wertz, James R.; "Orbit and Constellation Design and Management"; p. 171

on this “box” portion of the spacecraft, causing the spacecraft to spin about its center of mass.

The solar radiation flux at the Earth’s average orbit radius (Φ_{Earth}), also known as the “Solar Constant”, is shown in Eq. 13.4.

Eq. 13.4[139]

$$\boldsymbol{\Phi_{\mathbf{Earth}} = 1361\ \mathbf{W \cdot m^{2}}}$$

The value of the solar radiation flux can vary from 1315 $W \cdot m^{-2}$, at Earth’s perihelion in early January, to 1410 $W \cdot m^{-2}$ at Earth’s aphelion in early July. A longer-period variation occurs between solar maximum and solar minimum with a period of approximately 11 years between solar maxima. Solar Radiation Pressure (SRP) is related to the Solar Constant and the speed of light (c) by Eq. 13.5.

Eq. 13.5[140]

$$\mathbf{P_{rad}} = \frac{\boldsymbol{\Phi}_{\mathbf{Earth}}}{\mathbf{c}} = \mathbf{4.537x10^{-6}\ Pa}$$

The solar radiation pressure at the Earth can vary from $4.4\text{x}10^{-6}$ Pa to $4.7\text{x}10^{-6}$ Pa over the year. However, the average value of $4.537\text{x}10^{-6}$ Pa was assumed for all calculations. This average SRP value corresponds to totally absorptive surfaces (reflectivity of zero). The force on the entire solar panel that was caused by SRP was determined using Eq. 13.6. The average specular reflectance of a modern satellite’s solar panel (q) is approximately 0.1 [141].

---

[139] NASA Climate and Radiation Science Research Portal: http://atmospheres.gsfc.nasa.gov/climate/index.php?section=136

[140] Serway, Raymond A.; Physics for Scientists and Engineers; 3rd Ed.; p. 966

[141] Cao, Y. et al.; Measurement of Optical Characteristics of Solar Panels Used on Satellite; 9th International Symposium on Antennas Propagation and EM Theory (ISAPE); 2010; p. 748

Eq. 13.6[142]

$$\vec{\mathbf{F}}_{\mathbf{SRP}} = \left[(\mathbf{1}+\mathbf{q})\mathbf{P}_{\mathbf{rad}}\mathbf{A}_{\mathbf{panel}}\mathbf{cos\phi}\right]\hat{\mathbf{i}}$$

The maximum force on each of the satellite’s respective solar panels was determined by assuming that the angle of sunlight incidence (ϕ) was 0 (orthogonal to the solar panel surface). In this case, Eq. 13.6 simplified to Eq. 13.7.

Eq. 13.7

$$\vec{\mathbf{F}}_{\mathbf{SRP}_{\mathbf{max}}} = \left[(\mathbf{1.1})\mathbf{P}_{\mathbf{rad}}\mathbf{A}_{\mathbf{panel}}\right]\hat{\mathbf{i}}$$

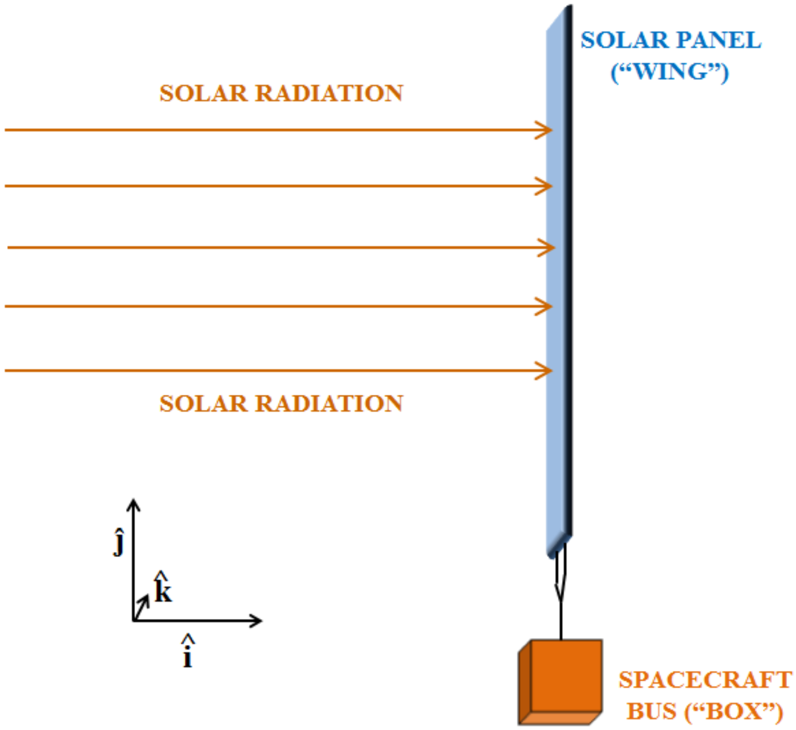

Figure 13.1: Maximum Force on Solar Panel due to SRP

---

[142] Wertz, James R.; “Orbit and Constellation Design and Management”; p. 171

If the satellite was originally motionless and its center of mass was in the geometric center of the "box" portion, then the satellite would begin to spin about the box's k-axis when exposed to sunlight.

The total SRP torque from a single solar panel was determined by using the sum of all of the torques produced by all areas of the solar panel acting on their corresponding torque arms. Consider an infinitesimal area of the solar panel called dA, shown in Figure 13.2, which is comprised of two infinitesimal lengths dy and dz, as shown in Eq. 13.8.

Eq. 13.8

$$\mathbf{dA_{panel} = dydz}$$

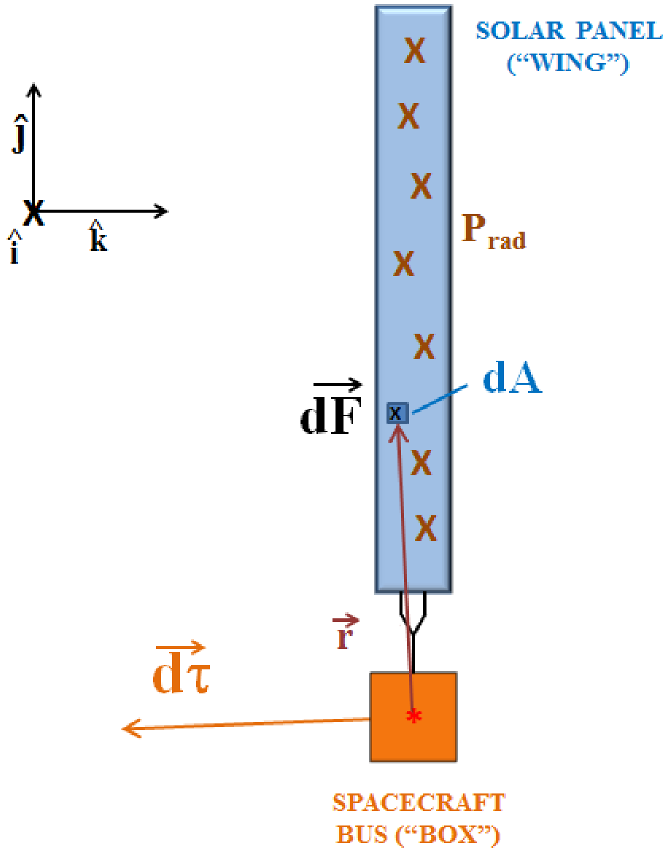

Figure 13.2: The Torque Produced by SRP Force (dF) on Area dA of the Solar Panel

The force due to SRP acting on the area dA would be determined using Eq. 13.9.

Eq. 13.9

$$\overrightarrow{\mathbf{dF}} = [(\mathbf{1.1})\mathbf{P_{rad}}(\mathbf{dydz})]\ \hat{\mathbf{i}}$$

The torque ($\overrightarrow{\mathrm{d\tau}}$) acting on the spacecraft is determined by taking the cross-product of the torque arm ($\vec{\mathrm{r}}$) with the force ($\overrightarrow{\mathrm{dF}}$) as shown in Eq. 13.10. The torque arm was assumed to be measured from the center of mass of the "box" to the area (dA) on the solar panel.

Eq. 13.10

$$\overrightarrow{\mathbf{d\tau}} = \vec{\mathbf{r}}\ \mathbf{x}\ \overrightarrow{\mathbf{dF}}$$

The torque arm was also expressed in component form, as shown in Eq. 13.11.

Eq. 13.11

$$\vec{\mathbf{r}} = \mathbf{y}\hat{\mathbf{j}} + \mathbf{z}\hat{\mathbf{k}}$$

The result of the cross product is shown in Eq. 13.12.

Eq. 13.12

$$\overrightarrow{\mathbf{d\tau}} = (\mathbf{zdF})\ \hat{\mathbf{j}} - (\mathbf{ydF})\ \hat{\mathbf{k}}$$

The net torque acting on the satellite's center of mass was determined by using an area integral over the entire solar panel's sun-illuminated surface, which consisted of its total length (*l*) and total width (*w*) as shown in Figure 13.3. The area integral is shown in Eq. 13.13.

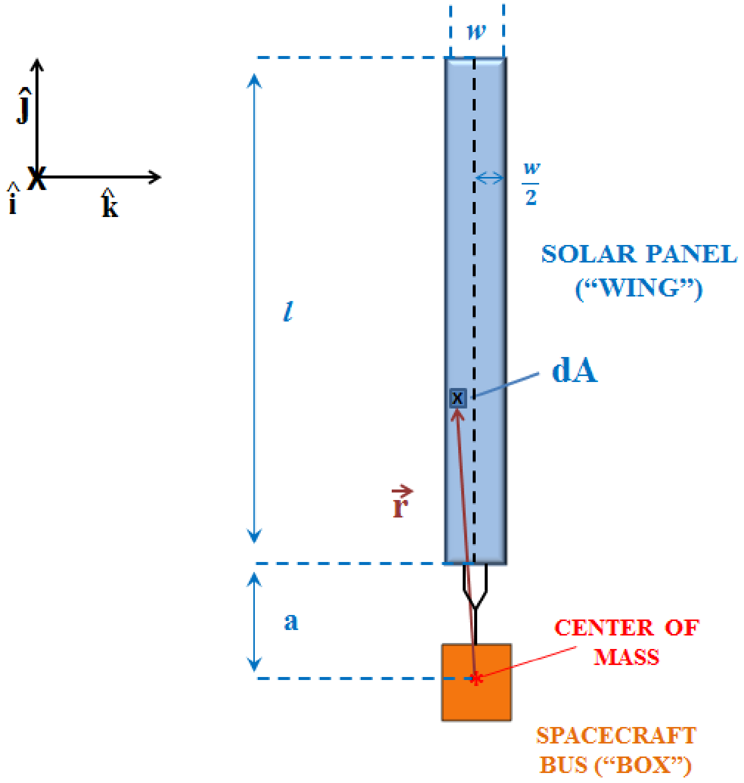

Figure 13.3: The Dimensions of the Solar Panel and the "Box"

Eq. 13.13

$$\vec{\boldsymbol{\tau}} = (\mathbf{1.1})\mathbf{P}_{\mathbf{rad}} \int_{\mathbf{a}}^{\mathbf{a}+\boldsymbol{l}} \int_{-\frac{w}{2}}^{+\frac{w}{2}} [(\mathbf{z})\,\hat{\mathbf{j}} - (\mathbf{y})\,\hat{\mathbf{k}}]\,(\mathbf{dydz})$$

The final expression is shown in Eq. 13.14. The expression shown in Eq. 13.14 is negative because of the coordinate convention shown in Figure 13.2. The value r_{CM} is the distance between the center of mass of a solar panel and the center of mass of the box.

Eq. 13.14

$$\vec{\boldsymbol{\tau}} = -[(\mathbf{1.1})\mathbf{P}_{\mathbf{rad}}\mathbf{A}_{\mathbf{panel}}\,(\mathbf{r}_{\mathbf{CM}})]\,\hat{\mathbf{k}}$$

Table 13.5 lists the maximum SRP torque and the percentage of the observed minimum and maximum apparent torque for each satellite. These results suggest that SRP is the largest disturbance torque on all four spacecraft, if all four spacecraft comprised of a single solar panel and if the incident sunlight were always orthogonal to that solar panel. However, the light curves of all four satellites suggest that the satellites are spinning. Therefore, the incident sunlight will have variable angles of incidence to the solar panel as a satellite spins. HGS-1 is the only satellite of the four that has one deployed solar panel, as previously described in Chapter 10.

Table 13.5: Maximum SRP Torque for each Satellite

QUANTITY	SATELLITE			
	Solidaridad 1	**Telstar 401**	**Echostar 2**	**HGS-1**
Maximum SRP Torque (μN·m)	520	1010	1010	1000
Percentage of Minimum Required Torque (Table 12.1)	186,000	67,000	107,000	96,000
Percentage of Maximum Required Torque (Table 12.1)	65,000	15,500	19,800	25,000

COMPARISONS WITH APPARENT SPIN ANGULAR ACCELERATION

The observed spin angular accelerations of Solidaridad 1, Telstar 401 and Echostar 2 (Figures 12.1, 12.2 and 12.3 respectively) suggest that the torque acting on these spacecraft has a long-period cyclical variation. Each of these cases suggests that the dominant external torque that is acting on the spacecraft is not short-term but can have a period of many days, even years in the case of Solidaridad 1.

Although the SRP torques (for one solar panel) are overwhelmingly large when compared to the other three disturbance torques, this still does not guarantee that SRP torques are solely responsible for the observed apparent spin period variations. Although aerodynamic and magnetic disturbance torques are inadequate to provide the maximum angular acceleration observed, they might influence the satellites' attitudes in subtler ways. The SRP effects on the satellites' spin torques are discussed in greater detail in Chapter 14.

CHAPTER 14: SRP AND SPIN ANGULAR ACCELERATION

The SRP torque was evaluated to be the largest of the four disturbance torques. Therefore, an investigation into its effects on a satellite's attitude, most notably the satellite's spin period, is required. This chapter investigates the effect of SRP on a satellite with a single deployed solar panel (in the case of HGS-1) and on a satellite with two deployed solar panels (in the case of the remaining selected satellites).

SINGLE SOLAR PANEL SATELLITE

Chapter 13 determined the maximum SRP torque that would act on a box-wing satellite if it had one solar panel. Of the four selected satellites, HGS-1 is the only satellite with one deployed solar panel. However, when determining the maximum torque (as seen in Chapter 13), it was assumed that the SRP force on the solar panel was at its maximum and that it constant over the entire spin period. In reality, the torque (and consequently the spin angular acceleration) would always be changing because of the satellite's spin. This is illustrated in Figure 14.1, again for the case of a single solar panel satellite.

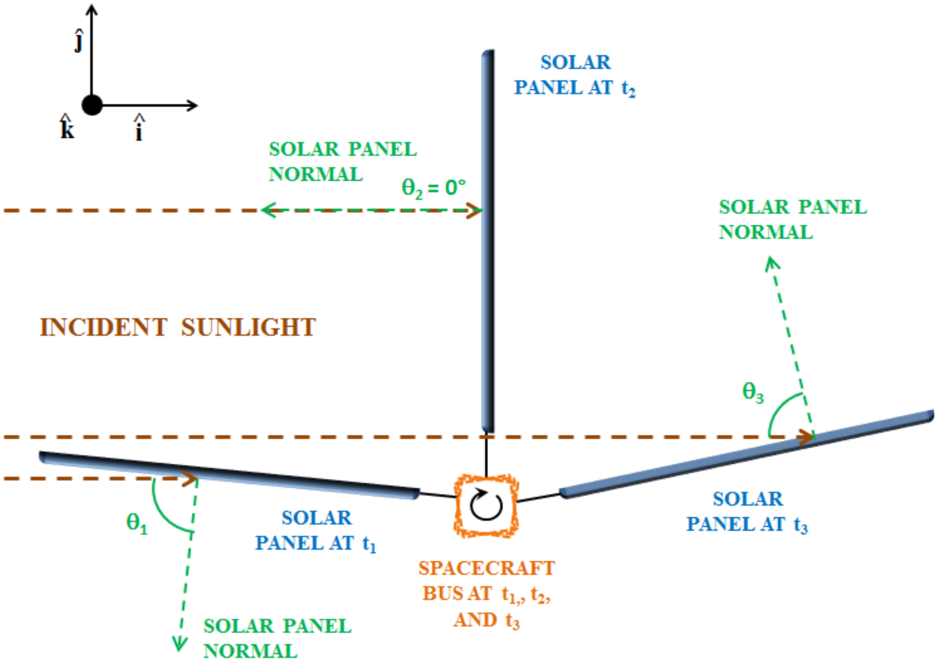

Figure 14.1: Varying Sunlight Incidence Angle with Spacecraft Spin

As the satellite spins, the sunlight incidence angle (θ) will change in a cyclical fashion. Each value of θ will have an associated torque and therefore an angular acceleration. For this case, it would become necessary to integrate the angular acceleration over the satellite's spin to find the total spin angular acceleration over one spin period. For a satellite configuration like that of HGS-1, the double integral shown in Eq. 13.13 would become a triple integral, with the changing incidence angle (θ) as the third integrated variable, as shown in Eq. 14.1.

Eq. 14.1

$$\vec{\alpha}_{tot} = \frac{(1+q)P_{rad}}{I}\int_{-\frac{\pi}{2}}^{+\frac{\pi}{2}}\int_{a}^{a+l}\int_{-\frac{w}{2}}^{+\frac{w}{2}}\left[(z)\,\hat{j}-(y)\,\hat{k}\right](\cos\theta)\,(dydzd\theta)$$

The expression in Eq. 14.1 can be shortened to that shown in Eq. 14.2. The variable $\vec{\alpha}_{max}$ represents the spin angular acceleration when the sunlight incidence angle (θ) is zero. Assuming that the satellite's spin axis is orthogonal to the incident sunlight and within the equatorial plane, the sunlight incidence angle will range from -π/2 to +π/2 (-90° to +90°) for one side of the solar panel over one half of the satellite's spin period (Figure 14.1).

Eq. 14.2

$$\vec{\alpha}_{tot} = \vec{\alpha}_{max} \int_{-\frac{\pi}{2}}^{+\frac{\pi}{2}} \cos\theta d\theta$$

where:

$$\vec{\alpha}_{max} = -\frac{(1+q)P_{rad}A_{panel}\,(r_{CM})}{I}\ \hat{k}$$

The total spin angular acceleration over one half of the spin period in which one side of the single solar panel is in sunlight was determined by using Eq. 14.3.

Eq. 14.3

$$\vec{\alpha}_{tot} = -\frac{2(1+q)P_{rad}A_{panel}\,(r_{CM})}{I}\ \hat{k}$$

Assuming the satellite spin axis, solar panel orientation and sunlight incidence are as shown in Figure 14.1, the satellite's spin would have to expose the opposite side of the solar panel to sunlight over the remaining half of the spin period, as shown in Figure 14.2. Figure 14.2 shows the opposite side of the solar panel moving against the solar radiation pressure, resulting in a decreasing satellite angular acceleration. Therefore, the net angular acceleration over one complete spin period of the satellite is calculated by determining the difference between the total angular accelerations for each half of the spin period. This is done by using Eq. 14.4. Note that if both sides of the solar panel have the same reflectivity, the net angular acceleration will be zero.

Eq. 14.4

$$\sum \vec{\alpha} = -\left[\frac{2P_{rad}A_{panel}\,(r_{CM})}{I}\right](q_1 - q_2)\,\hat{k}$$

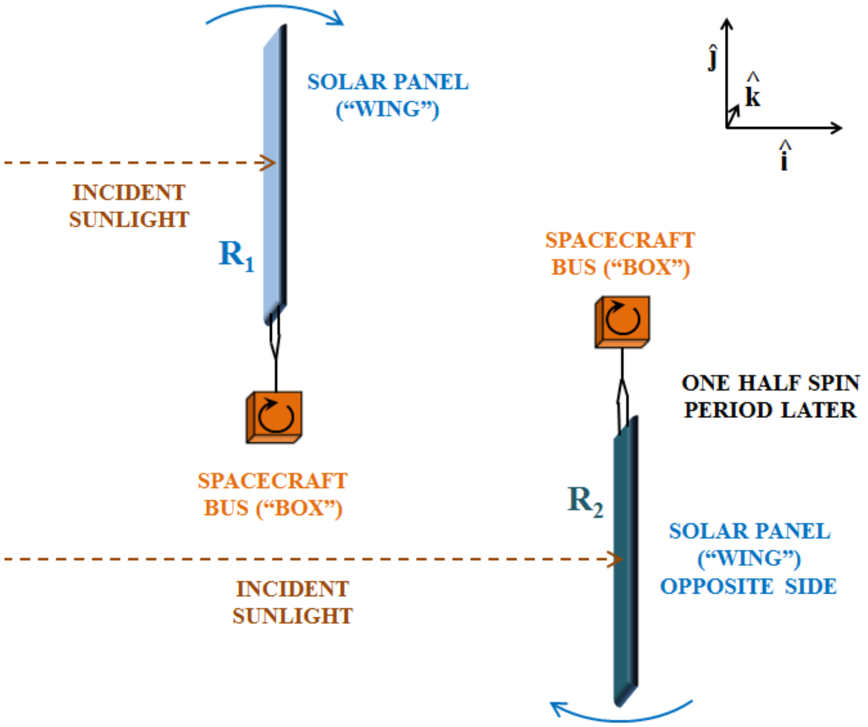

Figure 14.2: Incident Sunlight on Opposite Sides of Single Solar Panel

3-axis spin stabilized GEO telecommunications satellites are designed such that only one side of each solar panel is used for solar power generation. The opposite side of the solar panels are normally painted with high-emittance black paint[143]. Therefore, the total SRP angular acceleration from the opposite side of the solar panel will not likely be

---

[143] Gillmore, D. ed.; Spacecraft Thermal Control Handbook – Volume 1: Fundamental Technologies; p. 86

identical to the first side of the solar panel because the opposite side will likely have a different reflectivity value.

Eq. 14.4 suggests that if a single solar panel satellite (such as HGS-1) is experiencing the maximum SRP torque possible (the solar panel is orthogonal to sunlight at some time during the satellite's spin), the absolute difference in reflectivity of the sides of the solar panel could be determined. This relationship is shown in Eq. 14.5.

Eq. 14.5

$$\mathbf{q_2 - q_1 = \frac{|\vec{\tau}_{max}|}{\left[2P_{rad}A_{panel}\,(r_{CM})\right]}}$$

Using the maximum torque calculated for HGS-1 (4.0 μN·m) the difference in reflectivity was estimated to be 0.002. This initial determination suggests that a very small difference in reflectivity can result in the measured maximum spin angular acceleration for satellites with characteristics like HGS-1.

Solidaridad 1, Telstar 401 and Echostar 2 have two fully deployed solar panels, so the single solar panel model would not be adequate to describe the solar radiation pressure effects on these satellites.

DOUBLE SOLAR PANEL SATELLITE

A satellite with two solar panels, each attached to opposite sides of the "box" is illustrated in Figure 14.3. Figure 14.3 suggests that if one of the solar panels is assisting the spin of the satellite, then the other panel would be opposing the spin at the same time. If the two solar panels are identical, in both physical characteristics and orientation with respect to the Sun, then the torques exerted by both panels would be equal in magnitude but opposite in direction. Therefore, hypothetically, the net torque on such a spacecraft would be 0. If the reflectivity of one of the panels is slightly different from the other, a net torque would result, even if the solar panels were oriented at the same angle with respect to the incident sunlight. However, the opposite sides of the panels would likely have a different net torque which could assist or oppose the aforementioned net torque.

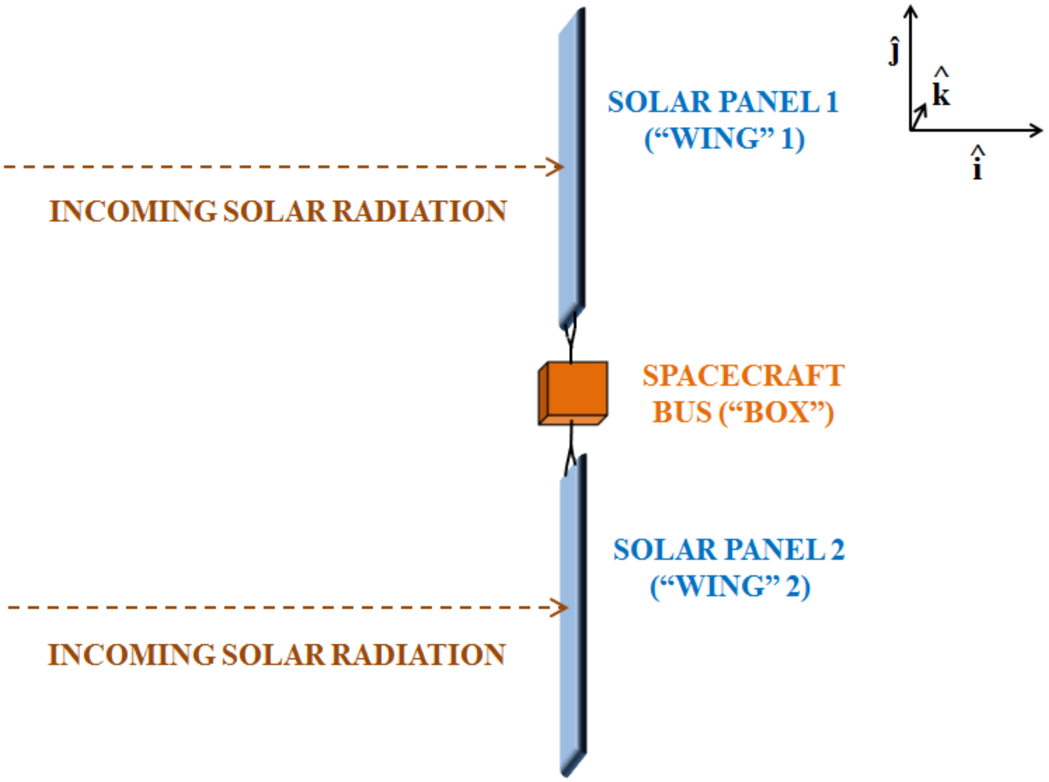

Figure 14.3: Box-wing Satellites with Double Solar Panels

INITIAL SATELLITE ATTITUDE

When Solidaridad 1, Telstar 401 and Echostar 2 were all active, their attitudes were controlled such that their solar panels were aligned north-south (nearly orthogonal to the Earth's equatorial plane), as shown in Figure 14.4. Their solar panels were controlled in such a way that both would be pointing at the Sun in order for them to generate the maximum amount of power for the spacecraft. Each of these satellites became inactive due to some catastrophic failure while in the geostationary belt, as previously described in Chapter 10.

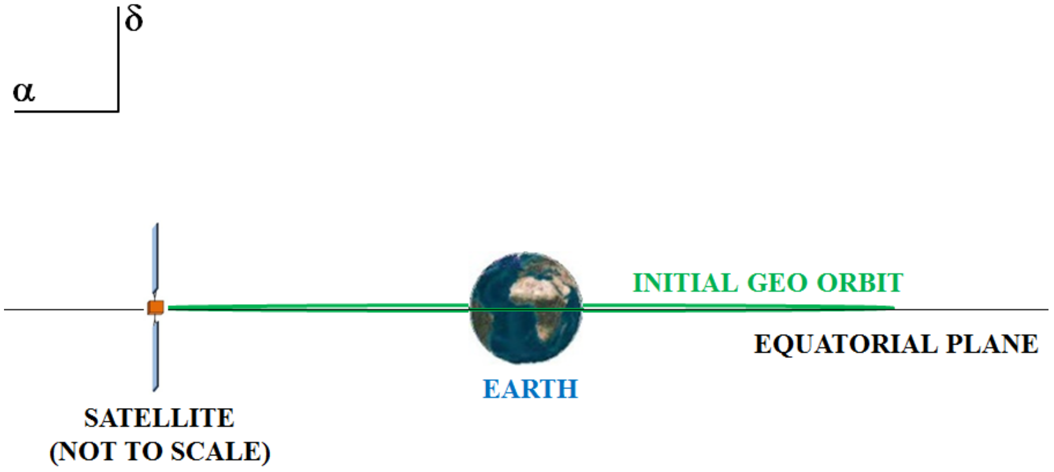

Figure 14.4: Attitude of an Active Geostationary Satellite [144]

Assuming that the attitude control system of each satellite lost all power immediately after its malfunction, its reaction wheels would begin to slow down (due to internal friction) after the main power was cut. The angular momentum lost by the reaction wheels would be slowly transferred into the satellites, thereby causing the satellite to spin. It is likely that the three reaction wheels slowed down at slightly different rates, thus possibly causing the satellite spin axis to move as well (a source of precession).

Before the solar radiation pressure could become the dominant force on the satellite's angular acceleration, the internal forces (reaction wheels) would have had to dissipate. The reaction wheels on some satellites might have been at a higher angular momentum when they failed than other similar satellites. This might be the reason why

---

[144] Kelso, Tom S.: "Satellite Times: More on Geostationary Orbits"; http://celestrak.com/columns/v04n09

Solidaridad 1, Telstar 401 and Echostar 2 have apparent spin periods of different magnitudes and amplitudes today.

The best method of confirming this hypothesis would be to observe a box-wing satellite that has just been placed into the junkyard orbit or has suffered a catastrophic failure in which its attitude control system has been rendered inoperative.

Since the exact spin axis orientations of the four satellites are unknown, it was assumed that their spin axes were located parallel to the equatorial plane of the Earth and were not moving in inertial space.

CYCLICALLY VARYING SUNLIGHT INCIDENCE ANGLES

Over the course of several hours, the solar panels would experience nearly the same periodic solar illumination as the satellite spins. However, the Sun’s apparent position with respect to the satellite’s spin axis would change from day to day as the Earth orbited the Sun. The motion of the Earth in its orbit would change the minimum sunlight incidence angle on the solar panels and would therefore change the net torque, thus affecting the satellite’s spin period. A basic illustration of this cyclical variation is shown in Figure 14.5.

Table 13.5 suggested that the torque produced by SRP on a single solar panel was hundreds of times larger than the torque that caused the observed maximum spin angular acceleration of the three double-panel satellites. Based on this evidence and assuming that both panels are physically identical, a hypothesis can be made that the total SRP torque is the result of a net torque of the two solar panels that are canted at some angle (ϕ) to one another.

The reflectivity coefficient (q) of each side of each solar panel is important to keep in mind because a very small difference in reflectivity can potentially result in a relatively large net torque, just like the case of a single solar panel. However, since the reflectivity coefficients of the solar panels are not known with certainty, it will be assumed that each will have a value of 0.1 on both sides.

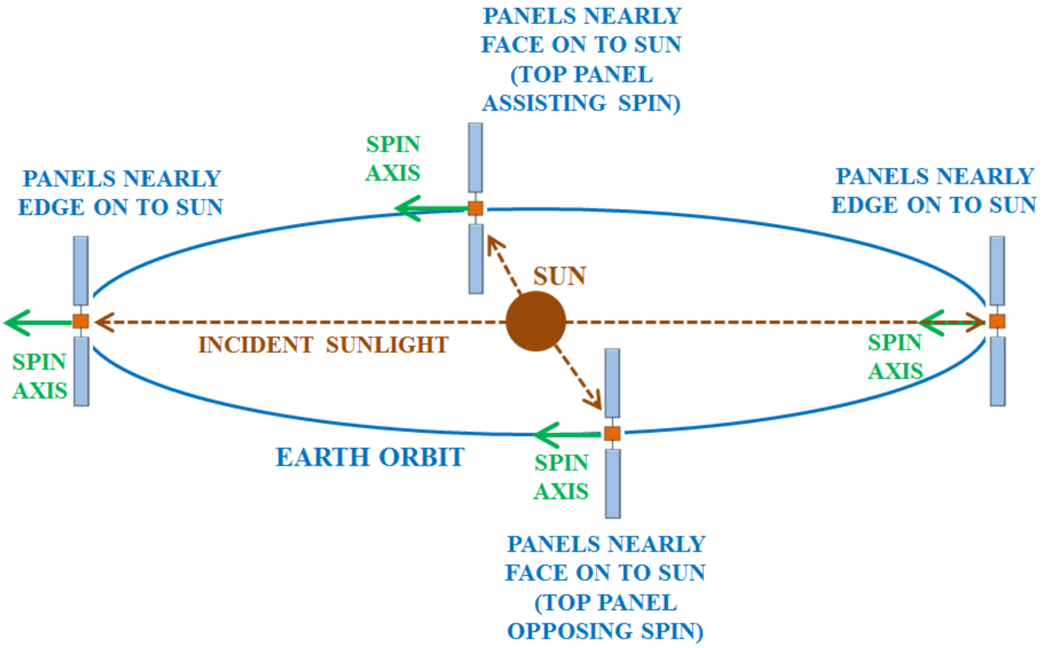

Figure 14.5: Varying Spin Axis Orientation with Respect to the Sun over Earth Orbit

An observer viewing the satellite`s canted solar panels edge-on to the width and down the length, as shown in Figure 14.6, would see two intersecting lines with the angle ϕ between them. The minimum angle of incident sunlight on the surfaces of the upper and lower solar panels would change by an average of one degree per day.

The solar panel orientations shown in Figure 14.6 are ideal examples and might not be the true orientations of any of the four satellites. Figure 14.6 illustrates the changing minimum angles of incident sunlight for both solar panels. Table 14.1 describes what is happening to the satellite’s angular acceleration and angular velocity at each specific time shown in Figure 14.6, assuming that the satellite had an initial angular velocity at time t_0.

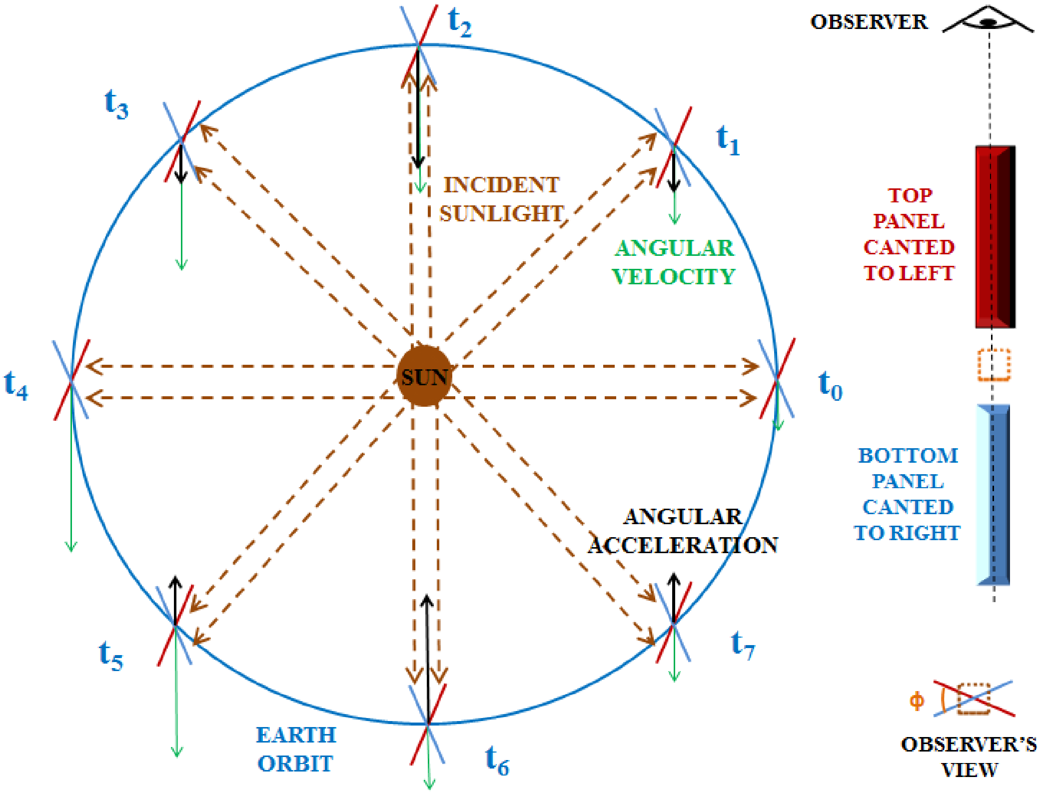

Figure 14.6: Differing SRP Torques Due to Varying Sun Incidence Angles on Solar Panels

Table 14.1: Explanation of the Torques on Spacecraft at Times t0 to t7 in Figure 14.6

TIME	PHYSICS	α	ω
t_0	The incident sunlight angles on the upper and lower solar panels are equal. Any torque produced by the upper panel is negated by the lower panel and vice-versa. The net SRP torque is 0 (null 1).	0	Constant Minimum
t_1	The incident sunlight angle on the lower panel is less than that on the upper panel, giving the lower panel the advantage. The satellite has a net torque in the direction that the satellite is already spinning (in Figure 14.6).	Increasing With Spin	Increasing
t_2	The incident sunlight angle is equal for both panels. Unlike the scenario at t_0, both panels are being pushed in the same direction. Therefore both panels are assisting with the satellite's spin.	Maximum With Spin	Increasing
t_3	The incident sunlight angle on the upper panel is less than that on the lower panel, giving the upper panel the advantage. The Sun is now lighting the opposite side of both panels. The net torque is still assisting the satellite's spin, but not as much as it did at time t_2.	Decreasing With Spin	Increasing
t_4	The incident sunlight angles on the upper and lower solar panels are equal. The net torque on the spacecraft is 0 (null 2).	0	Constant Maximum
t_5	The incident sunlight angle on the lower panel is less than that on the upper panel, giving the lower panel the advantage. The satellite has a net torque that is opposing the satellite's spin.	Increasing Against Spin	Decreasing
t_6	The incident sunlight angle is equal for both panels. Both panels are being pushed in the same direction, but opposing the satellite's spin.	Maximum Against Spin	Decreasing
t_7	The incident sunlight angle on the upper panel is less than that on the lower panel, giving the upper panel the advantage. The satellite still has a net torque opposing the satellite's spin.	Decreasing Against Spin	Decreasing
t_0	The satellite has returned to the first null point and will start the cycle again.	0	Constant Minimum

Figure 14.7 shows a magnified representation of the satellite at time t_1 in Figure 14.6. At time t_1, the sunlight incidence angle of the top panel is greater than the sunlight incidence angle of the bottom panel. Therefore, the solar radiation pressure will be greater for the bottom panel and a net angular acceleration shown in Figure 14.7 will result.

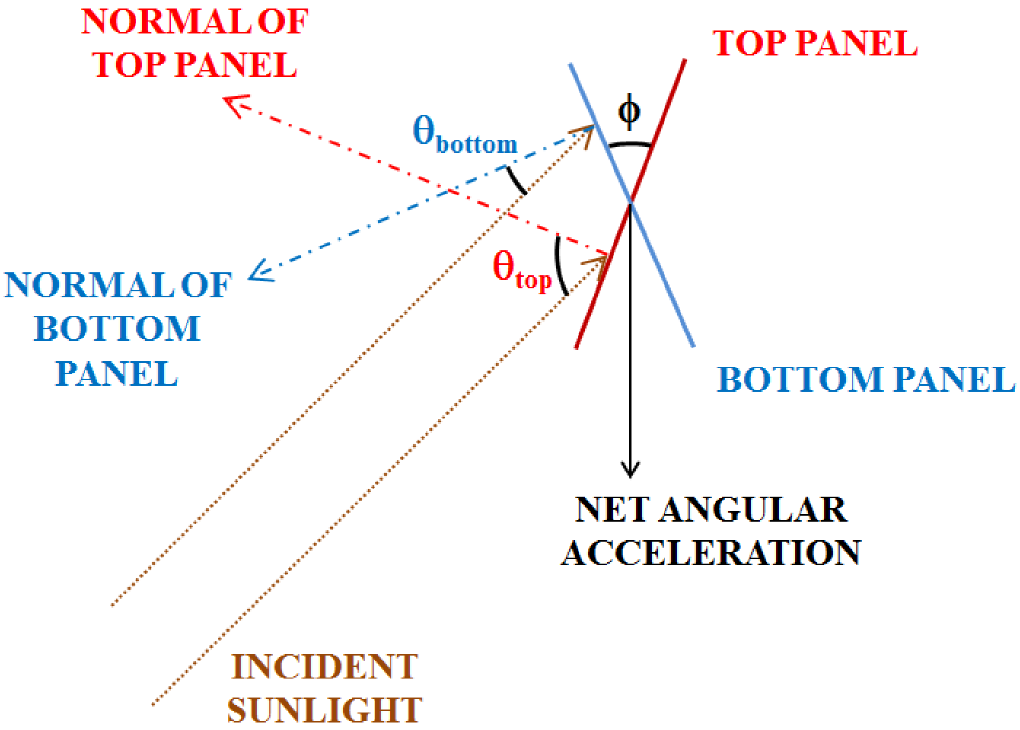

Figure 14.7: Explanation of the Sunlight Incidence Angles at time t_1 of Figure 14.6

After one half of the spin period has elapsed from the satellite orientation shown in Figure 14.7, what was the bottom panel will become the top panel and what was the top panel will become the bottom panel. The orientation of the top and bottom panels will be same, except that the opposite sides of both panels are illuminated by the Sun. Assuming that the reflectivity coefficient (q) of both sides of the panels are identical, the same net angular acceleration will result no matter which side of the satellite is illuminated.

The net angular acceleration of the system shown in Figure 14.7 is determined by taking the difference between the angular accelerations due to each of the solar panels. This calculation is shown in Eq. 14.6.

Eq. 14.6

$$\vec{\boldsymbol{\alpha}}_{\mathbf{net}} = -\frac{\mathbf{2(1+q)P_{rad}A_{panel}\,(r_{CM})}}{\mathbf{I}}\left[\mathbf{cos}\left(\boldsymbol{\theta}_{\mathbf{top}}\right) - \mathbf{cos}(\boldsymbol{\theta}_{\mathbf{bottom}})\right]\hat{\mathbf{k}}$$

The minimum sunlight incidence angles (θ) on both solar panels will change with time as the Earth orbits the Sun. Assuming that the satellite’s spin axis is not moving, the rate at which the minimum sunlight incidence angle is changing is the angular velocity of the Earth’s orbit around the Sun. This rate can be expressed in terms of the sidereal period of the Earth’s orbit (365.2422 days).

According to Figure 14.6, the time t_0 corresponds to when the net spin angular acceleration is zero. At this time, the sunlight incidence angles to the solar panels are equal and opposite of one another and have the absolute values of half the canting angle (ϕ). This means that when the total time is zero, the two solar panels have equal and opposite sunlight incidence angles whose absolute values are equal to half the canting angle.

Eq. 14.7 determines the net angular acceleration over one spin period of an inactive box-wing GEO satellite with two solar panels that have identical reflectivity coefficients and that are canted at an angle of ϕ with respect to one another. Note that when $t = t_0$, the sunlight incidence angles become half of the canting angles previously described.

Eq. 14.7

$$\vec{\boldsymbol{\alpha}}_{\mathbf{net}} = -\frac{\mathbf{2(1+q)P_{rad}A_{panel}\,(r_{CM})}}{\mathbf{I}}\left\{\mathbf{cos}\left[\frac{\mathbf{2\pi}}{\mathbf{T}}(\mathbf{t}-\mathbf{t_0})-\frac{\boldsymbol{\phi}}{\mathbf{2}}\right]-\mathbf{cos}\left[\frac{\mathbf{2\pi}}{\mathbf{T}}(\mathbf{t}-\mathbf{t_0})+\frac{\boldsymbol{\phi}}{\mathbf{2}}\right]\right\}\,\hat{\mathbf{k}}$$

In Eq. 14.7, the variables A_{panel}, r_{CM} and I are dependent on the satellite's physical characteristics (mass and dimensions). If the satellite's integrity has not been compromised since its launch, then these values should be nearly constant over a long period of time.

The value of the reflectivity coefficient (q) can be considered to be 0.1 for both sides of the solar panels. However, a small uncertainty in reflectivity could introduce a large uncertainty in the SRP angular acceleration, as was discovered earlier with the single solar panel example.

The free parameters in Eq. 14.7 are the period of the minimum sunlight incidence angle variability with respect to the solar panel normal (T) and the canting angle (ϕ). These two parameters are currently unknown with respect to the three satellites that have two deployed solar panels. However, the value of T for Telstar 401 and Echostar 2 was estimated from the spin period variability curves shown in Chapter 9 (Figures 9.2 and 9.3). It is currently unclear whether the observations of the spin period variability for these satellites constituted a full period.

The period of the spin period variability of Telstar 401 was estimated to be 290 days, based on the amount of time elapsed from the maximum to the minimum apparent spin periods. The period of Echostar 2's spin period variability was estimated to be 364 days, based on the amount of time elapsed from the minimum to the maximum apparent spin periods. Solidaridad 1's period could not be estimated because not enough data had been obtained. Although the HGS-1's period had been estimated, the satellite only has one deployed solar panel and therefore Eq. 14.7 is not suitable to determine its hypothetical spin angular acceleration behaviour.

A reflectivity coefficient (q) of 0.1 and an estimated period of spin period variability (T) corresponding to each satellite, were used to determine the canting angle (ϕ). This was done by fitting the theoretical curve (based on Eq. 14.7) over the observed angular acceleration vs. time plots (Figure 12.2 and 12.3) of Telstar 401 and Echostar 2, respectively, such that the slope of the hypothetical curve was similar and nearly coincident to the slope of the observation trend near the time (α=0) axis. This was done to reveal any discrepancies between the observed behaviour and the hypothetical curves.

Theoretical angular acceleration curves (based on Eq. 14.7) were overlaid onto the observed spin angular accelerations plots for Telstar 401 and Echostar 2 shown in Figures 12.2 and 12.3, respectively. The resultant plots are shown in Figure 14.8 (for Telstar 401) and Figure 14.9 (for Echostar 2).

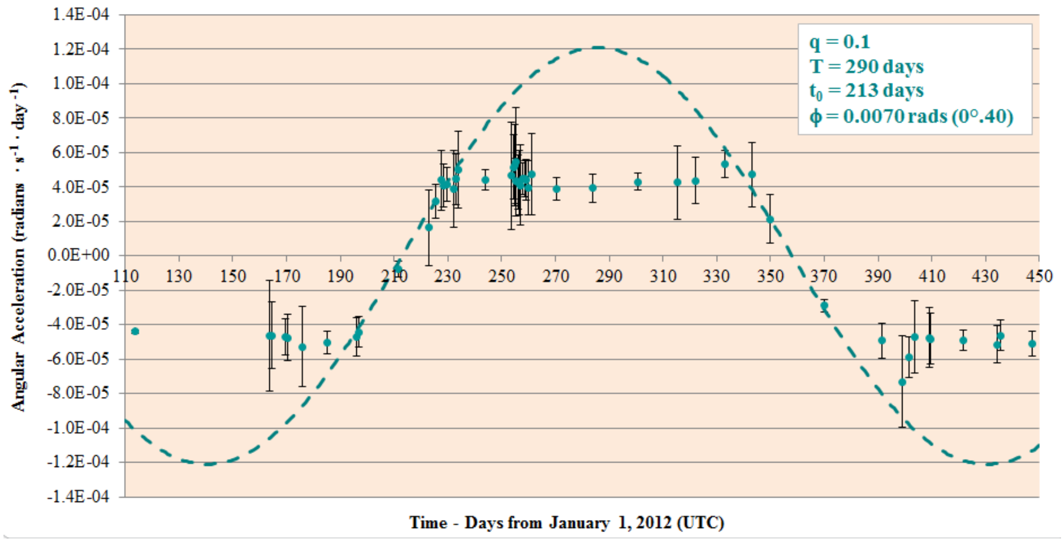

Figure 14.8: Theoretical vs. Observed Angular Acceleration for Telstar 401

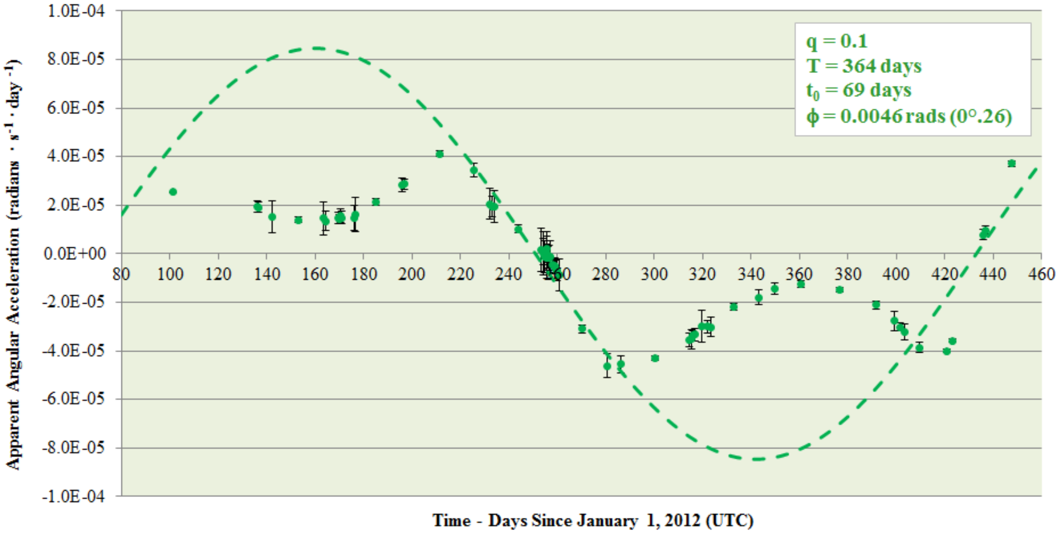

Figure 14.9: Theoretical vs. Observed Angular Acceleration for Echostar 2

Eq. 14.7 can be integrated to find an expression of the theoretical variation in the satellite’s angular velocity due to SRP over time. The expression for theoretical angular velocity due to SRP is shown in Eq. 14.8. The theoretical spin angular velocity curves for Telstar 401 and Echostar 2 are shown in Figures 14.10 and 14.11, respectively.

Eq. 14.8

$$\vec{\boldsymbol{\omega}} = \vec{\boldsymbol{\omega}}_0 - \frac{\mathbf{T(1+q)P_{rad}A_{panel}\,(r_{CM})}}{\mathbf{I\pi}}\left\{ \mathbf{sin}\left[\frac{\mathbf{2\pi}}{\mathbf{T}}(\mathbf{t}-\mathbf{t_0}) - \frac{\boldsymbol{\phi}}{\mathbf{2}}\right] - \mathbf{sin}\left[\frac{\mathbf{2\pi}}{\mathbf{T}}(\mathbf{t}-\mathbf{t_0}) + \frac{\boldsymbol{\phi}}{\mathbf{2}}\right]\right\}\hat{\mathbf{k}}$$

Each theoretical angular velocity data point can be transformed into its corresponding theoretical spin period data point. Therefore, a theoretical spin period curve due to SRP can be created and compared with the observed apparent spin period curve originally shown in Figures 9.2 and 9.3 for Telstar 401 and Echostar 2 respectively.

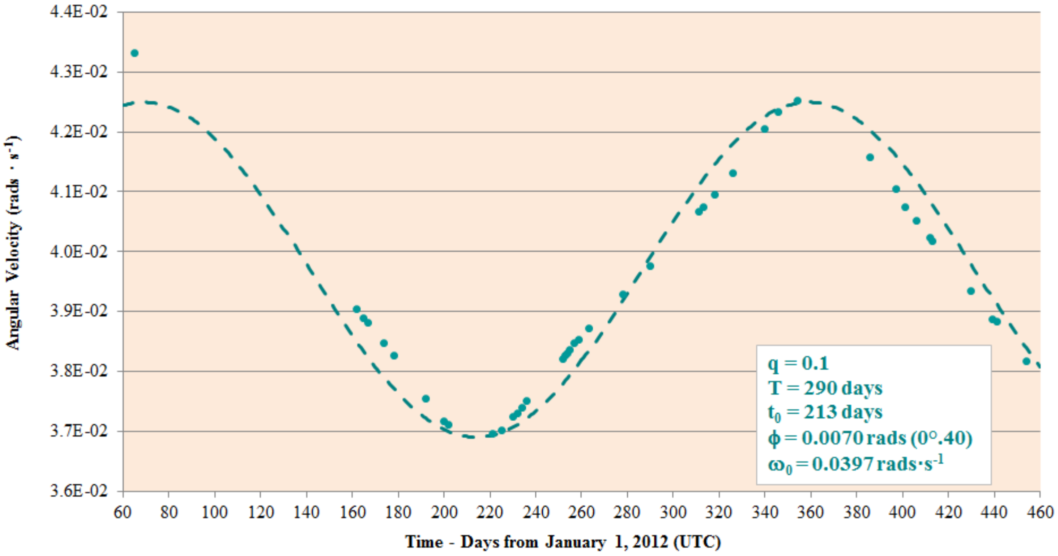

Figure 14.10: Theoretical vs. Observed Angular Velocity for Telstar 401

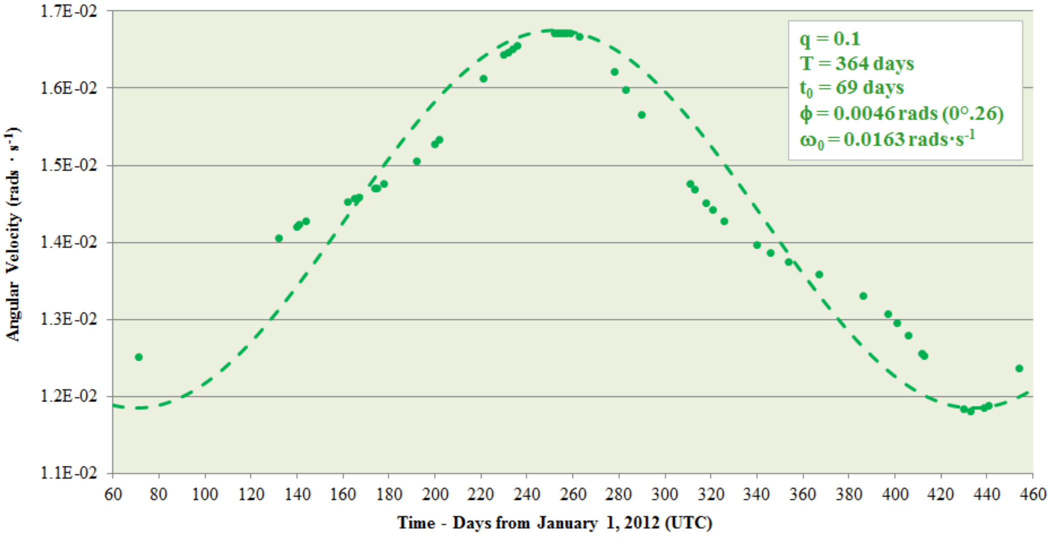

Figure 14.11: Theoretical vs. Observed Angular Velocity for Echostar 2

The theoretical spin angular velocity data were transformed into their corresponding theoretical spin period data. These data were subtracted from the corresponding data of the observed apparent spin period data. This resulted in the spin period discrepancy curves for Telstar 401 and Echostar 2, shown in Figures 14.12 and 14.13, respectively.

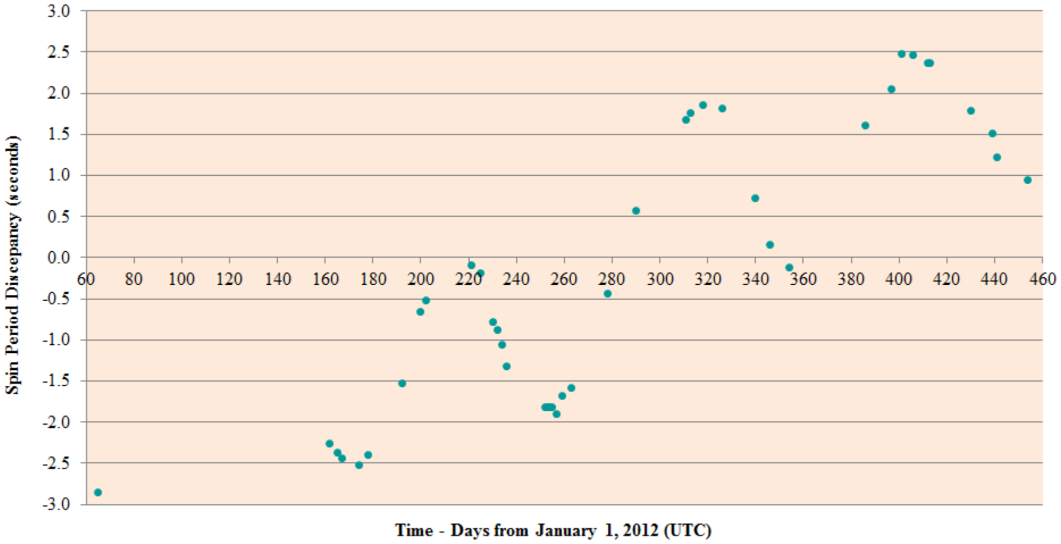

Figure 14.12: Spin Period Discrepancy for Telstar 401

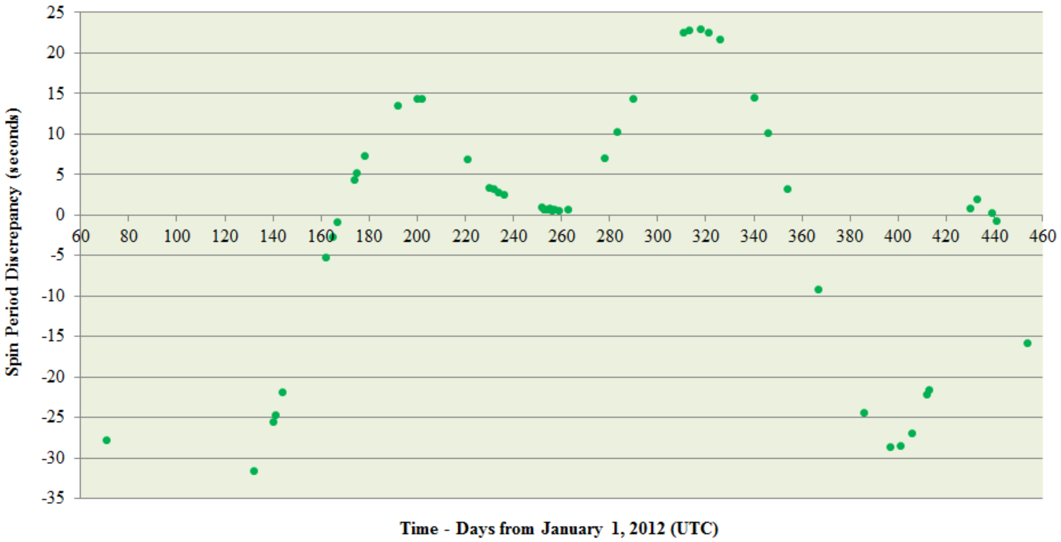

Figure 14.13: Spin Period Discrepancy for Echostar 2

The simple model of the spin angular acceleration due to SRP is partially successful in that it does follow the general trend of the observed spin periods. However, the model fails to explain the "non-linear" portion (deviation from the sinusoid trend) discussed in Chapter 12. It is evident from all of the graphs shown in this chapter that a basic model of solar radiation pressure torque on the solar panels of a box-wing GEO satellite is not adequate to fully explain its observed spin period variations. The reasoning for this is currently unclear, however an initial investigation into synodic effects might offer some answers.

The first impression from the spin period discrepancy graphs in Figures 14.12 and 14.13 is that the discrepancies seem to have a periodic behaviour. The amplitudes of the graphs are noticeably different in the sense that the amplitude of Telstar 401's graph is about a tenth of the amplitude of Echostar 2's graph. The model is not currently able to explain the 2.5-second spin period discrepancy for Telstar 401 or the approximately 30-second spin period discrepancy for Echostar 2.

CHAPTER 15: SYNODIC EFFECTS

When analyzing the dynamics of any inactive satellite, including those in a GEO orbit, the relative motion of the observer to the illumination source (such as the Sun) and of the satellite's orbit motion with respect to the satellite's spin axis is very important. Both of these relative motions will change the apparent (synodic) spin period of the satellite. The extent of the difference between the sidereal (true) and synodic (apparent) spin periods depends on the magnitude and direction of each relative motion.

In this chapter, the potential of synodic effects to explain the spin period discrepancies of Telstar 401 and Echostar 2 (computed in Chapter 14), will be explored.

RELATIVE MOTION BETWEEN OBSERVER AND SATELLITE

When observing each of the four selected satellites, there was a relative motion between the observation site and the orbiting satellite which was caused by the apparent change of declination of each satellite over time. An example of this apparent motion for the Echostar 2 satellite is shown in Figure 15.1. The date and time of the image as well as the duration of the imaging (nearly 9 minutes) is shown at the bottom of Figure 15.1. This apparent motion in declination was caused by the orbit inclination of the satellite with respect to the Earth's equatorial plane. This motion is shown in the Earth-Centered Inertial (ECI) reference frame in Figure 1.3 and the Earth-Centered Fixed (ECF) reference frame in Figure 15.2.

Figure 15.1 suggests that a GEO satellite's apparent motion in right ascension (RA) is very small. Although inactive, the satellite's orbit will still be nearly geosynchronous, therefore the relative angular velocity in RA between the observer and the satellite will remain low. During a full orbit (approximately 24 hours), the ground track of an inactive GEO satellite will resemble a very thin "Figure 8" pattern oriented along the declination axis. The ground tracks for all four of the selected GEO satellites are shown in Figure 15.3.

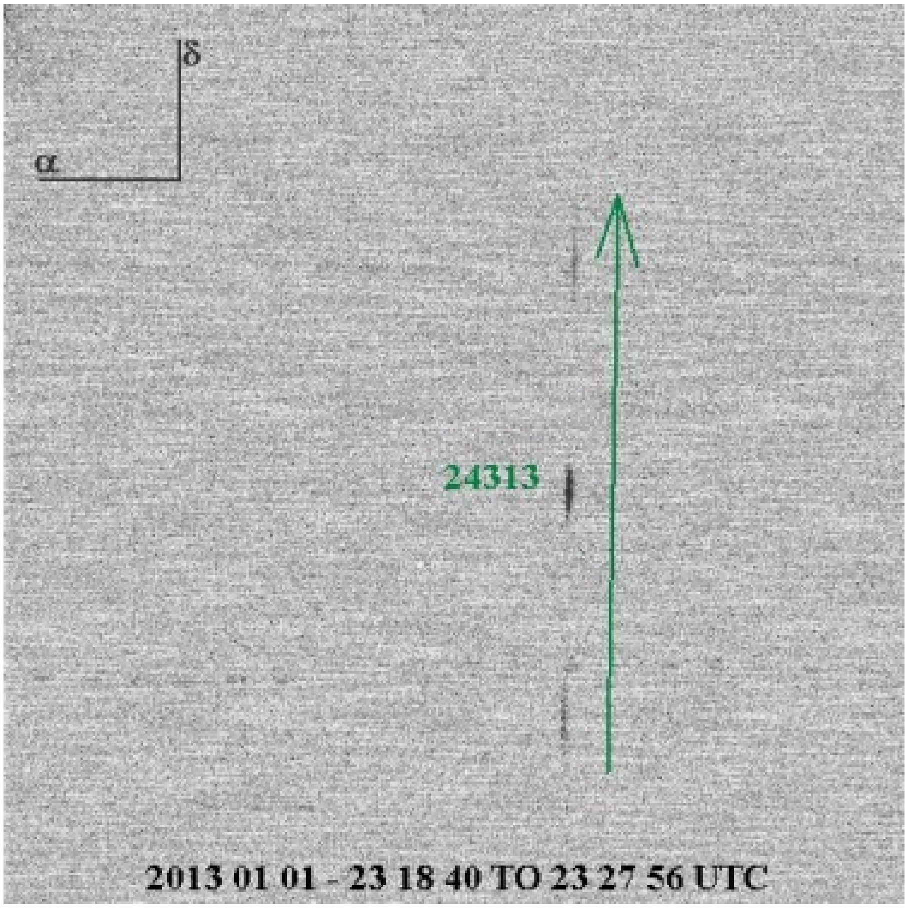

Figure 15.1: Apparent Motion of the Echostar 2 Satellite – January 1, 2013

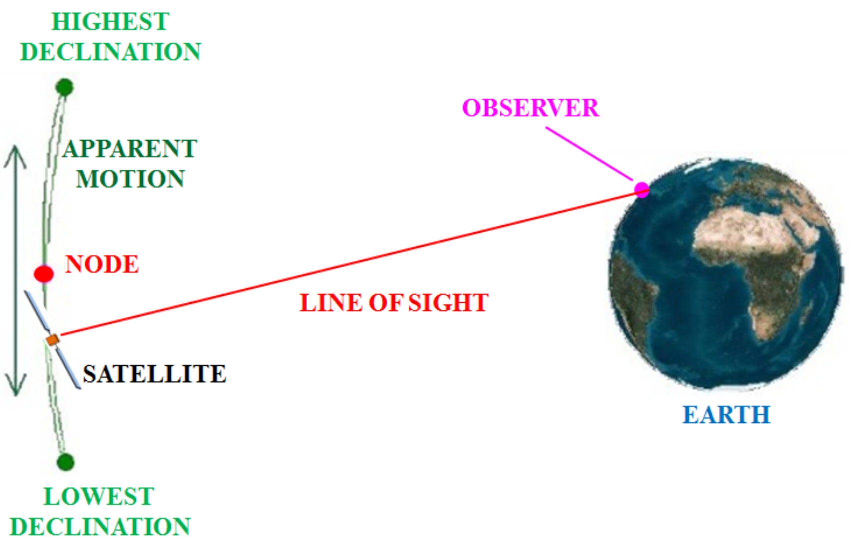

Figure 15.2: Apparent Motion of an Inactive GEO Satellite – ECF Frame[145]

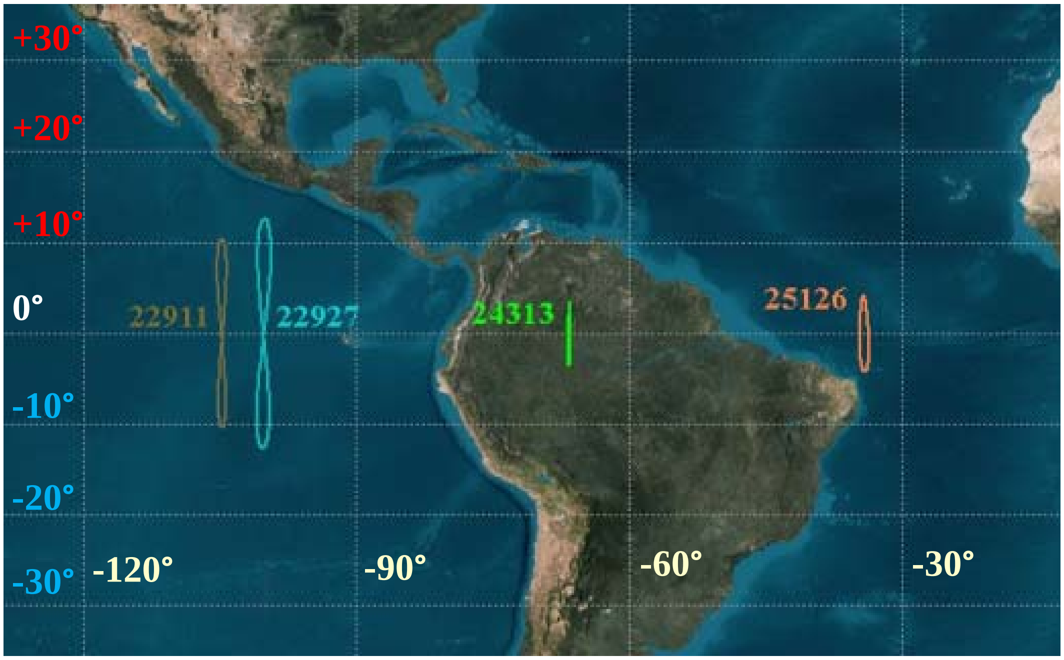

Figure 15.3: Ground Tracks of the Selected Box-Wing GEO Satellites over 24 Hours[146]

The satellite's motion in declination will be at its greatest when the satellite is at either ascending or descending node (Figure 15.2). When the satellite has reached its

---

[145] Analytical Graphics (AGI) – Satellite Tool Kit (STK)
[146] Image created by Analytical Graphics (AGI) – Satellite Tool Kit (STK)

highest or lowest declination (Figure 15.2), it will appear to be stationary in declination but will still have the small apparent motion in RA. The apparent angular velocity of the satellite’s orbit motion when at ascending or descending node will depend upon the inclination of the satellite’s orbit. GEO satellites with lower orbit inclinations (such as Echostar 2) will appear to have lower apparent angular velocities at the nodes than those GEO satellites with higher orbit inclinations (such as Telstar 401).

None of the four selected GEO satellites exhibited a large apparent motion in RA when observed over several hours. The relative motion in RA between the satellite orbit and the observer was thus considered to be negligible. However, this does not mean that the satellites were not actually moving in RA. The relative motion between the observer on a rotating Earth and the geosynchronous satellite orbit motion made the satellite appear to be moving much slower in RA than in Dec.

PHASE ANGLE

The phase angle is that angle at the satellite created by the intersection of the incident sunlight vector and the observer`s line of sight vector. Figure 15.4 shows three specific locations of a GEO satellite in its orbit (S_1, S_2 and S_3) and the phase angles the satellite makes with the incident sunlight and the observer’s location on the Earth (O_1, O_2 and O_3). As the satellite orbits the Earth, this phase angle will change continuously, as illustrated in Figure 15.4. The phase angle of a GEO satellite will compete a full cycle of values in one synodic GEO orbit period (24 solar hours). During a sidereal orbit of the GEO satellite, the Earth will move in its own orbit by approximately 1 degree, thus slightly changing the incident sunlight vector with respect to the Earth and the satellite orbiting it. A similar synodic orbit effect is responsible for the difference between the apparent (synodic) orbit period and the true (sidereal) orbit period of the Moon; 29.531 days and 27.322 days, respectively[147].

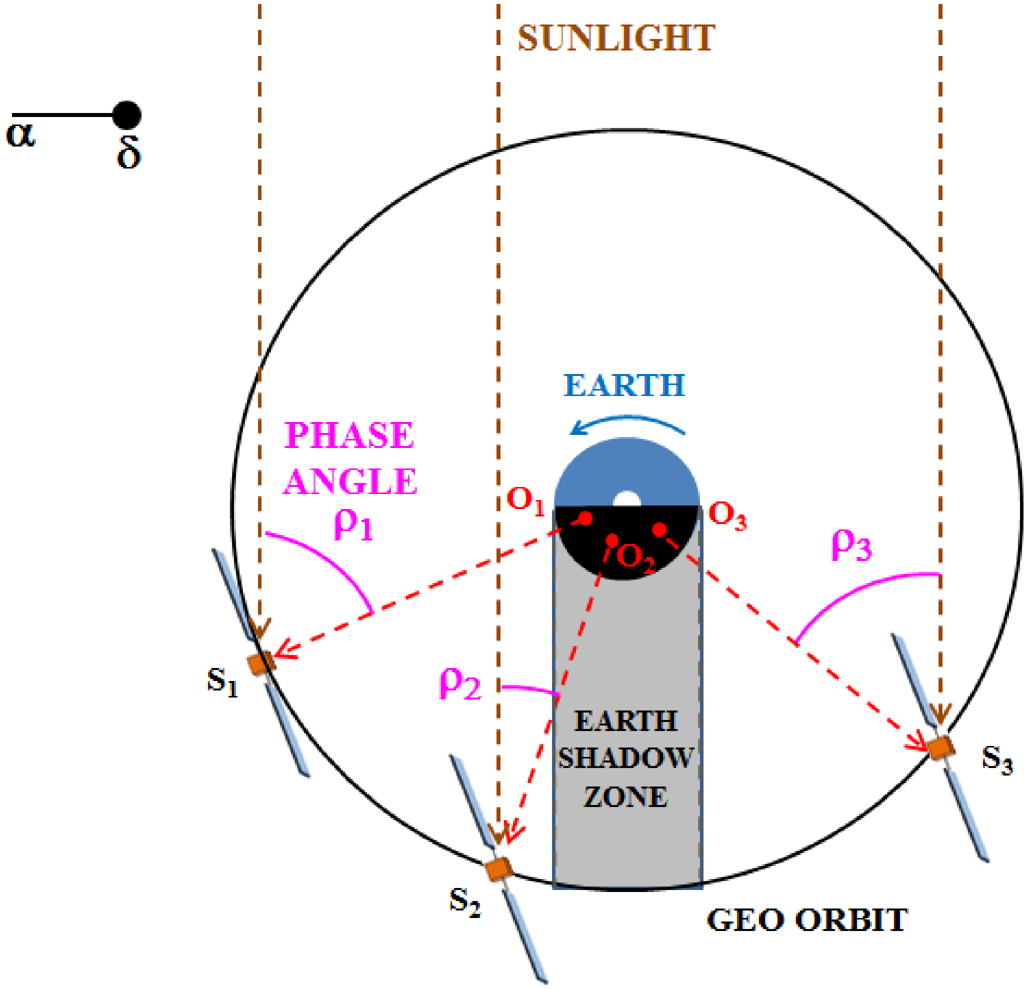

Figure 15.4: The Phase Angles of Three GEO Satellite Locations

A phase angle of 180° indicates that, from the observer's perspective, the satellite is being backlit by the Sun. This phase angle would place the apparent coordinates of the satellite at the location of the Sun's coordinates and therefore the satellite would be silhouetted by the Sun. A phase angle of 0°, with respect to the observer, refers to the

---

[147] Chapman, David M.F. ed.: Observer's Handbook; The Royal Astronomical Society of Canada (RASC); p.25

observer seeing the largest fraction of the sunlit portion of the satellite, unless the satellite is being eclipsed by the Earth. New Moon occurs when the Moon's phase angle is near 180°, Half Moon (also called "Quarter Moon") occurs when the Moon's phase angle is near 90° and Full Moon occurs when the Moon's phase angle is near 0°. A box-wing satellite is not spherical and therefore its apparent phase would appear different for a particular phase angle than would the Moon's phase.

A GEO satellite is not visible when its phase angle is near 0° because the Earth blocks (eclipses) the sunlight to the satellite. When eclipsed, a satellite is nearly undetectable by optical means.

A box-wing satellite's brightness does not necessarily dim as its phase angle increases (like the Moon's brightness would). The many surfaces of a box-wing satellite will reflect sunlight in many different directions and therefore the phase angle of a satellite at its brightest reflection could be any value; unless the satellite is being eclipsed by the Earth.

PHASE ANGLE BISECTOR

The phase angle bisector (PAB) is defined as the line that bisects the phase angle into two equal half-angles, as shown in Figure 15.5. The angle defined by the phase angle bisector (β) is the incident sunlight angle at the time a reflective surface of a satellite is being detected by an observer. If an observer sees a momentary bright sunlight reflection off of a satellite, the incident sunlight angle will be equal to the reflected sunlight angle, as shown in Figure 15.5.

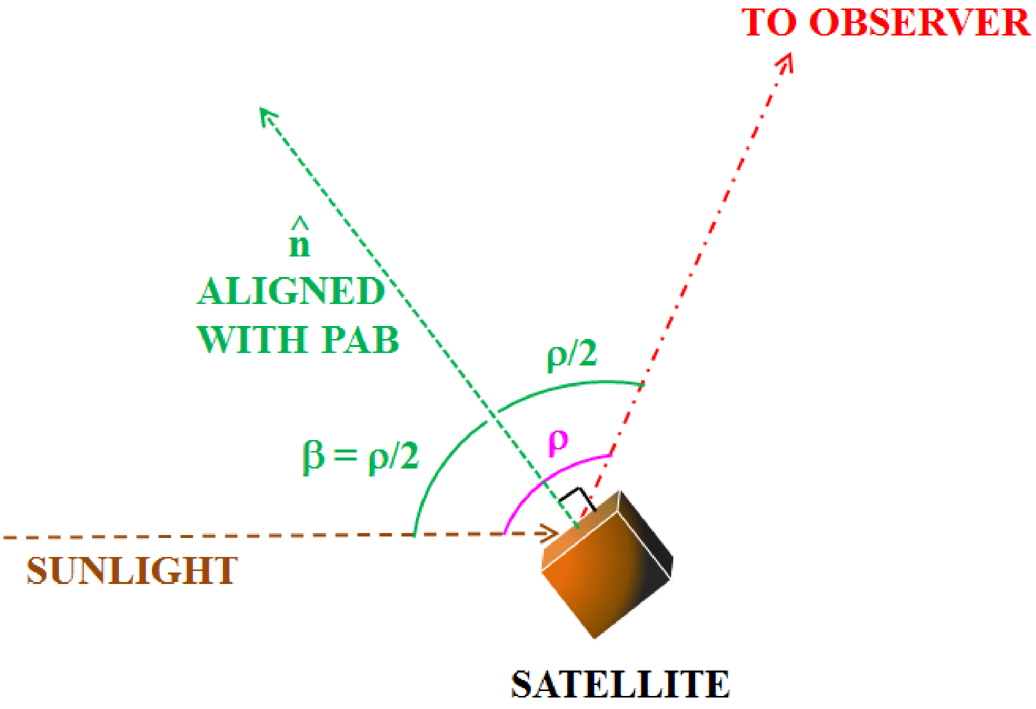

Figure 15.5: A Surface Normal is Aligned to the PAB Causing a Reflection to an Observer

Each unique surface of a spacecraft will have its own surface normal unit vector. An observer would see a reflection from the satellite if one of these surface normal unit vectors were to align itself (or be nearly aligned with) with the PAB.

When a sunlight reflection is detected from any of the four selected GEO box-wing satellites, the phase angle and the phase angle bisector half-angle are known. However, the spin axis is not known and therefore the relationship between the surface normal that is reflecting sunlight and the spin axis is also unknown. This relationship is one of the many satellite characteristics that define its synodic spin period.

FACTORS THAT DEFINE THE SYNODIC SPIN PERIOD

The factors that the synodic spin period depends upon are listed in Table 15.1. Changing any of these factors will change the observed synodic spin period of a satellite.

Table 15.1: The Synodic Period - Dependent Factors

FACTOR	DESCRIPTION	NOTES FOR GEO
Sidereal Spin Period	The true spin period of the satellite	This can be any possible value
Synodic Orbit Period	The orbit period of the satellite with respect to the Sun	A GEO's synodic orbit period is nearly 24 solar hours
Relative Angular Velocity of Orbit	The relative angular velocity of the satellite's orbit motion with respect to the observer (relative motion in the ECF frame)	For GEO, the relative angular velocity in RA is normally very small compared to the relative angular velocity in Dec., except near highest and lowest possible Dec.
Orbit Inclination	The inclination of the satellite's orbit plane with respect to the Earth's equatorial plane (Figure 1.3)	For the majority of GEOs, the orbit inclination is between 0° and 15°
Angle between Spin Axis and Surface Normal Unit Vector	The angle between the satellite's spin axis and the reflecting surface's normal unit vector	This can be any value from 0° to 180°

SYNODIC SPIN PERIOD SCENARIOS

If a GEO satellite's spin axis is static (not precessing) with respect to the ECI reference frame, the observer will see different lighting perspectives of the satellite over its 24-hour synodic orbit period. Therefore, if a satellite's sidereal spin period is zero (it is not spinning), an Earth-bound observer will see a synodic spin period of 24 solar hours. Conversely, if the satellite's sidereal spin period is the same as its sidereal orbit period, it will appear to have no spin at all. A good example of this is the Moon appearing to keep the same face towards us. This happens because its sidereal spin period is the same as its sidereal orbit period.

Box-wing satellites are comprised mainly of planar surfaces, as shown in Figure 1.1. When determining the preliminary boundary conditions for the development of synodic spin period to sidereal spin period transformation equations, a simple rectangular plane was used as a model. This simple plane was imagined to be spinning about some known spin axis and with a known synodic spin period. For simplicity's sake, the plane's spin axis was assumed not to be precessing. The remaining dependent factors were varied in order to study their effects on the synodic spin period. Three scenarios, each having increasing complexity, were studied.

SCENARIO 1: SPIN AXIS ORTHOGONAL TO EQUATORIAL ORBIT PLANE AND SURFACE NORMAL

This scenario involved a satellite spin axis that was orthogonal to both the Earth's equatorial plane and the satellite's surface normal, as shown in Figures 15.6 and 15.7. The satellite was considered to have a geostationary orbit (an inclination of 0°). This meant that any observer on the spinning Earth would see the satellite appear stationary in their local sky (at the same local topocentric coordinates) for the entire orbit period.

Figures 15.6 and 15.7 show the observer's at position O_1 observing the satellite at position S_1 which is reflecting sunlight off of a surface normal to him/her. As the satellite spins, it is also moving in its orbit, thus it is changing its phase angle (ρ). The satellite at position S_2 has completed one full synodic spin period (T_{syn}). The satellite's true anomaly has changed by the angle $\Delta\nu$ in the same amount of time. After one synodic spin period, the observer will see a reflection from the same surface normal. The difference between the synodic and sidereal spin angles is the synodic angle offset (χ). The value of χ could be negative or positive, depending on the orientation of the spin axis. The phase angle bisector angle β_2 between the new location of the satellite (S_2) and the Sun must be one half the new phase angle ρ_2 of the satellite when the reflection is once again observed.

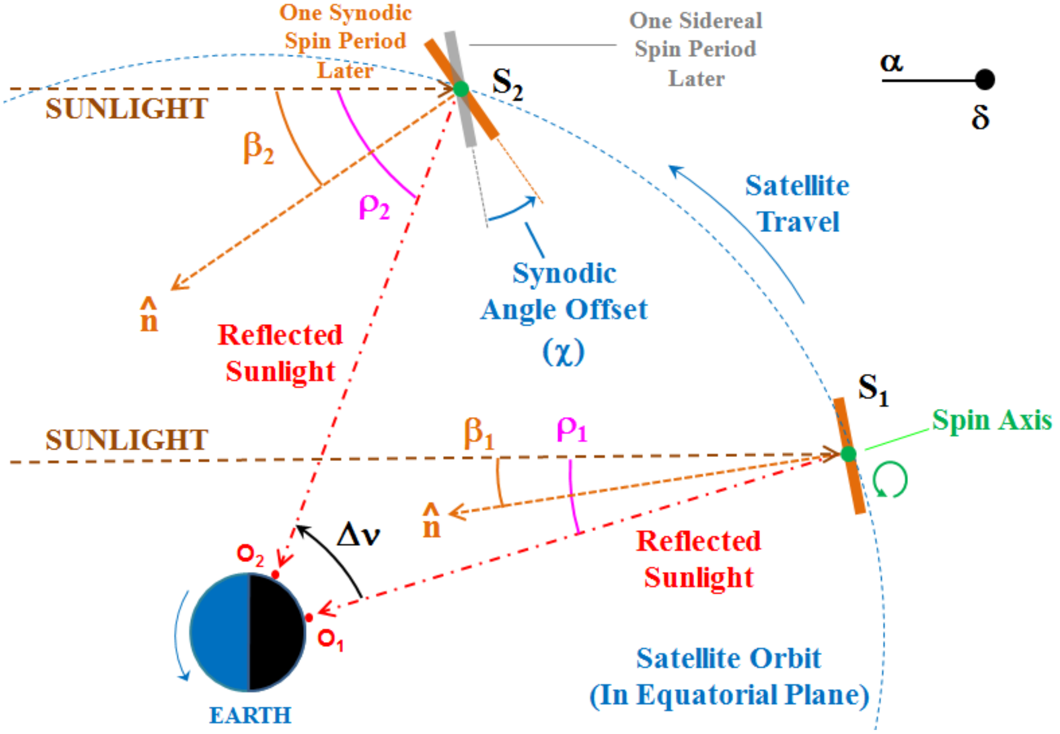

Figure 15.6: Illustration of the Synodic Period for Scenario 1 – Orbit Face-on

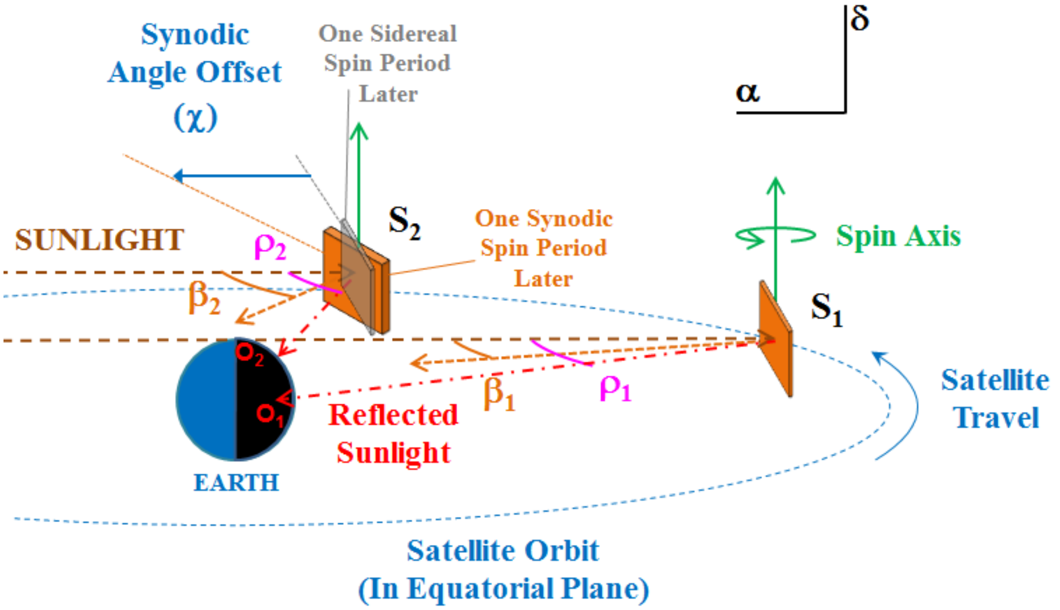

Figure 15.7: Illustration of the Synodic Period for Scenario 1 - Orbit Nearly Edge-on

During one synodic spin period, the satellite’s surface normal will rotate by a sidereal spin angle which will not correspond to one sidereal spin period. The synodic angle offset (χ) is the difference between the sidereal and synodic angular positions, shown in Figures 15.6 and 15.7. In this scenario, χ is also the difference of the two phase angle bisector angles, as shown in Eq. 15.1.

Eq. 15.1

$$\boldsymbol{\chi = \beta_2 - \beta_1}$$

Since the phase angle bisector angle β is one half of the phase angle ρ, Eq. 15.1 can be rewritten as shown in Eq. 15.2.

Eq. 15.2

$$\boldsymbol{\chi = \frac{\rho_2 - \rho_1}{2}}$$

Eq. 15.2 is only valid for this specific scenario and cannot be used for the general treatment of the problem. This scenario can be used to test a general solution using the specific criteria listed in Table 15.2.

Since the orbit plane is coincident with the equatorial plane in this scenario, the satellite's phase angle ρ will change at the same rate as the satellite's true anomaly ν, as shown in Eq. 15.3. Therefore, the synodic angle offset can also be expressed by Eq. 15.4.

Eq. 15.3

$$\boldsymbol{\rho_2 - \rho_1 = \nu_2 - \nu_1 = \Delta\nu}$$

Eq. 15.4

$$\boldsymbol{\chi = \frac{\Delta\nu}{2}}$$

The time elapsed between the satellite locations S_1 and S_2 in Figures 15.6 and 15.7 is the observed synodic spin period (T_{syn}). Since the majority of GEO orbits can be considered nearly circular, the orbit angle ($\Delta\nu$) travelled by the satellite from location S_1 to S_2 can be expressed as a fraction of the synodic GEO orbit period (T_{orb}) travelled over the synodic spin period (Eq. 15.5).

Eq. 15.5

$$\boldsymbol{\Delta\nu = 2\pi\left(\frac{T_{syn}}{T_{orb}}\right)}$$

Therefore, the equation for the synodic offset angle χ can also be expressed by Eq. 15.6.

Eq. 15.6

$$\boldsymbol{\chi = \pi\left(\frac{T_{syn}}{T_{orb}}\right)}$$

The time that the satellite would need to spin to travel the synodic angle offset χ can be expressed as a fraction of its sidereal spin period T_{side}, as shown in Eq. 15.7. The synodic time offset Δt_{spin} is the time required for the satellite to spin the synodic angle offset χ. Note that this travel time can be negative if the satellite spin axis vector is pointing to the South Celestial Pole (SCP), hence the "±" in Eq. 15.7 and onward for this scenario.

Eq. 15.7

$$\boldsymbol{\Delta t_{spin} = T_{syn} - T_{side} = \pm\left(\frac{\chi}{2\pi}\right)T_{side}}$$

Substituting Eq. 15.6 into Eq. 15.7 yields the solution of the sidereal spin period T_{side}, as shown in Eq. 15.8. This equation is very similar to the synodic orbit equation used to find the sidereal orbit periods of solar system objects observed from the Earth.

Eq. 15.8

$$\mathbf{T_{side}} = \left[\frac{\mathbf{1}}{\mathbf{T_{syn}}} \pm \frac{\mathbf{1}}{\mathbf{2T_{orb}}}\right]^{-\mathbf{1}}$$

Figure 15.8 shows a plot of the absolute value of the synodic time offset ($|\Delta t_{spin}|$) vs. the synodic spin period for an equatorial GEO satellite with a synodic spin period between 0 and 2000 seconds. The synodic offset of all four selected GEO box-wing satellites are included, with the assumption they had spin axes orthogonal to the equatorial plane of the Earth.

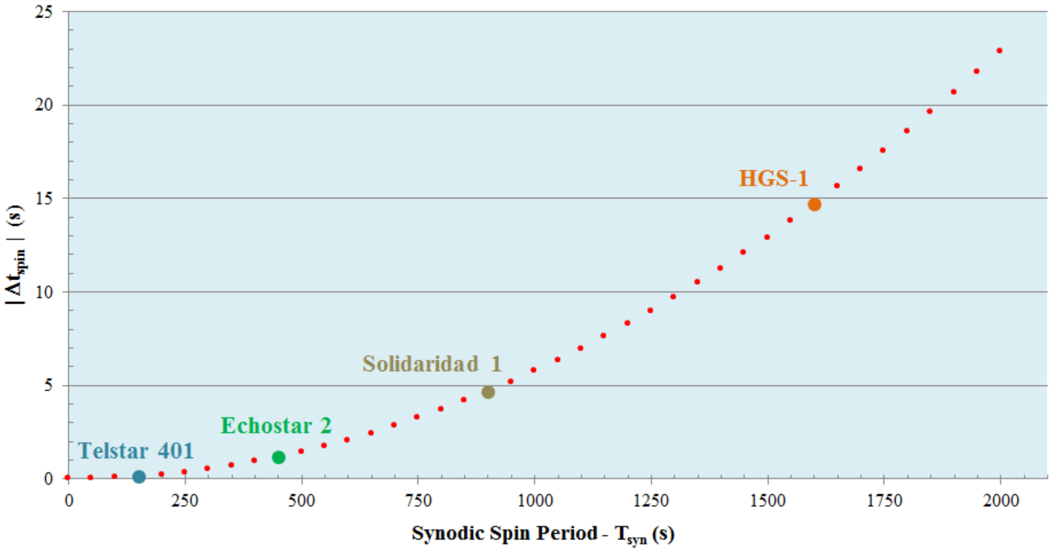

Figure 15.8: Synodic Time Offset vs. Synodic Spin Period for Scenario 1

Figure 15.8 suggests that the difference between the sidereal and synodic spin periods for both Telstar 401 and Echostar 2 would be very low if their spin and orbit characteristics were similar to those listed in Table 15.2. This suggests that this scenario cannot account for the entire spin period discrepancy between the theoretical and observed spin period variations shown in Figures 14.12 and 14.13. It is currently unknown whether this synodic model can adequately explain eventual estimations of Solidaridad 1's and HGS-1's spin period deviations.

SCENARIO 2: SPIN AXIS ORTHOGONAL TO EQUATORIAL ORBIT PLANE AND VARIABLE SURFACE NORMAL

Scenario 1 had described the apparent synodic motion of a box-wing satellite with a spin axis that was nearly orthogonal to its orbit plane, with the observer seeing reflections from surfaces with normal that were nearly orthogonal to that spin axis. This might not have been the case for any of the selected satellites at any time of observation.

The only difference between Scenario 2 and Scenario 1 is that the surface normal is not necessarily orthogonal to the spin axis, as shown in Figure 15.9. Scenario 2 can be considered a generalization of Scenario 1 in which the angle η between the surface normal and the spin axis is not necessarily 90°.

In Scenario 1, the angle that the surface normal unit vector sweeps out as the satellite spins is the same as the angle the satellite spins about its spin axis. However, when the surface normal unit vector is not orthogonal to the spin axis, the angle that the surface normal vector sweeps out in some time will be different than the angle the satellite spins about the spin axis. This will affect the observed synodic spin period.

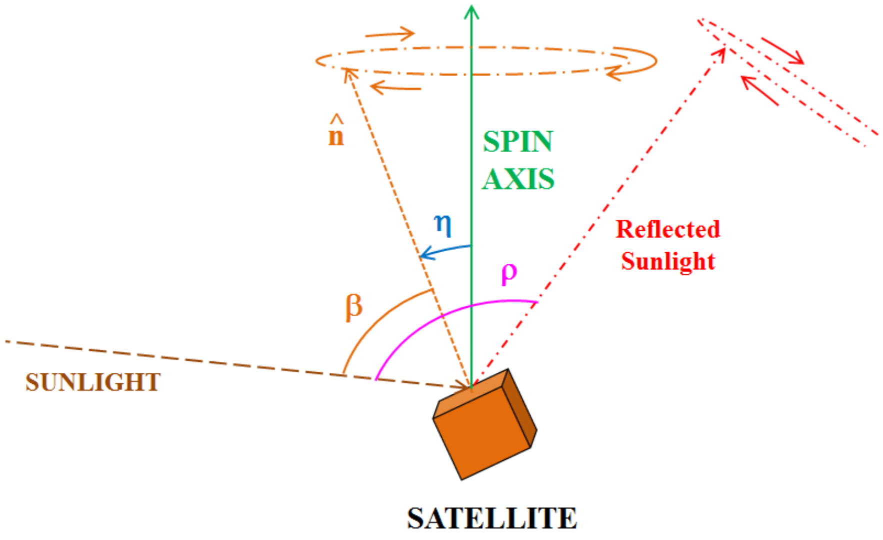

Figure 15.9: Orientation of Surface Normal to Spin Axis for Scenario 2

Observed from the surface of the Earth, the stars in the sky appear to trace out a complete circle, centered at the Earth's spin axis, every sidereal day. The stars near the celestial equator will appear to trace out the largest circles and the stars near the celestial poles (NCP and SCP) will appear to trace out the smallest circles. A several-hour exposure image of stars near the NCP is shown in Figure 15.10. The stars closest to the NCP appear to have the smallest trails over the exposure time. Figure 15.10 shows that the apparent size of a star trail depends on the angle the star is from the NCP, i.e. its declination coordinate.

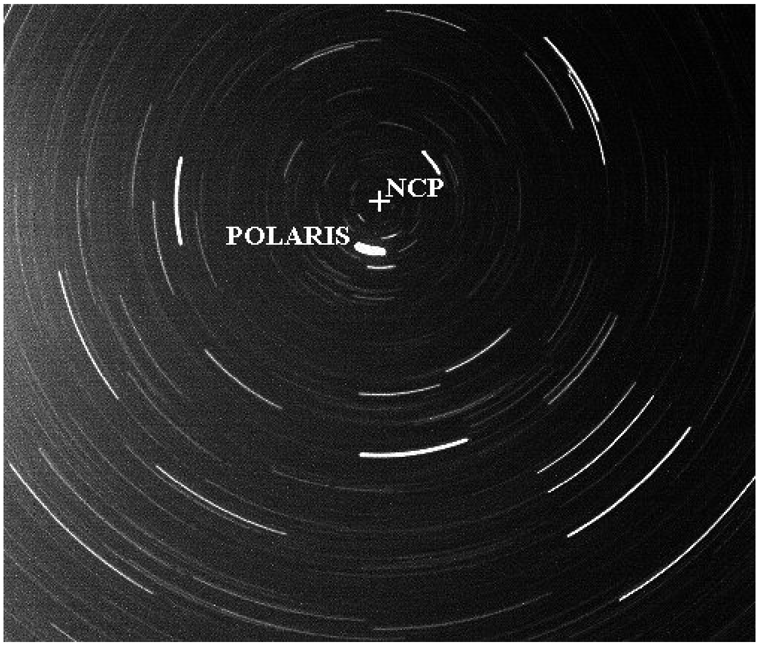

Figure 15.10: Time Exposure of Stars near the NCP

The relationship between the apparent angular velocity of a star and its declination can be derived using spherical trigonometry. When determining the angle between two points on the celestial sphere (γ), Eq. 15.9 is used, where μ is the difference in the right ascension coordinate of the two points and δ_1 and δ_2 are the two declination coordinates of the two points.

Eq. 15.9 [148]

$$\cos(\gamma) = \cos(90-\delta_1)\cos(90-\delta_2) + \sin(90-\delta_1)\sin(90-\delta_2)\cos(\mu)$$

If the two declination coordinates are the same, as is the case for a single star appearing to move in the sky over time, Eq. 15.9 simplifies to Eq. 15.10.

Eq. 15.10

$$\cos(\gamma) = \cos^2(90-\delta) + \sin^2(90-\delta)\cos(\mu)$$

---

[148] Green, R.M.; Spherical Astronomy; pp. 8-9

Eq. 15.10 shows that the apparent angular travel of each star (γ) will depend on the sidereal angle that the Earth has spun (the quantity μ) and the star's specific declination (δ). This is illustrated in Figure 15.11.

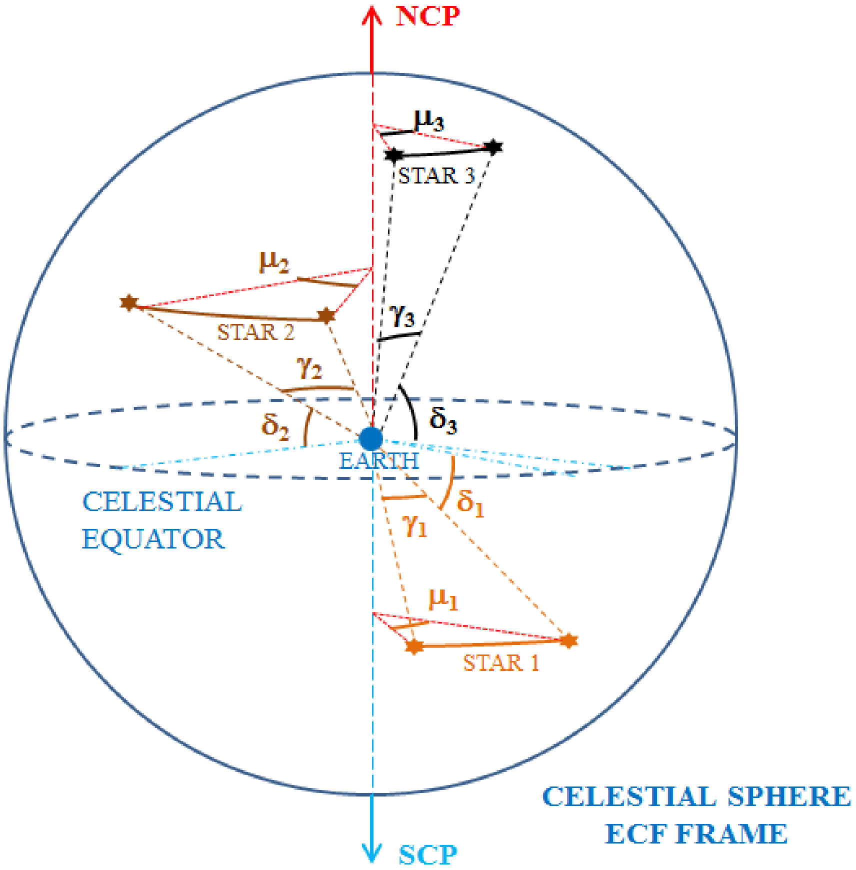

Figure 15.11: Apparent Star Trail Angle Dependence on the Declination Coordinate

The sidereal angular velocity of the Earth (ω_{Earth}) is the sidereal angle the Earth has spun over some specific elapsed time. Therefore, Eq. 15.10 can be simplified to show a relationship between the apparent angular velocity of a star ($\omega_{apparent}$) and the sidereal angular velocity of the Earth (Eq. 15.11). Note that if the declination of a star is 0°, i.e. on the celestial equator, the apparent angular velocity of that star is equal to the Earth's sidereal angular velocity.

Eq. 15.11

$$\cos(\omega_{\text{apparent}}) = \cos^2(90-\delta) + \sin^2(90-\delta)\cos(\omega_{\text{Earth}})$$

Table 15.4 lists several examples of the difference between the sidereal angular velocity of the Earth and the apparent angular velocity of some of the brightest naked eye stars with different declinations from each other. The sidereal spin angular velocity of the Earth (ω_{Earth}) is 15°.041 per hour.

Table 15.2: The Apparent Angular Velocities of Several Naked Eye Stars

STAR	J2000 DECLINATION (°)[149]	APPARENT ANGULAR VELOCITY (°·hr^{-1})
Polaris	+89.325	0.177
Kochab	+74.096	4.111
Thuban	+64.307	6.506
Capella	+46.011	10.431
Castor	+31.856	12.765
Regulus	+11.899	14.716
Procyon	+5.187	14.979
Mintaka	-0.293	15.041
Sirius	-16.739	14.400
Canopus	-52.708	9.096
Acrux	-63.169	6.773
Sigma Octantis	-88.903	0.287

Consider a spinning spherical object with four coloured plates glued onto its surface at four different "latitudes", as illustrated in Figure 15.12. An observer will see the plates moving at four different angular rates as the object spins. Although all four plates will complete an angle of 2π radians with every full spin, each of their angular velocities will appear different to the observer. The equatorial plate will be seen to move with the fastest angular velocity, while the polar plate will not be perceived to be moving at all.

---

[149] Chapman, David M.F. ed.: "Observer's Handbook"; The Royal Astronomical Society of Canada (RASC); pp. 274-282

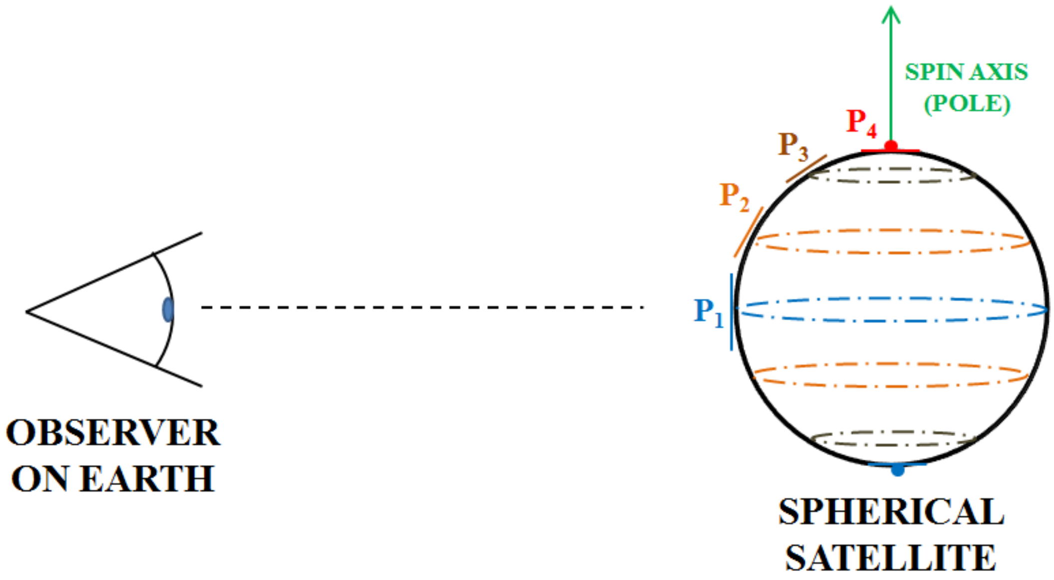

Figure 15.12: Observing Points at Different Latitudes on a Spinning Spherical Satellite

The spin axis of the spherical LAGEOS 2 satellite (introduced in Chapter 2) was determined by measuring the time between each reflection from adjacent retro-reflectors. The retro-reflectors that were nearer the spin axis (pole) would appear to have a lower angular velocity than those that were nearer the "equator".

Incident sunlight would "see" the same apparent angular velocities of the different "latitudes" of the spherical satellite. Consider an observer on the Earth observing a GEO satellite reflecting sunlight at some initial time t_1. If the observer observes the same satellite reflecting sunlight from the same surface normal at time t_2, the time elapsed between t_1 and t_2 is the satellite's synodic spin period T_{syn}. Since the spin axis is in the direction of the NCP (or SCP), the satellite's orbit motion will be in the same plane as that plane traced out by the surface normal over a sidereal spin period, as illustrated in Figure 15.13.

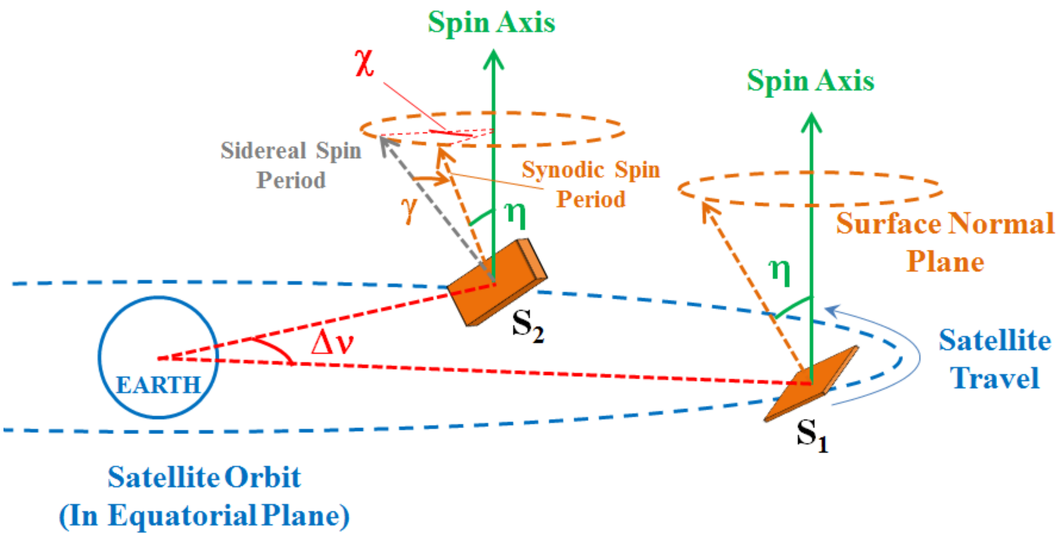

Figure 15.13: Illustration of the Synodic Period for Scenario 2

The synodic angle offset (χ) is the component of the sidereal spin angle that compensates for the orbit motion of the satellite. In this scenario, the observer will be seeing the satellite's apparent spin angular velocity and not its real sidereal spin angular velocity. The apparent spin angle (γ) difference between a sidereal and synodic spin period is determined in Eq. 15.12.

Eq. 15.12

$$\boldsymbol{\gamma = \pi \left(\frac{T_{syn}}{T_{orbit}}\right)}$$

Eq. 15.12 only describes the apparent synodic offset angle and not the real one (sidereal). The satellite will have to spin some synodic offset angle (χ) in order to cover the apparent spin angle difference (γ). The synodic offset angle (χ) is related to the apparent spin angle difference (γ) by Eq. 15.13. This equation is similar to Eq. 15.11

except that the variables have been changed to correspond to a spinning satellite rather than a spinning Earth.

Eq. 15.13

$$\cos(\gamma) = \cos^2(\eta) + \sin^2(\eta)\cos(\chi)$$

The synodic offset angle χ can therefore be determined by inverting and rearranging Eq. 15.13, as shown in Eq. 15.14.

Eq. 15.14

$$\cos(\chi) = 1 + \frac{\cos(\gamma) - 1}{\sin^2(\eta)}$$

The difference between the synodic and sidereal spin periods can be described by the time required for the satellite to spin at its sidereal rate over the angle χ, as shown in Eq. 15.15.

Eq. 15.15

$$T_{syn} - T_{side} = \pm\left(\frac{\chi}{2\pi}\right)T_{side}$$

Finally, the sidereal spin period of the satellite in Scenario 2 can be determined by using Eq. 15.16. Note that if η is 90°, this equation simplifies to Eq. 15.8 in Scenario 1. Similar to Scenario 1, the "±" is used for the direction of the orthogonal spin axis; "+" for the spin axis directed to the NCP and "-" for the spin axis directed to the SCP.

Eq. 15.16

$$T_{side} = \frac{T_{syn}}{1 \pm \frac{1}{2\pi}\cos^{-1}\left\{1 + \frac{\cos\left[\pi\left(\frac{T_{syn}}{T_{orb}}\right)\right] - 1}{\sin^2\eta}\right\}}$$

If the angle η is equal to 0, the spin axis and the surface normal are coincident and Eq. 15.16 is undefined. This is because no angle χ can compensate for any orbit motion of the satellite when the surface normal unit vector is coincident with the spin axis. If η is equal to 90°, Eq. 16 simplifies to Eq. 15.8 (Scenario 1).

A plot of the synodic time difference ($|\Delta t_{spin}|$) and the synodic period (T_{syn}) for several values of η is shown in Figure 15.14.

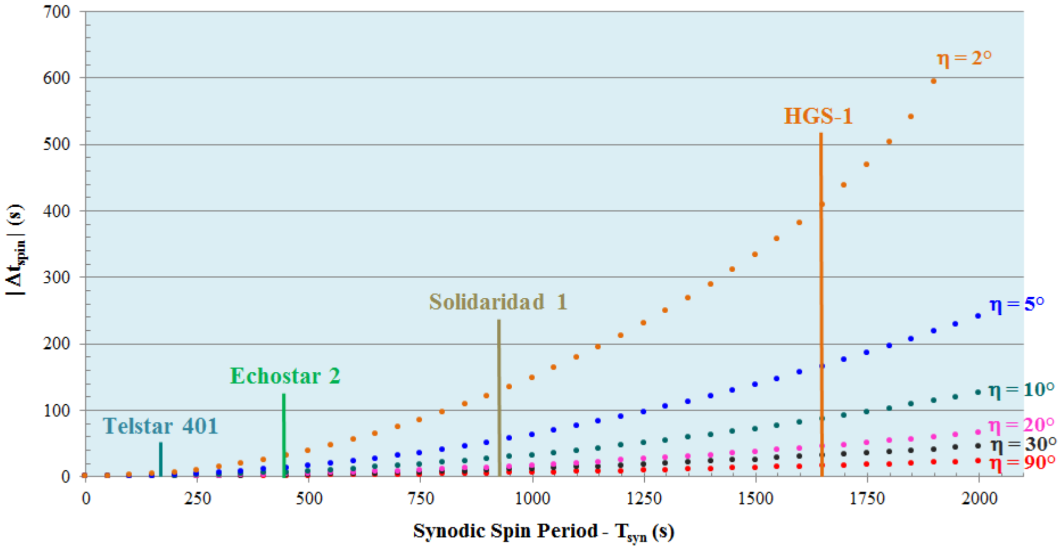

Figure 15.14: Synodic Offset vs. Synodic Spin Period for Various Surface Normal Angles

The plot shown in Figure 15.14 is significant because it shows that the absolute time difference between the sidereal and synodic spin periods heavily depends on the sidereal spin period of the satellite and the angle η between the surface normal and the spin axis. Note the very small range of time for Telstar 401 (less than 20 seconds) and the very large range of time for HGS-1 (over 400 seconds). The synodic spin periods of these two satellites differ by less than 30 minutes.

SCENARIO 3: INCLINED SPIN AXIS AND SURFACE NORMAL

In Scenario 1 and Scenario 2 the spin axis was always orthogonal to the equatorial plane. In reality, the spin axis can be in any orientation and will most likely be precessing. Scenario 3 represents the most general synodic effect case presented in this thesis.

For this scenario, the orientation of the plane traced out by the surface normal as it revolves about the spin axis is not necessarily parallel to the equatorial plane, as shown in Figure 15.15. This means that as the satellite orbits the Earth, the change in the phase angle will only affect that component of the surface normal plane that is parallel to the equatorial plane. Determining this component requires a coordinate transformation between the equatorial plane and the surface normal plane.

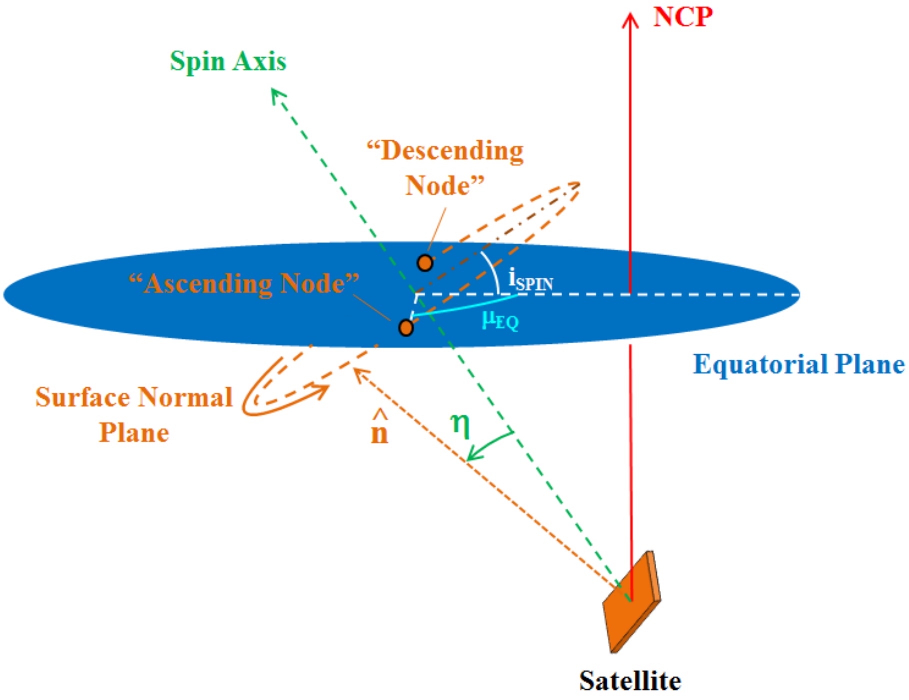

Figure 15.15: Satellite Spin and Surface Normal Orientations for Scenario 3

The surface normal plane is inclined to the equatorial plane because the spin axis is tilted at an angle (i_{spin}) with respect to the NCP. As the satellite spins, the created surface normal plane slices into the equatorial plane twice, creating two nodes. These nodes are euphemistically called the “Ascending Node” and the “Descending Node”, as shown in Figure 15.15.

The motion of the satellite in its orbit will change the phase angle of the satellite, as in the previous scenarios. The apparent spin angle γ forms a spherical triangle with two equatorial angles: one parallel to the celestial equator (μ_{EQ}) and the other perpendicular to the celestial equator (δ_{EQ}), as shown in Figure 15.16. In this scenario, only the μ_{EQ} component can compensate for the orbit motion of the satellite. The change in this component is shown in Eq. 15.18.

Eq. 15.18

$$\Delta\mu_{EQ} = \pi \left(\frac{T_{syn}}{T_{orbit}}\right)$$

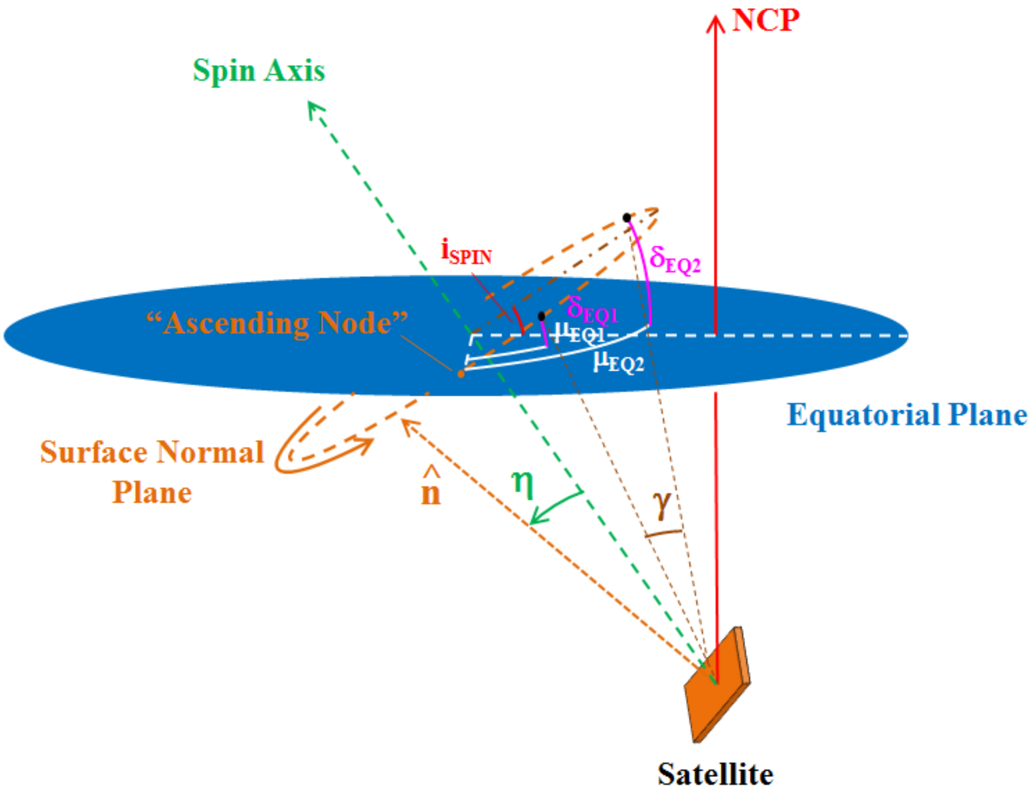

Figure 15.16: Spherical Triangle Formed by the Spin Angle γ and Equatorial Coordinates

The equatorial angle that is perpendicular to the celestial equator (δ_{EQ}) can be expressed as a function of the parallel component (μ_{EQ}), as shown in Eq. 15.19. The variable "i" refers to the two positions of the surface normal unit vector that define the synodic offset angle. The value of μ_{EQ} is the angle measured within the equatorial plane from the "Ascending Node" to the position of the surface normal unit vector.

Eq. 15.19 [150]

$$\boldsymbol{\delta_{EQi} = \pm \cos^{-1}\left[\frac{\cos(i_{SPIN})}{\sqrt{1-\cos^2(\mu_{EQi})\sin^2(i_{SPIN})}}\right] \quad i = 1, 2}$$

---

[150] See Appendix B: Derivations

Eq. 15.19 Conditions

$$\boldsymbol{\delta_{EQi} > 0 \text{ when } 0 < \mu_{EQi} < \pi}$$

$$\boldsymbol{\delta_{EQi} < 0 \text{ when } \pi < \mu_{EQi} < 2\pi}$$

The apparent spin angle (γ) required to change the parallel equatorial component to compensate for the change in the phase angle change can then be found using Eq. 15.20.

Eq. 15.20

$$\boldsymbol{\cos(\gamma) = \sin(\delta_{EQ1})\sin(\delta_{EQ2}) + \cos(\delta_{EQ1})\cos(\delta_{EQ2})\cos(\Delta\mu_{EQ})}$$

The synodic angle offset χ that is required to change γ by the required amount is found by using Eq. 15.21.

Eq. 15.21

$$\boldsymbol{\cos(\chi) = 1 + \frac{\cos(\gamma) - 1}{\sin^2(\eta)}}$$

Once χ is known, the sidereal spin period can be found with Eq. 15.22.

Eq. 15.22

$$\boldsymbol{T_{side} = \frac{T_{syn}}{1 \pm \frac{\chi}{2\pi}}}$$

The "±" in Eq. 15.22 denotes the direction of the spin axis. The spin axis unit vector can have two distinct directions, each the opposite of the other.

The orientation of the surface normal plane with respect to the equatorial plane is required to determine the apparent spin angle γ. This is because the δ_{EQ} component of γ does not change uniformly with the change in the μ_{EQ} component of γ over the satellite's spin.

If the spin axis is orthogonal to the equatorial plane, i_{SPIN} is 0 and Eq. 15.19 states that δ_{EQ} is 0 no matter what the value of μ_{EQ}, i.e. always in the equatorial plane. In this case, Eq. 20 states that γ is equal to μ_{EQ}. This is the case in Scenario 2.

If the spin axis is within the equatorial plane, i_{SPIN} is 90° and Eq. 15.19 states that δ_{EQ} is 90° (or 270°) no matter what the value of μ_{EQ}, i.e. always perpendicular to the equatorial plane. In this case, Eq. 15.20 states that γ is equal to 0 at all times during the satellite spin. This means that the synodic offset angle χ is also 0 (Eq. 15.21). This ultimately means that the sidereal spin period of the satellite will be the same as the synodic spin period no matter what the value of η is. Therefore, if i_{SPIN} is 90°, the motion of the satellite spin will be independent of the motion of the satellite and the synodic and sidereal spin periods will be identical for all values of η.

Because Scenario 3 can also result in very high synodic effects when the η angle is very low, this method has the same potential to explain the spin period discrepancy amplitudes as Scenario 2. However, this scenario would more likely be able to explain the variations of these discrepancies, assuming that the simple SRP torque model fully explains the external forces acting on the satellites, because the orientation of the spin axis can be varied relative to the surface normal and to the equatorial plane.

Scenario 3 is offered here as an initial hypothesis of the apparent motion of a box-wing GEO satellite. The observations of the four satellites are not sufficient to determine the unknowns (spin axis orientation, surface normal orientation and surface normal plane orientation) that are required to accurately determine the satellites' sidereal spin periods at all times. However, future observations of these four satellites might be used to determine all of these spin dynamics variables.

CHAPTER 16: SUMMARY AND CONCLUSIONS

SUMMARY

Specific criteria were used to select several inactive box-wing GEO satellites for this research, including their accessibility from the observation site from March 2012 to March 2013. Four satellites were selected for study: Solidaridad 1 (#22911), Telstar 401 (#22927), Echostar 2 (#24311) and HGS-1 (#25126).

Light curves for the four selected satellites were obtained from frequent ground-based observations (at least one observation every 1-2 weeks, weather permitting) from March 5, 2012 to March 31, 2013. Image data (time tag and satellite flux) extraction was performed using a MATLAB code created by the author specifically for this thesis research. The light curves were used to determine the satellites' apparent (synodic) spin periods over the one-year time frame. The apparent spin periods of each satellite appeared to vary with time. The spin period variations of Telstar 401, Echostar 2 and HGS-1 each appeared to have a cyclical behaviour. The period of this apparent spin period variation was estimated for Telstar 401, Echostar 2 and HGS-1. Additional observations are required to determine if Solidaridad 1's apparent spin period variation is cyclical or not.

The characteristics of each selected satellite were researched in order to determine the total moment of inertia (MOI) for three specific spin axes. These MOIs were used to determine the apparent maximum spin torque which was incident on each satellite over the one-year time frame.

A comparison was made of the four largest disrupting forces that could have affected the satellites' attitudes. These disrupting forces were; aerodynamic, magnetic, gravity-gradient and solar radiation pressure (SRP). This comparison was performed to determine which of these forces could supply the maximum observed spin torque estimated for each satellite.

Once the largest disrupting force had been identified, theoretical angular acceleration curves, based on differing solar incidence angles on the satellites' solar panels, were plotted for Telstar 401 and Echostar 2. Their theoretical curves were then fitted to the observations by making assumptions, which included the average value of a satellite solar panel's reflectivity coefficient and the value of Telstar 401's and Echostar 2's spin period variation period. The curve fitting process revealed an estimate of the canting angle between Telstar 401's two solar panels and between Echostar 2's two solar panels.

The theoretical angular acceleration curves were used to produce theoretical spin period plots that would be used to compare the apparent spin period variations to the theoretical spin period variations. In order to reveal any residual cyclical or secular effects, the difference between the theoretical spin periods and the apparent (observed) spin periods over the one-year time frame were plotted. These differences were collectively known as "spin period discrepancy".

In order to determine if synodic effects could explain the spin period discrepancy, a preliminary investigation into the synodic (apparent) spin period to sidereal (apparent) spin period transformation was conducted. Three scenarios were investigated:

- Scenario 1 investigated the synodic effect of a satellite with a spin axis perpendicular to the equatorial plane and a reflecting surface normal that was always orthogonal to the spin axis;

- Scenario 2 investigated the synodic effect of a satellite with a spin axis perpendicular to the equatorial plane and a reflecting surface normal that was at any angle with respect to the spin axis; and
- Scenario 3 investigated the synodic effect of a satellite with a spin axis oriented at any angle with respect to the equatorial plane and a reflecting surface normal that was at any angle with respect to the spin axis.

In order to determine if synodic effects could cause the maximum discrepancy, these theoretical synodic effects were compared with the maximum discrepancy between the theoretical spin periods and the observed spin periods. The synodic effects estimated using synodic Scenario 1 were too small to explain the spin period discrepancy. The synodic effects of synodic Scenarios 2 and 3 were more than adequate to explain the maximum amplitudes of the spin period deviations, however further investigation may reveal if synodic effects can account for all variations in the spin period deviation.

CONCLUSIONS

Of the nearly 1,200 GEO satellites currently in orbit, 4 inactive box-wing GEO satellites were chosen for study: Solidaridad 1 (#22911), Telstar 401 (#22927), Echostar 2 (#24313) and HGS-1 (#25126). Observations of each of these GEO satellites revealed that they were spinning with a period that could be reliably measured by determining the elapsed time between recurring light curve characteristics.

Each satellite’s apparent spin period appeared to vary over time, suggesting that the satellites were being influenced by external force(s). Forces internal to the satellites (such as reaction wheels) were not considered because the power systems of the four satellites had either been intentionally shut down (in the case of HGS-1), or had suffered a serious electrical malfunction (in the cases of the Solidaridad 1, Telstar 401 and Echostar 2).

Solidaridad 1 was observed to have had an apparent spin period that appeared to decrease from 968 seconds to 784 seconds. Telstar 401 was observed to have had an apparent spin period that appeared to cyclically vary between 145 seconds and 170 seconds with a period of 290 days. Echostar 2 was observed to have had an apparent spin period that appeared to cyclically vary between 375 seconds and 532 seconds with a period of 364 days. HGS-1 was observed to have had an apparent spin period (that may or may not be cyclical) with a maximum of 1847 seconds and a minimum of 1249 seconds.

The most likely source of external torque on all four satellites was determined to be solar radiation pressure (SRP). At the outset, gravity-gradient looked to be a likely source of external torque. However, since gravity-gradient is a stabilizing torque, it is less likely that this torque would cause the large variations in spin period that were observed.

Theoretical curves of Telstar 401's and Echostar 2's angular accelerations that were due to SRP, revealed a sudden deviation between the ideal SRP model and the observed angular acceleration. This deviation suggested that synodic effects were affecting the apparent angular acceleration of the spacecraft and/or that the SRP model was not robust enough to accurately model the satellite's dynamics.

The deviation between the theoretical sidereal spin period and the observed synodic spin period with respect to Telstar 401 and Echostar 2 appeared to be periodic. These deviations could be the result of synodic and/or additional SRP effects on other satellite components (such as the communications dishes); however other external forces cannot be ruled out in general.

The synodic effect described in Scenario 3 can produce a synodic offset that is the same or greater than the spin period deviations observed for Telstar 401 and Echostar 2. The spin period deviation of Telstar 401 was much smaller than the spin period deviation of Echostar 2 by a ratio of approximately 10-to-1. This could be the result of the synodic effect being much smaller for Telstar 401 because of its lower spin period. However, this could be a coincidence and this difference in spin period deviation does not necessarily mean that the synodic effect is the direct cause. Therefore, additional observations of these and other box-wing GEO satellites and better modelling of the SRP and synodic effects are required to isolate the cause(s) of this spin period deviation.

If this thesis represents the first attempt at explaining the causes of spin period variations of inactive box-wing GEO telecommunications satellites, then additional observations and further work will be necessary to confirm these findings and improve the concepts presented herein.

CHAPTER 17: DISCUSSION, FUTURE WORK AND RECOMMENDATIONS

DISCUSSION

The research covered in the literature review (Chapter 2) represented a several-month search for information concerning long-period high-resolution determination of apparent spin period trends for inactive box-wing GEO satellites. As Papushev et al. had noted, the accessible academic literature contained very little that showed in-depth investigation of these apparent spin periods. This thesis is one of the few efforts undertaken to investigate the long-term apparent spin period variation of a small percentage of the total inactive box-wing GEO satellite population.

Literature that contains satellite characterization research goes into great detail with respect to matching reflection signatures (acquired with images of the satellites in U, V, B and/or I filters) with their possible reflecting surfaces. However, much of this literature does not mention long-term high-resolution observation, except in the case of SLR and optical observations of LAGEOS 2. However, LAGEOS 2 is not a box-wing GEO satellite. The research presented in this thesis could motivate others to observe a larger percentage of the inactive GEO box-wing satellite population at larger time scales and with a higher frequency of observation.

Somewhat concerning is the fact that Papushev et al. acquired some of their long-term apparent spin period data from an amateur astronomer database (PPAS catalogue). Although there are some standardized procedures involved when volunteering data for this catalogue, the spin period variations of several satellites shown in the Papushev et al. paper suggest that the observations mixed flash periods and spin periods, thereby producing confusing results. The research for this thesis involved careful observations and analysis which were conducted in controlled conditions and that were subject to rigid procedural protocols. This might be the first time that a study of the long-period spin variation has been conducted with such standards in mind.

The choice to use unfiltered images was made because the maximum amount of flux for each satellite was desired. During satellite observation, it was not known whether filtering would cause flux attenuation such that at times the satellite's signal could be below that of the background signal. Since satellite characterization was not the goal of the thesis, filters were not required. However, future research based on this thesis should involve observations using filters in order to identify the satellite's critical components and to help identify the "latitudes" of each reflecting surface. This could assist in determining the spin axes of the satellites observed.

The spin period variations of all four satellites observed for this thesis are interesting. Their shapes appear different from one another yet all have similar traits. One such trait is the deviation that occurs when the satellite is observed in between the maximum and minimum apparent spin period. This deviation is more pronounced in the angular acceleration and angular velocity plots since a theoretical curve is compared to the observations in both cases. The trends in each observed spin period graph suggest that a satellite with a higher apparent spin period will have a greater deviation from the hypothetical curve.

Telstar 401's and Echostar 2's observed spin period variation periods appear to be different by nearly 75 days. Echostar 2's apparent spin period variation period appears to be very near one full Earth orbit period (about 365 days), suggesting that its spin axis is not precessing very quickly. This hypothesis is based on the solar radiation pressure's effect on a satellite with two solar panels, as discussed in Chapter 14.

The physical characteristics of each satellite were heavily researched. However, obtaining any detailed information on the masses and dimensions of each satellite’s components proved to be extremely difficult. Attempted contact with the satellite manufacturers and owners was largely unsuccessful and academic papers did not include any information on the satellites’ “box”, dish and solar panel masses and dimensions. The only method available to determine these characteristics was to obtain an artist’s conception of the satellite (preferably a face-on portrait) and to use the scaling factor of the image to determine the lengths and widths of the components. One such artist’s conception was obtained from an image of a scale model of the Telstar 401 satellite which was found within a newspaper article that was being sold on E-Bay. The uncertainties corresponding to each of the physical characteristics were therefore understandably large. The masses of the solar panels were determined by using the published values of the area densities of “black” silicon and triple-junction (3-J) gallium-arsenide (GaAs) solar cells. Further study concerning the physical characteristics of these satellites would have to involve easier access to the specifications of either the individual satellites or their general model designs.

When determining the moment of inertia of the total satellite system, the communications dishes were omitted for two reasons:

- no literature concerning the physical characteristics of the satellite dishes could be found; and
- the communications dishes probably would not have contributed much to the mass or the moment of inertia of the satellite.

The heaviest elements of the four satellites were assumed to be their central “box” and their solar panels, the former having a much higher mass than the latter.

When more accurate data with respect to the physical characteristics of these four satellites is obtained, it will become possible to determine more accurate MOIs; thus the theoretical curves of the angular acceleration and angular velocity will be more accurate. Such higher accuracy determinations would alter the spin period deviation curves; however the extent of the difference is currently unclear.

Telstar 401's and Echostar 2's observed spin period deviation might be occurring for unique reasons or for the same reason. If a synodic effect is the sole reason for this deviation, then cyclical spin axis precession might explain these apparent periodic deviations. It might be also possible that the solar panels are not perfectly symmetrical, either physically or reflectively, about the width of the panel. Therefore, the SRP might not only cause the satellite to spin end over end, but it might also cause the satellite to spin about an additional spin axis along the length of the solar panels. This additional motion might create a spin axis precession and this might partially explain Telstar 401's spin period variation period. One more possibility is that the two larger communications dishes were acting as solar sails. If the SRP on the dishes were not equal to one another, then a net torque acting nearly perpendicular to the length axes of the solar panels would cause the satellite to spin with a spin axis perpendicular to the spin axis due to the solar panels.

The spin period deviation could be caused by any, some or all of the aforementioned effects. Determining the true effects of the spin period deviations, with the correct proportionalities, will require more observations over a period of months, if not years. The workload may be somewhat lightened by observing similar or identical box-wing designs (such as the AS-7000 series in the case of Telstar 401 and Echostar 2).

The theoretical synodic effect scenarios presented in Chapter 15 represented an initial basic attempt at understanding the relative motions of the satellite in its orbit and the satellite’s spin motion with respect to the illumination source (the Sun) and an Earth-bound observer. Other factors that can affect a satellite’s synodic spin period of a satellite include the inclination of the satellite’s orbit and the relative motion of the observer with respect to a (nearly) geosynchronous satellite. None of the selected satellites are truly “geosynchronous” because their positions in the observing site’s local sky did change slowly over the course of the year. For instance, HGS-1 appeared to change its position from the low eastern sky to the mid southern sky from March 2012 to March 2013; representing an angle change of approximately 60 degrees in right ascension. It is currently unclear whether this motion had significantly affected the satellite’s spin axis or its synodic spin period. Subsequent models of this motion’s effects on the synodic spin period will be required to answer this question.

The questions that will arise from this research will no doubt be too numerous to mention here. The only way to answer these questions is to continuously monitor the apparent spin periods of these four satellites and possibly other inactive box-wing GEO satellites.

FUTURE WORK

The research presented in this thesis represents only a small fraction of the amount of research remaining to fully describe the spin dynamics of inactive box-wing GEO satellites. More research is required to obtain and study the light curves of all inactive box-wing GEO satellites; not just the four satellites selected for this thesis.

Much of the research presented in this thesis would need to be verified with observations of other inactive box-wing GEO satellites. Future research should determine if other box-wing satellites in GEO orbits exhibit the same characteristics and are affected by the same factors.

The image data extraction software that was used to extract FITS header time tags and satellite flux will be improved in the summer of 2013. Plans include automating the entire front to back interface; including automatic detection (and rejection) of stars as well as the automatic detection of the satellite at the beginning of each new “block”. This software enhancement would further reduce the amount of time required to extract image data and therefore would reduce the overall time of image analysis.

Observations of the four inactive box-wing GEO satellites studied in this thesis will have to continue for several more years in order to confirm the relationship between the theoretical and observed angular acceleration curves and in order to confirm the effects of solar radiation pressure and other external forces. One year is not an adequate period of time to determine the overall behaviour of a spinning box-wing GEO satellite because the four satellites’ periods of spin period variability are still not known.

Observations of the four selected satellites in this thesis were made with an unfiltered CCD detector because detection of the dim GEO satellites required a non-attenuated light path from the telescope to the CCD chip. Obtaining images of the four selected satellites using U, I, V and/or B filters and a larger aperture telescope is planned for the fall of 2013.

Special effort will be made to gain more knowledge of the physical characteristics of each of the four satellites studied here. This additional information will decrease the uncertainties, especially for the solar panel dimensions and the masses of the components. This effort may consequently reduce the uncertainties of the satellites’ moments of inertia.

Further development of the theoretical synodic effect concepts described in this thesis is planned. This work will include the addition of the orbit inclination effects. It is especially important to model the synodic effects of these satellites in order to determine their real sidereal dynamics. Such an effort would assist public and private efforts to rescue, salvage or deorbit derelict geosynchronous satellites.

RECOMMENDATIONS

Additional regular and accurate spin period observations of the four satellites described in this thesis and as many others that can be monitored should be made. The attitude dynamics of these types of satellites will need to be known to a higher degree of accuracy if future rescue, salvage and deorbit missions are to succeed. If the four satellites studied in this thesis are any indication, the spin dynamics of these types of satellites could be like fingerprints. Monitoring the dynamics of box-wing and other designs of satellites could be of great benefit to space science and satellite industries.

Once known, the spin dynamics, external forces and the synodic effects of these types of satellites will be of invaluable use to help inform future generations of cadets and civilian students who wish to know more about the satellite population. It is hoped that the concepts described in this thesis can be used to motivate others to take this research further.

A Canadian satellite characterization database could be initiated so that light curves and spin periods can be stored in one place. This can be done so that the spin dynamics of all derelict box-wing GEO satellites in orbit can be studied. The CASTOR Satellite Catalogue (CSC) lists those satellites that can be detected with electro-optical equipment similar to that which was used for this thesis. The CSC can be expanded to include the satellite characterizations and specific spin dynamics of each of these satellites. This thesis is the result of one person’s effort with one telescope and one CCD camera. If additional sensors are dedicated to the long-term high frequency observation of

GEO satellites’ spin periods, a more complete picture of synodic effects and external forces will be realized.

LIST OF REFERENCES

Bergin, C., “Sea Launch lofts Echostar 11 – Echostar 2 dies on orbit,” NASA Spacefilight.com: www.nasaspaceflight.com/2008/07/sea-launch-lofts-echostar-11-echostar-2-dies-on-orbit.

Boeing Defense Space and Security, “Asiasat 3 Fact Sheet,” www-prd-09.boeing.com/boeing/defensespace/space/bss/factsheets/601/asiasat_3/asiasat_3.page.

Boeing Defense Space and Security, “Solidaridad 1 Fact Sheet,” http://www.boeing.com/boeing/defensespace/space/bss/factsheets/601/solidaridad/solidaridad.page.

Boeing Satellite Services (BSS) Archives, http://web.archive.org/web/20091230143546/http://boeing.com/defense-space/space/bss/factsheets/601/solidaridad/solidaridad.html.

Cao, Y. et al., “Measurement of Optical Characteristics of Solar Panels Used on Satellite,” *9th International Symposium on Antennas Propagation and EM Theory (ISAPE)*, 746-748, 2010.

Cattabiani, M. F., “One small step along the information highway,” *The Morning Call*, Newspaper Article, September 29, 1993.

Chapman, David M.F. ed., *Observer’s Handbook 2013*, The Royal Astronomical Society of Canada (RASC), Webcom Inc., 2013.

Chu, D., “GOES-R Stationkeeping and Momentum Management,” *29th Annual AAS Guidance and Control Conference*, Breckenridge, Colorado, 2006.

Earl, M. A., “A Sea of Satellite Dishes”, *the Royal Astronomical Society of Canada*, http://ottawa-rasc.ca/articles/earl_mike/Satellite_Tracking/Dishes/Satellite_Dishes.html.

Earl, M. A., “The CASTOR Satellite Catalogue,” http://www.castor2.ca/13_Catalogue.

Encyclopedia Astronautica, http://www.astronautix.com.

Gillmore, D. ed., “Spacecraft Thermal Control Handbook – Volume 1: Fundamental Technologies,” The Aerospace Press, 2002.

Glover, D., “NASA Experimental Communications Satellites: 1958-1995,” *Beyond the Ionosphere: The Development of Satellite Communications*, the NASA History Series, NASA History Office, 51-64, 1997.

GOES-R Mission Website, http://www.goes-r.gov/multimedia/sc_images.html.

Green, R.M., “Spherical Astronomy,” Cambridge University Press, 1985.

Hall, D. et al., “ÀMOS Observations of NASA’s IMAGE Satellite,” *The 2006 AMOS Technical Conference Proceedings*, Kihei, Hawaii, 2006.

Karavaev, Yu. et al., “Astrophotometrical Observation of Artificial Satellites and Study of the Technical Status of Parental Bodies of Space Debris at Geostationary Ring,” *Proceedings of the Fourth European Conference on Space Debris*, Darmstadt, Germany, 18-20 April 2005.

Kelso, T. S., “Satellite Times: More on Geostationary Orbits,” http://celestrak.com/columns/v04n09.

Kinney, L. and Michalopolous, P., “Before the Federal Communications Commission – In the Matter of Echostar Corporation - Amendment to Application for New Earth Station Under Call Sign E080120 to Add EchoStar 8 Operating as a Mexican Licensed Satellite at 77° W.L. as a Point of Communication,” File No. SES-LIC-20080516-00652, July 24, 2008.

Krebs, G. D., “Gunter’s Space Page,” http://space.skyrocket.de.

Kucharski, D. et al., “16 years of LAGEOS-2 Spin Data - from launch to present,” *Proceedings of the 16th International Workshop on Laser Ranging*, 358-364, 1992.

Lambert, J. et al., “Observations of Retired Boeing 376 Spacecraft,” Air Force Maui Optical and Supercomputing Observatory (AMOS), 2003.

Lockheed Martin, “Lockheed Martin Commercial GEO Satellites Surpass 1,000 Years in Orbit”, Press Release, June 26, 2012.

Magnusson, P. et al., “Determination of the Pole Orientation and Shapes of Asteroids,” *Asteroids II*, University of Arizona Press, 67-95, 1989.

McCants, M., “PPAS Database,” http://www.prismnet.com/~mmccants/bwgs/.

NASA, NASA Climate and Radiation Science Research Portal: http://atmospheres.gsfc.nasa.gov.

NASA, NASA Goddard Space Flight Center, http://www-istp.gsfc.nasa.gov.

NASA, NASA National Space Science Data Center, http://nssdc.gsfc.nasa.gov.

NASA, “Whisker Failures,” http://nepp.nasa.gov/whisker/failures/index.htm.

Ocampo, C., “Trajectory analysis for the lunar flyby rescue of AsiaSat-3/HGS-1,” *Annals of the New York Academy of Sciences*, Vol. 1065, 232-53, 2005.

Papushev, P. et al., “Investigations of the evolution of optical characteristics and dynamics of proper rotation of uncontrolled geostationary artificial satellites,” *Advances in Space Research*, Vol. 43, 1416-1422, 2009.

Reddy, M. R., “Space solar cells – tradeoff analysis,” *Solar Energy Materials & Solar Cells*, Vol. 77, 2003.

Ricardo’s GEO-Orbit Quick-Look, http://www.geo-orbit.org.

Santa Barbara Instrument Group (SBIG), ST-9XE CCD User Manual, www.sbig.com/site/assets/files/18223/usbmanrev14.pdf.

Satbeams SPRL, www.satbeams.com.

Satellite Encyclopedia, www.tbs-satellite.com.

Serway, R. A., "Physics for Scientists and Engineers, 3rd Ed.," Saunders College Publishing, 1990.

Somers, P., "Cylindrical RSO Signatures, Spin Axis Orientation and Rotation Period Determination," *The 2011 AMOS Technical Conference Proceedings*, Kihei, Hawaii, 2011.

Space-Track: The Source for Space Surveillance Data, https://www.space-track.org.

Telesat Canada: http://www.telesat.com/about-us/why-satellite.

Vallado, D.A., "Fundamentals of Astrodynamics and Applications – 3rd ed.," Microcosm Press / Springer, 2007.

Wallace, B. et al., "Determination of spin axis orientation of Geosynchronous objects using space-based sensors: an initial feasibility investigation", Defense Research and Development Canada (DRDC) – Ottawa, 2010.

Wertz, J. R., "Orbit and Constellation Design and Management," Microcosm Press / Springer, 2009.

Whitlock, D., "History of On-orbit Satellite Fragmentations – 13th ed.," NASA Orbital Debris Program Office, 2004.

Wood, R., "Lageos 2 spin rate and orientation", NERC Space Geodesy Facility, UK, 2002.

APPENDIX A: OBSERVATION LOGS

Observations made of the four selected satellites are listed in temporal order in Tables A.1 to A.4.

The headers of the tables are described as follows:

- **Observation Date** lists the date of the observation session in UTC. The dates containing two consecutive days indicate that the observation session was conducted through 00:00 UTC
- **Observation Session Time Range** lists the range of times (in UTC) within which the observations of the satellite were made. The time range does not include gaps in the observations
- **Image Exposure Time** lists the integration time for all images obtained with the corresponding observation session time range
- F**lux Range** lists the observed brightness range (in ADU / 100) of the satellite within the observation session time range for the specific exposure time indicated
- **Measured Synodic Spin Period** lists the observed apparent spin period (in seconds) of the satellite for the corresponding observation session
- **Notes** contain information pertaining to a satellite's observing session, where required for clarification

Table A.1: Solidaridad 1 (NORAD #22911) Observations

Observation Date (UTC) (yy/mm/dd)	Observation Session Time Range (UTC) (hh:mm – hh:mm)	Image Exposure Time (s)	Flux Range (ADU/100)	Measured Synodic Spin Period (s)	Notes
12/03/06	04:14 – 04:33	1.0	323 - 772	N/A	Test images Insufficient number of observations for determining one complete apparent spin period Background signal not subtracted
12/06/15	02:23 – 04:39	1.5	2 - 509	968 ± 3	
12/06/23	07:19 – 08:23	1.0	1 - 196	958 ± 5	
12/06/24	02:23 – 03:55	1.0	1 - 886	956 ± 12	Large spin period variations observed
12/07/11	05:41 – 06:54	1.0	6 - 1336	938 ± 10	Large spin period variations observed
12/07/19	06:25 – 08:28	1.0	1 - 690	928 ± 6	
12/07/21	05:38 – 08:32	1.0	16 - 680	929 ± 7	
12/07/25	02:05 – 04:32	1.0	1 – 1169	923 ± 38	Large spin period variations observed
12/08/09	05:01 – 05:12	1.5	N/A	N/A	Clouds obscured seeing Insufficient number of observations for determining one complete apparent spin period
12/08/18	04:06 – 06:09	1.0	1 - 755	897 ± 2	
12/08/20	03:44 – 05:18	1.0	1 - 285	894 ± 4	
12/08/23	04:30 – 05:34	1.5	1 - 356	895 ± 6	
12/08/25	04:14 – 05:42	1.0	1 – 233	890 ± 2	
12/09/10	04:51 – 05:59	1.0	1 – 411	880 ± 6	
12/09/12	04:27 – 05:52	1.0	1 - 277	877 ± 3	
12/09/13	03:29 – 05:14	1.0	1 – 152	877 ± 7	
12/09/16	04:22 – 06:00	1.0	2 – 554	871 ± 9	

Table A.1 Continued

12/09/20	04:32 – 04:54	1.0	N/A	N/A	Clouds obscured seeing Insufficient number of observations
12/10/05	04:53 – 05:50	1.0	0 – 1495	859 ± 2	
12/10/17	04:12 – 05:03	1.0	0 – 1062	850 ± 6	
12/11/07	05:17 – 07:03	1.0	0 – 350	846 ± 9	
12/11/09	04:17 – 05:55	1.0	1 – 357	848 ± 10	Large spin period variations observed
12/11/16	04:01 – 05:26	1.0	1 – 288	849 ± 6	
12/12/06	07:45 – 09:01	1.0	2 – 440	845 ± 7	
12/12/12	05:04 – 05:52	1.0	1 – 194	845 ± 7	
12/12/20	04:23 – 05:35	1.0	1 – 429	845 ± 7	
13/02/05	05:40 – 06:03	1.0	N/A	N/A	Clouds obscured seeing Insufficient number of observations
13/02/10	06:08 – 06:58	1.0	1 – 2147	820 ± 2	
13/02/16	06:37 – 06:55	1.0	N/A	N/A	Clouds obscured seeing Insufficient number of observations
13/02/17	05:29 – 05:41	1.0	N/A	N/A	Clouds obscured seeing Insufficient number of observations
13/03/31	03:12 – 04:28	1.0	1 - 2610	784 ± 8	

Table A.2: Telstar 401 (NORAD #22927) Observations

Observation Date (UTC) (yy/mm/dd)	Observation Time Range (UTC) (hh:mm – hh:mm)	Image Exposure Time (s)	Flux Range (ADU/100)	Estimated Synodic Spin Period (s)	Notes
12/03/06	02:48 – 03:15	1.0	0 - 397	145.0 ± 0.3	Test images
12/06/11	04:49 – 07:06	1.0	7 – 162	160.9 ± 0.1	
12/06/14	04:29 – 06:13	1.0	8 – 121	161.5 ± 0.1	
12/06/16	04:34 – 06:09	0.5	2 – 54	161.9 ± 0.1	
12/06/23	04:15 – 06:26	1.0	10 – 162	163.3 ± 0.1	
12/06/27	04:08 – 05:06	1.0	10 – 384	164.2 ± 0.2	
12/07/11	04:39 – 05:38	0.5	7 – 231	167.3 ± 0.2	
12/07/19	04:33 – 06:23	1.0	3 – 264	169.0 ± 0.1	
12/07/21	03:59 – 05:17	1.0	5 – 266	169.3 ± 0.2	
12/08/09	04:09 – 04:56	1.0	1 – 289	170.0 ± 0.8	
12/08/13	03:13 – 04:48	1.0	1 – 56	169.7 ± 0.2	
12/08/18	02:44 – 04:04	0.5	1 – 280	168.7 ± 0.2	
12/08/20	02:48 – 03:40	1.0	1 – 190	168.4 ± 0.2	
12/08/22	01:12 – 02:45	1.0	1 – 439	168.0 ± 0.1	
12/08/24	04:54 – 05:36	1.0	4 – 276	167.5 ± 0.2	
12/09/09	05:00 – 05:45	1.0	4 – 295	164.4 ± 0.2	
12/09/10	03:56 – 04:49	1.0	4 – 263	164.2 ± 0.2	
12/09/11	03:28 – 04:04	1.0	3 – 265	164.0 ± 0.2	
12/09/12	03:35 – 04:25	1.0	3 – 258	163.8 ± 0.2	
12/09/14	03:26 – 04:05	1.0	1 – 198	163.3 ± 0.2	
12/09/16	03:25 – 04:20	1.0	3 – 273	163.1 ± 0.2	
12/09/20	03:33 – 04:18	1.0	2 – 173	162.3 ± 0.6	

Table A.2 Continued

12/10/05	03:20 – 04:48	1.0	1 – 175	159.9 ± 0.2	
12/10/10	02:22 – 02:41	1.0	N/A	N/A	Clouds obscured seeing Insufficient number of observations
12/10/17	01:41 – 04:10	0.5	3 – 111	158.0 ± 0.2	
12/11/07	04:46 – 05:15	1.0	4 – 436	154.5 ± 0.3	
12/11/09	03:55 – 04:15	1.0	5 – 120	154.2 ± 0.5	
12/11/14	05:10 – 06:11	1.0	6 - 1371	153.4 ± 0.3	
12/11/22	06:23 – 06:58	1.0	2 – 195	152.1 ± 0.3	
12/12/06	06:32 – 07:41	0.5	1 – 414	149.4 ± 0.2	
12/12/12	03:58 – 05:02	1.0	2 – 1289	148.4 ± 0.2	
12/12/20	03:31 – 04:20	1.0	4 – 391	147.8 ± 0.4	
13/01/21	05:13 – 05:47	1.0	5 – 854	151.1 ± 0.3	
13/02/01	02:54 – 03:15	1.0	1 – 209	153.1 ± 0.4	
13/02/05	04:34 – 05:38	1.0	1 – 189	154.2 ± 0.2	
13/02/10	04:50 – 06:05	1.0	4 – 141	155.1 ± 0.1	
13/02/16	05:09 – 06:34	1.0	4 – 168	156.2 ± 0.1	
13/02/17	03:09 – 04:25	1.0	5 – 335	156.4 ± 0.1	
13/03/06	04:20 – 05:41	1.0	1 – 176	159.7 ± 0.1	
13/03/15	04:22 – 04:49	1.0	2 – 105	161.6 ± 0.4	
13/03/17	05:50 – 07:03	1.0	12 – 169	161.8 ± 0.2	
13/03/30	01:59 – 03:01	1.0	5 - 99	164.6 ± 0.2	

Table A.3: Echostar 2 (NORAD #24313) Observations

Observation Date (UTC) (yy/mm/dd)	Observation Time Range (UTC) (hh:mm – hh:mm)	Image Exposure Time (s)	Flux Range (ADU/100)	Measured Synodic Spin Period (s)	Notes
12/03/12	01:37 – 03:21	1.0	8 – 1028	502.5 ± 0.3	Test images
12/05/12	01:53 – 09:03	1.0	10 – 379	447.2 ± 0.1	
12/05/20	01:53 – 04:03	1.0	3 – 184	442.3 ± 0.1	
12/05/21	01:55 – 03:57	1.0	4 – 167	441.8 ± 0.2	
12/05/24	02:02 – 06:34	1.0	7 – 192	440.4 ± 0.1	
12/06/11	02:20 – 04:47	1.0	7 – 190	432.8 ± 0.2	
12/06/14	02:25 – 04:27	1.0	7 – 226	431.5 ± 0.2	
12/06/16	02:19 – 04:32	0.5	2 – 116	430.8 ± 0.2	
12/06/23	02:25 – 04:14	0.5	5 – 177	427.6 ± 0.2	
12/06/24	07:52 – 08:46	1.0	6 – 230	427.3 ± 0.5	
12/06/27	02:28 – 04:06	0.5	6 – 259	425.9 ± 0.2	
12/07/11	02:19 – 04:36	0.5	4 – 285	417.5 ± 0.1	
12/07/19	02:28 – 04:30	0.5	6 – 262	411.3 ± 0.2	
12/07/21	02:16 – 03:54	0.5	1 – 151	409.7 ± 0.2	
12/08/09	02:52 – 04:06	0.5	2 – 95	389.8 ± 0.2	
12/08/13	04:34 – 04:40	0.5	N/A	N/A	Clouds obscured seeing Insufficient number of observations
12/08/18	01:24 – 02:42	0.5	2 – 396	382.4 ± 0.2	
12/08/20	01:16 – 02:45	0.5	1 – 684	381.5 ± 0.2	
12/08/22	02:48 – 03:53	0.3	3 – 460	380.5 ± 0.2	
12/08/24	01:14 – 03:30	0.5	2 – 3753	379.7 ± 0.2	Bright specular reflections observed
12/09/09	01:14 – 03:01	0.5	1 – 228913	376.0 ± 0.2	Bright specular reflections observed

Table A.3 Continued

12/09/10	00:40 – 02:20	0.5	1 – 195902	375.8 ± 0.2	Bright specular reflections observed (naked eye)
12/09/11	02:03 – 03:21	0.5	1 – 256347	375.8 ± 0.2	Bright specular reflections observed (naked eye)
12/09/12	01:46 – 03:21	0.5	1 – 139295	375.9 ± 0.2	Bright specular reflections observed (naked eye)
12/09/13	02:03 – 03:20	0.5	2 – 173766	375.8 ± 0.2	Bright specular reflections observed (naked eye)
12/09/14	02:05 – 03:20	0.5	1 – 176495	375.9 ± 0.2	Bright specular reflections observed (naked eye)
12/09/16	02:05 – 03:19	0.5	2 – 268569	376.0 ± 0.2	Bright specular reflections observed (naked eye)
12/09/20	02:06 – 05:15	0.5	1 – 155015	376.8 ± 0.1	Bright specular reflections observed (naked eye)
12/10/03-04	23:47 – 01:18	0.5	1 – 831	387.6 ± 0.2	
12/10/10	00:08 – 02:19	0.5	1 – 137889	393.2 ± 0.2	Bright specular reflections observed (naked eye)
12/10/16-17	23:23 – 01:39	0.5	1 – 1823	401.2 ± 0.2	Bright specular reflections observed (naked eye)
12/11/06-07	23:54 – 01:34	0.5	2 – 123	425.7 ± 0.2	
12/11/09	02:31 – 03:52	0.5	2 – 129	427.8 ± 0.2	
12/11/14	03:38 – 05:08	0.5	1 – 117	433.0 ± 0.2	
12/11/16-17	22:46 – 23:54	1.0	1 – 270	435.7 ± 0.3	
12/11/22	04:45 – 06:19	0.5	2 – 152	440.3 ± 0.2	
12/12/06	00:50 – 01:55	0.5	1 – 85	450.0 ± 0.2	
12/12/12	02:00 – 02:45	1.0	3 – 189	453.5 ± 0.7	
12/12/19-20	23:13 – 00:29	1.0	3 – 243	457.3 ± 0.3	
12/12/20	11:12 – 11:44	1.0	1 – 454	457.3 ± 0.8	
13/01/01-02	23:16 – 01:09	1.0	3 – 359	462.8 ± 0.5	
13/01/21	05:51 – 06:29	1.0	7 – 443	472.5 ± 0.7	
13/02/01	00:45 – 02:00	1.0	2 – 367	480.9 ± 0.3	
13/02/04-05	23:36 – 00:25	1.0	4 – 310	485.0 ± 0.2	
13/02/10	00:00 – 01:25	1.0	2 – 222	491.1 ± 0.3	
13/02/16	04:31 – 08:05	1.0	1 – 254	500.4 ± 0.6	
13/02/17	00:21 – 02:33	1.0	1 – 179	501.7 ± 0.2	
13/03/06	00:12 – 02:11	1.0	5 – 1138	530.9 ± 0.2	Bright specular reflections observed

Table A.3 Continued

13/03/09	00:19 – 02:07	1.0	2 – 13803	532.2 ± 0.2	Bright specular reflections observed
13/03/15	00:21 – 02:02	1.0	1 – 480	530.1 ± 0.2	
13/03/17	00:17 – 02:21	1.0	2 - 398	528.7 ± 0.2	
13/03/30	00:43 – 05:18	1.0	2 - 1279	508.1 ± 0.1	

Table A.4: HGS-1 (NORAD #25126) Observations

Observation Date (UTC) (yy/mm/dd)	Observation Time Range (UTC) (hh:mm – hh:mm	Image Exposure Time (s)	Flux Range (ADU/100)	Synodic Spin Period (s)	Notes
12/03/12	04:56 – 05:16	1.0	228 – 302	N/A	Test images Insufficient number of observations to determine one complete spin period
12/06/15	07:01 – 08:29	0.5	4 – 47	1648 ± 6	
12/07/25	04:34 – 06:19	1.0	6 – 87	1713 ± 22	Large spin period variations observed
12/08/18	06:45 – 08:24	0.5	0 – 28	1782 ± 1	
12/08/19	01:18 – 05:21	0.5	0 – 32	1758 ± 7	
12/08/22	04:03 – 05:50	0.5	2 – 249	1729 ± 4	
12/09/09	03:10 – 04:57	1.0	0 – 60	1725 ± 15	
12/09/11	00:36 – 05:11	1.0	0 – 141	1788 ± 12	
12/09/12	00:34 – 01:41	1.0	5 – 49	1797 ± 4	
12/09/13	00:26 – 02:00	1.0	6 – 71	1814 ± 11	
12/09/14	00:27 – 02:01	1.0	8 – 361	1847 ± 7	
12/09/16	00:24 – 02:01	1.0	3 – 350	1844 ± 2	
12/09/20	00:39 – 02:04	1.0	12 - 77	1747 ± 4	
12/10/05	01:21 – 03:10	1.0	2 – 64	1717 ± 30	Large spin period variations observed
12/10/17	03:06 – 03:19	0.5	5 – 300	1762 ± 5	
12/11/07	01:36 – 04:43	1.0	12 – 71	1622 ± 21	
12/11/08	03:26 – 05:07	1.0	3 – 80	1610 ± 3	
12/11/08-09	23:36 – 02:12	1.0	10 – 243	1591 ± 13	
12/11/15-16	23:50 – 03:58	1.0	3 – 426	1620 ± 12	
12/11/22	00:13 – 04:42	1.0	2 – 52	1561 ± 17	
12/12/06	03:18 – 06:21	1.0	6 – 78	1519 ± 12	

Table A.4 Continued

12/12/11-12	22:49 – 01:55	1.0	5 – 126	1445 ± 7	
12/12/20	00:35 – 03:28	1.0	13 – 815	1457 ± 4	
13/01/02	01:11 – 03:27	1.0	8 – 598	1368 ± 7	
13/02/05	01:27 – 03:50	1.0	8 – 989	1258 ± 6	Bright specular reflections observed
13/02/16	08:07 – 09:56	1.0	3 - 97	1249 ± 3	
13/03/31	00:36 – 05:25	1.0	6 - 483	1310 ± 10	

APPENDIX B: DERIVATIONS

DERIVATION OF EQUATION 15.19

A simplified illustration of Figure 15.16 is shown in Figure B.1. Eq. 15.19 finds the equatorial declination (δ_{EQ}) of an inclined plane (with respect to the Equatorial Plane) from the equatorial right ascension angle (μ_{EQ}) measured from the "ascending node".

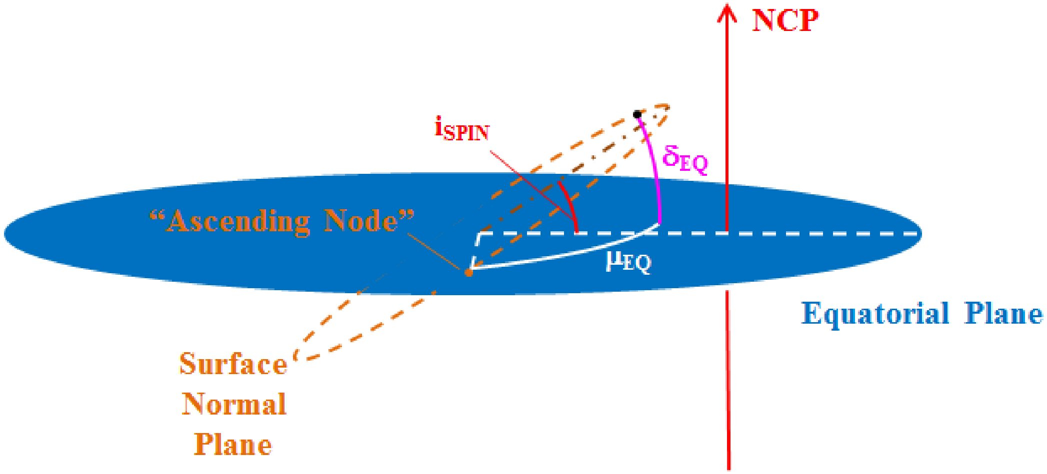

Figure B.1: A Simplified Illustration of Figure 15.16 Showing the Equatorial Coordinates of a Point on the Surface Normal Plane

If the inclined plane is projected onto the Equatorial Plane, an ellipse will be formed, as shown in Figure B.2. Let the semi-major axis of the ellipse (a) be some unit distance d. Therefore, the semi-minor axis of the ellipse (b) will be $d \cdot \cos(i_{spin})$. The length of any point on the ellipse will be $d \cdot \cos(\delta_{EQ})$. The equation of the ellipse in Cartesian coordinates is shown in Eq. B.1

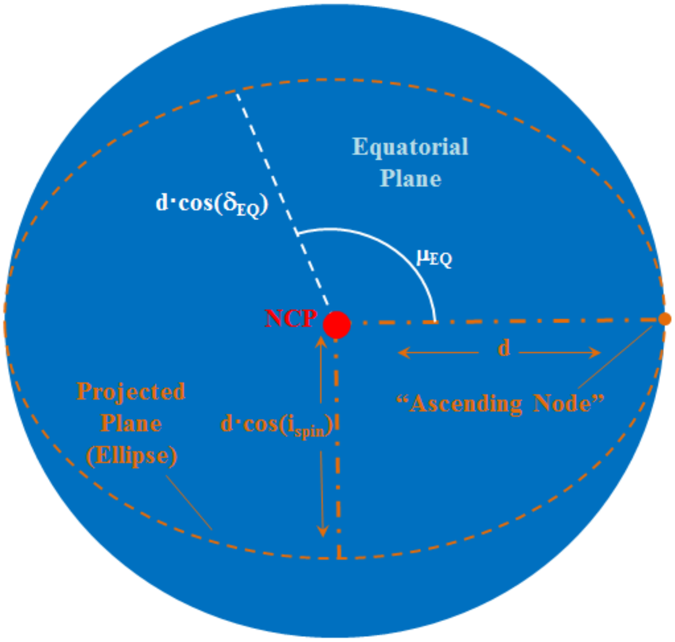

Figure B.2: Ellipse Formed by Projecting Surface Normal Plane onto Equatorial Plane

Eq. B.1

$$\frac{\mathbf{x^2}}{\mathbf{d^2}} + \frac{\mathbf{y^2}}{\left[\mathbf{dcos}(\mathbf{i_{spin}})\right]^2} = \mathbf{1}$$

The Cartesian coordinates (x, y) can be expressed in spherical coordinates, as shown in Eq. B.2 and Eq. B.3.

Eq. B.2

$$\mathbf{x = dcos(\delta_{EQ})cos(\mu_{EQ})}$$

Eq. B.3

$$\mathbf{y = dcos(\delta_{EQ})sin(\mu_{EQ})}$$

The spherical coordinate representations of x and y can be substituted for x and y in Eq. B.1, resulting in Eq. B.4.

Eq. B.4

$$\frac{\left[\mathbf{d}\cos\left(\boldsymbol{\delta}_{\mathbf{EQ}}\right)\cos\left(\boldsymbol{\mu}_{\mathbf{EQ}}\right)\right]^{\mathbf{2}}}{\mathbf{d}^{\mathbf{2}}}+\frac{\left[\mathbf{d}\cos\left(\boldsymbol{\delta}_{\mathbf{EQ}}\right)\sin\left(\boldsymbol{\mu}_{\mathbf{EQ}}\right)\right]^{\mathbf{2}}}{\left[\mathbf{d}\cos\left(\mathbf{i}_{\mathbf{spin}}\right)\right]^{\mathbf{2}}}=\mathbf{1}$$

Eq. B.4 can be simplified to what is shown in Eq. B.5. Note that the unit distances (d) cancel, leaving only the angles.

Eq. B.5

$$\left[\cos\left(\boldsymbol{\delta}_{\mathbf{EQ}}\right)\cos\left(\boldsymbol{\mu}_{\mathbf{EQ}}\right)\cos\left(\mathbf{i}_{\mathbf{spin}}\right)\right]^{\mathbf{2}}+\left[\cos\left(\boldsymbol{\delta}_{\mathbf{EQ}}\right)\sin\left(\boldsymbol{\mu}_{\mathbf{EQ}}\right)\right]^{\mathbf{2}}=\cos^{\mathbf{2}}\left(\mathbf{i}_{\mathbf{spin}}\right)$$

Eq. B.6 shows the solution for the declination.

Eq. B.6

$$\cos^{\mathbf{2}}\left(\boldsymbol{\delta}_{\mathbf{EQ}}\right)=\frac{\cos^{\mathbf{2}}\left(\mathbf{i}_{\mathbf{spin}}\right)}{\left[\cos\left(\boldsymbol{\mu}_{\mathbf{EQ}}\right)\cos\left(\mathbf{i}_{\mathbf{spin}}\right)\right]^{\mathbf{2}}+\sin^{\mathbf{2}}\left(\boldsymbol{\mu}_{\mathbf{EQ}}\right)}$$

Finally, with the assistance of the Pythagorean trigonometric identity, Eq. B.7 shows the final result, which is the square of Eq. 15.19.

Eq. B.7

$$\cos^{\mathbf{2}}\left(\boldsymbol{\delta}_{\mathbf{EQ}}\right)=\frac{\cos^{\mathbf{2}}\left(\mathbf{i}_{\mathbf{spin}}\right)}{\mathbf{1}-\cos^{\mathbf{2}}\left(\boldsymbol{\mu}_{\mathbf{EQ}}\right)\sin^{\mathbf{2}}\left(\mathbf{i}_{\mathbf{spin}}\right)}$$

Taking the square root of Eq. B.7 will yield two answers which will depend on the quadrant of the angle μ_{EQ}. If μ_{EQ} is between 0 and 180° from the “ascending node”, δ_{EQ} is positive. If μ_{EQ} is between 180° and 360° from the “ascending node”, δ_{EQ} is negative. These conditions are also shown in “Eq. 15.19 Conditions” in Chapter 15.

CURRICULUM VITAE

CURRICULUM VITAE

MICHAEL A. EARL

214 Old Orchard Drive
Bath, Ontario
K0H 1G0

Tel: 613-352-7544

Email: earl-m (at) castor2.ca

SUMMARY OF EXPERTISE

Over 15 years of practical experience in space science projects, space science education, astronomical research, computer technology and project administration, including:

Extensive knowledge of satellite tracking with electro-optical equipment, celestial coordinate systems, orbital mechanics, orbit propagation and astronomy software.

Independently detected, catalogued and tracked over 4,000 individual orbiting satellites using independently designed satellite tracking facility from 2007 to 2011. This accomplishment is a first for any professional science institution in Canada and the first for any single individual in the world.

Extensive knowledge of satellite physics, deriving and analytically solving mathematical equations related to astronomy and spherical coordinate systems.

Extensive knowledge of astronomy, including authoring professional astronomy research papers and coordinating astronomy education programs.

Extensive experience in teaching the subject of astronomy to novices and advanced students.

Excellent knowledge of satellite dynamics and orbit modelling and astrodynamics software, especially AGI’s “Satellite Tool Kit” (STK).

Extensive experience with PC computer maintenance; hardware and software, desktops and laptops.

Extensive experience with website construction, maintenance, administration and management.

Extensive knowledge of all Microsoft Office products, including Word, Excel, PowerPoint, Outlook, FrontPage and SharePoint Designer.

Extensive knowledge of Windows-based computers, operating systems and networking.

Extensive knowledge of Database Management, Requirements Management, Configuration Management and Change Management.

Extensive knowledge of Telelogic’s “Dynamic Object-Oriented Requirements Suite” (DOORS).

Familiarity with Unix-based systems, especially Sun Solaris OS.

Familiarity with MATLAB coding.

PROFESSIONAL EXPERIENCE

In order of most recent to earliest

Sep 2012 ~ Mar 2013 **Calian Technologies**

Researcher

Observing and obtaining light curve data for up to 100 unique inactive box-wing telecommunications satellites for the Department of Research and Development Canada (DRDC) - Ottawa.

Aug 2012 ~ May 2013 **Royal Military College of Canada - Kingston, Ontario**

Teaching Assistant

Marking assignments, tests and final exam of 2nd year physics courses PHE 225/226 (modern physics), PHE 205 (mechanics), PHE 260B (astronomy) and first-year laboratory PHE104.

Nov 2011 ~ Mar 2012 **Calian Technologies**

Researcher

Determining best targets for observing inactive box-wing geosynchronous satellites' light curves in partnership with the Department of Research and Development Canada (DRDC) Ottawa.

Sep 2011 ~ May 2013 **Royal Military College of Canada - Kingston, Ontario**

Graduate Student – MSc Physics (Space Science)

Currently working to complete Physics (Space Science) MSc thesis at RMC. Thesis research is the observation and light curve analysis of inactive (spinning) “box-wing” design geosynchronous telecommunications satellites.

Mar 2011 ~ Aug 2011 **Lions Club - Port Dover, Ontario**

Astronomy Course Coordinator and Instructor

Coordinated and conducted a high-calibre 10-week astronomy course for 20 students in the Port Dover and Simcoe area.

Constructed and presented PowerPoint presentations at every class describing, in detail, the specific concepts being taught.

Designed, constructed and managed a CASTOR Astronomy Course website.

Feb 2011 ~ Apr 2011 **Lions Club - Port Dover, Ontario**

Computer Course Coordinator and Instructor

Coordinated and conducted a 10-week basic computer course for students in the Port Dover and Simcoe area.

Constructed and presented PowerPoint presentations at every class describing, in detail, the specific concepts being taught.

Nov 2010 ~ Sep 2011 **Norfolk County, Ontario**

Computer Technician

Servicing computers owned by private individuals and businesses.

In one month, serviced computers with problems ranging from slow performance, to bad hard drive sectors, to removing high risk viruses, spyware, malware and ransomware.

Currently assisting customers with basic and advanced computer setup, file organization and wireless networking.

For every visit, a detailed report is written documenting the exact technical details.

Every computer has been satisfactorily repaired with 100% customer satisfaction.

Apr 2010 ~ Jun 2010 **Lanark Community Programs - Carleton Place, Ontario**

Astronomy Course Coordinator

Coordinated and conducted a high-calibre 10-week astronomy course for 25 students, ages 10 and up.

Constructed and presented PowerPoint presentations at every class describing, in detail, the specific concepts being taught.

Designed, constructed and managed the CASTOR Astronomy Course website.

Sep 2008 ~ Jun 2010 **Mississippi Valley Conservation Authority - Lanark, Ontario**

Coordinator: Night Sky Conservation Program

Proposed the Night Sky Conservation (NSC) program to consolidate existing Mississippi Valley Conservation public astronomy and light pollution abatement programs.

Coordinated all NSC program components, including all astronomy courses and night sky tours.

Conceived, engineered, constructed and maintained the original Night Sky Conservation web site.

Jun 2007 ~ Aug 2008 **SNC Lavalin ProFac Ltd. - Ottawa, Ontario**

DOORS Database Administrator

Created, set up and managed the DOORS ERS database for the Joint Support Ship (JSS) project requirements.

Authored a DOORS user guide with special emphasis on the JSS specific requirements of the software.

Jan 2007 ~ Oct 2011 **Canadian Astronomy, Satellite Tracking and Optical Research**

Owner and Founder

Founded CASTOR in 2007 as a privately owned satellite tracking business, focused on introducing the science of satellite tracking to the private satellite industry.

Initiated a privately funded research project that detected and tracked nearly 2,053 individual satellites over the 2007 year to celebrate Sputnik’s 50th anniversary and to raise awareness of the emerging science of satellite tracking.

Continued a privately funded research project that detected and tracked an additional 1,100 satellites to celebrate the International Year of Astronomy (IYA) in 2009 and to raise awareness of the emerging science of satellite tracking.

Continued a privately funded research project that detected and tracked an additional 400 satellites in 2010.

Concluding a privately funded research project that will detect and track over 4,000 satellites from January 1, 2007 to August 31, 2011.

Authored technical and research papers concerning the emerging science of satellite tracking, including the February 10, 2009 collision of Iridium 33 and Cosmos 2251. One of these papers were internally distributed to senior leaders within the United States Strategic Command (USSTRATCOM) and acknowledged by General Kevin P. Chilton, Commander of USSTRATCOM.

Conceived, engineered, and maintains the Canadian Astronomy, Satellite Tracking and Optical Research (CASTOR) website: **www.castor2.ca**.

Mar 2005 **Northeast Space Company Inc. – Ottawa, Ontario**

Subcontractor for Bristol Aerospace (Ottawa)

Derived and delivered a geodetic correction quaternion for the design of the SWIFT satellite.

Sep 2004 ~ Apr 2005 **Carleton University Mechanical and Aerospace Engineering Department, Ottawa, Ontario**

Lead Engineer – AEGIS Project

One of several lead engineers who offered their assistance, guidance and expertise to 4th year Aerospace Engineering students in the Aegis remote sensing satellite project.

May 2004 ~ Oct 2010 **Mr. Paul G. Comision – Ottawa, Ontario**

Contractor: Observatory Upgrade;

Engineered, constructed, integrated and tested remote control circuitry for Mr. Paul G. Comision’s personal astronomical observatory.

Responsible for remote control electronics maintenance, observatory upkeep and computer maintenance.

Aug 2002 ~ Nov 2003 **Calian Technologies, Ottawa, Ontario**

Requirements Manager and Intermediate Engineering Specialist: DND Surveillance of Space Project (SofSP)

Installed, configured, coordinated, and managed the DOORS database for the SofSP.

Imported all existing SofSP requirements documents into the SofSP DOORS database.

Managed all SofSP technical requirements using DOORS, including recording all rationale for each specific requirement and how they relate to other critical requirements.

Authored several DOORS user guides with special emphasis on the SofSP specific requirements of the software.

Provided DOORS technical support and training for all SofSP team members.

Installed, configured and utilized Telelogic's "Proposal Evaluation Solutions" (PES) for SofSP evaluation of proposed Sapphire satellite designs.

Tracked and provided tracking data for several lost satellites to the U.S. 1st Command and Control Squadron (1CACS) (Cheyenne Mountain) using own equipment based on the original CASTOR design.

Apr 2001 ~ Aug 2002 **Calian Technologies - Ottawa, Ontario**

Junior Engineering Specialist: DND Surveillance of Space Project (SofSP)

Participated in the definition of the Sapphire Satellite Mission Requirements by using satellite tracking expertise gained while employed at the SSRAL at RMC.

Provided assistance in the optical astronomy aspects of satellite tracking for the SofSP.

Provided planning and performed the calibration and alignment of the Canadian Automated Small Telescope for Orbital Research in Valcartier (CASTOR V) satellite tracking facility at the Defence Research and Development Centre in Valcartier (DRDC Valcartier) in Val Belair, Quebec.

Acquired knowledge of Database Management, Requirements Management, Configuration Management, and use of the Telelogic DOORS ERS software.

May 1997 ~ Apr 2001 **Calian Technologies - Ottawa, Ontario**

Senior Technician - Space Surveillance Research and Analysis Laboratory (SSRAL): Royal Military College of Canada - Kingston, Ontario

Engineered, supervised construction, tested, calibrated, operated and maintained the Canadian Automated Small Telescope for Orbital Research (CASTOR) ground-based optical satellite tracking facility.

Engineered, and maintained specialized in-house software for automated satellite tracking.

Derived orbit mechanics, coordinate transformation and coordinate translation equations specifically for use with the CASTOR facility.

Initiated and performed thorough searches for lost and missing satellites for the American 1st Command and Control Squadron (1CACS) (Cheyenne Mountain).

Facilitated public relations activities for CASTOR and the SSRAL.

Initiated and performed tumble period analysis of inactive Russian Molniya satellites.

Created and maintained an orbit element database of nearly 10,000 artificial satellites.

Communicated regularly with representatives of the U.S. Space Surveillance community.

Performed periodic orbit determination using CASTOR observations of satellites.

Provided satellite tracking and astronomy expertise in several RMC Space Science graduate level theses.

VOLUNTEER EXPERIENCE

In order of most recent to earliest

May 2005 ~ Jan 2007 **Royal Astronomical Society of Canada – Ottawa Centre, Ottawa, Ontario**

Webmaster

Critical management of the Ottawa RASC website, including the creation of new pages to accommodate RASC Members' suggestions and requests.

Reorganized the entire Ottawa RASC website structure to maximize its efficiency.

Dec 2004 ~ Sep 2005 **Royal Astronomical Society of Canada – Ottawa Centre, Ottawa, Ontario**

Vice-President

Assisted the President of the Ottawa RASC with planning of the 2006 RASC General Assembly.

May 2004 ~ Dec 2006 **Royal Astronomical Society of Canada – Ottawa Centre, Ottawa, Ontario**

Artificial Satellites Coordinator

Periodically presented lectures concerning observations of artificial satellites at monthly Ottawa RASC meetings.

A key point of contact within the Ottawa RASC concerning the observation of artificial satellites by astronomers.

Dec 2002 ~ Dec 2004 **The Royal Astronomical Society of Canada – Ottawa Centre, Ottawa, Ontario**

Ottawa Centre Meeting Chair

Organized all speakers for the monthly meetings.

Organized and chaired monthly meetings.

Managed all RASC Observing Coordinators.

Apr 2001 ~ Oct 2005	**Royal Astronomical Society of Canada – Ottawa Centre, Ottawa, Ontario**

SMARTScope Member and Technical Assistant

Engineered and constructed a daylight sensor that would automatically close SMARTScope's observatory dome shutter at dawn and prevent any user from opening the dome shutter during daylight hours.

Provided technical assistance to the SMARTScope team, especially in the areas of remote control observatory troubleshooting, reliability testing and routine maintenance.

PUBLISHED RESEARCH PAPERS

The Iridium 33 - Cosmos 2251 Collision / Creating Liability Awareness for Space Property and the Future of Space Surveillance. May 2009. Internally distributed to Senior Leaders within the United States Strategic Command and acknowledged by General Kevin P. Chilton: Commander of USSTRATCOM.

The CASTOR "Sputnik 50th Anniversary Satellite Tracking Bonanza": Project Overview and Preliminary Analysis*:* The Journal of the Royal Astronomical Society of Canada, August 2008.

Determining the Orbit Height of a Low-Earth Orbiting Artificial Satellite Observed near the Local Zenith. The Journal of the Royal Astronomical Society of Canada, October 2006.

Determining the Range of an Artificial Satellite Using its Observed Trigonometric Parallax. The Journal of the Royal Astronomical Society of Canada, April 2005.

Coincidental Supernovae in Spiral Galaxy NGC 772. The Journal of the Royal Astronomical Society of Canada, April 2004.

The Space Surveillance Research and Analysis Laboratory. The Journal of the Royal Astronomical Society of Canada, December 2000.

Progress in Research and Development on the CASTOR K Satellite Tracking Facility**:** Presented at the Canadian Aeronautic and Space Institute (CASI) Astro2000 Conference, Ottawa, Ontario Canada, 9 November 2000.

Progress Report for the Canadian Automated Small Telescope for Orbital Research (CASTOR) Satellite Tracking Facility: Presented at the MIT Lincoln Laboratory 2000 Space Control Conference, Boston, Massachusetts U.S.A., 13 April 2000.

The Canadian Automated Small Telescope for Orbital Research (CASTOR) - A RAVEN System in Canada: Presented at the Air Force Maui Optical Station (AMOS) Conference, Kihei, Hawaii U.S.A., 3 September 1999.

PUBLISHED ARTICLES

Iridium 33 and Cosmos 2251: A Historic Collision. Ottawa RASC AstroNotes March 2009.

Hickson 50 and the Question of Magnitude. Ottawa RASC AstroNotes July 2008 - **Winner of the 2008 Ottawa RASC AstroNotes Article of the Year**.

CASTOR's "Sputnik 50th Anniversary Satellite Tracking Bonanza". Ottawa RASC AstroNotes April 2008.

The Astro Power Cube. Ottawa RASC AstroNotes, March 2006.

Finding the Chandra X-Ray Observatory. Ottawa RASC AstroNotes, January/February 2006.

A Sea of Satellite Dishes. Ottawa RASC Website, January 10, 2006.

Tracking Telesat's Past from Rideau Ferry. Ottawa RASC Website, November 25, 2005.

Why Amateur Astronomers would make Excellent Satellite Trackers. Ottawa RASC Website, October 4, 2005.

Coincidental Supernovae in Spiral Galaxy NGC 772. The Journal of the Royal Astronomical Society of Canada, April 2004.